Tailored Online Diagnostics for a Laser-driven Plasma Ion Source Prototype

Daniel Haffa

München 2019

Tailored Online Diagnostics for a Laser-driven Plasma Ion Source Prototype

Dissertation

an der Fakultät für Physik
Ludwig–Maximilians–Universität München

vorgelegt von

Daniel Haffa
geboren in Karlsruhe

München, den 05.08.2019

Erstgutachter: Prof. Dr. Jörg Schreiber

Zweitgutachter: Prof. Dr. Ulrich Schramm

Tag der mündlichen Prüfung: 27. September 2019

"Feynman was a truly great teacher. He prided himself on being able to devise ways to explain even the most profound ideas to beginning students. Once, I said to him, "Dick, explain to me, so that I can understand it, why spin one-half particles obey Fermi-Dirac statistics." Sizing up his audience perfectly, Feynman said, "I'll prepare a freshman lecture on it." But he came back a few days later to say, "I couldn't do it. I couldn't reduce it to the freshman level. That means we don't really understand it."

David L. Goodstein about Richard Feynman [1].

Zusammenfassung

Diese Arbeit beschreibt die Entwicklung verschiedener Elemente einer lasergetriebenen Ionenquelle im Centre for Advanced Laser Application (CALA). Das Herzstück von CALA ist der ATLAS-3000, ein Titan-Saphir Laser System, dass mit seiner Spitzenleistung von 3 Petawatt und einer Repetitionsrate von 1 Hz zu den weltweit führenden seiner Art gehört. Ziel ist es, eine für Anwendungen nutzbare Ionenquelle zu entwickeln. In einer 2-jährigen Prototypentestphase im **L**aboratory for **EX**treme Photonics (LEX Photonics) wurden verschiedene Elemente der lasergetriebenen Ionenquelle weiterentwickelt und Neuentwicklungen implementiert. Die zuverlässige Beschleunigung von Protonen mit einer Repetitionsrate von 0.5 Hz und mehreren 100 Schüssen innerhalb weniger Stunden zählt zu den Errungenschaften, die unter anderem erste Bestrahlungen von Zebrafisch-Embryonen ermöglichte.

Der Hauptteil der Arbeit behandelt die Entwicklung zweier neuartiger online Diagnostikmethoden. Mit einer chirped-pulse Probingmethode waren wir in der Lage, die Dynamik der Laser-Plasma Interaktion innerhalb eines Schusses in 9, um jeweils ca. 200 fs zeitlich getrennten Schnappschüssen mit einer räumlichen Auflösung von ca. 25 µm aufzunehmen. Die Messungen erlaubten, die zeitliche und räumliche Intensitätsverteilung des Laserpulses bei voller Energie während der Interaktion zu analysieren, eine Methode die wir **T**emporally **R**esolved **I**ntensity **C**ontouring (TRIC) getauft haben. Die entwickelte Probingmethode ermöglicht darüber hinaus ein Monitoring der Plasmainteraktion während des Vollschussbetriebs und kann somit weitere wichtige Erkenntnisse zur Optimierung der Ionenquelle liefern. Mit **I**on-**B**unch **E**nergy **A**coustic **T**racing (I-BEAT) wurde ein Detektor entwickelt, der in der Lage ist, das Energiespektrum von einzelnen sehr intensiven Ionenpulsen zu vermessen. Grundlage von I-BEAT ist die Messung von Schallwellen, die erzeugt werden, wenn Ionen in Wasser abgebremst werden und dadurch Energie deponieren. Die zeitliche Form der Schallwellen enthält die Information über die räumliche Verteilung der Energiedeposition, woraus sich die Anfangsenergieverteilung der Ionen bestimmen lässt. In zwei experimentellen Kampagnen in LEX Photonics und am Draco Lasersystem in Dresden haben wir die Funktionalität von I-BEAT demonstriert. Dabei haben wir I-BEAT zur Diagnostik von fokussierten Ionenpulsen verwendet und die Ergebnisse mit denen von Gafchromic Film-Stacks verglichen. I-BEAT besticht vor allem durch seine Einfachheit, hohe Repitionsrate, seinen dynamischen Messbereich hin zu hohen Ionendichten und der Insensitivität auf elektromagnetische Störsignale. Ein weiterer großer Vorteil ist, dass die Ionen mit Hilfe der Schallwelle in Zukunft auch bei biomedizinischen Bestrahlungen direkt im Sample nachgewiesen werden könnten.

Die Neuentwicklungen und Erkenntnisse dieser Arbeit finden sich in großer Breite im Forschungszentrum CALA wieder und werden dazu beitragen, die experimentelle Arbeit auf einem hohen Niveau wieder aufzunehmen.

Abstract

This work describes the development of various elements of a laser-driven ion source at the **C**entre for **A**dvanced **L**aser **A**pplications (CALA). At the heart of CALA is the ATLAS-3000, a titanium sapphire laser system that, with its peak performance of 3 petawatts and a repetition rate of 1 Hz, is one of the world's leading high power systems of its kind. The goal is to develop an ion source for applications. In a two-year prototype test phase at the **L**aboratory for **EX**treme Photonics (LEX Photonics), various elements of the laser-driven ion source were optimized and new developments implemented. The reliable acceleration of protons with a repetition rate of 0.5 Hz and capability of several 100 shots within a few hours is one of the achievements that, among other things, enabled the first irradiation of zebrafish embryos.

The main part of this thesis deals with the development of two novel online diagnostic methods. Using a chirped-pulse probing method, we were able to record the dynamic of the laser plasma interaction dynamics during a single laser shot in 9 snapshot images with a temporal separation of about 200 fs and a spatial resolution of about 25 µm. The measurements allowed us to analyze the temporal and spatial intensity distribution of the laser pulse at full energy during the interaction; a method we referred to as **T**emporally **R**esolved **I**ntensity **C**ontouring (TRIC). In addition, this probing method enables monitoring the plasma interaction during operation with full laser energy and can thus provide further important insights that enable optimizing of the laser-driven ion source. With **I**on-**B**unch **E**nergy **A**coustic **T**racing (I-BEAT), a detector has been developed that can measure the energy spectrum of single, very intense ion bunches. The basis of I-BEAT is the measurement of sound waves that are generated, when ions in water are decelerated and thus deposit energy. The temporal shape of the sound waves contains the complete information about the spatial distribution of the energy deposition, from which the incident energy distribution of the ions can be determined. In two experimental campaigns; one at LEX Photonics and one at the Draco laser system in Dresden, we demonstrated the functionality of I-BEAT. We used I-BEAT to diagnose focused ion bunches and compared the results with those from Gafchromic film stacks. I-BEAT is distinguished by its simplicity, high repetition rate capability, high dynamic range towards high ion densities and insensitivity to known deleterious effects of electromagnetic pulses on signals. Another great advantage is that the ions could, by detecting the emerging sound waves, be detected directly in the sample of future applications, as for example with biomedical irradiations.

At the CALA research facility, the new developments and findings of this work can be

found on a larger scale. These can facilitate the planned high level experimental research program and that will help to resume the experimental research on a high level.

Contents

Zusammenfassung vii

Abstract ix

Contents xiv

List of Figures xvii

List of Tables xix

1 Scientific Context and Motivation 1

1.1 Particle Acceleration . . . 2

1.1.1 Merits of Laser-Accelerated Ions . . . 2

1.2 Laser-Driven Ion Sources . . . 4

1.2.1 High Power Laser Systems . . . 4

1.2.2 Laser-Driven Ion Acceleration . . . 6

1.2.3 Applications of Laser-Driven Ions . . . 9

1.3 Centre for Advanced Laser Application . . . 10

1.4 Thesis Structure . . . 12

2 Theoretical Concepts: Waves, Light and Plasmas 15

2.1 Waves . . . 16

2.2 Electromagnetic Waves . . . 17

2.2.1 Vector Potential . . . 19

2.2.2 Laser Pulses . . . 19

2.2.3 Temporal and Spatial Intensity . . . 20

2.2.4 Focusing Device . . . 22

2.3 Laser-Induced Plasmas . . . 23

2.3.1 Laser Interacting with a Single Particle . . . 23

2.3.2 Introduction to Plasmas . . . 24

2.3.3 Ionization and Damage Threshold . . . 27

2.4 Laser-Driven Ion Acceleration . . . 30

2.4.1 Collisionless Absorption . . . 30

2.4.2 Heating of Electrons . . . 31
2.4.3 Acceleration Mechanism for Ions . . . 33
2.5 Acoustic Measurements of Ions . . . 34
2.5.1 Interaction of Ions with Matter . . . 35
2.5.2 Thermodynamics . . . 36
2.5.3 Acoustic Waves . . . 39
2.6 The Beauty of Waves . . . 43

3 LION at LEX Photonics 45
3.1 ATLAS-300 . . . 46
3.1.1 Temporal Intensity Distribution . . . 47
3.1.2 Spatial Intensity Distribution in the Focal Plane . . . 48
3.1.3 Additional Laser Diagnostics . . . 49
3.2 Experimental Area and Setup . . . 50
3.2.1 LION Chamber in LEX Photonics . . . 51
3.2.2 Ion Wide Angle Spectrometer . . . 53
3.2.3 Quadrupoles - Focusing the Ion Bunch . . . 54
3.2.4 Setup Assembly . . . 54
3.3 Summary and Result . . . 56
3.3.1 Lessons Learned in LEX Photonics . . . 59

4 TRIC: Temporally Resolved Intensity Contouring 61
4.1 Introduction to TRIC . . . 62
4.1.1 Spatio-Temporal Intensity Distribution . . . 62
4.2 Setup and Configuration of the Experiment . . . 64
4.2.1 Pump-Probe Configuration . . . 65
4.3 Interpretation of the Observation . . . 68
4.3.1 Relation of Laser Intensity and Plasma Contour . . . 68
4.3.2 Determination of the Threshold Intensity . . . 73
4.4 Analysis and Evaluation of the Measurement . . . 73
4.4.1 Marginals of the Complete Distribution: Contrast Curve and Laser Focus . . . 76
4.4.2 Increased Dynamic Range of the Focus Picture . . . 76
4.4.3 The Temporal Intensity Distribution . . . 77
4.5 Summary and Discussion . . . 79

5 I-BEAT: Ion-Bunch Energy Acoustic Tracing 81
5.1 Ion Bunch Instrumentation - Detector Systems . . . 82
5.1.1 Detector Schemes for Laser-Driven Ions . . . 82
5.2 Introduction to I-BEAT . . . 83
5.2.1 Background . . . 84
5.2.2 Concept of I-BEAT . . . 85
5.3 Design and Development of I-BEAT . . . 86
5.3.1 Detector for I-BEAT . . . 86
5.3.2 Calibration . . . 87
5.3.3 Simulated Annealing . . . 92
5.3.4 Validation Measurements at the MLL Tandem Accelerator . . 94
5.4 Experimental Campaigns and Results . . . 95
5.4.1 Experimental Campaign at LEX Photonics . . . 95
5.4.2 Experimental Campaign at the DRACO . . . 101
5.4.3 Conclusion of the Measured Results . . . 104
5.5 Applications of I-BEAT at (Laser-Driven) Ion Sources . . . 104
5.6 Discussion and Outlook . . . 108

6 Summary and Outlook 115
6.1 Summary: LEX Photonics . . . 116
6.2 Outlook: CALA . . . 117
6.3 Epilogue: I-TRIC . . . 120

A Experimental Setups in LEX Photonics and CALA 121
A.1 Laboratory for Extreme Photonics - Closer Look . . . 122
A.1.1 Components of High Power Laser Systems . . . 122
A.1.2 Optimization of the Laser Contrast . . . 123
A.1.3 The Risk of Back-Reflection . . . 127
A.1.4 The Vacuum Microscope . . . 128
A.1.5 Transmitted Laser Light . . . 129
A.1.6 Back-Reflected / Back-Scattered Laser Light . . . 130
A.1.7 Targets for Laser-Driven Ion Acceleration . . . 131
A.1.8 Ion Wide Angle Spectrometer . . . 134
A.1.9 Quadrupoles . . . 136
A.2 Centre for Advanced Laser Applications . . . 139
A.2.1 ATLAS-3000 . . . 140

A.2.2 Laser Beam Delivery . . . 142
A.2.3 Experimental Cave(s) . . . 144

B Theoretical Parts - a Deeper Look 147
B.1 Solving the Wave Equation - Fourier Optics . . . 147
B.1.1 Green's Theorem . . . 148
B.1.2 Excursion Green's Function . . . 149
B.1.3 Integral Theorem of Helmholtz and Kirchhoff . . . 151
B.1.4 Fresnel-Kirchhoff Diffraction Formula . . . 152
B.1.5 Rayleigh-Sommerfeld Formulation of Diffraction . . . 154
B.1.6 Common Approximations for the Propagation of Waves . . . 155
B.1.7 The Fourier Transform . . . 157
B.1.8 Time Dependence . . . 158
B.1.9 Conclusion . . . 159
B.2 Some Basics of (Laser) Light . . . 161
B.2.1 Polarization of Light . . . 161
B.2.2 Reflectance and Brewster Angle . . . 162
B.2.3 Group Velocity Dispersion . . . 162
B.2.4 Spatial Intensity Distribution . . . 163
B.2.5 Resolution of an Optical System . . . 164
B.3 Nonlinear Optics . . . 164
B.4 Optical Devices for High-Power Laser Systems . . . 166
B.4.1 Sequoia and Tundra: Third-Order Autocorrelators . . . 166
B.4.2 Pockels Cell . . . 166

List of Symbols and Abbreviations 169

Publications and conference contributions 173

Bibliography 177

Acknowledgements 199

List of Figures

1.1 History of laser intensity 4
1.2 Chirped pulse ampfliciation 5
1.3 Ti:sapphire petawatt laser facilities 6
1.4 Laser-driven protons 7
1.5 The concept of ILDIAS 8
1.6 The Bragg peak 9
1.7 CALA - Centre for Advanced Laser Applications 10

2.1 Ionization processes 29
2.2 Plasma regimes 32
2.3 Stopping power for protons in water 35

3.1 ATLAS-300 46
3.2 The ATLAS-300 contrast 48
3.3 HDR focus in LEX Photonics 49
3.4 Diagnostic of incoming laser light 50
3.5 Two experimental chambers at LEX Photonics 51
3.6 Experimental setup at LEX Photonics 52
3.7 Proton energy spectrum evaluated with WASP 53
3.8 Ion focus 54
3.9 Application setup at LEX Photonics 55
3.10 Shot summary at LEX Photonics 56
3.11 Irradiation of Zebrafish embryos 58

4.1 The trick of TRIC 65
4.2 Experimental setup for TRIC 66
4.3 Nexus of intensity distribution and plasma shape 70
4.4 Illustration of the principle of TRIC 72
4.5 Spatio-temporal intensity distribution 75
4.6 Comparison of TRIC to contrast curve and HDR focus image 77

5.1 I-BEAT 85
5.2 The detector of I-BEAT 87

5.3 Setup at the MLL Tandem accelerator . . . 88
5.4 Calibration required . . . 89
5.5 Transferfunction of I-BEAT . . . 90
5.6 Workflow of simulated annealing . . . 93
5.7 I-BEAT at the MLL Tandem accelerator . . . 94
5.8 I-BEAT in the vacuum chamber . . . 96
5.9 I-BEAT at LEX Photonics . . . 97
5.10 Evaluation of different ion bunch diameters for I-BEAT . . . 98
5.11 Comparison of I-BEAT to the WASP. . . . 100
5.12 Dark current of the Radeye . . . 101
5.13 I-BEAT at DRACO - setup . . . 101
5.14 I-BEAT at DRACO - results . . . 103
5.15 I-BEAT in a TNSA regime . . . 105
5.16 A multi-species spectrum with I-BEAT . . . 106
5.17 The detector of I-BEAT . . . 109
5.18 I-BEAT 3-D . . . 111
5.19 I-BEAT at PHELIX . . . 112

6.1 Succesful experimental campaigns at LEX Photonics . . . 117
6.2 Lessons learned for CALA . . . 118
6.3 Picture of the LION chamber . . . 119

A.1 Laser contrast . . . 123
A.2 Generation of prepulses by postpulses . . . 124
A.3 Optimization of the REGEN . . . 125
A.4 Generation of direct prepulses . . . 126
A.5 Discovery of more prepulse . . . 127
A.6 Plasma and light diagnostics . . . 130
A.7 Target wheel . . . 132
A.8 Wide angle Spectrometer at LEX Photonics . . . 135
A.9 Ion diagnostic at LEX Photonics . . . 136
A.10 Quadrupoles at LEX Photonics . . . 137
A.11 Evolution of the LION cave . . . 139
A.12 Centre for Advanced Laser Application . . . 139
A.13 ATLAS-3000 . . . 140
A.14 Contrast with the Ring-REGEN . . . 141

A.15 Laser beam delivery 143
A.16 The LION cave 144
A.17 Experimental chamber and setup in LION 145
A.18 Picture of the LION chamber 146

B.1 Historical development of wave theory 148
B.2 Integral theorem of Helmholtz and Kirchoff 151
B.3 Fresnel, Kirchhoff, Sommerfeld 153
B.4 Approximations for near-field and far-field 157
B.5 Sketch of a laser focus 163

List of Tables

2.1 Thermodynamic quantities 37

4.1 Intensities used for TRIC 69

5.1 Notation of different types of acoustics 84
5.2 Calculation of energy spectrum obtained with I-BEAT 99

A.1 Parabolas for CALA 146

B.1 Laser quantities 161

"Over the past 6 decades lasers and laser-based devices have become indispensable in many different areas of society. With its long-range narrow beam, that can be focused on a tiny spot, a laser provides high power over a small area, useful for cutting drilling welding and micro-machining. Other applications abound. Billions of people make daily use optical disc-drives, laser printers and bar-code scanners or are entertained by amazing laser-light shows. Millions undergo laser surgery or laser-skin treatment. The laser is truly one of the many examples of how a so called blue sky discovery in fundamental science eventually may transform our daily lives"

Olga Botner (Nobel Prize Speech 2018)

Chapter 1

Scientific Context and Motivation

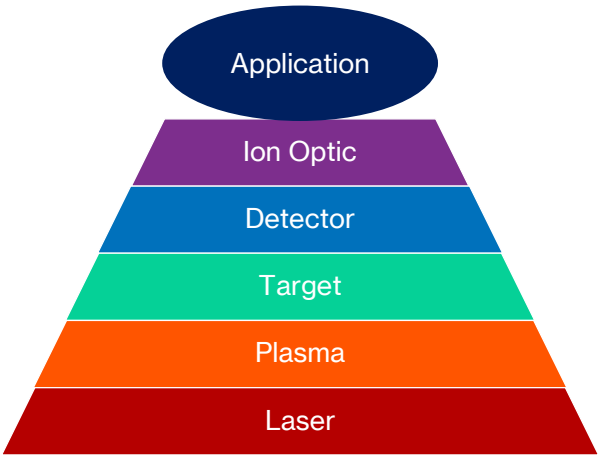

Concept of ILDIAS explained in Fig. 1.5.

Contents

1.1 Particle Acceleration 2
1.2 Laser-Driven Ion Sources 4
1.3 Centre for Advanced Laser Application 10
1.4 Thesis Structure 12

This chapter gives the reader an introduction to the topic of laser-driven ion acceleration and outlines the background and roadmap towards CALA.

1.1 Particle Acceleration

Particle acceleration has been one of the most elaborated topics of physical research for more than a century. Especially the large scale facilities such as CERN[1] or DESY[2] are among the largest projects of current physical research. Particle accelerators serve in many fields of fundamental research (nuclear physics, discovery of elementary particles or understanding our universe). But also on the application side, especially in the field of biomedical applications, particle accelerators have become more and more important. Imaging with X-rays [2–4] but also radiation therapy with X-rays or electrons [5, 6] are among the most common tools in our medical world. In the last decades, a therapy based on irradiation with ions due to the favorable Bragg-peak shape depth-dose distribution has gained more and more interest [7, 8].

The acceleration field of so called conventional accelerators[3] is limited by material breakdown due to the electric fields to $\approx$ 0.1 - 1 kV/µm [9, 10]. This limitation results in large acceleration lengths of about 10 m per GeV as an absolute limit, but more realistically 50-100 m per GeV[4]. Particle accelerators aiming for high energetic particles are hence often built in ring shape configurations using the acceleration cavities multiple times. Hereby, the maximum energy for electrons is ultimately limited by synchrotron radiation[5]. In laser-plasma acceleration, the much higher frequency of the laser supports higher acceleration gradients ($>$ MV/µm) and thus, shorter acceleration lengths. This fundamental difference to conventional radio-frequency accelerators in theory promises high kinetic energies on short distances. This work concentrates on the acceleration of ions, but laser-plasma acceleration finds wide use for electron [11] and neutron [12] acceleration as well as the generation of X-rays [13].

1.1.1 Merits of Laser-Accelerated Ions

The key differences and characteristics of **L**aser-driven **ION** acceleration (LION) acceleration, when compared to conventional accelerators, that deliver ions with similar velocities, are [14–16]:

[1] Conseil européen pour la recherche nucléaire.
[2] Deutsche Elektronen-Synchrotron.
[3] Conventional accelerators are based on an electrostatic or radio-frequency (RF) field. High energies can be obtained by staging multiple so called RF cavities after each other.
[4] Private communication with Thomas Rösch.
[5] Higher energies would require a larger radius of the accelerator ring.

1. **Small source size and low emittance:** The source size is dependent on the focal spot size of the laser and the extension of the plasma target during the interaction. It can thus be chosen to be only a few µm. This leads further to a very low transversal emittance beyond to 10^{-3} mm mrad and despite the wide energy spectrum due to the short acceleration time also a small longitudinal emittance beyond 10^{-4} eV [17].

2. **Short Bunch Length:** Due to the ultra-short duration of the laser pulse, typically few fs to 1 ps, the acceleration time, and thus the bunch duration at the source is also of this order. Due to the broad energy spectrum of the ion bunches the bunch length disperses with the distance to the source. The small longitudinal emittance is likely conserved [17].

3. **High ion flux:** Describes the number of ions per area and time. Typically, a large number of ions is emitted from a plasma. Paired with the small area and short bunch duration, the peak flux can reach 10^{12} protons/ (MeV · ns · cm^2) at 1 cm behind the target[6], and thus reach a current density of 160 A/(cm^2·MeV). Recovering those conditions at a remote application site remains one important technical aspect of beam transport and delivery [18]. The high ion flux results in high dose rates, that could reveal relevant effects for biomedical applications [19].

4. **Wide spread energy spectrum:** Even though the different mechanisms of laser- ion acceleration vary in their characteristics, a broad energy spectrum with an exponential decrease remains typical. For applications, that require well defined and narrow distributions, energy selective elements or even post-acceleration can be used. At current energy levels, this is possible, but approaching higher energy levels will require careful consideration of the thereby generated secondary radiation.

5. **Synchronized acceleration of different particle species and types of radiation:** One of the major potentials is that a laser induced plasma emits several particles species such as different ions and electrons as well as X-rays simultaneously. The synchronism of these is defined by the short pulse duration and can allow a wide range of multi-modal experiments [20].

[6] Assuming a bunch length of 100 ps, and a particle number of 10^8/ (MeV · msr) protons.

1.2 Laser-Driven Ion Sources

1.2.1 High Power Laser Systems

A fundamental prerequisite for the development of laser-ion acceleration techniques was the generation of ultra-intense laser fields. This development started with the invention of the laser [21].

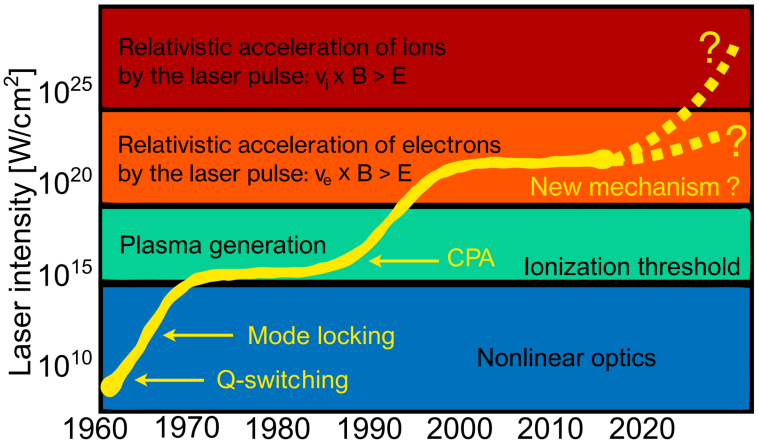

Figure 1.1 | History of laser intensity. The figure shows the increasing laser intensity over the past decades and the most relevant inventions (yellow). The colors mark different interaction regimes. The graph is adapted from [20, 22, 23].

Todays high-power laser systems are capable to reach peak intensities up to 10^{22} W cm^{-2} [24, 25]. In Fig. 1.1 the development of the laser intensity from the invention up to today is sketched. Several milestones are marked and the colors show how the increasing intensity has enabled the generation of a plasma, the acceleration of electrons to relativistic energies and will eventually reach a regime where ions can be accelerated to relativistic energies by the laser field. Among the most important enabling technologies in increasing intensity were the development of Q-switching ([26]) and mode-locking ([27–30]). **C**hirped **P**ulsed **A**mplification (CPA) has been the most significant principle that is used in the amplification of high-power laser-systems [31, 32]. CPA has been awarded with the Nobel Prize in 2018 since its concept is used in short pulse laser systems, which have enabled a wide range of applications (see epigraph of this chapter). The CPA does not change the amplification process, but rather makes high-power laser systems affordable. The damage threshold of the deployed optics is in first order dependent on the intensity and higher intensities require a larger beam size and thus, larger optic. CPA circumvents the necessity for large optics by lowering the intensity via stretching

the laser pulse in time. The short laser pulse is thus chirped (frequency dependent path-lengths) in time. The resulting decreased intensity allows an amplification at much smaller beam-size and thus, significantly reduced costs. In the final step of CPA the previously introduced chirp is inverted and the pulse compressed again to reach its final high intensity. The process of CPA is depicted in Fig. 1.2. However, Fig. 1.1 also shows that the laser intensity did stagnate recently. A further increase of the laser intensity might need another invention, such as CPA, Q-switching or mode locking.

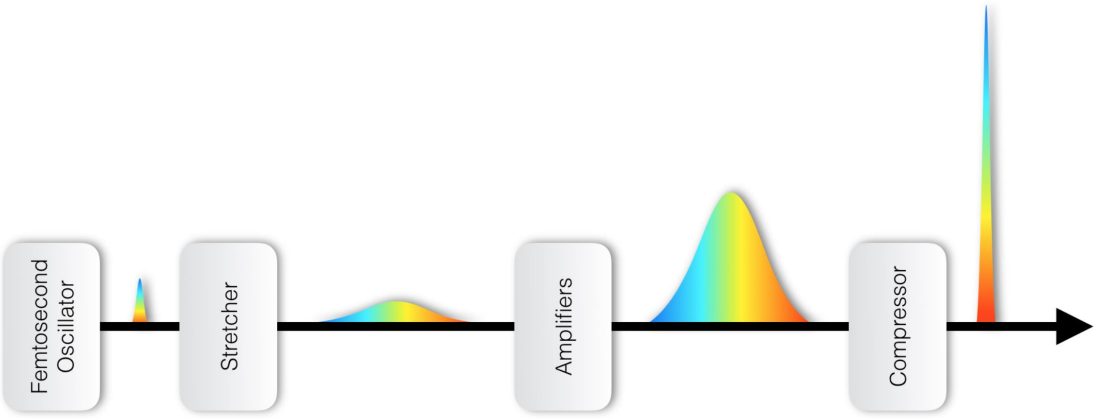

Figure 1.2 | Chirped pulse amplification. A short laser pulse is chirped and thus stretched in time to lower the intensity for amplification. The introduced chirp is compensated and the pulse is compressed to reach its final ultra-high intensity. Taken with courtesy from Ostermayr [20].

Another milestone for today's laser systems was the discovery of **T**itanium **S**apphire (Ti:sapphire) as a laser medium [33]. With its broadband amplification Ti:sapphire has been developed to the leading medium for highly intense laser systems with repetition rates in the 1 Hz regime, while the first generation of petawatt-class laser systems has been based on glass laser systems with an repetition rate of about 1 shot per hour. This tremendously increased repetition rate is one major step towards the use of laser-accelerated ions as a source for further research and application. Figure 1.3 shows existing and upcoming petawatt-class laser facilities based on Ti:sapphire laser systems.

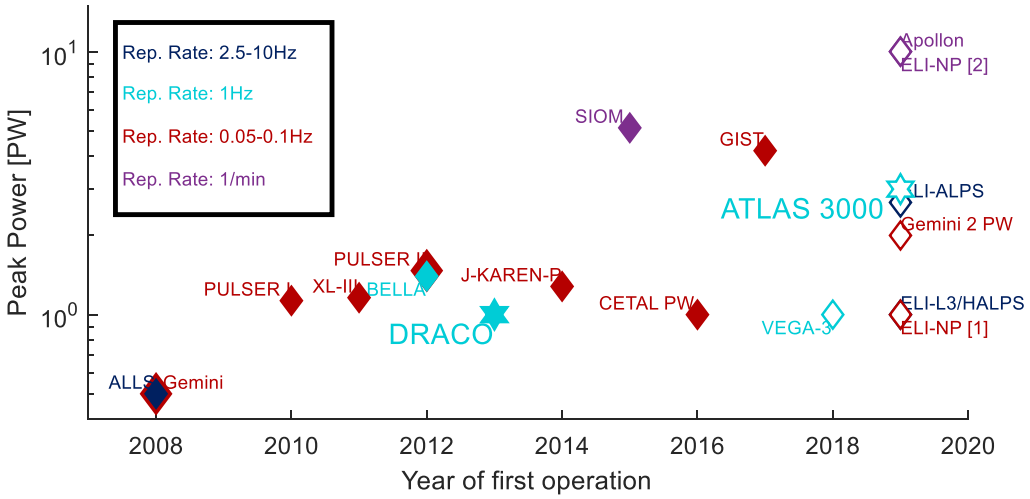

Figure 1.3 | Ti:sapphire petawatt laser facilities. This figure shows existing and upcoming petawatt-class laser facilities based on Ti:sapphire laser systems. The color depicts the repetition rate of the system. The unfilled laser systems have not yet been used for acceleration but are expected to start operation soon. The ATLAS-3000 and DRACO are highlighted with stars since they play a role in the framework of this thesis. The data has been taken from [34] with minor modifications. Laser systems that had been planned to be finished in 2017 or 2018 have been moved to 2019 and are marked unfilled, because they have not been fully demonstrated (to the author's knowledge the status in July 2019). Note that the start date of laser systems can vary since operation often starts carefully and it takes time till the full power has been achieved.

1.2.2 Laser-Driven Ion Acceleration

The first theoretical study of today's laser-driven particle acceleration techniques has been proposed by Veksler [35] in 1957. For example, the radiation pressure acceleration is one representation of a coherent acceleration process and it is interesting that he proposed it even before the laser was experimentally demonstrated for the first time. It turns out, that only today we are able to realize some of his thoughts in experiments. So it will need further effort to reach intensities (Fig. 1.1) high enough to directly act on and accelerate ions[7] and up today ion acceleration is an indirect process using electrons mediating the laser energy. The first work describing the acceleration mechanisms of electrons (wakefield acceleration) has been outlined in 1979 by Tajima [36] and since then studied intensively [37]. The first demonstration of multi MeV ions [38–40] is often regarded as the first demonstration of laser-accelerated ions even though there has been earlier demonstrations of keV ions [41, 42]. A summary of recent experimentally obtained ion yields was pub-

[7] Intensities of 10^{24} W cm^{-2} are needed. This will be explained later in Eq. (2.28).

lished in Schreiber, Bolton, and Parodi [16] and is maintained reasonably updated at https://www.alpa.physik.uni-muenchen.de. An exert from this website is shown in Fig. 1.4.

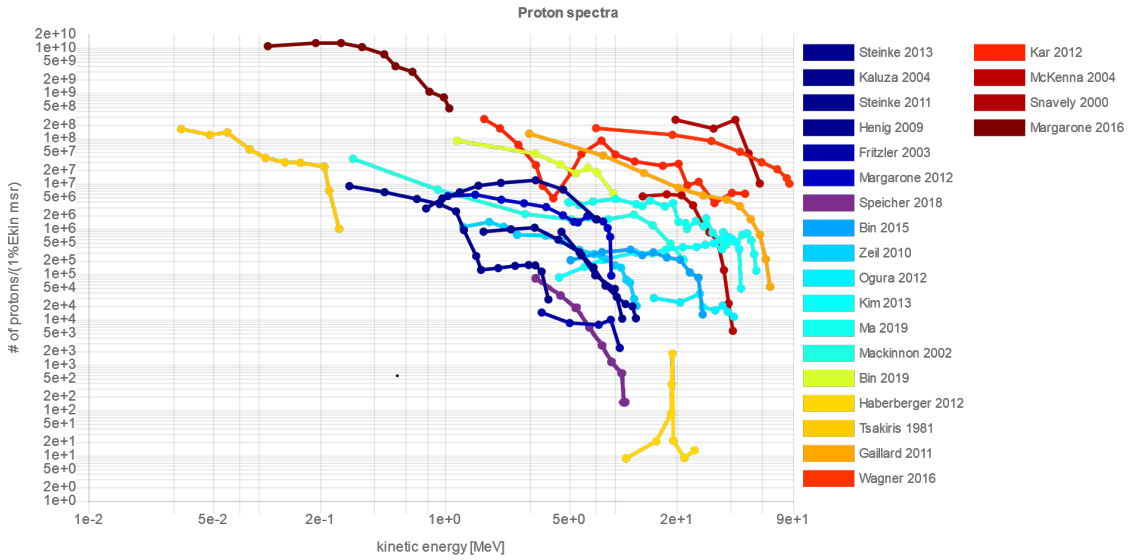

Figure 1.4 | Laser-driven protons. This is a collection of different proton spectra from https://www.alpa.physik.uni-muenchen.de. The color indicate the laser energies from low energies dark blue to high energies dark red. The data points of Speicher are taken at LEX Photonics [43]. Its color was changed from blue to purple for visibility.

The highest reported proton energies today approach 100 MeV [44–46]. The apparently modest development of maximum ion energy over the past two decades can be misleading, as it does not measure our progress correctly. A successful use of laser-driven particles requires an interplay between various components and developments. This is summarized for example in the concept of **I**ntegrated **L**aser-**D**riven **I**on **A**ccelerator **S**ystem (ILDIAS) [16]. The concept is illustrated in Fig. 1.5 and shows the pillars required for application.

During this work all pillars are tackled to improve the system towards a more reliable ion source.

1. **Pillar 1 - laser systems:** The development of lasers in the last decades has been pushed to higher repetition rates and with the generation of the multi petawatt laser systems also to increasing peak power as can be seen in Fig. 1.3.

2. **Pillar 2 - laser-plasma engineering:** This pillar describes the design and control of the plasma. This essentially requires online diagnostics to study the plasma and its evolution during the interaction. Especially probing and the

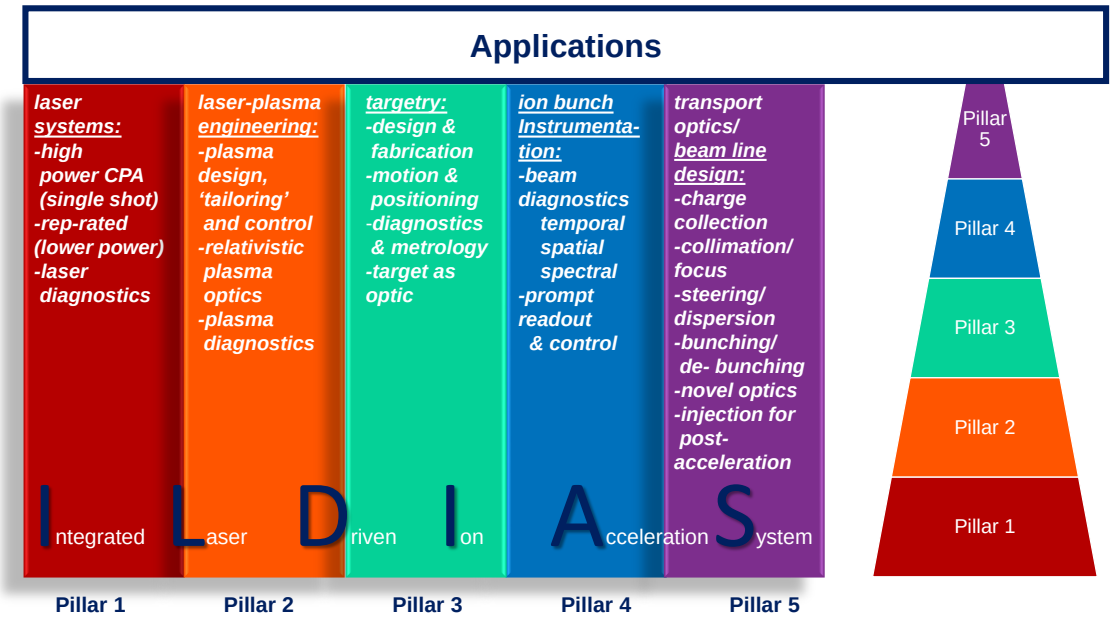

Figure 1.5 | The concept of ILDIAS. ILDIAS describes five pillars that are key to develop laser ion acceleration towards a system that can be used for applications on a daily basis. The pyramid on the right part emphasizes, that while all pillars can be studied and developed independently, they are also based upon each other, since the target choice is highly dependent on the plasma condition such as the ion transport on the ion spectra. The figure has been adapted from [16, 47].

analysis of scattered light has been exploited for gaining deeper understanding of the underlying processes.

3. **Pillar 3 - targetry:** A laser-plasma experiment basically contains the laser and the target. Since a variation of the target is often simpler than changing the laser or the plasma condition, large efforts have been devoted to design and development of new targets. The motivation for new targets was diverse, reaching from the development of mass-limited [48–54] and complex structured or multilayer targets [55–58] to high repetition rate targets [59–66].

4. **Pillar 4 - ion bunch instrumentation:** This pillar describes measurement devices and techniques that are required to analyze the ion bunch regarding its temporal, spatial and spectral profile [67].

5. **Pillar 5 - transport optics:** Transport optics describe measures that can modify the trajectory of particles. Due to the typically large energy spread and divergence of laser-accelerated ions, particle optics to guide the ions, and

thereby preserve the high particle number at an application site, are required. Solenoids [18, 68], **Q**uadru**P**oles (QPs) [69–72] or plasma lenses [73, 74] are used to focus a certain energy of the ion bunch. More complex ion energy selection system have also been developed [75, 76].

1.2.3 Applications of Laser-Driven Ions

The ILDIAS concept describes necessities to develop laser ion acceleration towards a source that can be used for applications. One of the strongest driver for developments in the last decades has been the idea of developing a more compact and cheaper source for ion beam therapy [77–79]. The clear advantage of ions for irradiation is its depth dose distribution. The so called Bragg peak is depicted in Fig. 1.6. The majority of the energy is thus dissipated in a certain depth dependent on the original energy. The clear advantage is that the Bragg peak can be set to the tumor position, while surrounding and more importantly tissue directly behind the tumor is kept from harm (or at least the dose is minimized). The role of laser-driven acceleration in ion beam therapy is not yet foreseeable. Current efforts concentrate on radiation biological studies and aim at exploiting the specifics that are supported by the laser-driven case.

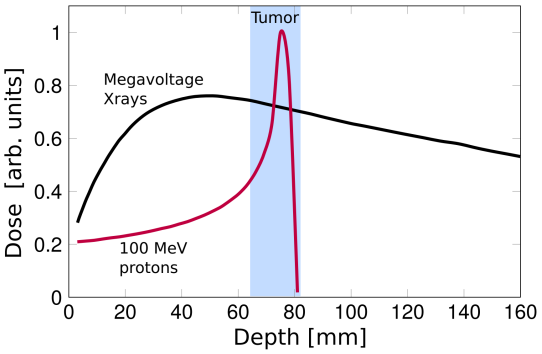

Figure 1.6 | The Bragg peak. The depth-dose distribution of a 100 MeV proton bunch is compared to the one of an X-ray beam. The localized energy deposition of protons can be set to a tumor location, and thus surrounding healthy tissue can be spared. Figure has been taken from [20].

The low emittance is one such specific and renders laser-accelerated ions, for example, an interesting source for radiography and imaging [80–82]. The broad energy spectrum that may be tailored to represent the solar wind bares potential to study space radiation effects on different materials [83, 84] or astrophysical effects in general [85]. Further applications are thinkable in inertial confinement fusion as ignitor for fast ignition [86] or in nuclear physics, for example in the concept of fission-fusion reactions to generate massive, neutron-rich nuclei [87–89].

1.3 Centre for Advanced Laser Application

The **C**entre for **A**dvanced **L**aser **A**pplications is located in Garching near Munich. It has been built to bring all infrastructure, dealing with advanced laser systems, together in order to find synergies and form a platform serving for future applications. The aim of CALA is to develop the acceleration processes further, especially regarding repetition rates, stability but also higher energies. Collaborations with biomedical faculties and others shall develop and demonstrate the feasibility of using laser-accelerated particle beams in more advanced biomedical studies and applications. With the **A**dvanced **T**i:Sapphire **LAS**er **3000** Terawatt (ATLAS-3000) laser, the CALA has one of the world's leading laser systems (compare Fig. 1.3). In addition to the ATLAS-3000 laser, two other laser systems with less pulse energy but even shorter pulses and higher repetition rate (**P**etawatt **F**ield **S**ynthesizer (PFS) and PFS-pro) are currently built and can also be sent to the experimental areas, enabling more complex and two-beam experiments in the future. The developments presented herein have been highly motivated by challenges and the preparation of the commissioning phase of CALA. The overview of CALA in Fig. 1.7 shows the experimental areas and laser systems.

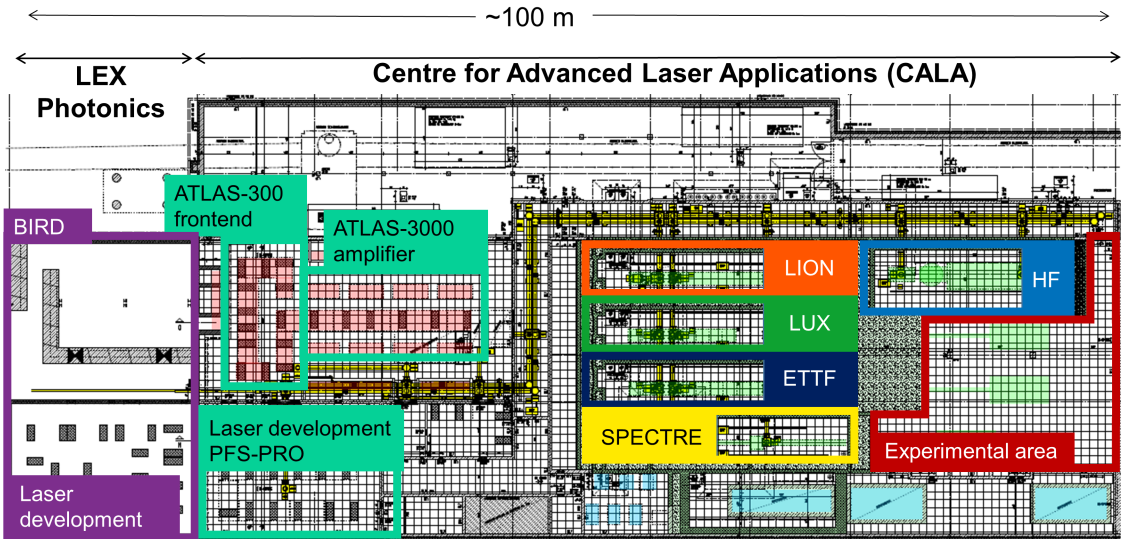

Figure 1.7 | CALA - Centre for Advanced Laser Applications. This figure gives an overview of CALA. It shows the location of different projects and also a scheme of the ATLAS-3000, the beam line and the experimental caves.

One central theme of CALA are laser-based plasmas experiments and their applications within five experimental areas.

1. **LION**: the Laser-driven ION acceleration cave is the most important cave in the context of this thesis. The main goal is to accelerate protons and carbons up to energies of 100 MeV/u and beyond and develop the ion source towards a viable controlled acceleration system with repetition rates up to 1 Hz. The accelerated ions (protons) shall further be used for applications, especially in research on tumor therapy with ion bunches and proton imaging [47].

2. **LUX**: The **L**aser-driven **U**ndulater **X**-ray source (LUX) is an undulator-based synchrotron radiation source based on laser-accelerated electrons [90]. Its aim is, on the one hand, to generate brilliant, spontaneous undulator radiation with photon energies in the range of 1 to 25 keV and pulse durations of a few femtoseconds and, on the other hand, to perform research towards laser-plasma-accelerator-based **F**ree **E**lectron **L**asers (FEL) [91, 92].

3. **ETTF**: The main goal of the **E**lectron and **T**homson **T**est **F**acility (ETTF) is the acceleration of electrons and to test different schemes for producing brilliant, energetic radiation with emphasis on photon-electron collisions. Their usability for, in particular biomedical, applications shall also be demonstrated.

4. **HF**: The general aim of the **H**igh **F**ield Physics (HF) cave is to explore physics at highest field strengths and extreme conditions. One goal is to investigate the fission-fusion process [87, 88]. A first step is the acceleration of heavy particles such as gold to sufficiently high energies [89].

5. **SPECTRE**: The **S**ource for **P**owerful **E**nergetic **C**ompact **T**homson **R**adiation **E**xperiments (SPECTRE) shall be operated with the kHz laser system of the PFS-pro. The generation of X-ray pulses with high brilliance and large average flux are desired for phase contrast imaging for example in medical applications.

A further research project in CALA is the **B**road **I**nfra**r**ed **D**iagnostics (BIRD) [93]. BIRD uses infrared spectroscopy to analyze the bio-molecular fingerprint of molecules. It aims at improving the efficiency of early cancer diagnostics. The **Mu**nich **C**ompact **L**ight **s**ource (MuCLs) [94] is based on a conventional electron storage ring combined with intra-cavity laser technology and provides a brilliant X-ray beam, that can be used for biomedical imaging.

Even though our understanding of the physical processes of laser-particle acceleration is not complete yet, applications have become within reach of today's table-top laser systems. This work tackles several aspects and developments at CALA. The

step from the successful demonstration of acceleration mechanisms towards applications requires thoughtful strategic developments, that lead to higher repetition rates and stability. The experimental campaigns at LEX Photonics during 2015/16 can be regarded as a prototype test campaign for CALA. One part of this work includes the development towards a high-repetition-rate ion source and tackles the challenges that occurred during the experimental campaign at LEX Photonics. Those experiences led to approaches that have now been implemented at CALA. The main part introduces two new online diagnostics, TRIC and I-BEAT. TRIC has been used to measure the plasma evolution with sub-picosecond temporal resolution. From this, it examines the spatio-temporal intensity distribution of the laser directly in the interaction plane (focal plane of the laser.) I-BEAT is a new online measurement technique for the ion energy distribution. The last part outlines some major efforts and progress in CALA.

1.4 Thesis Structure

Chapter 2 introduces the theoretical basis relevant to all topics touched in this work. It starts with the general concept of waves and leads to various parts of this thesis, thereby covering the principles of laser-plasma interactions and ion acceleration. Principles of laser-plasma dynamics (required in Chapter 4) and the sound waves, that are generated by an ion bunch (basis for Chapter 5) are introduced.

Chapter 3 describes the experimental setup at LEX Photonics, where the majority of the research presented herein has been realized. It summarizes a two-year-long period of optimizing the system and preparation experiments towards I-BEAT and TRIC.

Chapter 4 presents a novel probing technique. With temporally resolved intensity contouring, an imaging method with THz frame rates, the spatio-temporal intensity distribution of the ATLAS-300 laser is measured directly on target with full energy.

Chapter 5 presents the functionality and results of the developed I-BEAT detector. It shows its performance at two different laser-ion-acceleration systems.

Chapter 6 gives a summary of presented work. It shows how the experience in LEX Photonics hast been used to optimize CALA and outlines upcoming challenges

and future steps.

Appendix covers two major area. It gives deeper insight into some basics of waves and light, in particular covering the propagation of waves using Fourier optics. The second part covers additional experimental details of LEX Photonics and describes various components of the setup in CALA.

Note on laser beam times This note is meant to clarify the special nature of experimental environments that were used to record data presented in this thesis. LEX Photonics and also CALA are large-scale facilities for laser-particle interaction experiments. The ATLAS-300 laser was an upgrade and used for the first time during our experimental campaign. Since the laser was used at different experimental areas, the laser was usually assigned for one experiments for one or two days. Therefore, experimental days were quite extended and complex, requiring the contribution of a number of scientists, usually responsible for a subset of tasks such as target preparation, laser performance, diagnostics, focusing optics. Since any experiment of this kind involves more than the effort of a single scientist, the specific contribution of the author to experiments presented herein will be specified at the beginning of each chapter.

If you can look at one of these waves and you don't believe that there's something greater than we are, then you've got some serious analyzing to do and you should go sit under a tree for a very long time.

Laird Hamilton

Chapter 2

Theoretical Concepts: Waves, Light and Plasmas

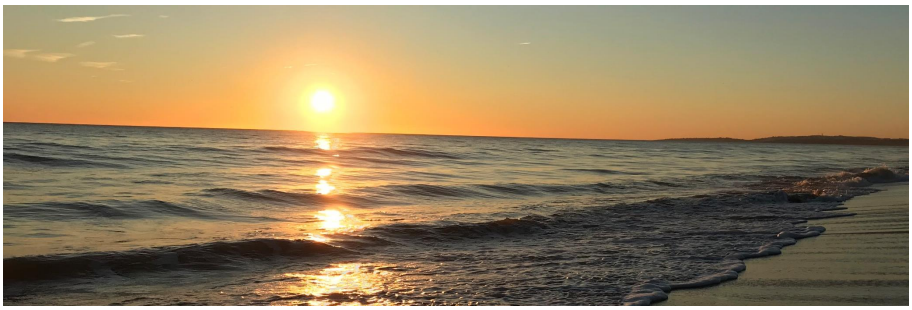

Contents

2.1 Waves 16
2.2 Electromagnetic Waves 17
2.3 Laser-Induced Plasmas 23
2.4 Laser-Driven Ion Acceleration 30
2.5 Acoustic Measurements of Ions 34
2.6 The Beauty of Waves 43

This chapter introduces the theoretical concepts of this thesis. The basic principles of waves are introduced since they apply to several parts covering laser, plasma properties and ultrasound. The idea of laser-plasma ion acceleration is outlined and relevant equations are introduced.

Picture with courtesy of Lukas Strübel.

2.1 Waves

Waves influence our daily life in almost every situation. A wave describes the transfer of energy with little or no associated mass transport. In daily life we typically face two types of waves: mechanical (such as sound waves) or electromagnetic (light). A wave is an oscillation of a medium or field around a relatively fixed location, originating from a perturbation within the medium or field. The oscillation can be transverse to the propagation direction (transverse wave) or parallel (longitudinal wave).

The basic of a wave is the harmonic oscillation[1]. The general expression for a harmonic wave is

$$\left(\nabla^2 - \frac{1}{c^2}\frac{\partial^2}{\partial t^2}\right) U(\vec{r}, t) = 0. \tag{2.1}$$

This equation is the general form of the wave equation in a homogeneous medium without a source. Another commonly used expression is the Helmholtz equation. It can be derived by assuming that U is separable[2] $U(\vec{r}, t) = A(\vec{r})T(t)$. Eq. (2.1) then becomes

$$\frac{\nabla^2 A}{A} = \frac{1}{c^2 T}\frac{d^2 T}{dt^2}. \tag{2.2}$$

This equation is only a general solution if both sides are a constant and can for convenience be set to $-k^2$. This leads to the time-independent Helmholtz equation:

$$\left(\nabla^2 + k^2\right) A = 0. \tag{2.3}$$

Analogously we can also obtain the temporal part of this equation using $\omega = kc$:

$$\left(\frac{d^2}{dt^2} + \omega^2\right) T = 0. \tag{2.4}$$

Equation (2.3) describes the spatial distribution of a time-independent wave, while Eq. (2.4) describes temporal evolution of a wave at a certain position. The equations above govern the propagation of a wave in a homogeneous medium, where the solution depends on the boundary conditions. In the presence of a source, the wave equation becomes inhomogeneous and yields:

[1] A harmonic oscillator is a system wherein the restoring force is proportional to the displacement.

[2] The separation of the variables can be applied in many circumstances to solve the wave equation but fails for example for gravitational waves, where space is no longer time independent.

$$(\nabla^2 - \frac{1}{c^2}\frac{\partial^2}{\partial t^2})U(\vec{r},t) = -f(\vec{r'},t'), \tag{2.5}$$

where $f(\vec{r'},t')$ describes the source. This inhomogeneous wave equation is of significant importance in the framework of this thesis. For example the vector potential (see Eq. (2.12a)) with the current density $\vec{j}$ as a source or the acoustic pressure wave (see Eq. (2.51)) where the source of the wave is the so called heating function.

As described in detail in Section B.1.2 we can solve this equation by applying the concept of the Green's function and get an approximated (neglecting initial and boundary conditions) solution of

$$U(\vec{r},t) = \int_0^{t^+} dt' \int_{V'} dr' G(\vec{r},t;\vec{r'},t') f(\vec{r'},t'). \tag{2.6}$$

With the free-space Green's function, a unit-amplitude spherical wave expanding about $\vec{r}$

$$G(\vec{r},\vec{r'}) = \frac{e^{ik\left|\vec{r}-\vec{r'}\right|}}{\left|\vec{r}-\vec{r'}\right|}, \tag{2.7}$$

Eq. (2.6) basically describes Huygens principle. As shown in Section 2.5.3, a time dependence can be added with a modified Green's function:

$$G(\vec{r},t;\vec{r'},t') = \frac{\delta(t-t'-\frac{\left|\vec{r}-\vec{r'}\right|}{c})}{4\pi\left|\vec{r}-\vec{r'}\right|}. \tag{2.8}$$

Here we introduce the concept of the retarded time $t' = t - \left|\vec{r}-\vec{r'}\right|/c$. The retarded time describes the time t' when an event happened at the location r' that is detected at r at the time t and has traveled with the speed c.

We can deduct one particular important statement: **The shape (amplitude and phase) of a wave typically carries all information about the spatial and temporal structure of its source, given that the medium and its properties are known variables.**

2.2 Electromagnetic Waves

Light is an electromagnetic wave. Most commonly we refer to light when it is visible to the human eye, but the physics are the same for the entire electromagnetic

spectrum. The breakthrough in the description of light has been done by Maxwell condensed in the four equations given by Jackson [95]:

$$\textbf{Gauss' law:} \nabla \cdot \vec{\mathcal{E}} = \begin{cases} 0 & \text{no source} \\ \frac{\rho}{\epsilon} & \text{with source} \end{cases} \tag{2.9a}$$

$$\textbf{Gauss' law for magnetism:} \nabla \cdot \vec{\mathcal{B}} = 0 \tag{2.9b}$$

$$\textbf{Faraday's law:} \nabla \times \vec{\mathcal{E}} = -\frac{\partial \vec{\mathcal{B}}}{\partial t} \tag{2.9c}$$

$$\textbf{Ampère - Maxwell law:} \nabla \times \vec{\mathcal{B}} = \begin{cases} \mu\epsilon \frac{\partial \vec{\mathcal{E}}}{\partial t} & \text{no source} \\ \mu(\vec{j} + \epsilon \frac{\partial \vec{\mathcal{E}}}{\partial t}) & \text{with source.} \end{cases} \tag{2.9d}$$

The vectorial component of the electric $\vec{\mathcal{E}}$ and magnetic field $\vec{\mathcal{B}}$ denote the polarization of the field. The charge density ρ and current density $\vec{j}$ mark the source term of the fields. The electric permittivity ϵ and magnetic permeability μ are dependent on the medium and determine the phase velocity $c = 1/\sqrt{\epsilon\mu}$. In vacuum the speed of light is thus $c_0 = 1/\sqrt{\epsilon_0\mu_0}$. In the following, waves are considered to be in vacuum and $c = c_0$ is used. The homogeneous wave equations can be derived using Maxwell's equations without a source:

$$\left(\nabla^2 - \frac{1}{c^2}\frac{\partial^2}{\partial t^2}\right)\vec{\mathcal{E}}(\vec{r}, t) = 0 \tag{2.10a}$$

$$\left(\nabla^2 - \frac{1}{c^2}\frac{\partial^2}{\partial t^2}\right)\vec{\mathcal{B}}(\vec{r}, t) = 0. \tag{2.10b}$$

The inhomogeneous wave equations describe the wave in presence of a source:

$$\left(\nabla^2 - \frac{1}{c^2}\frac{\partial^2}{\partial t^2}\right)\vec{\mathcal{E}}(\vec{r}, t) = -\left(\frac{1}{\epsilon_0}\nabla\rho + \mu_0\frac{\partial j}{\partial t}\right) \tag{2.11a}$$

$$\left(\nabla^2 - \frac{1}{c^2}\frac{\partial^2}{\partial t^2}\right)\vec{\mathcal{B}}(\vec{r}, t) = \mu_0 \nabla \times \vec{j}. \tag{2.11b}$$

2.2.1 Vector Potential

A more symmetric expression of Eq. (2.11) can be derived using the magnetic vector potential $\vec{A}$ and the scalar potential Φ. The vector potential is defined with:

$$\vec{\mathcal{B}} = \nabla \times \vec{\mathcal{A}} \tag{2.12a}$$

$$\vec{\mathcal{E}} = -\nabla\Phi - \frac{\partial \vec{\mathcal{A}}}{\partial t}. \tag{2.12b}$$

With the use of the Lorenz gauge condition [96] $\nabla\vec{\mathcal{A}} + \partial\Phi/c^2\partial t = 0$ the inhomogeneous wave equations simplify to

$$\nabla^2\vec{\mathcal{A}} - \frac{1}{c^2}\frac{\partial^2\vec{\mathcal{A}}}{\partial t^2} = -\mu_0\vec{j} \tag{2.13a}$$

$$\nabla^2\Phi - \frac{1}{c^2}\frac{\partial^2\Phi}{\partial t^2} = -\frac{\rho}{\epsilon_0}. \tag{2.13b}$$

A general solution of homogeneous wave equations is the plane wave with

$$\vec{\mathcal{A}}(\vec{r},t) = \vec{A}_0 e^{-i\omega_0 t - \vec{k_0}\vec{r} + \varphi_0}. \tag{2.14}$$

This is a complex wave function. To describe a physical quantity, the real part has to be taken.

2.2.2 Laser Pulses

Laser is one of the most important innovations in the 20th century. The laser serves as light source for many application and has enabled a wide range of research and development. Although stimulated emission was firstly predicted by Albert Einstein [97] the first experimental demonstration of a laser was realized 40 years later by Maiman [98]. Since this first demonstration of a lasing medium the development of lasers has been tremendous, covering the discovery of various laser materials, higher energies, pulsed lasers and even more so shortest pulse lengths.

Starting with the vector potential Eq. (2.13a) in vacuum a laser pulse can simply be described by

$$\vec{\mathcal{A}}(\vec{r},t) = \vec{\mathcal{A}}_A(\vec{r},t)\sin\left(\vec{k}_L\vec{r} - \omega_L t + \varphi_0\right), \tag{2.15}$$

with the phase φ_0 and the dispersion relation $\omega_\mathrm{L} = c\vec{k_\mathrm{L}}$. Note that we have now used

the real part of Eq. (2.14) since it describes the physical field of the wave equation. The electric and magnetic field in the laser are thus given by

$$\vec{\mathcal{E}}(\vec{r},t) = \vec{\mathcal{E}_{\mathrm{A}}}(\vec{r},t)\cos\left(\vec{k}_{\mathrm{L}}\vec{r} - \omega_{\mathrm{L}}t + \varphi_0\right) \tag{2.16a}$$

$$\vec{\mathcal{B}}(\vec{r},t) = \vec{\mathcal{B}_{\mathrm{A}}}(\vec{r},t)\cos\left(\vec{k}_{\mathrm{L}}\vec{r} - \omega_{\mathrm{L}}t + \varphi_0\right). \tag{2.16b}$$

Whereas $\vec{\mathcal{A}}_{\mathrm{A}}$, $\vec{\mathcal{E}_{\mathrm{A}}}$ and $\vec{\mathcal{B}_{\mathrm{A}}}$ are the envelope functions with the relation[3] $\left|\vec{\mathcal{E}_{\mathrm{A}}}\right| = c\left|\vec{\mathcal{B}_{\mathrm{A}}}\right| = \omega_{\mathrm{L}}\left|\vec{\mathcal{A}}_{\mathrm{A}}\right|$. Two, in the framework of this thesis, relevant quantities for $\mathcal{E}_{\mathrm{A}}$ are:

1. **Plane wave**: Plane waves are often used to calculate the propagation of laser pulses and its effects in plasmas. In many realistic scenarios this can only be seen as an estimation neglecting its spatial and temporal dependence.

2. **Gaussian pulse in the focal plane**: The intensity distribution in the focal plane, that is often referred to as laser focus, is a key element of laser-driven ion acceleration. Even though, the spatial distribution of many flat-top laser systems is described by a sinc function, Gaussian distribution is often used for approximations. Note that the following equation describes the Gaussian pulse solely in the focal plane.

$$\vec{\mathcal{E}}_{\mathrm{A}}(\vec{r},t) = \begin{cases} \vec{\mathcal{E}}_0 & \text{plane wave} \\ \vec{\mathcal{E}}_0 e^{-t^2/(2\sigma^2_{\mathrm{E}\tau})} e^{-(x^2)/(2\sigma^2_{\mathrm{Ex}})} e^{-(y^2)/(2\sigma^2_{\mathrm{Ey}})} & \text{Gaussian pulse in focal plane.} \end{cases} \tag{2.17}$$

Where σ_{Ex} and σ_{Ey} are the standard deviations of the electric field of a laser pulse in the focal plane in x and y dimension[4]. The sigma of its temporal distribution is $\sigma_{\mathrm{E}\tau}$.

2.2.3 Temporal and Spatial Intensity

Detectors such as cameras often measure the intensity and not the amplitude of the field. The intensity is defined as the cycle-averaged magnitude of the pointing vector

[3] The magnitudes can also be related as follows $\left|\vec{\mathcal{E}}_{\mathrm{A}}\right| = \mathcal{E}_{\mathrm{A}}$, $\left|\vec{\mathcal{B}}_{\mathrm{A}}\right| = \mathcal{B}_{\mathrm{A}}$ and $\left|\vec{\mathcal{A}}_{\mathrm{A}}\right| = \mathcal{A}_{\mathrm{A}}$.

[4] The Gaussian width is typically defined by the beam waist $w_0 = \sqrt{2}\sigma$ (see Fig. B.5). The nomination with x and y allows an elliptical shape of the focus.

$\vec{\mathcal{S}} = 1/\mu_0 \left(\vec{\mathcal{E}} \times \vec{\mathcal{B}}\right)$ and is for a plane wave[5]

$$I_0 = \langle \vec{\mathcal{S}} \rangle_{\mathrm{T}} = \kappa_{\mathrm{Pol}} \frac{1}{2} \epsilon_0 c \mathcal{E}_0^2, \tag{2.18}$$

where κ_{Pol} is 1 for linear polarization and 2 for circular polarization. In the case of a Gaussian pulse in focal plane the intensity distribution becomes

$$I\left(x, y, t\right) = \kappa_{\mathrm{Pol}} \frac{1}{2} \epsilon_0 c \mathcal{E}_0^2 \underbrace{e^{-t^2/(2\sigma_{\mathrm{I}\tau}^2)}}_{g'(t)} \underbrace{e^{-(x^2)/(2\sigma_{\mathrm{Ix}}^2)} e^{-(y^2)/(2\sigma_{\mathrm{Iy}}^2)}}_{f'(x,y)}. \tag{2.19}$$

The intensity is therefore proportional to the square of the electric (or magnetic) field amplitude. Note that the standard deviations of the intensity and the electric field[6] consequently differ by a factor $\sqrt{2}$: $(\sigma_{\mathrm{I}} = 1/\sqrt{2} \cdot \sigma_{\mathrm{E}})$. Note, that the standard deviation of the intensity differs from the one of the electric field The **F**ull **W**idth at **H**alf **M**axiumum (FWHM)[7] is often used to describe the dimension of a laser focus or the pulse length and is related to the standard deviation via $d_{\mathrm{x}} = 2\sqrt{2\ln(2)}\sigma_{\mathrm{Ix}}$, $d_{\mathrm{y}} = 2\sqrt{2\ln(2)}\sigma_{\mathrm{Ix}}$ and $\tau_{\mathrm{L}} = 2\sqrt{2\ln(2)}\sigma_{\mathrm{It}}$.

The total energy contained in a laser pulse E_L can be obtained by integrating the intensity over space and time

$$E_{\mathrm{L}} = \iiint_{-\infty}^{\infty} I(x, y, t) dt dx dy. \tag{2.20}$$

Using E_{L} and normalizing the functions $g'\left(t\right)$ (temporal) and $f'\left(x, y\right)$ Spatial of Eq. (2.19) yields

$$I(x, y, t) = E_{\mathrm{L}} \cdot \underbrace{\frac{\tilde{N}}{\tau_{\mathrm{L}}} g'(t)}_{g(t)} \cdot \underbrace{\frac{\tilde{N}^2}{d_{\mathrm{x}} d_{\mathrm{y}}} \cdot f'(x, y)}_{f(x,y)}. \tag{2.21}$$

$\tilde{N}$ can be derived by expressing the normalization of a Gaussian distribution $(1/\sqrt{2\pi\sigma^2})$ in terms of the FWHM value, exemplarily shown for the time t:

[5] With $1/\mu_0 = \epsilon_0 c^2$ and using the trick that the cycle average of $\left\langle \cos(x)^2 \right\rangle = \left\langle \sin(x)^2 \right\rangle$ and $\cos(x)^2 + \sin(x)^2 = 1$.

[6] This often causes confusions, especially when theorists and experimentalist collaborate.

[7] The FWHM describes the complete width where the intensity has dropped to half of its maximum.

$$\frac{1}{\sqrt{2\pi\sigma_{\mathrm{It}}^2}} = \frac{1}{\sqrt{2\pi}} \frac{2\sqrt{2\ln(2)}}{\tau_{\mathrm{L}}} = \underbrace{\frac{2\sqrt{\ln(2)}}{\sqrt{\pi}}}_{\tilde{N}} \frac{1}{\tau_{\mathrm{L}}} \approx \frac{0.94}{\tau_{\mathrm{L}}}. \tag{2.22}$$

The peak intensity I_0 of the laser pulse can thus be calculated with

$$I_0 = \underbrace{0.83}_{\tilde{N}^3} \cdot \frac{E_{\mathrm{L}}}{\tau_{\mathrm{L}} d_{\mathrm{x}} d_{\mathrm{y}}}. \tag{2.23}$$

Those equations are useful since the intensity in the focal plane is often not directly measurable and only the spatial distribution $f(x, y)$, laser energy E_{L} and temporal distribution are separately accessible quantities in the experiment. The peak intensity of the laser I_0 is often the most important quantity and can directly be calculated by the laser energy, pulse duration and spatial extend using Eq. (2.23). Assuming that spatio-temporal coupling (see [99]) can be neglected, the spatio-temporal intensity distribution in focal plane can be calculated with Eq. (2.21) by using the temporal distribution $g(t)$ and the spatial distribution $f(x, y)$.

2.2.4 Focusing Device

The focus or far-field of a high-power ultra-short laser pulse is typically generated with an **O**ff-**A**xis **P**arabolic mirror (OAP). There are multiple reasons why an OAP is favorable over a lens. The wider spectrum and large diameter (combined with a desired short focusing distance) of a short-pulse laser makes it impossible for a lens to equalize all optical path lengths for all frequencies and **G**roup **V**elocity **D**ispersion (GVD) (see Section B.2.3) would disperse the pulse in time. Due to the high intensity and onset of nonlinear effects in a medium, the laser pulse, traversing a lens, would collect B-integral (see Eq. (B.47)), deteriorating the quality of the laser pulse. Working in reflection, an OAP with the correct material and coating can ideally focus the entire wavelength range of the short pulse without compromising the pulse quality. Since at zero degree reflection, the focal point would lie at the center of the incoming beam, an off-axis parabola is used to simultaneously deflect the beam while preserving the focusing effect.

2.3 Laser-Induced Plasmas

We have now introduced the concept of a laser as an optical, electromagnetic wave. For simplicity, we will assume linear polarization and plane waves and thus $\vec{\mathcal{E}}_\mathrm{A} = \mathcal{E}_0$, $\vec{\mathcal{B}}_\mathrm{A} = \mathcal{B}_0$ and $\vec{\mathcal{A}}_\mathrm{A} = \mathcal{A}_0$. The basics of the interaction dynamics and the acceleration mechanism for ions are explained. A deeper debate about different acceleration mechanisms and the corresponding regimes can be found in [15, 20, 100, 101].

2.3.1 Laser Interacting with a Single Particle

As we will see later, collective effects play a significant role in laser plasma dynamics. Nevertheless, the basis is the impact of an electromagnetic wave onto a single particle such as an electron, which is described by the Lorentz force

$$\vec{F}_\mathrm{l} = e\left[\underbrace{\vec{\mathcal{E}}\left(\vec{r},t\right)}_{F_\perp} + \underbrace{\vec{v_e}\times\vec{\mathcal{B}}\left(\vec{r},t\right)}_{F_\parallel}\right]. \tag{2.24}$$

Since $\mathcal{B}_0 = \mathcal{E}_0/c$, the second term is, apart from an additional factor v_e/c, equal to the first term. In the non-relativistic treatment we can assume v_e/c to be $\ll 1$, and Eq. (2.24) can thus be approximated with $\vec{F}_\mathrm{l} \approx e\mathcal{E}(\vec{r},t)$. An electron, initially at rest, will first be accelerated along the direction of the oscillating electric field of the laser.

$$\vec{v}_\mathrm{e}(t) = \vec{e}_\mathrm{y}\frac{e\mathcal{E}_0}{\omega_\mathrm{L} m_\mathrm{e}}\cos(k_\mathrm{l}x - \omega_\mathrm{L}t) \tag{2.25a}$$

$$\Rightarrow v_{max} = \frac{e\mathcal{E}_0}{\omega_\mathrm{L} m_\mathrm{e}}. \tag{2.25b}$$

This oscillation further interacts with the magnetic field of the laser pulse resulting in an additional motion along the propagation direction of the laser. The fraction of the Lorentz force acting along the propagation direction and transversal to it defines the dimensionless laser amplitude that is a key parameter defining different regimes in laser-based plasmas

$$a_0 = \frac{F_\parallel}{F_\perp} = \frac{e\left(\vec{v}_\mathrm{e}\times\vec{\mathcal{B}}\right)}{e\vec{\mathcal{E}}} = \frac{e\mathcal{E}_0}{m_e c\omega_L}. \tag{2.26}$$

In other words a_0 is defined by equating the maximum velocity of an electron (see Eq. (2.25b)) with the speed of light. The dimensionless quantity $a_0 = 1$, thus describes the limit, where the non-relativistic description breaks down (in reality this already happens well before $a_0 \approx 1$). Nevertheless, we speak of a relativistic laser pulse if a_0 exceeds unity.

The field amplitude and the intensity of a high power laser are typically described with a_0 (using Eq. (2.26)) and λ_L:

$$\mathcal{E}_0 = a_0 \frac{\omega_L m_e c}{e} = \frac{a_0}{\lambda_L} 2\pi \frac{m_e c^2}{e} = \frac{a_0}{\lambda_L\,[\mu\mathrm{m}]} 3.21 \cdot 10^{12} \frac{\mathrm{V}}{\mathrm{m}} \tag{2.27a}$$

$$\mathcal{B}_0 = \frac{\mathcal{E}_0}{c} = \frac{a_0}{\lambda_L\,[\mu\mathrm{m}]} 1.07 \cdot 10^{4} \mathrm{T} \tag{2.27b}$$

$$I_L = \frac{\epsilon_0 c^2}{2} \mathcal{E}_0^2 = \frac{a_0^2}{\lambda_L^2\,[\mu\mathrm{m}^2]} 1.37 \cdot 10^{18} \frac{\mathrm{W}}{\mathrm{cm}^2}. \tag{2.27c}$$

These equations are taken from Karsch [102] and can be used to calculate laser properties (e.g. of the ATLAS-300). Another important information that can be deduced here is the intensity required to directly accelerate the heavier protons to relativistic intensities. The relation of the masses $m_p/m_e \approx 1835$ gives the required a_0. This would require an intensity of

$$I_\mathrm{L} = 4.6 \cdot 10^{24} \frac{1}{\lambda_\mathrm{L}^2\,[\mu\mathrm{m}^2]} \frac{\mathrm{W}}{\mathrm{cm}^2}. \tag{2.28}$$

Such intensities have not yet been realized, and thus the acceleration of protons till today is an indirect acceleration process using the electrons to mediate acceleration potentials.

2.3.2 Introduction to Plasmas

After introducing the laser as the first important part of laser plasma acceleration and its impact onto other particles, this section gives an overview about the plasma and its properties.

A plasma naturally occurs at very high temperatures and can thus be regarded as the fourth state of matter. On earth, the natural occurrence of such temperatures is rare and can only be observed in occasions as for example the flash of a lightning bolt. Since the vast majority of the universe's matter is in the plasma state, it can be said: *"we live in the 1 % of the universe where plasmas do not naturally*

occur" [103]. A plasma is a quasi-neutral gas of charged and neutral particles, which exhibits collective behavior. This Section and Section 2.4 are based on [20, 101, 104–108].

Plasma Properties

Plasma, as the "fourth state" of matter, describes a partially ionized multi-body system composed of free charged and neutral particles. One of the important characteristics of a plasma is its quasi-neutrality in charge. Characteristic for a plasma is also its collective behavior. In the framework of laser-produced plasmas and laser ion-acceleration, the neutral condition can be locally violated. Nevertheless, the effects of locally introduced charge is effectively shielded $(1/e)$ at the characteristic Debye length λ_D. The phrase quasi-neutrality describes that situation: a local violation of neutrality within the plasma but a neutral behavior in a spatial scale larger than λ_D

$$\lambda_\mathrm{D} = \sqrt{\frac{\epsilon_0 k_\mathrm{B} T_\mathrm{e}}{e^2 n_\mathrm{e}}}. \tag{2.29}$$

In the presence of an additional charge or an acting field (e.g. a laser), electrons are displaced from their equilibrium position. Within the Debye length, a collective, oscillating motion of the plasma can be initiated by a strong laser pulse. While the electrons can react with their thermal velocity

$$v_\mathrm{te} = \sqrt{\frac{k_\mathrm{B} T_\mathrm{e}}{\overline{\gamma} m_\mathrm{e}}}, \tag{2.30}$$

where $\overline{\gamma}$ is the time-averaged Lorentz factor that is often expressed by $\sqrt{1 + a_0/2}$. The other newly introduced quantity T_e is the electron temperature that is of particular importance in the case of laser-driven ion acceleration. Using the electron velocity, it is possible to calculate the response time to recover quasi-neutrality in the plasma.

$$t_\mathrm{pe} = \frac{\lambda_\mathrm{D}}{v_\mathrm{te}} = \omega_\mathrm{pe}^{-1}. \tag{2.31}$$

When the response time is shorter than the period of an external electromagnetic field the radiation will be shielded. In the case of a laser pulse, this would mean that the laser can not propagate into the plasma and is thus reflected. The response time or, more commonly used, the plasma frequency ω_pe defines the oscillation of

the electrons in the plasma

$$\omega_{\mathrm{pe}} = \frac{v_{\mathrm{te}}}{\lambda_{\mathrm{D}}} = \sqrt{\frac{e^2 n_{\mathrm{e}}}{\epsilon_0 m_{\mathrm{e}} \overline{\gamma}}}. \tag{2.32}$$

The plasma frequency of ions is, due to their heavier mass, much smaller. We use $\omega_{pe} = \omega_p$ for the rest of this work. The plasma frequency significantly influences the interaction of an incoming laser pulse with the plasma itself. When the plasma frequency exceeds a certain value the plasma becomes opaque for laser light, which fundamentally changes the interaction processes. The refractive index of an optical medium in general is $\eta_{\mathrm{R}} = c/v_{\mathrm{medium}}$:

$$\eta_{\mathrm{R}} = \sqrt{1 - \frac{\omega_{\mathrm{p}}^2}{\omega_{\mathrm{L}}^2}} = \sqrt{1 - \frac{n_{\mathrm{e}}}{n_{\mathrm{c}}}}. \tag{2.33}$$

The first term relates the plasma frequency with the laser frequency ω_{L}. The second expression uses the electron density[8] n_e and the critical density n_{c} stating that the plasma will become opaque whenever the electron density exceeds the critical density. Since the physics change fundamentally when the plasma becomes opaque, the electron density, often given in terms of the critical density is one of the most important parameters when describing the laser-plasma target. The critical density is obtained by equating Eq. (2.32) with ω_{L}

$$n_{\mathrm{c}} = \frac{\epsilon_0 m_{\mathrm{e}} \overline{\gamma} \omega_{\mathrm{L}}^2}{e^2} = 1.1 \cdot 10^{21} \left(\frac{\overline{\gamma}}{\lambda\,[\mu\mathrm{m}^2]} \right) \mathrm{cm}^{-3}. \tag{2.35}$$

When the laser impinges on the target at a certain angle, the critical density is already reached at the smaller electron density $n_{\mathrm{e}} = n_{\mathrm{c}} \cos(\Theta_i)^2$. The electron density divides plasmas into transparent (underdense plasma $n_e < n_c$) and opaque (overdense plasma $n_{\mathrm{e}} > n_{\mathrm{c}}$). The acceleration of electrons is most efficient within an underdense target, where the laser can co-propagate along with the electrons and thus increase the acceleration time [11]. For the acceleration of ions, a steep density gradient is beneficial, and thus overdense plasmas are favorable. In the case of an overdense plasma, the laser cannot propagate in the plasma. Nevertheless,

[8] In general, the electron density can be calculated with

$$n_{\mathrm{e}} = \frac{N_{\mathrm{a}} \cdot Z \cdot \rho}{A \cdot M_{\mathrm{u}}}, \tag{2.34}$$

with ρ being the density, N_{A} the Avogadro number, M_{u} is the Molar mass constant, Z the atomic number and A the relative atomic mass.

it propagates evanescently into the overdense plasma. The so called characteristic plasma scale length (or skin depth) l_s describes the depth in which the electric field has dropped to $1/e$:

$$l_\mathrm{s} = \frac{c}{\sqrt{\omega_p^2 - \omega_\mathrm{L}^2}} \approx \frac{c}{\omega_\mathrm{L}}, \tag{2.36}$$

where the approximation is valid for steep density gradients. But before looking deeper into those processes it is worth to have a look at the ionization process originally transforming the target into a plasma.

2.3.3 Ionization and Damage Threshold

During all laser plasma experiments, the first step is the transition from the "target", that can be provided in gaseous, liquid or solid form, into its plasma state. Therefore, the target has to be ionized. Before we start with a deeper understanding of ionization processes, the ultimate limit at which for example a Hydrogen atom will be ionized, and thus a plasma is created can be calculated. Using the Bohr radius $a_\mathrm{Bohr} = 5.3 \times 10^{-9}$ cm, we get

$$\mathcal{E}_\mathrm{b} = \frac{e}{4\pi\epsilon_0 a_\mathrm{Bohr}^2} \approx 5.1 \frac{\mathrm{GV}}{\mathrm{m}}. \tag{2.37}$$

This field corresponds to the ionization intensity I_ionize for the coulomb field that binds the electron to the proton.

$$I_\mathrm{ionize} = \frac{\epsilon_0 c \mathcal{E}_\mathrm{b}^2}{2} \approx 3.51 \times 10^{16} \frac{\mathrm{W}}{\mathrm{cm}^2}. \tag{2.38}$$

Ionization Processes

Different material dependent processes lead to an ionization starting at much lower intensities. This section provides an overview of different processes that can happen at high intensities but avoids a deeper discussion. Ionization means that a bound electron gets enough energy to overcome the Coulomb potential and to become a free charge. The Nobel prize of 1921 was given to Einstein for the photoelectric effect, that states that the energy of a photon must be higher than the work function to ionize an atom. In the context of solid state physics materials are distinguished as conductors and insulators. An insulator has a certain band gap. In order to ionize the material, an energy larger than the band gap has to be passed to an electron. As

Einstein postulated, the energy must be given by a single photon. In the presence of very intense laser fields there are different processes changing that behavior.

Multi-Photon Ionization describes the process that more than one photon is absorbed by one electron until it can flee the Coulomb potential. Further, the presence of an electromagnetic field can suppress the Coulomb barrier, and thus the electron needs less and less energy to become free. This process is called **Barrier Suppression Ionization**. The third process is **tunneling**, where the electron can tunnel with a certain probability through the barrier. Tunneling is often combined with BSI since the lowered Coulomb potential increases the tunneling probability. Those processes can lead to the initial ionization of an atom and are depicted in Fig. 2.1. At a certain ionization level the so called **avalanche ionization** starts to kick in. The process of avalanche ionization describes that an energetic quasi-free electron provides enough energy to transfer some of its energy to another electron and thus, generating a second quasi-free electron, which in turn can generate another and hence create an avalanche. The energy was previously gained in collisional absorption, often also referred to as inverse Bremsstrahlung. It describes the process of a photon that is absorbed by an electron in the conduction band, resulting in an energy gain of this electron [109]. The cross section of such collisional absorption processes is highly dependent on the energy of the electrons. The carried energy needs to be higher than the bandgap of the other electrons (a multiple is most efficient). On the other hand, higher energies lead to shorter interaction times and thus, a drop off in the cross section. The absorption of such mechanisms has been studied by Lotz [110]. Due to the scaling laws of hot electrons, those effects are dominating at intensities smaller than 10^{15} W cm^{-2}.

Damage of Material

This ionization of matter will eventually lead to damage of the material. The laser-induced damage and its threshold of different materials has been discussed widely over the last decades. The correlation between the conduction band (free) electron density reaching the critical density (Eq. (2.35)) and damage due to ablation, is broadly accepted [111, 112]. However, newer research indicates that higher electron densities are required until damage occurs [113, 114]. The word damage in principle describes any modification of the target, starting from alteration of the surface to ablation of material up to complete destruction of such.

Apart from understanding the processes that lead to damage of matter, this is

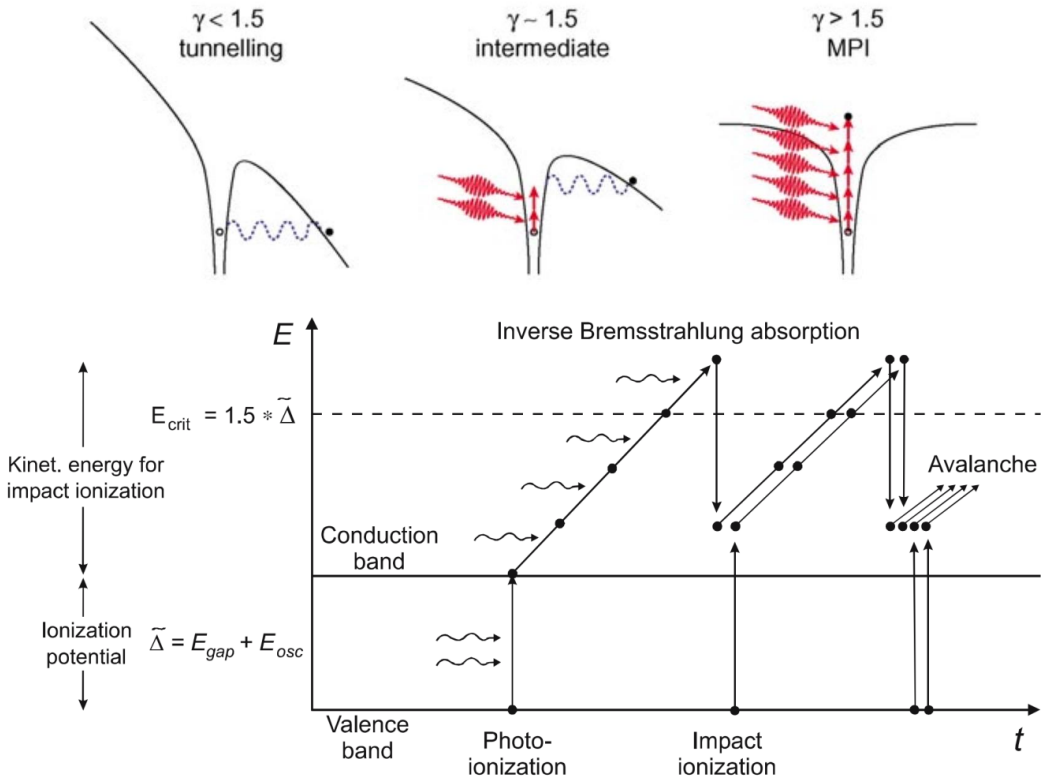

Figure 2.1 | Ionization processes. The processes of ionization are depicted. The top part illustrates the effect of **M**ulti-**P**hoton **I**onization (MPI), tunneling and a mixed process. The bottom part shows the concept of avalanche ionization, taken from Vogel et al. [109].

of particular interest for high-power laser systems. Building an high-power laser system is quite expensive since the optics have to be larger with increasing intensity and energy in the pulse. The minimum size of the optical elements is defined by the damage threshold. And since the price of optical elements is exponentially increasing with the size an increased damage threshold can severely lower the costs [107].

Expansion of a Plasma

Ablation creates a blow off of matter that expands with the ion sound velocity, which is given by:

$$c_s = \sqrt{\frac{Z k_\mathrm{B} T_\mathrm{e}}{m_\mathrm{i}}} \approx 3.1 \cdot 10^7 \sqrt{\frac{T_\mathrm{e}}{\mathrm{keV}}} \sqrt{\frac{Z}{A}} \left[\frac{\mathrm{cm}}{\mathrm{s}}\right]. \tag{2.39}$$

This describes an expansion of the plasma that in the case of laser-driven ion acceleration could lead to significant alteration in the acceleration process.

2.4 Laser-Driven Ion Acceleration

We have now derived how the laser pulse ionizes atoms and creates a plasma. We have further derived the interaction of a high power laser with a free electron. With both ingredients and an initially solid target, an overdense plasma can be created. The acceleration of protons mainly but not exclusively takes place in an overdense plasma regime.

Overdense Plasma – Solid Targets

The interaction of a laser pulse with a plasma consisting of many charged particle gets a lot more complex. Due to the shielding of free charges in the plasma, it was shown that an electromagnetic field cannot propagate in an overdense plasma. The field of the laser drops of to 1/e within the so called skin depth l_s (Eq. (2.36)). Despite this fact the laser pulse can still pass energy to the plasma. As it was shown earlier the absorbed energy of the laser is passed on to the electrons. Different absorption mechanisms can play a role and result in an energy gain of the electrons. We have previously stated that collisional absorption dominates at intensities around 10^{15} W cm^{-2}. This is due to the kinetic energies of electrons. If electrons gain more and more energy (keV level), the interaction probability drops and collisionless absorption mechanisms become dominant.

2.4.1 Collisionless Absorption

Resonant absorption, Brunel heating and $\vec{j}\times\vec{\mathcal{B}}$ heating, are the dominating processes in the regime of collisionless absorption.

Resonance Absorption

Resonance absorption [115, 116] requires the propagation within the plasma of the laser for several wavelengths. It further requires one component of the polarization of the laser being parallel to the density gradient of the plasma. Since the density gradient of the plasma will always form along the normal of the target surface and

the polarization is transversal, the angle of incidence on the target (Θ_i) must be non-zero (p-polarized laser). The critical density in this case is changed by the factor $n_\mathrm{e} = n_\mathrm{c} \cos(\Theta_\mathrm{c})^2$. The second prerequisite is that the plasma scale length (see Eq. (2.36)) has to be large enough to create a shallow plasma density gradient. A fraction of the electric field such penetrates into the overdense region and resonantly excites electron oscillation, and thus laser energy can be coupled into the overdense plasma.

Vacuum Heating

The mechanism denominated as vacuum heating [117] is similar to resonance absorption except that no resonance occurs. When a p-polarized laser impinges onto a plasma with steep density gradient and thus short plasma scale length (i.e. shorter than one wavelength), the oscillation of electrons starts and electrons are pulled from the vacuum-plasma boundary into the vacuum. Following the electric field they will turn around and be pushed back into the plasma. Due to the short scale length the laser cannot influence the electrons anymore, and thus energy has been transferred from the laser to the injected electrons.

j x B Heating

The name of $\vec{j} \times \vec{\mathcal{B}}$ heating [118] is given by its origin, the second term of the Lorentz force (Eq. (2.24)) and is thus dominating for relativistic laser intensities. A longitudinal oscillation of the electrons with a frequency of $2\omega_\mathrm{L}$ is introduced. Again analog to the effect in vacuum heating, electrons that oscillate beyond the plasma scale length are shielded and not affected by the laser anymore. In contrast to the other mechanisms, it works best for normal incidence onto the target since the force is directed along the pointing vector of the laser field. Since it requires an oscillation of electrons along one axis it can be suppressed by circularly polarized light.

2.4.2 Heating of Electrons

Since the electron heating is a mixture of different processes and dependent on many different parameters such as density and thickness of the target as well as the complete laser parameters, it is hard to be described quantitatively. Several models

[119] have developed, while the scaling law by Wilks [120] is the most common one:

$$k_{\mathrm{B}}T_{\mathrm{h}} \approx m_{\mathrm{e}}c^2(\sqrt{1+\frac{a_0^2}{2}}-1). \tag{2.40}$$

This scaling law is directly derived from the ponderomotive potential and is thus also referred to as ponderomotive scaling. One can directly see that the hot electron temperature is dependent on the laser intensity. The laser intensity can thus be seen as one of the most important parameters for the heating of energetic electrons that affect consequently proton acceleration, as will be explained later.

The effect of a high power laser onto matter depends highly on the intensity of the laser pulse. In Fig. 2.2, four different levels can be identified. At intensities below 10^{12} W cm^{-2} as typical for ns pulses, thermal heating is the dominating effect. We have described processes that lead to the ionization of matter and thus the generation of a plasma at intensities around 10^{14} W cm^{-2}, generating free electrons that will cause an expansion of the plasma. Eventually with intensities beyond 10^{18} W cm^{-2} collisionless absorption mechanism are able to generate hot electrons with energies in the MeV level, that will drive the acceleration of ions.

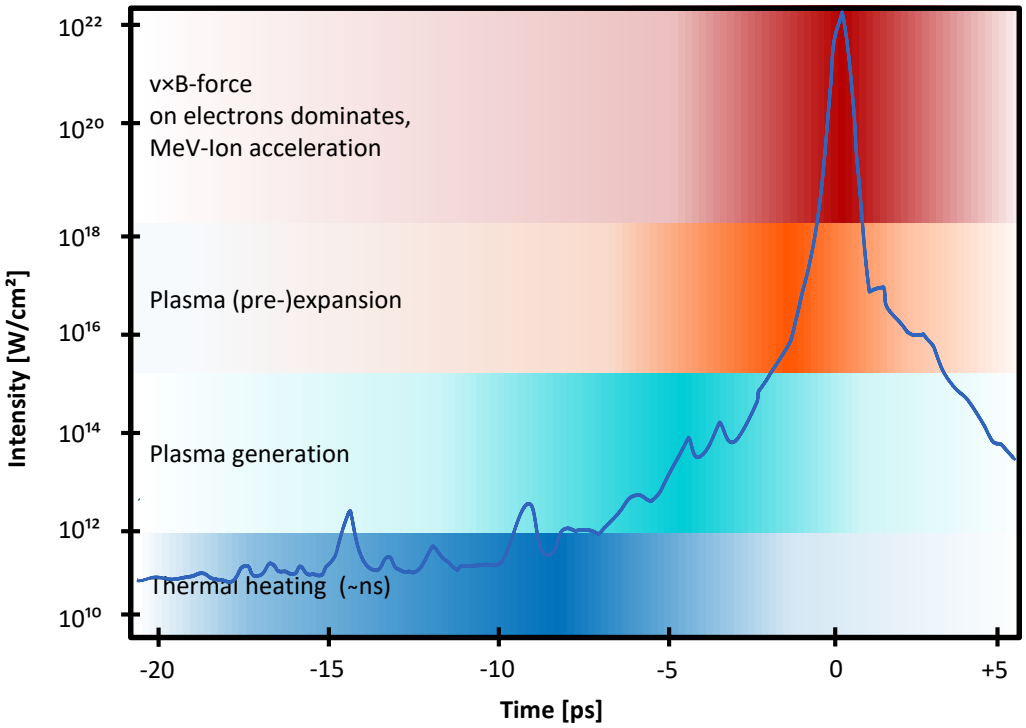

Figure 2.2 | Plasma regimes. This graph shows relevant regimes of matter-plasma interactions at various intensities. The figure has been adapted from [16].

A more detailed description of this fundamental physics and scaling laws for electron energies is given by [101, 104].

2.4.3 Acceleration Mechanism for Ions

We have seen several mechanism how laser energy can be coupled into a plasma and accelerate electrons to relativistic energies. We further have seen that today's laser intensities are not sufficient to directly act on the much heavier ions and accelerate them. In all mechanisms that have been found for LION, the energy is transferred to the ions via the electrons. With the first meaningful acceleration of ions at the beginning of this century [121–123] a great number of simulations and models have been derived describing various mechanisms of laser-induced ion acceleration. The direct observation of different processes is challenging since in reality it is often a mixture of different mechanisms. Further, several of the regimes require certain and often challenging conditions such as a clean laser contrast, specific target shapes and densities or very high intensities. The most elaborated and up to this stage dominating process is the **T**arget **N**ormal **S**heath **A**cceleration (TNSA) [122–124]. The name TNSA already indicates the principle of this mechanism. The acceleration is directed along the target normal at both the rear and the front side of the target. In the previous section it has been described how electrons can be collisionless heated by the laser pulse. Those heated electrons will traverse the target and eventually form an electron sheath at the rear side of the target, where consequently a charge separation field is formed. Electrons are pulled back to the target and simultaneously replaced by newly arriving hot electrons from the target front. This electron sheath at the backside with a thickness of roughly the Debye length forms a quasi-static electric field acting on the ionized atoms at the rear side of the target. Consequently, due to the Coulomb forces, those ions will be accelerated. The characteristic exponential energy spectrum generated by TNSA often characterized by its cut-off energy. Further acceleration mechanisms are:

1. **Radiation pressure acceleration:** The RPA mechanism has first been described in 2004 [125] as a method to accelerate ions with narrowed energy distribution. The high intensity beyond 10^{23} W cm^{-2}required for this mechanism marks its main challenge. However, circular polarized light can circumvent this fact [126]. In 2009, the mechanism has first been demonstrated [127] and is, even though frequently sought, still challenging due to the lack in laser intensity.

2. **Collisionless shock acceleration:** Is similar to RPA but typically with thicker targets such that the hole boring effect of the plasma never perturbates the target completely and reaches the rear. Experimental demonstrations can be found in [128–130].

3. **Coulomb explosion:** The process of Coulomb explosion dominates when all electrons have been pushed out of the target leaving behind the heavier ions. Coulomb forces then cause an explosion of the purely positively charged targets in 4π [131–134], or a more directed mechanism [135], depending on geometry.

4. **Magnetic vortex acceleration:** This process occurring in low density targets describes an acceleration based on dipole magnetic fields [136, 137].

The number of different acceleration mechanisms, that have been demonstrated in simulations or experiments is large. However, in most cases the acceleration process involves various mechanisms. In order to clearly show the effect of one mechanisms, it is mandatory to suppress other effects by an advanced choice of the laser-target-setup combination.

2.5 Acoustic Measurements of Ions

This section introduces the concepts of how accelerated ions can be analyzed via acoustic waves. We have shown earlier that the temporal shape of a wave contains information about its source. This is the key idea of I-BEAT introduced in Chapter 5. When ions traverse matter they interact with the surrounding material and deposit part of their energy while being decelerated. This localized energy deposition eventually leads to a local heating and expansion process. This expansion causes a pressure wave. A pressure wave, as described earlier, is an acoustic wave that can now be measured with several techniques. Piezoelectric transducers are one of the common techniques and are used in this work. While one measurement point (one detector) can acquire the information along 1 axis, the local heating map can be evaluated by measuring the pressure wave at different locations. The source of the energy can be quite diverse. The most common source is absorption of laser light that is referred to as photoacoustics [138]. In this work though, we will concentrate on ion bunches that are stopped within water.

2.5.1 Interaction of Ions with Matter

The loss of energy, when ions traverse matter, is defined by the so called stopping power. Several processes can lead to an absorption of energy:

1. Coulomb interaction with the atomic electrons (electronic stopping power)
2. Coulomb interaction with the atomic nucleus (nuclear stopping power)
3. Nuclear interaction
4. Bremsstrahlung

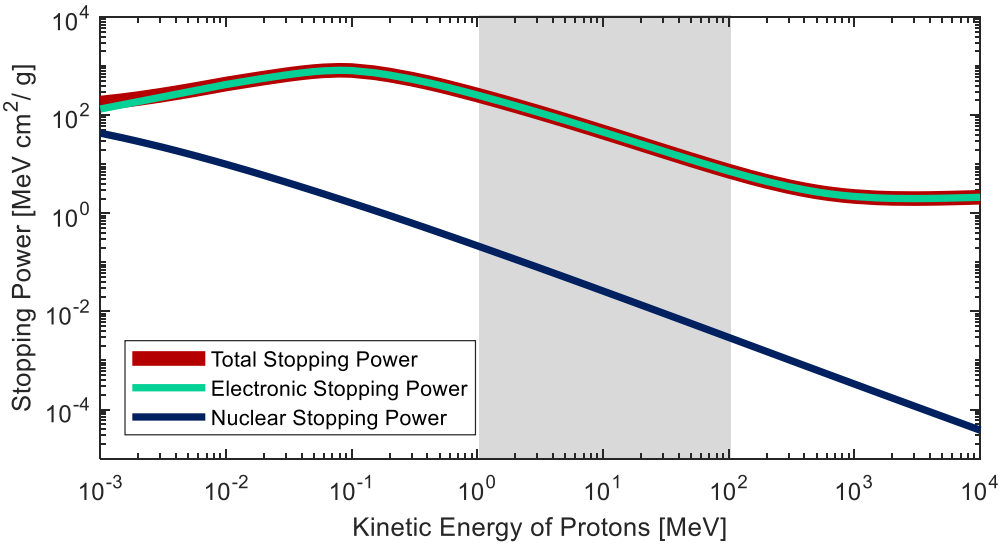

Figure 2.3 | Stopping power for protons in water. This plot depicts the stopping power of protons ins water. At low kinetic energies the nuclear stopping power has some impact. At higher energies it is negligible and the stopping power is dominated by the so called electronic stopping power. The gray part highlights the relevant energy band in the framework of this work. Data taken from [139].

The electronic stopping power is considered to be the dominating effect in particular for high energetic ions (for protons $>$ 100 keV) as depicted in Fig. 2.3. Ions colliding with the surrounding electrons will eventually pass on enough energy to an electron to set it free, thus ionizing its atom. Similar to what has been observed for collisional absorption in a plasma the cross-section is strongly dependent on the interaction time and thus the velocity of an ion. This explains the Bragg-peak shape of the depth dose distribution since the majority of the energy is absorbed when the ion becomes slow and is finally stopped as depicted in Fig. 1.6. The freed electrons have

a certain velocity and will dissipate their energy by further ionizing surrounding matter and distributing their energy to it. This transfer of energy from the ion to surrounding matter can be considered as fast relative to the dynamics of sound waves. The expression for the stopping power has been derived by Bethe and Bloch [140, 141] and is written here following the notation of [142]:

$$\langle -\frac{dE}{dx} \rangle = 4\pi N_{\mathrm{A}} r_{\mathrm{e}}^2 m_{\mathrm{e}} c^2 \frac{Z}{A} \frac{z^2}{\beta^2} \left[\frac{1}{2} \ln \left(\frac{2 m_e c^2 \gamma^2 \beta^2 W_{\max}}{I^2} \right) - \beta^2 - \frac{\delta(\beta\gamma)}{2} \right], \tag{2.41}$$

with z the charge number of the incident particle, Z and A the atomic and mass number of the absorber material, I the mean excitation energy, $\delta(\beta\gamma)$ a correction term and $W_{\max}$ the maximum energy transfer in a single collision. The stopping of ions in matter is a statistical process causing lateral and also longitudinal straggling of an ion bunch. It is thus not possible to calculate the trajectory of an ion exactly but a normalized distribution can also be assigned to a single ion. We define $B(E_{\mathrm{kin}}, z)$ as the depth dose profile, describing the deposited energy per unit volume depending on the energy E_{kin} at $z = 0$ (and for completeness also on the density of the material and the ion species). For non mono-energetic bunches of mixed species we introduce a normalized energy distribution $f(E_{\mathrm{kin}})$ and thus $B_{\mathrm{s}}(z)$ represents the instantaneously generated spread out Bragg-curve:

$$B_{\mathrm{s}}(z) = \sum_{\mathrm{i}} \left[n_{\mathrm{i}} \int B_{\mathrm{i}}(E_{\mathrm{kin}}, z) \cdot f_{\mathrm{i}}(E_{\mathrm{kin}}) \, dE_{\mathrm{kin}} \right], \tag{2.42}$$

where n_{i} is the number of ions of each species, indicated with i.

2.5.2 Thermodynamics

We have stated that the deposited energy is the source of an acoustic pressure wave. For a deeper understanding of this transition a few thermodynamic quantities are examined. The nexus of quantities such as pressure, temperature and density form the basis of thermodynamic models. In the framework of this work a few statements can be made

1. **Boyle's law:** When the density increases the pressure increases $\rho \propto p$.

2. **Charles's law:** When the temperature increases, matter expands and thus the density decreases $\rho \propto 1/T$.

Name	Symbol	Further information
Volume	V	
Mass	m	
Speed of sound	v_s	$v_s = 1/\sqrt{\rho\kappa}$
Density	ρ	$\rho = m/V$
Injected heat per unit volume and time	Q_i	
Thermal expansion coefficient	β_t	$\beta_\mathrm{t} = 1/V \cdot (\partial V/\partial T)_p$
Specific heat coefficient (isochoric)	C_v	$C_v = \delta Q_i/(m\delta T)$
Specific heat coefficient (isobaric)	C_p	$C_p = \delta Q_i/(m\delta T) = \kappa\rho C_v v_s^2$
Isothermal compressibility	κ	$\kappa = -1/V \cdot (\partial V/\partial p)_T = C_p/(\rho v_s^2 C_v)$
Grüneisen coefficient	Γ	$\Gamma = \beta_\mathrm{t}/(\kappa\rho C_v) = \beta_\mathrm{t} v_s^2/C_p$
Heating function	$H(\vec{r}, t)$	

Table 2.1 | Thermodynamic quantities. This table introduces thermodynamic quantities that are used to describe how ions can be the source of a pressure wave.

3. **Gay-Lussac's law:** When the temperature increases, the pressure also increases $p \propto T$.

The volume expansion $\delta V/V$ can be written as

$$\frac{\delta V}{V} = -\kappa\delta p + \beta_\mathrm{t}\delta T. \tag{2.43}$$

The behavior of this equation is strongly dependent on the time scales of the perturbation. There are three different regimes. In the non-adiabatic regime the time scale is large enough that a thermal equilibrium can be formed by diffusive processes. In the so called thermal confinement regime the time scale is too short to form a thermal equilibrium and the volume expansion of Eq. (2.43) can be neglected. Thirdly, the stress confinement is valid when the time scale τ_{sc} is shorter than the pressure wave would need to pass a certain characteristic length d_{sc}:

$$\tau_{sc} = \frac{d_{sc}}{v_s}. \tag{2.44}$$

For a given heating pulse with duration τ_{sc} the stress confinement is valid for a maximum length of d_{sc} and defines a resolution limit at witch the heating function can be regarded as instantaneous. Equation (2.43) therefore can be written as

$$\delta p = \frac{\beta_\mathrm{t}}{\kappa}\delta T. \tag{2.45}$$

This equation directly shows one important aspect. A change of pressure and thus a sound wave is generated when the temperature changes. This means that a constant heating would not result in any acoustic signal; a pulsed energy deposition is required. In the framework of this thesis short ion bunches and short laser pulses are used to deposit heat in water. Therefore all further considerations are within the stress confinement regime. The next step is to relate the pressure directly to the introduced heat. With $C_v = \delta Q/m\delta T$ and the heat $Q = \xi \cdot E$ the Eq. (2.45) transforms to

$$\delta p = \frac{\beta_\mathrm{t}\xi}{\kappa C_v m}\delta E = \Gamma\xi\rho \underbrace{\frac{\delta E}{m}}_{\delta D} = \Gamma\frac{\delta Q}{V}, \tag{2.46}$$

where ξ is a coefficient that describes the how much energy E is converted to heat and can be treated as 1 [143]. The dose D is the absorbed energy per unit mass and is of particular importance in the bio-medical field. Additionally, the Grüneisen coefficient Γ was introduced here [144] . The Grüneisen coefficient is material dependent and correlates pressure with the absorbed energy:

$$\Gamma = V\frac{\partial p}{\partial E} = \frac{\beta_\mathrm{t}}{\kappa\rho C_\mathrm{v}} = (\beta_\mathrm{t}c_\mathrm{s}^2)/C_\mathrm{p}. \tag{2.47}$$

The Grüneisen coefficient for water is given by

$$\Gamma_\mathrm{w} = 0.0043 + 0.0053 \cdot T_\mathrm{w}, \tag{2.48}$$

where T_w is the water temperature given in Kelvin.

At this point, we have introduced relevant thermodynamic quantities and can finally introduce the particularly important heating function $H(\vec{r}, t)$ as the transferred energy per volume and time

$$H(\vec{r}, t) = \rho C_v \delta T = \frac{\delta E}{V} = \rho\delta D. \tag{2.49}$$

Note that the heating function is linear dependent to the dose, which becomes particularly relevant in Chapter 5.

2.5.3 Acoustic Waves

We have introduced the concept of waves and studied the basic principles of a prominent type, the transverse electromagnetic wave. One of the most important longitudinal waves are sound waves. The following description of sound waves is based on work presented in [138, 144–147]. A sound wave can be described as a propagating pressure or density change within a medium. Deduced from the general form of a harmonic wave (Eq. (2.1)), a pressure wave can be described as [144]

$$\left(\nabla^2 - \frac{1}{c^2}\frac{\partial^2}{\partial t^2}\right) p\left(\vec{r},t\right) = \begin{cases} 0 & \text{without any source} \\ -\dfrac{\beta_\mathrm{t}}{\kappa v_s^2}\dfrac{\partial^2 T\left(r,t\right)}{\partial t^2} & \text{with a heat source.} \end{cases} \tag{2.50}$$

Implementing the heating function in Eq. (2.50) yields

$$\left(\nabla^2 - \frac{1}{c^2}\frac{\partial^2}{\partial t^2}\right) p\left(\vec{r},t\right) = -\frac{\beta_\mathrm{t}}{C_\mathrm{p}}\frac{\partial H\left(\vec{r'},t'\right)}{\partial t}. \tag{2.51}$$

Solving the Wave Function

In Section B.1.2 it has been demonstrated that an inhomogeneous wave equation can be solved with the proper Green's function. The Green's function for this particular case is given by [144]

$$G(\vec{r},t;\vec{r'},t') = \frac{\delta(t-t'-\frac{\left|\vec{r}-\vec{r'}\right|}{v_s})}{4\pi\left|\vec{r}-\vec{r'}\right|}. \tag{2.52}$$

The general solution for an inhomogeneous wave equation with the Green's function approach was given by equation Eq. (B.9). In this case, the second term can be regarded as zero by sending the boundaries to infinity and assuming the field drops off to zero there. The third term can also be neglected by choosing a large time, where a thermal equilibrium has developed and thus the derivatives vanish. The solution of equation Eq. (2.51) is thus given by:

$$p(\vec{r},t) = \int_0^{t^+} dt' \int_{V'} d^3r' \frac{\delta(t-t'-\frac{\left|\vec{r}-\vec{r'}\right|}{v_s})}{4\pi\left|\vec{r}-\vec{r'}\right|} \cdot \frac{\beta_\mathrm{t}}{C_p}\frac{\partial H(\vec{r'},t')}{\partial t'}. \tag{2.53}$$

After the integration over t' it becomes:

$$p(\vec{r},t) = \frac{\beta_\mathrm{t}}{4\pi C_\mathrm{p}} \int_{V'} d^3r' \frac{1}{\left|\vec{r}-\vec{r'}\right|} \frac{\partial H(\vec{r'},t')}{\partial t'}, \tag{2.54}$$

where $t' = t - \left|\vec{r}-\vec{r'}\right|/v_\mathrm{s}$ is now the retarded time[9]. It can further be assumed that the temporal and spatial behavior of the heating function are not coupled and thus $H(\vec{r},t) = H_s(\vec{r}) \cdot H_t(t)$. As a result equation Eq. (2.54) transforms to

$$p(\vec{r},t) = \frac{\beta_\mathrm{t}}{4\pi C_\mathrm{p}} \frac{\partial}{\partial t} \int_{V'} \frac{d^3r'}{\left|\vec{r}-\vec{r'}\right|} H_\mathrm{s}(\vec{r'}) H_\mathrm{t}\left(t - \frac{\left|\vec{r}-\vec{r'}\right|}{v_\mathrm{s}}\right). \tag{2.55}$$

In many of such experiments the heating is either turned on or turned off without a considerable rise time. It can therefore be regarded as a Heaviside-Stepfunction[10]. In the regime of stress confinement this can be further simplified by regarding the heating as a single event and thus $H_\mathrm{t} = \delta(t')$. We thus get

$$p(\vec{r},t) = \frac{\beta_\mathrm{t}}{4\pi C_\mathrm{p}} \frac{\partial}{\partial t} \int_{V'} \frac{d^3r'}{\left|\vec{r}-\vec{r'}\right|} H_\mathrm{s}(\vec{r'}) \delta\left(t - \frac{\left|\vec{r}-\vec{r'}\right|}{v_\mathrm{s}}\right). \tag{2.56}$$

This equation can be further simplified by using $\vec{R} = \vec{r} - \vec{r'}$ and thus $|R| = \left|\vec{r}-\vec{r'}\right|$.

$$p(\vec{r},t) = \frac{\beta_\mathrm{t}}{4\pi C_\mathrm{p}} \frac{\partial}{\partial t} \int_{V'} \frac{d^3R}{|R|} H_\mathrm{s}(\vec{R}+\vec{r}) \delta\left(t - \frac{|R|}{v_\mathrm{s}}\right). \tag{2.57}$$

This derivation shows that the source term for fast and short heating can be interpreted as an initial spatial condition, that reaches the detector at the retarded time.

[9] The retarded time describes the time t' when an event happened at the location r' that is detected at r at the time t and has traveled with the speed c that is in this case v_s.

[10] $H_\mathrm{t}(t) = H_\Theta(t) - H_\Theta(t - \tau_\mathrm{p})$ with τ_p being the pulse length of the heating pulse.

Calculation for I-BEAT

For further simplification we set the origin of the coordinate system to the detector $\vec{r} = 0$. The pressure wave at the detector thus yields:

$$p(t) = \frac{\beta_\mathrm{t}}{4\pi C_\mathrm{p}} \frac{\partial}{\partial t} \int_{V'} \frac{d^3R}{|R|} H_\mathrm{s}(\vec{R}) \delta\left(t - \frac{|R|}{v_\mathrm{s}}\right). \tag{2.58}$$

We have derived the description of a pressure wave that is generated by a short heating pulse. In the framework of this thesis the pressure wave that is generated by a short proton bunch dissipating its energy within a water phantom is measured. The proton bunch is assumed to have a lateral Gaussian shape and to be directed along z. Therefore also the heating function consists of a depth-dose profile $h(z)$ with a lateral Gaussian distribution[11] with cylindrical symmetry $H_\mathrm{s}(x, y, z) = h(z) \cdot N(x; 0, \sigma) N(y; 0, \sigma)$. Despite the cylindrical symmetry of the heating function it is beneficial to work in spherical coordinates because its radius marks the propagation distance of a wave and the concept of the retarded time applies directly. The heating function can thus be expressed as

$$H_\mathrm{s}(R, \Theta, \Phi) = h(R\cos(\Theta)) \cdot \frac{1}{2\pi\sigma^2} \cdot e^{-\frac{R^2 \sin(\Theta)^2 \left(\sin(\Phi)^2 + \cos(\Phi)^2\right)}{2\sigma^2}}. \tag{2.59}$$

Rewriting Eq. (2.58) in spherical coordinates yields

$$p(t) = \frac{\beta_\mathrm{t}}{4\pi C_\mathrm{p}} \frac{\partial}{\partial t} \int_{V'} d\Theta d\Phi dR\, R^2 \sin(\Theta) \frac{H_\mathrm{s}(R, \Theta, \Phi)}{|R|} \delta\left(t - \frac{|R|}{v_s}\right). \tag{2.60}$$

The integration over R and thus the delta function with the identity $\delta(\alpha x) = \frac{1}{|\alpha|}\delta(x)$ sets $|R| = v_\mathrm{s} t$:

$$p(t) = \frac{\beta_\mathrm{t} v_\mathrm{s}^2}{4\pi C_\mathrm{p}} \frac{\partial}{\partial t} \iint d\Theta d\Phi \sin(\Theta)\, t \cdot H_\mathrm{s}(v_\mathrm{s} t, \Theta, \Phi). \tag{2.61}$$

In the next step we insert the heating function Eq. (2.59)

$$p(t) = \frac{\beta_\mathrm{t} v_\mathrm{s}^2}{4\pi C_\mathrm{p}} \frac{1}{2\pi\sigma^2} \frac{\partial}{\partial t} \iint d\Theta d\Phi \sin(\Theta)\, t \cdot h(v_\mathrm{s} t \cos(\Theta))\, e^{-\frac{v_\mathrm{s}^2 t^2 \sin(\Theta)^2}{2\sigma^2}}. \tag{2.62}$$

[11] σ is the standard deviation of the Gaussian determining the width of the heating function.

Integrating over Φ results in

$$p(t) = \frac{\beta_\mathrm{t} v_\mathrm{s}^2}{4\pi C_\mathrm{p}} \frac{1}{\sigma^2} \frac{\partial}{\partial t} \int d\Theta \sin(\Theta)\, t \cdot h\left(v_\mathrm{s} t \cos(\Theta)\right) \cdot e^{-\frac{v_\mathrm{s}^2 t^2 \sin(\Theta)^2}{2\sigma^2}}. \tag{2.63}$$

In a last step we re-substitute $z = v_\mathrm{s} t \cos(\Theta)$

$$p(t) = \frac{\beta_\mathrm{t} v_\mathrm{s}^2}{4\pi C_\mathrm{p}} \frac{1}{\sigma^2} \frac{\partial}{\partial t} \int_{-v_\mathrm{s} t}^{v_\mathrm{s} t} \frac{1}{v_\mathrm{s} t} dz\, t \cdot h(z) \cdot e^{-\frac{1}{2\sigma^2}\left(v_\mathrm{s}^2 t^2 - z^2\right)}. \tag{2.64a}$$

$$= \frac{\beta_\mathrm{t} v_\mathrm{s}}{4\pi C_\mathrm{p}} \frac{1}{\sigma^2} \frac{\partial}{\partial t} \int_{-v_\mathrm{s} t}^{v_\mathrm{s} t} dz \cdot h(z) \cdot e^{-\frac{1}{2\sigma^2}\left(v_\mathrm{s}^2 t^2 - z^2\right)} \tag{2.64b}$$

This equation can be used to relate the measured signal of I-BEAT with the heating function caused by the ion bunch dissipating the energy in water. The σ is the Gaussian width of the ion bunch and can later be used to retrieve the best fitting width and thus get a first 2-dimensional information with only a single transducer. Note that the propagation of the wave was not approximated herein[12]. In our case, the heating function describes the energy that is induced by a short proton bunch and thus $h(z)$ is directly correlated to $B_\mathrm{s}(z)$ (see Eq. (2.42)).

[12] In the Fraunhofer approximation we could have used that $z \approx R$.

2.6 The Beauty of Waves

In this chapter we have seen several areas where waves play a significant role. The beauty is that the concept of waves can describe many different phenomena such as:

1. Electromagnetic waves and the description of a laser pulse.
2. Plasma waves, which are generated during acceleration processes and play a significant role especially in Chapter 4, where the plasma is modified from transmissive to opaque.
3. Ultrasonic waves, that carry the information of their spatial source term and are used for retrieval of the energy distribution of ions in Chapter 5.

Nevertheless we only tackle few of the various topics that can be explained by wave phenomena in this work. The concept of waves for example further plays significant roles in the fields of:

1. **Quantum mechanics:** $\lambda = h/p = h/mv$ (de Broglie) and $i\hbar \cdot \partial\Psi/\partial t = \hat{H}\Psi$ (Schrödinger) where matter is described as a wave with the amplitude being the probability of finding the particle at a specific location.
2. **Solid state physics** where phonons describe quantum excitations of lattice vibrations in matter, defining several material properties.
3. **Astronomy** as for example the newly discovered gravitational waves are waves in space-time.

Chapter 3

LION at LEX Photonics

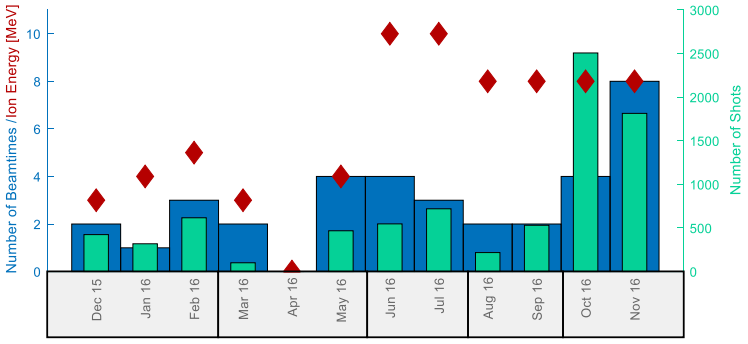

Summary of the experimental campaings in LEX Photonics (see Fig. 6.1).

Contents

3.1 ATLAS-300 . . . . . **46**

3.2 Experimental Area and Setup **50**

3.3 Summary and Result **56**

This chapter describes the experimental setup at LEX Photonics and gives an overview of results obtained in the 2 years operation period of experiments at LEX Photonics. The two main motivations of LEX Photonics were prototype development for CALA and one next step towards a viable laser-driven ion source.

Author contribution: *This chapter describes a large experimental campaign that was in particular lead by the author. Most of the modifications presented herein were advanced and guided by the author. Nonetheless, nothing of this would have been possible without the countless effort of Jianhui Bin, Ying Gao, Jens Hartmann, Christian Kreuzer, Florian Lindner, Tobias Ostermayr, Thomas Rösch, Martin Speicher and Prof. Stefan Karsch and his group.*

3.1 ATLAS-300

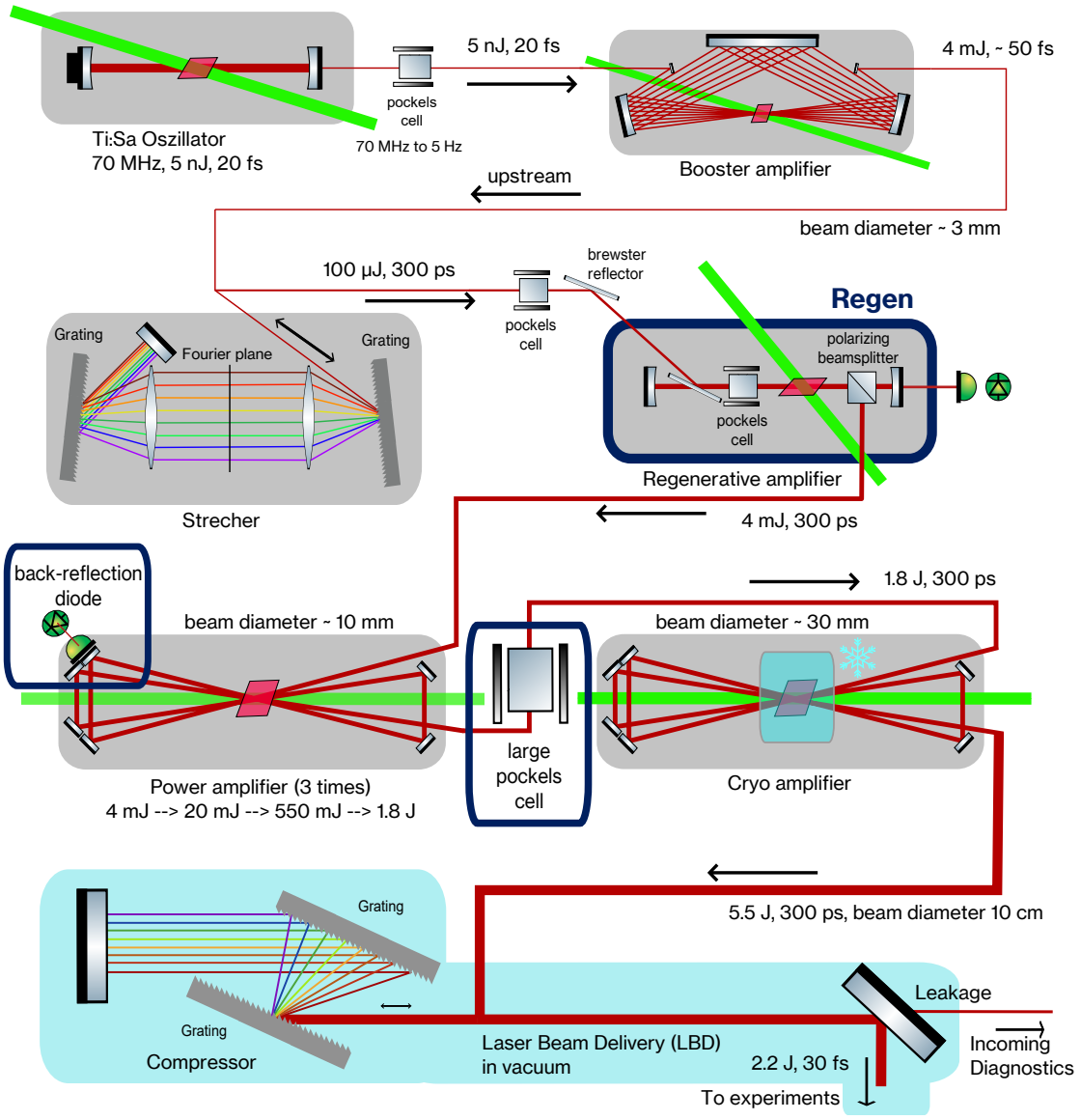

Figure 3.1 | ATLAS-300. The scheme of the ATLAS-300 is illustrated. It shows the main components that are typical for a high power laser system. The energy and pulse length after each stage is given. The REGEN is highlighted since it has been identified to be the main cause for prepulses, which had limited operation of the ion acceleration experiments. The figure is adapted with the courtesy from Kreuzer [107].

The centerpiece of LEX Photonics is the ATLAS-300[1], a laser that is built and operated by the group of Prof. Stefan Karsch. It is a Ti:sapphire based CPA system

[1]The laser was designed to an energy of 7.5 J in 25 fs hence reaching a peak power of 300 TW. The ATLAS-300 contains commercial components from Amplitude Technologies.

(Fig. 1.2) with a spectrum from 760 nm to 840 nm supporting a pulse duration of 30 fs. Several stages amplify the energy of the stretched pulse up to 5.5 J, whereas the **Regen**erative amplifier (REGEN) will be of most interest during this work. The laser pulse had to be guided through vacuum after re-compression. Nonlinear effects of air itself would be too large and the desired features such as the ulta-short pulse and the resulting ultra-high intensity would be deteriorated otherwise. The laser-pulse is thus transported in a vacuum beam line to the desired experimental area. The LBD in LEX Photonics contained 6 mirrors redirecting the beam and was approximately 15 m long. The laser could be guided to two experimental areas that were dedicated to ion and electron acceleration. The leakage of a mirror close by the experiment was used to analyze the incoming laser light. The energy was reduced to about 2.2 J on target (the energy is primarily lost in the compressor and the off-axis parabola in the target chamber), and thus an effective peak power on target of about 70 TW is reached. A detailed sketch of the ATLAS-300 and its components is illustrated in Fig. 3.1.

Apart from laser pulse duration and laser energy there are multiple parameters that can significantly alter the laser plasma interaction and hence affect the acceleration process. Among the most influential for laser-ion acceleration are the temporal pulse-contrast and the spatial intensity distribution. In addition, the back-reflection from an overdense plasma into the **L**aser-**B**eam-**D**elivery (LBD) and subsequently the laser system has to be considered and avoided to minimize risk of damage of laser components.

3.1.1 Temporal Intensity Distribution

The temporal intensity distribution of the laser pulse is often referred to as laser contrast. The peak intensity of laser pulses often exceeds the ionization threshold of matter by orders of magnitude. So even lower intense prepulses or **A**mplified **S**pontaneous **E**mission (ASE) delivered picoseconds and nanoseconds in advance of the main laser pulse can be sufficiently for creating a plasma and thus altering the initial conditions of the laser-target interaction significantly, as described in Fig. 2.2 and Section 2.3.2. The laser contrast is typically measured with third order auto-correlators [148, 149] as described in Section B.4.1. The laser contrast in LEX Photonics has been among the limiting factors for proton energies. This was supported when the use of an integrated double plasma-mirror target [43] resulted in proton energies of about 12 MeV corresponding to a doubling of the proton energy

[43]. The removal of several prepulses (see Section A.1.2) did not change the results significantly. Using a third-order-auto-correlator (Tundra) with a long measuring range led to the discovery of two previously unmeasurable prepulses (at ≈ 500 ps and ≈ 660 ps), which were the limiting factor. They originated from reflections of the surfaces of the Pockels cell within the cavity of the REGEN (see Fig. A.4) and were direct prepulses and not created from former postpulses. This is significant since the prepulse is typically less intense than its corresponding postpulse, and thus the direct prepulses have higher intensities. A small tilt of the Pockels cell lowered the intensity of those prepulses, but could also cause a reduced amplification and an increased ASE level of the REGEN. With this findings and modification the measured proton energies increased significantly (as can be seen in June and July 2016 Fig. 3.10). Nonetheless, it was no solution to the problem, since the prepulses were only attenuated and realignment and optimization of the REGEN impaired the contrast again.

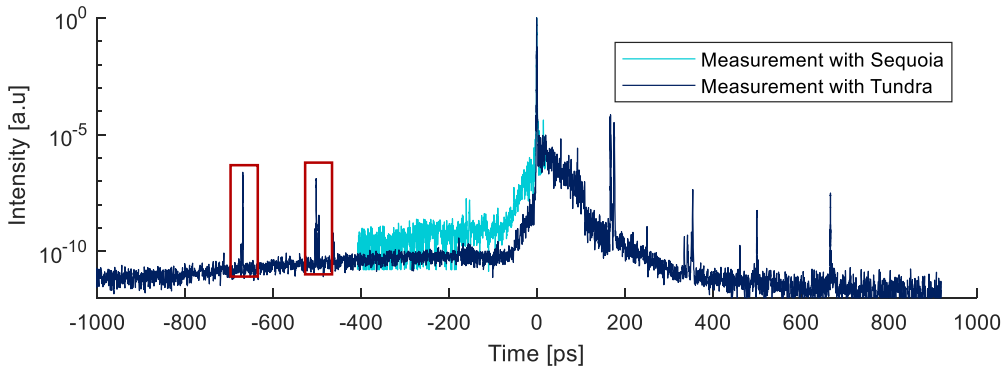

Figure 3.2 | The ATLAS-300 contrast. This figure shows two measured contrast curves. The Tundra is capable of measuring 2 ns, and thus two significant prepulses at 500 and 660 ps prior to the main pulse have been identified. In contrast to previous prepulses those are origin from direct reflections in the REGEN and not transformed from postpulses.

3.1.2 Spatial Intensity Distribution in the Focal Plane

The spatial intensity distribution of the laser in the focal plane of the experimental chamber was measured with a vacuum microscope (see Fig. 3.6). This was done by recording images with attenuated laser pulses at different filter settings. Those images were stitched together and the intensity was calculated using Eq. (2.23) (see [150] for more details). The typical energy of the ATLAS-300 was about 6 J before

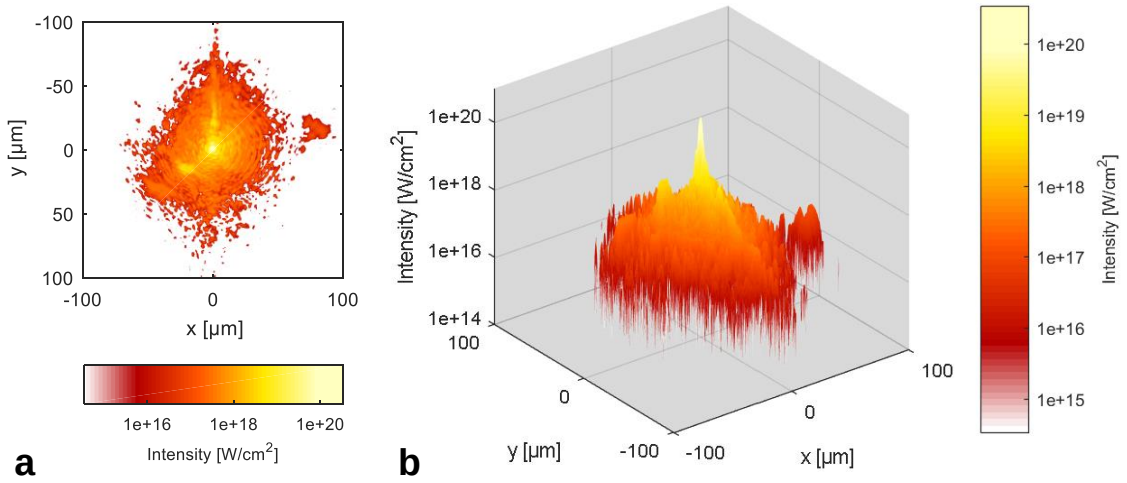

Figure 3.3 | HDR focus in LEX Photonics. The figures show the spatial intensity distribution in the focal plan of LEX Photonics. The distribution is obtained by stacking multiple images, recorded with different filter settings.

compression reducing to about 2.2 J in the target chamber[2]. The scaled intensity distribution can be seen in Fig. 3.3. Even though the FWHM is evaluated to be 3.2 µm a large amount of energy is distributed to a larger area. This is important since the peak intensity of $I_0 = 3.3 \cdot 10^{20}\mathrm{W\,cm^{-2}}$would otherwise be significantly overestimated. We can further calculate the characteristic laser intensity a_0 using Eq. (2.27c). The calculated a_0 for the ATLAS-300 was about 12.4 and the corresponding acceleration gradient (electric field) is of the order 50 MV/µm.

3.1.3 Additional Laser Diagnostics

An online shot diagnostic was built using a designated leakage through a mirror close to the experimental chamber and measuring the energy and the spectrum of the laser pulse, that arrived at the LION chamber. The monitoring of the energy allowed to determine long-term stability and drifts of the laser performance and the shot-to-shot fluctuations. The monitoring of the spectrum further allowed a control when optimizing the timings of the fast Pockels cell as explained in Fig. 3.4. The spectrum is altered when timing of the Pockels cell is delayed until it starts cutting into the stretched pulse and thus, the spectrum. One can see that in such a case the part of the shorter wavelength is attenuated. This careful adjustment is crucial, because

[2]This loss is a combination of the loss in the compressor, a loss in the beam line and the parabola.

the unbalanced spectral energy distribution can lead to an unbalanced temporal intensity distributions and ultimately destruction of optics within the CPA system.

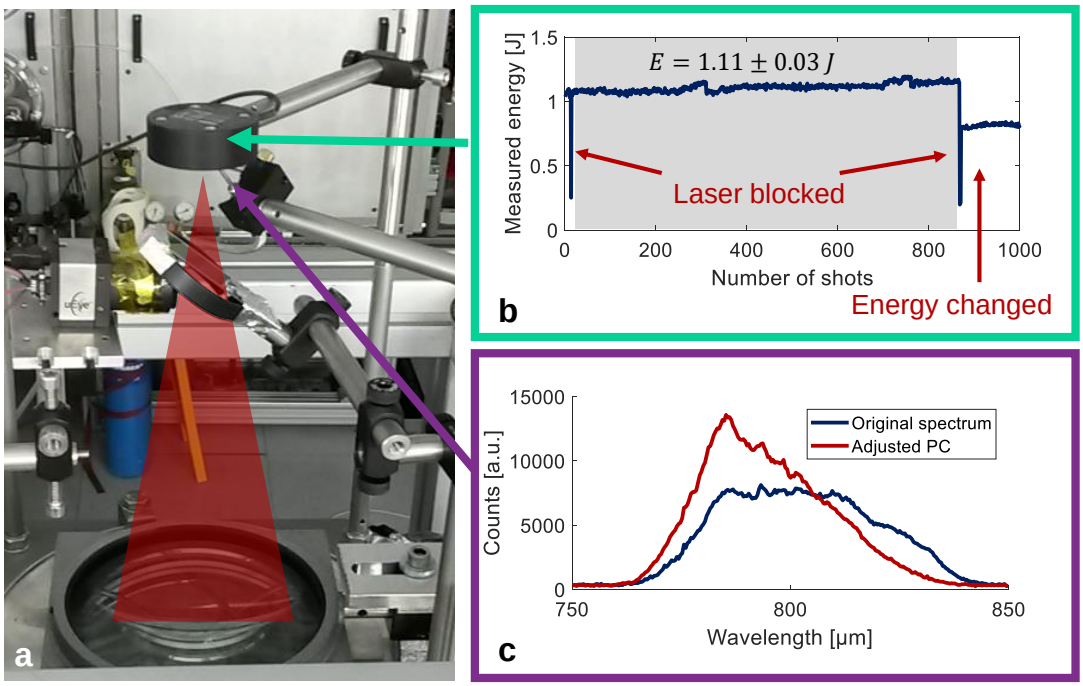

Figure 3.4 | Diagnostic of incoming laser light. The leakage of the incoming laser light is focused (**a**) onto a energy meter (**b**) and a spectrometer (**c**).

3.2 Experimental Area and Setup

One purpose of LEX Photonics was to serve as a prototype experiment for CALA. One experimental vacuum chamber was designated for testing a setup and components viable for high-repetition rate ion acceleration for applications. These parts should later be moved to CALA. A second adjacent experimental chamber provided space for new approaches and ideas. A sliding mirror allowed to guide the laser pulse to either setup (see Fig. 3.5). The second experimental[3] chamber was mainly used for the development of TRIC as demonstrated in Chapter 4.

[3]This chamber was referred to as storage chamber.

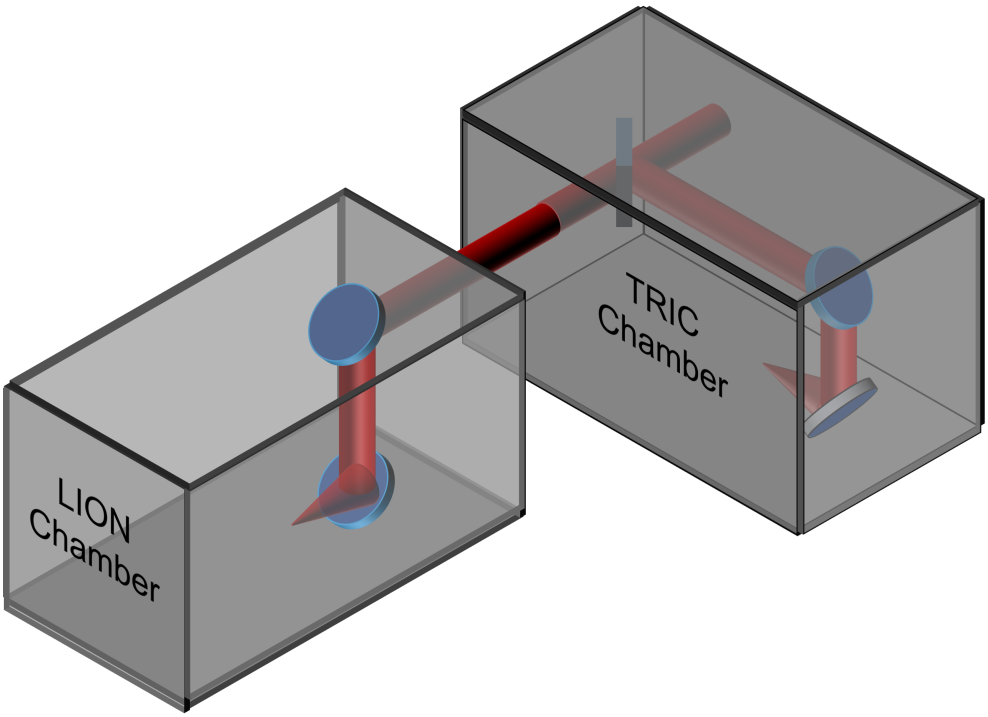

Figure 3.5 | Two experimental chambers at LEX Photonics. At LEX Photonics two vacuum chambers were used. While in the LION chamber the experimental setup was rather strictly aiming for applications with ions, the second chamber was used TRIC and is described in Chapter 4. With a sliding mirror the beam could be coupled out.The figure is adapted from [151].

3.2.1 LION Chamber in LEX Photonics

The setup of the LION chamber can be seen in Fig. 3.6a. In accordance with the requirements at CALA and other overarching reasons [152], the beam height was set to 42 cm above the bread-board of the target chamber. The designated interaction point, and thus the position of the laser focus is in the following referred to as **T**arget **C**hamber **C**enter (TCC), even though it is not the geometrical center of the vacuum chamber. The laser pulse is focused with an F/2 parabola[4] with an off-axis angle of 90 degree (Fig. 3.6d). A microscope that can be fully operated in vacuum, developed under the supervision of Christian Kreuzer [107, 153], enabled a very compact solution for focus diagnostics and also positioning of the targets. It is depicted in Fig. 3.6b, and is described in more detail in Section A.1.4. The target wheel (Fig. 3.6e) [59] enabled a positioning of various targets with a repetition rate of 0.5 Hz (see Section A.1.7 for more details). The light, emitted off the plasma is

[4]The F number is F=f/d with f being the focal length and d the diameter of the laser beam on the parabola.

guided to the top of the chamber (as shown in Fig. 3.6c), where several diagnostics have been built (see Section A.1.6 for more details).

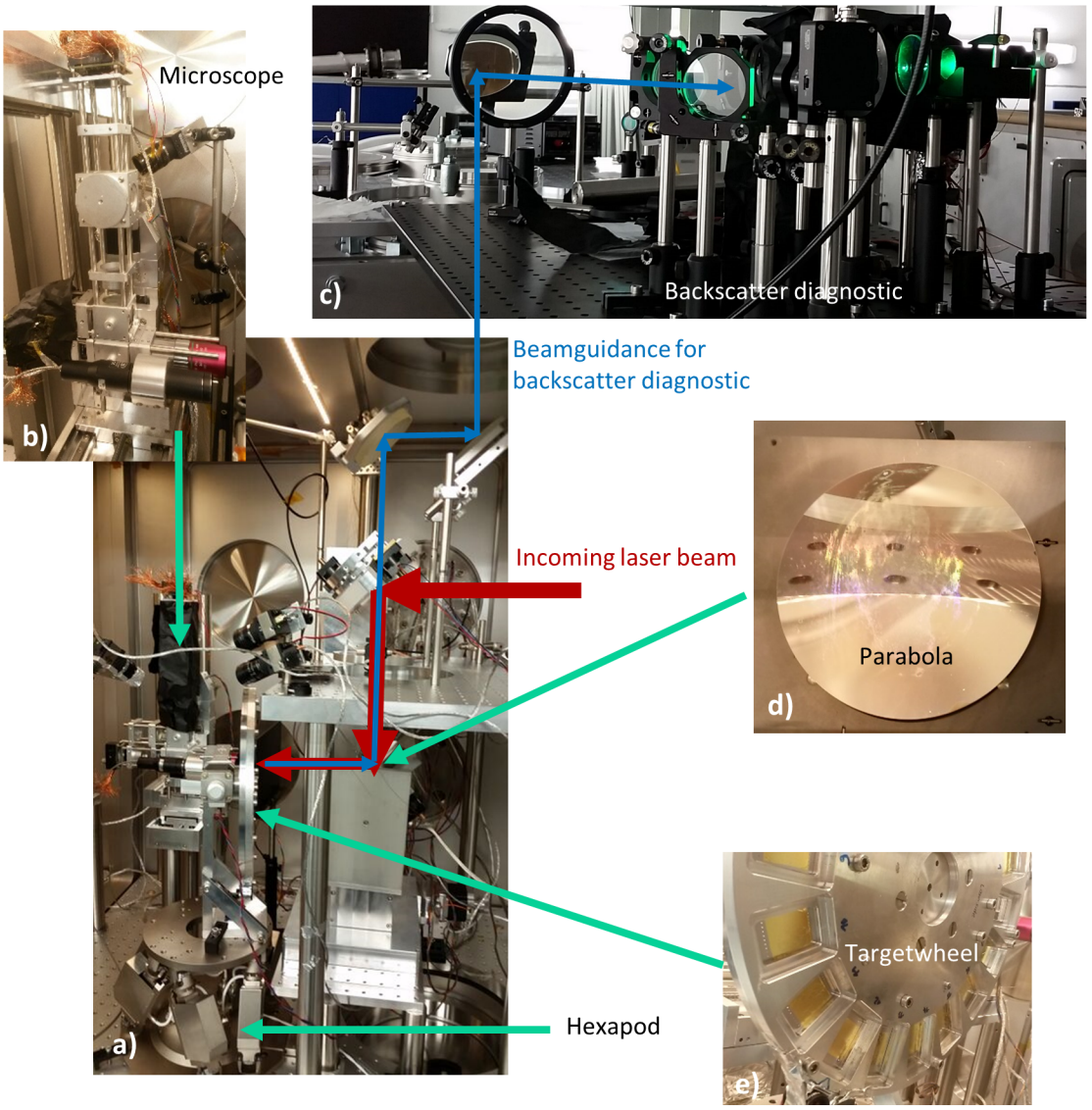

Figure 3.6 | Experimental setup at LEX Photonics. A picture of the setup in the experimental chamber is shown in **a**. The laser pulse is focused with a 90° OAP (**d**) onto the target (**e**). The target is mounted in the target wheel (**e**) that is positioned onto a hexapod. The vacuum microscope (**b**) is used to analyze the focus and overlap the target position. The back-scattered light (blue) is guided out of the vacuum chamber and analyzed on top as shown in **c**.

3.2.2 Ion Wide Angle Spectrometer

Since we were mainly interested in the energy distribution of protons, our choice for characterizing the energy spectrum and the angular distribution, we implemented a **W**ide **A**ngle **SP**ectrometer (see Section A.1.8 for details) equipped with Radeye detectors [154, 155].

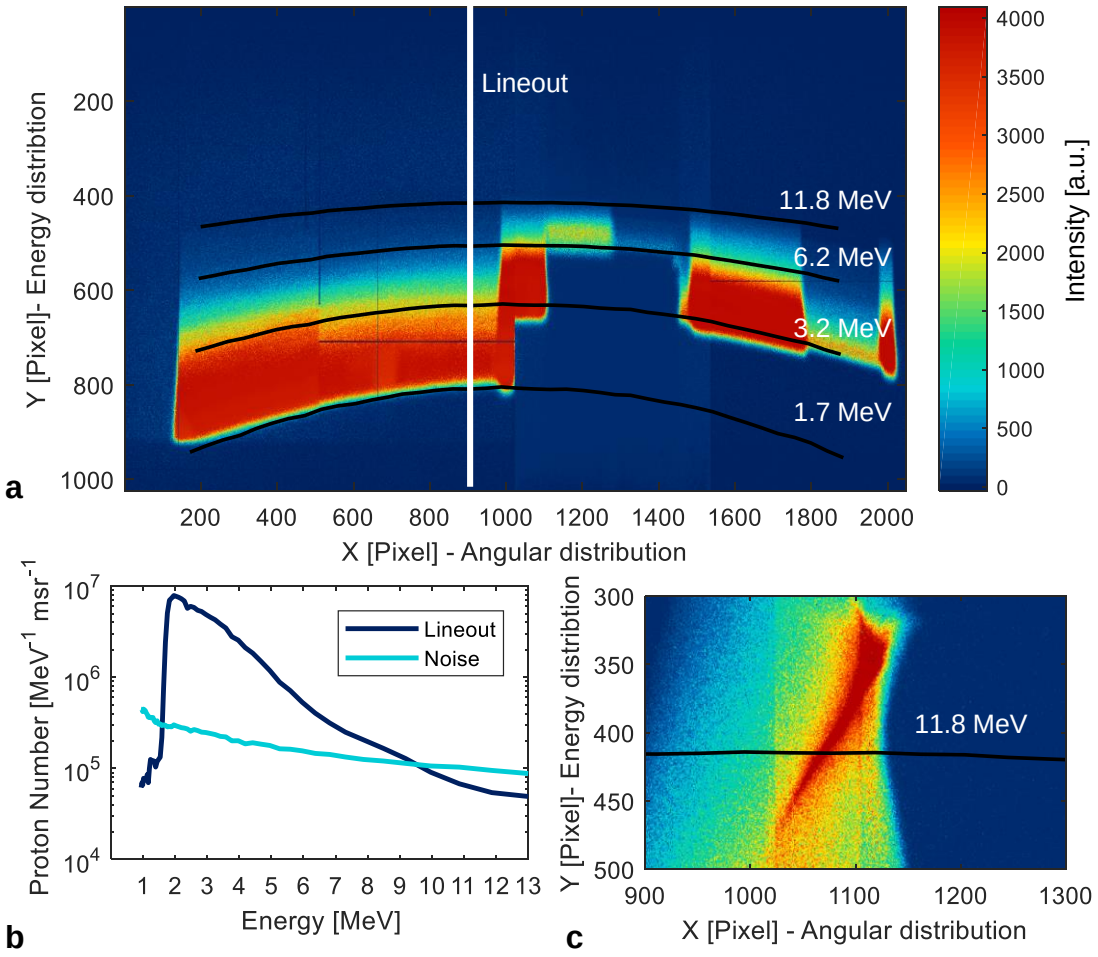

Figure 3.7 | Proton energy spectrum evaluated with WASP. The evaluation of the data taken with the WASP (see Fig. A.8) is shown. The measured image (**a**) contains three different layers of aluminum creating three cut-off energy lines at 1.7 3.2 and 6.2 MeV. The proton spectrum over the lineout is shown in **b**. An ion focus, where the PMQ have been set to a design energy of 11.8 MeV is shown in **c**.

In Fig. 3.7a, a typical image, taken with a Radeye, is shown. Protons were deflected downwards by the magnetic field. Various thicknesses of aluminum in front of the detector were used to identify several cut-off energies and could be used for energy calibration. The curvature in the signal is due to inhomogeneities of the

magnetic field caused by the wide gap between magnetic poles. A vertical lineout was used to calculate the absolute energy distribution of the proton spectrum (see Fig. 3.7b).

3.2.3 Quadrupoles - Focusing the Ion Bunch

Typical features of laser-accelerated ions are the large divergence angle as well as the broad-band energy spectrum and ultra-high ion flux. Nevertheless those features cause a drop-down in the flux for increasing distance from TCC. To exploit that uniquely high particle flux for applications that commonly have to be positioned further downstream of the source, particle optics have to be used. Therefore we implemented a doublet of **P**ermanent **M**agnetic **Q**uadrupole (PMQ) that is described in more detail in Section A.1.9. With the use of the PMQ we were able to re-focus a specific design energy to the application site. The design energy can be set by adjusting the distances of both PMQ to the target and also the distance of the ion focus to TCC. The focus of the PMQs was measured with **I**mage **P**lates (IPs) (Fig. 3.8a), scintillators (Fig. 3.8b) and also on the Radeye detector (see Fig. 3.7c). A closer study of the focus of the PMQ can be found in [156].

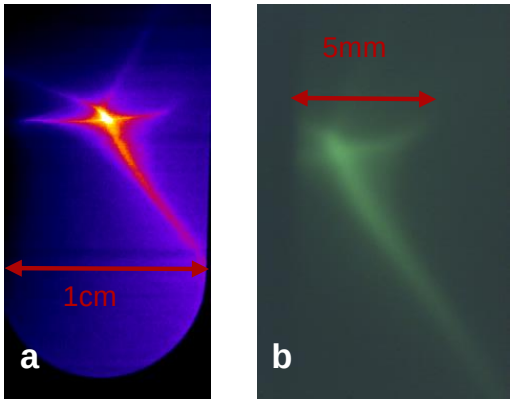

Figure 3.8 | Ion focus. This pictures show an ion focus obtained with the PMQ doublet. The ion bunch was guided about 1.50 m out of the vacuum and measured with an IP in **a** and a scintillator in **b**.

3.2.4 Setup Assembly

A typical setup for applications can be seen in Fig. 3.9. The ions have been focused with the PMQ and guided out of the vacuum chamber. The DM that was also used for the WASP was used to filter out electrons and contamination of low energetic

particles. A Kapton foil of 50 µm thickness, 1 cm width and 5 cm height served as vacuum-exit window.

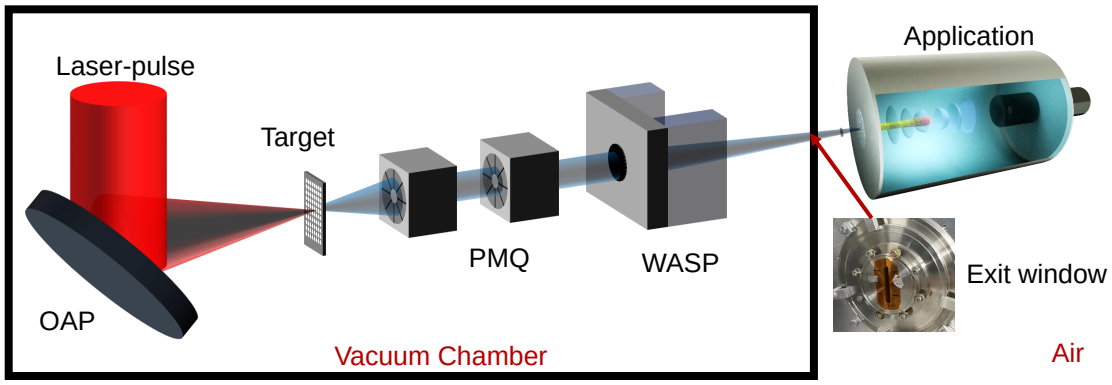

Figure 3.9 | Application setup at LEX Photonics. The laser-pulse is focused via an OAP onto a target. The herefrom accelerated ion bunch is focused and guided with the QPs. A DM filters out electrons and low energetic particles. Traversing a Kapton-foil window, the ion bunch is guided out of the vacuum chamber, where it could be used for application such as I-BEAT.

3.3 Summary and Result

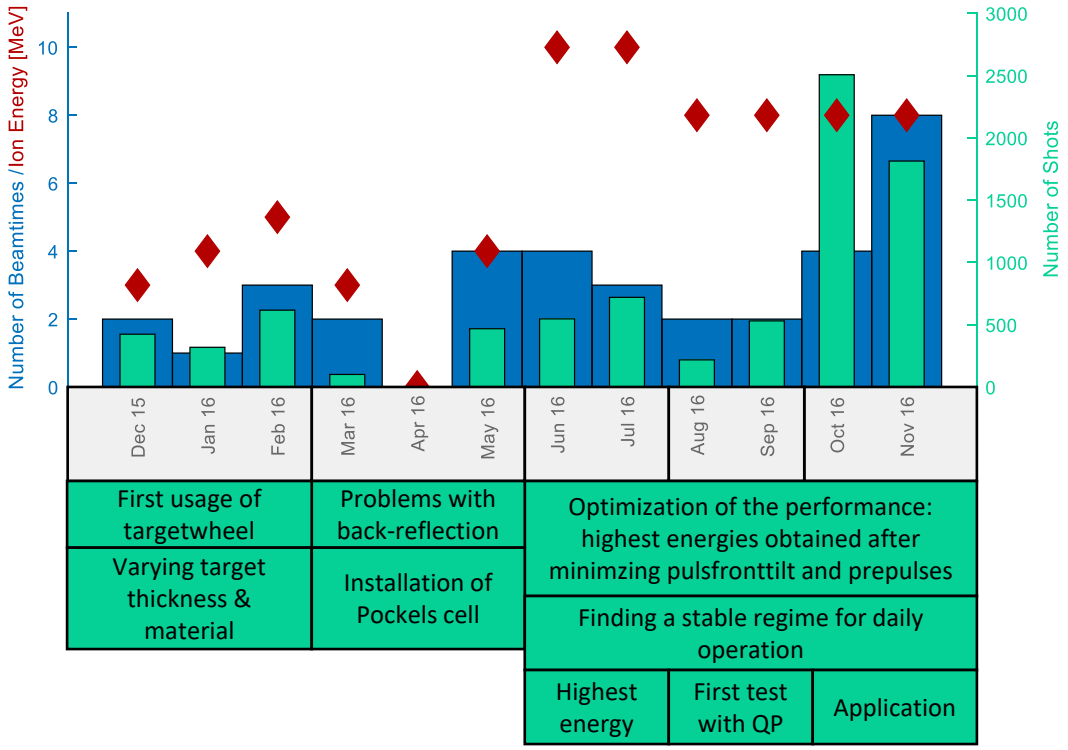

Figure 3.10 | Shot summary at LEX Photonics. This figure shows the performance at LEX Photonics. It shows the number of beamtimes and the number of shots per month. If further depicts an appraisal of the maximum proton energy of each month evaluated with the WASP as demonstrated in Fig. 3.7. The proton energy is partially based on evaluations carried out in [157].

The experimental campaigns at LEX Photonics have been carried out from April 2015 to beginning of December in 2016. The first few months contained several experiments with few shots per day. Those campaigns were mostly used to debug the system and install diagnostics step by step. With the implementation of the target wheel in December 2015 the repetition-rate and shot-number increased significantly. In Fig. 3.10 the presented data starts with the implementation of the target wheel. The depicted proton energy is an estimated monthly average and resembles the maximum proton energy of an average shot. The proton energy is evaluated with the WASP (Fig. A.8 and Fig. 3.7) and the data is partially based on evaluation in [157]. The whole experimental campaign can be divided into five stages. The first stage was the implementation of the target wheel. This enabled

a tremendous increase in repetition rate and number of shots per beam time [59]. This development also required the automation of the data acquisition. In the first stage various target scans were performed, including the use of double foil targets that contained two layers of targets with a distance of few hundred µm. Despite a wide parameter scan the proton energy did not exceed 5 MeV. The second stage was characterized by problems with the back-reflection. A damage in the crystal of the first pro-pulse amplifier, probably caused by back- reflection limited the usable laser-energy. A second incidence, probably caused by back-reflections destroyed several mirrors in the beam-line and gratings. Due to the monitoring of the back-reflection experiments LION could be excluded as the cause of those damages. The operation was stopped until the safety Pockels cell was installed and performance was tested in May 2016. This allowed the removal of the quarter-wave-plate and rotating the target back to zero degree incidence. Even though the back-reflection did not completely vanish it was kept at an acceptable level. In the third stage (June - July 2016) the performance was optimized. With the successful use of the integrated plasma mirror the contrast was identified as one of the main limitations. The identification of pulse-front-tilts and its removal further boosted the proton energy significantly. Further the early prepulse were revealed and minimized by slightly misaligning the Pockels cells in the REGEN. The highest energies were achieved with the use of the integrated plasma mirror, while of course the repetition rate dropped severely. Therefore a stable regime with normal targets was sought. This was finally found using 250 or 500 nm thick gold foils as a target to accelerate protons. In the fourth stage (August - September 2016) the QPs were implemented and tested for the first time. This required several iterations and due to their debugging less beam times and number of shots were performed. In the fifth and most rewarding stage (October - November 2016) ions were used for applications. Most of the valuable and later published data was taken in this period. The increased number of beam times and shot-numbers illustrates clearly the value of those last two month. The routine usage and stability of the laser and the target enabled quite successful period of experiments.

During the 1.5 year of operation in LEX Photonics more than 8000 shots[5] have been delivered to the LION chamber. The total shot number, which also includes a beam time, where 1000 shots have been demonstrated within several hours, is a milestone achievement compared to previous experiments. As mentioned in the

[5]This evaluation excludes the experiments for TRIC that are demonstrated in Chapter 4. Those experiments were mostly executed from June to September 2016.

introduction the first laser systems were based on glass lasers with repetition rates of 1 shot per hour. For comparison The PHELIX [158] has been operated for about 5000 shots[6] in over 10 years of operation.

The irradiation of Zebrafish embryos, and thus the first living vertebrate organisms, with laser-accelerated protons has been one of the highlights of the experimental campaigns in LEX Photonics. We hereby demonstrated the suitability of LEX Photonics for applications and the progress in particular regarding repetition rate and number of shots compared to previous studies (see [159, 160]). With over 20-60 shots per embryo and a repetition rate of 0.5 Hz no irradiation process took longer than 2 minutes. We exposed the embryos to different doses and analysis have clearly shown the effect of the irradiation. The second aim was to show that Zebrafish embryos are well suited for such experiments and to examine what further would be required for more advanced experiments of such kinds. Since the experiment happened in the last week of operation with a very limited preparation time we could not include a decent on-shot dose control. Therefore the obtained results are more of a qualitative nature. In Fig. 3.11 the setup outside of the vacuum chamber is depicted. The embryos are positioned within a dwell plate (each dwell has a width of 2 mm). Remarkably the fluid was kept inside the dwell solely by its adhesion. The results have been evaluated by Thomas Rösch et al. and are currently prepared for publication.

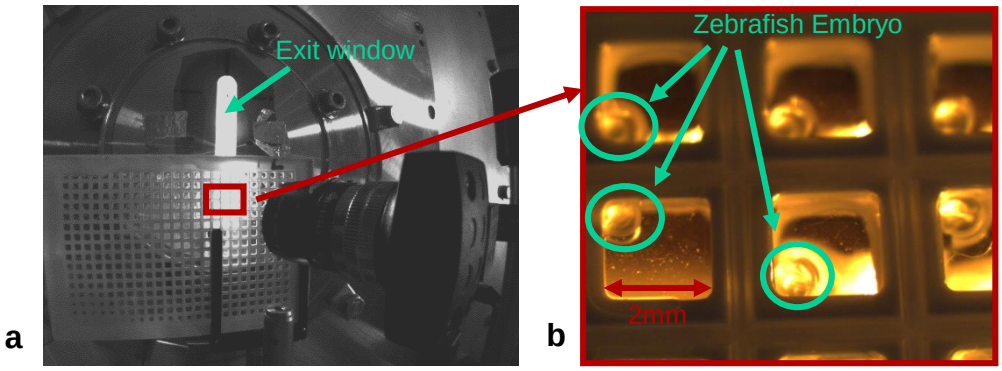

Figure 3.11 | Irradiation of Zebrafish embryos. As the last experiment in LEX Photonics we have irradiated Zebrafish embryos with laser-accelerated protons. The embryos were placed in a dwell plate and exposed to varying doses.

[6] Bernhard Zielbauer, GSI PHELIX, private communication.

3.3.1 Lessons Learned in LEX Photonics

Since LEX Photonics was a prototype test for CALA the most important findings that we learned are collected herein. Those *"lessons learned"* are partially based on data presented within this work but also include the authors opinion and experience of daily operation.

Lesson 1. ***Regen prepulse:*** *The temporal laser contrast is a limiting factor of the ion acceleration process. Significant prepulses are created inside the REGEN, preventing an efficient acceleration of ions, especially using thin targets.*

Lesson 2. ***Back-reflection:*** *It is essential to monitor the back-reflected light in order to keep the laser safe. An operation under non-zero degree suppresses back-reflected light.*

Lesson 3. ***Pockels cell:*** *A Pockels cell in the laser chain is essential in order to enable the opportunity to hit the target at normal incidence. For practical reasons the alignment possibilities of the Pockels cell are crucial and the height has to be adjustable as well as the angles of the cell and the polarizers to reach its best performance.*

Lesson 4. ***Laser beam delivery:*** *Observing the scattered light of the laser on each mirror (after compression) facilitates reproducible adjustment of the laser through the Laser beam delivery on a daily basis. An absolute mirror position or end-switches would be a beneficial advancement.*

Lesson 5. ***Incoming laser light:*** *Input laser pulse parameters must be known and well characterized for each shot and directly available to the operator. Characterizing the laser directly in the target chamber has the further advantage that problems in the LBD can potentially be detected directly. When the transmission mirror had to be reworked the lack of information was clearly perceivable during the experiment so a spare one would be desirable in CALA.*

Lesson 6. ***Back-scattered light:*** *The analysis of the back-reflected light can provide useful information. In LEX Photonics the transmission of a mirror of the LBD was used, thereby suppressing the fundamental laser wavelength λ_L. A mirror with determined transmission for λ_L would be favorable. It was further useful that the mirror was highly transmissive to green lasers that could be used for alignment or potentially also heating of targets to remove contaminant layers.*

Lesson 7. ***Spatial Intensity:*** *The spatial distribution of the laser focus reveals that a significant amount of energy can be distributed to larger areas. The careful analysis, for example through the HDR imaging described in [150], yields accurate peak intensity values. Those are otherwise significantly overestimated.*

Lesson 8. ***Debris:*** *A high repetition rate with a large number of shots causes severe debris problems that significantly alloy the parabola and mirror surface. In LEX Photonics we had no solution to this problem.*

Lesson 9. ***Plasma Mirror:*** *It can be a very cost efficient and effective way to use a thin foil as a plasma mirror. The prototype version demonstrated the functionality but lacked the possibility to optimize the alignment and neighboring targets were often corrupted.*

Lesson 10. ***WASP calibration:*** *The energy measurement with the Radeyes placed behind an WASP worked quite well. However, the analysis of the data required precise knowledge of the magnetic fields, distances and positions. Since the evaluation was very sensitive an inherent calibration would be beneficial.*

Lesson 11. ***Shielding QP:*** *The shielding of the entrance of the QPs is crucial and causes severe ablation of laser light transmitted through the target. The ablated matter is deposited onto the target due to the vicinity and can even destroy targets.*

Lesson 12. ***Orientation QP:*** *A good control of the rotation and tip/tilt angle of the QPs is important and misalignment cause the star-like shape of the ion focus. The new procedure of pre-alignment was very useful. However, it would be beneficial to further adjust the rotation of the PMQ during the experiment, thus being able to optimize the focal shape analogously as it is done for the primary laser focus.*

Lesson 13. ***Data monitoring:*** *An automatized data acquisition was one of the major improvements compared to previous experiments. However, the data acquisition did not include all diagnostics yet and should thus be further improved. It could also include further safety mechanisms. For example interlocks to prevent a laser shot with full power when the microscope is at focus position.*

Chapter 4

TRIC: Temporally Resolved Intensity Contouring

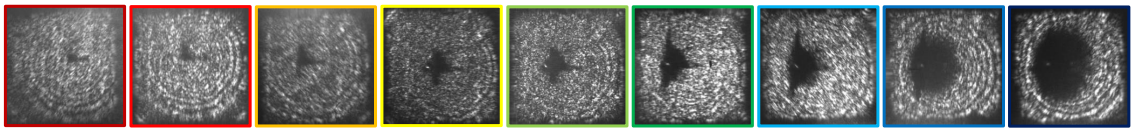

Plasma dynamics measured in a single-shot (see Fig. 4.2).

Contents

4.1 Introduction to TRIC 62
4.2 Setup and Configuration of the Experiment 64
4.3 Interpretation of the Observation 68
4.4 Analysis and Evaluation of the Measurement 73
4.5 Summary and Discussion 79

This chapter covers the method of TRIC. We developed a single-shot multi-frame probing technique, that enables a time-resolved study of the plasma during the interaction with a pump beam, in our case the laser pulse. It thereby can be associated to pillar two of the ILDIAS concept. As a first application of this technique we determined the spatio-temporal intensity distribution of the ATLAS-300 laser pulse at full energy directly at the focal position. This experiment has been carried out in the second vacuum chamber (see Fig. 3.5). This chapter and its figures closely follow the publication of TRIC [161].

Author contribution: *This project has been conducted with all co-authors of [161], in particular together with Martin Speicher and Jianhui Bin. The experimental campaign and the analysis of the results have been led by the author.*

4.1 Introduction to TRIC

Two of the most influential parameters relevant to laser-ion acceleration are the temporally resolved intensity contrast [162] and the transverse intensity distribution in the focal plane (as shown in Chapter 2). The hot electron temperature, and thus also the ion energy is dependent on the laser intensity (see Eq. (2.40)). A good temporal laser contrast is required to prevent a pre-expansion of the plasma, and a flattening of the density profile that would prevent the use of very thin targets and the access of desired regimes where RPA dominates the acceleration mechanism. Due to the sub-picosecond duration and the high peak intensity, a direct measurement of such remains challenging. In principle there are several possibilities to analyze the interaction process. One contains the analysis of transmitted light or light emitted off the plasma [163–166]. The frequencies and also source size of such emitted light can reveal information of the process. Another option would be the use of a probe beam. The term probe beam describes in the easiest form a small fraction of the laser pulse that is coupled out and used for further analysis. Analyzing the interaction of the probe beam with the generated plasma (reflectance, transmission, diffraction) also reveals information about the plasma at a certain time frame. By varying the delay between the laser pulse and its probe, the plasma condition can be scanned in time and a temporal evolution can be obtained.

In the field of laser plasma physics pump-probe configurations have been among the most rewarding diagnostic tools [167–169]. The intrinsic synchronization and ultra-short pulse duration of the probe beam enable sub-100 fs resolution and µm-level spatial resolution. Typically temporal information is obtained combining data from multiple pulses, varying the delay between the main laser pulse and the probe pulse. First attempts to record multiple frames of a single pulse have been realized by probing with different harmonics of the laser-frequency [169, 170]. TRIC describes the method to recorded nine temporally separated images of the laser-plasma interaction in a single-shot and the retrieval of the **S**patio-**T**emporal **I**ntensity **D**istribution (STID) of the ATLAS-300 during the interaction.

4.1.1 Spatio-Temporal Intensity Distribution

In fact, the spatial and temporal intensity distributions are often determined independently, for separate shots and with attenuated beams.

Temporal Intensity Distribution

The temporal intensity contrast is typically measured relatively (in relation to the peak intensity) with auto correlation methods (see Section B.4.1). Recently methods have been developed to measure the temporal contrast in a single-shot [171, 172]. Those enable important steps towards an online monitoring of the laser contrast. The temporal laser contrast of the ATLAS-300 laser that was used during those experiments has been shown in Fig. 3.2.

Spatial Intensity Distribution

The spatial intensity distribution is usually measured with time-integrating beam profilers using an attenuated laser pulse and the anticipated high intensities require mapping with high dynamic range (at least five orders of magnitude) in order to avoid an overestimation of the peak intensity at focus [150]. Also several methods have been developed to measure the peak intensity of high-power laser pulses [173–175].

Measurement of Spatio-Temporal Intensity Distribution

A combined spatio-temporal measurement of an attenuated high-power laser focus has recently been demonstrated for the first time by Pariente et al. [176]. Although several techniques allow the analysis of the spatial and temporal intensity distribution of a high-power laser focus [148, 149, 171, 172, 177–179], it has not been directly accessible during a laser-plasma interaction. Here we describe a technique that measures the spatio-temporal evolution of a laser-induced plasma on target for a single-shot. This not only yields information about the evolution of plasma formation, but can be further interpreted to retrieve the absolute spatio-temporal intensity distribution STID of a high-power laser in the focal plane at full intensity. Within a single-shot we measure temporally resolved intensity contours with sub-picosecond temporal resolution and about 25 µm spatial resolution. With each additional measurement with modified laser intensity (in our example five pulses, Table 4.1) we add about one order of magnitude to the covered dynamic range of our measurement. Because there are no direct comparisons with our novel technique, we extract the transverse spatial and the temporal profiles of the three-dimensional intensity distribution function, and compare them to the standard techniques, i.e. a spatial **H**igh **D**ynamic **R**ange (HDR) focus image (integrated over the full laser pulse

duration) and a temporal contrast measurement with a third-order auto-correlator.

Spatio-Temporal Coupling

We have derived the intensity of a laser pulse so far as a linear independent function of the temporal and the spatial distribution Eq. (2.21). This assumption nevertheless is just an approximation and can be altered by the effect of **S**patio-**T**emporal **C**oupling (STC) [99]. STC can have diverse origins. The simplest example is a pulse front tilt which causes a lengthening of the pulse length in the focal plane of a focusing optic. Other effects that lead to STC can for example be caused by misalignment of the compressor [180].

4.2 Setup and Configuration of the Experiment

The ATLAS-300 laser described in Chapter 3 is a Ti:sapphire laser system with 30 fs pulse length and a repetition rate of 5 Hz. The available energy was varied and the used settings can be seen in table Table 4.1. The background level of the laser intensity (temporal contrast) has been found to be in the order of 10^{-9} (Fig. A.1) from a few ns up to $\sim$ 50 ps prior to the main pulse. Two short prepulses with $\sim 10^{-6}$ of the peak power have been identified about 600 ps prior to the main pulse, originating from reflections in the regenerative amplifier. Further measurements with saturated photodiodes have not shown any significant prepulses in the ns-range prior to the pulse. Therefore the majority of the energy is contained within the main pulse. To monitor the energy of each shot an energy meter is positioned behind a leakage mirror close to the experiment (see Fig. 3.4a). At lower energies the sensitivity of the energy meter was not sufficient. In this case, the energy was estimated by integrating over the spectrum measured with a spectrometer[1] for each shot (Fig. 3.4c). The neutral density filters that are used to attenuate the beam during the experiment are positioned in the stretched beam before the compressor ($\sim$ 400 ps pulse length). The main laser is focused with a 90°, F/2 silver parabola with 20 cm focal length (see Fig. 3.6d) impinging onto target with p-polarization. The HDR picture of the focal spot distribution is depicted in figure 4.5 with a resulting FWHM of about 3 µm. The HDR image of this time-integrated focal spot distribution provides the basis for calculating the peak intensity [150].

[1] Ocean Optics.

4.2.1 Pump-Probe Configuration

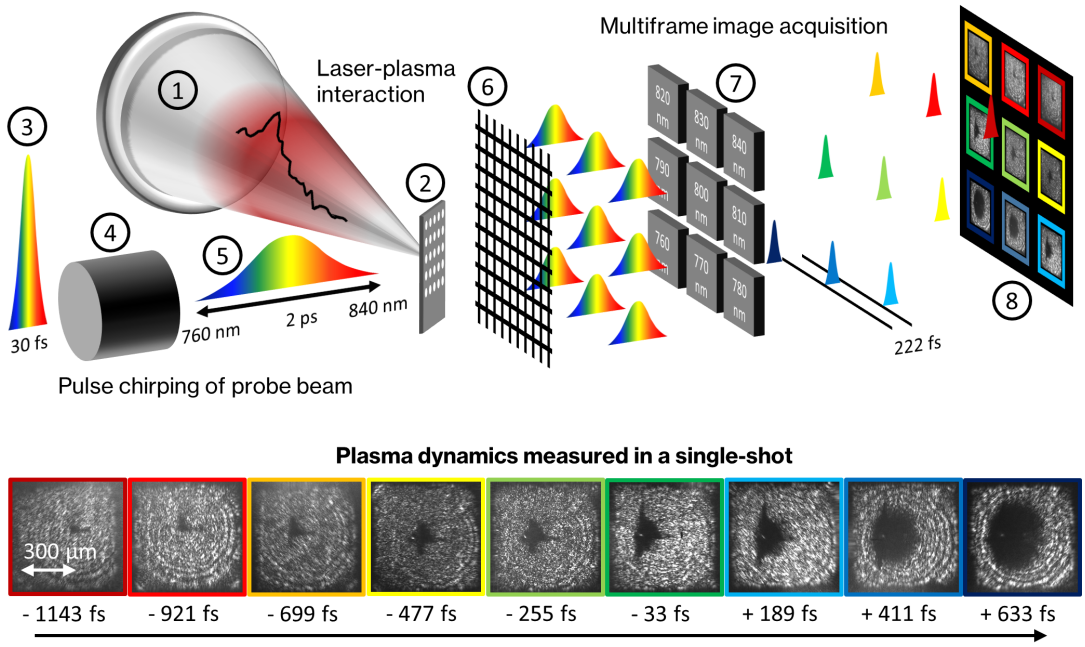

Figure 4.1 | The trick of TRIC. A Ti:sapphire laser pulse (**1**) is focused onto a 200 nm thick Formvar target (**2**) at 45° angle of incidence. A small part of the short laser pulse is coupled out earlier (**3**) and sent through a glass rod (**4**). The emerging chirped pulse (**5**) passes the target perpendicular to the main pulse. In the imaging path, the probe beam is multiplied using a low dispersion transmission grating (**6**). A small frequency range is cut out of each of the replicas by narrow bandpass filters (**7**) before being recorded with a camera (**8**). The bottom row shows a sample picture series recorded in a single-shot. The figure is adapted from [161].

The complete experimental setup resembles a typical pump-probe configuration and is shown in Fig. 4.1. The Ti:sapphire system provides up to 370 mJ on target within 30 fs with a spectral range of 760 nm to 840 nm (see Fig. 3.4c). The laser is focused onto a 200 nm thick transparent Formvar foil target [65] with a diameter of 2 mm which is positioned for irradiation at 45 degree angle of incidence. A small fraction of the 30 fs laser pulse was coupled out with a pick-off mirror at the edge of the main laser pulse in the target chamber (spatial sampling) to provide the probe beam (Fig. 4.2a). The timing of the probe beam with respect to the main laser pulse was controlled with a delay stage. The probe beam was then guided through an aperture of 7.5 mm diameter. This aperture was imaged onto the TCC with a demagnification of 9, resulting in an illuminated area of $\sim 830\,\mu m$. A glass rod of 3 cm length was introduced in the beam path (Fig. 4.2b) prior to target in order to

chirp the pulse up to 2 ps. The energy of the probe beam was ~ 0.5 % of the energy of the main pulse, resulting in a maximum of 20 mJ and an intensity of $1 \cdot 10^{12}$ W cm^{-2} on target. The intensity of the probe was thus five orders of magnitude lower than the intensity of the main pulse and further distinctly smaller than the threshold intensity for plasma formation. The energy of the probe beam could further be filtered in front of the camera (for high energies). An intended good contrast between the image created by the probe and self-emission from the target favored filtering in front of the camera instead of filtering prior to the target. Note that spectrum of the emitted light was dominated by the fundamental wavelength and even more the second harmonic of the laser pulse. The probe beam was overlapped perpendicularly

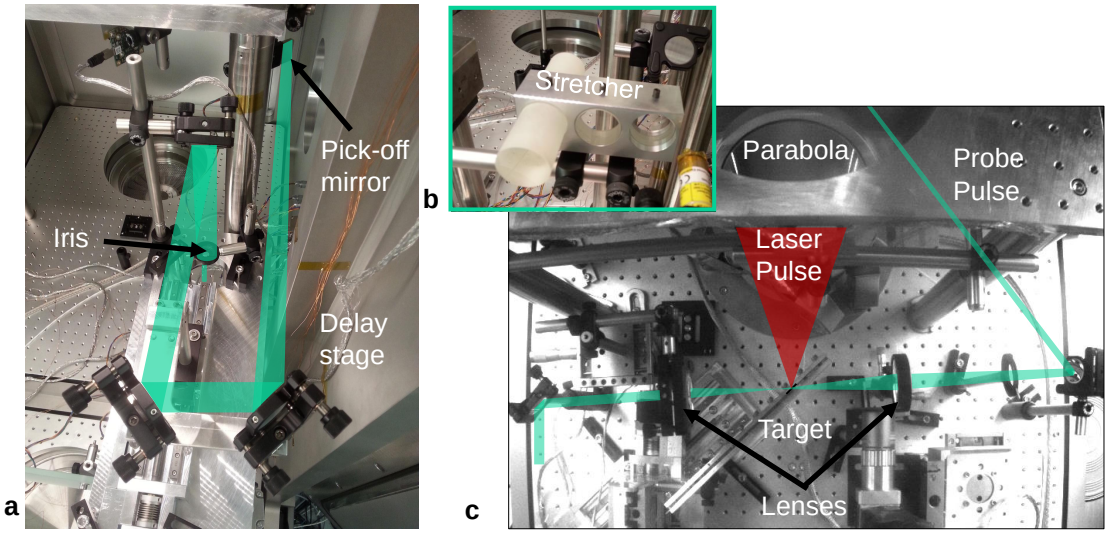

Figure 4.2 | Experimental setup for TRIC. **a**, Shows the probe pulse before the target. A small portion of the laser pulse is coupled out with a pick-off mirror at the edge of the beam. A delay line enables to add an adjustable delay to it. The iris is later imaged onto the target to have a well defined intensity distribution. **b**, Shows the glass rods that were used to chirp the pulse. Three different length (10, 3 and 2 cm) enabled a modification of the chirp. **c**, Depicts the geometry of the laser pulse and the target. It shows how the iris is imaged onto the target and later imaged and guided out of the vacuum chamber for further analysis. The pictures have been adapted with the courtesy of Speicher [151].

with the main laser pulse at the target. The transmitted probe light is collected with a lens, guided out of the vacuum chamber and imaged with another lens onto a camera[2] with a magnification of ~ 6.5 and a spatial resolution of roughly 2 µm. The illuminated area at TCC has a vertical extent of 830 µm. The spatial resolution of the

[2]Prosilica GT 4907, Allied Vision.

complete setup was determined experimentally to about 25 µm. This is significantly lower than the theoretical resolution of the imaging system, which would support about 2 µm (Abbe limit Eq. (B.42)). The main limiting factor is the low quality of the beam profile of the probe beam, which shows strong intensity fluctuations on the order of 10 µm spatial scale. A 2-D large pitch transmission grating[3] is positioned between the lens and the CCD chip, such that nine spatially separated replicated images are accommodated on the camera chip. At this stage, each image still contains the complete spectrum. By adding nine different narrow band-pass filters (band-width of 10 nm)[4] in front of the camera chip at the positions of the replicas they will be spectrally filtered, and thus correlated temporal information is imprinted [181, 182] onto each image. The time delay between subsequent images is set to 222 fs. We thus measure nine sequenced images with a frame rate of almost 5 THz, revealing the plasma evolution in response to a high-power laser pulse interacting with a solid density target.

Temporal Overlap between Probe Pulse and Main Pulse

Probing techniques with sub-ps resolution require a very accurate knowledge of the temporal relation between main and probe pulse at TCC. This zero timing describes the coincidence of probe and main pulse on the target. It was measured with the use of an air plasma ignited by the attenuated pump pulse in air. A high-power laser pulse can generate an air plasma when the intensity is larger than a certain threshold [183]. Therefore the laser intensity was attenuated until the air plasma was solely visible in one or two of the nine frames, and thus marking the peak of the laser pulse with an accuracy of ±222 fs . Notice that for this measurement the probe and the main pulse have been in air from the moment the probe is picked and therefore no speed of light difference in vacuum and air has to be considered.

Frame Rate of 5 THz

The frame-rate of the camera is set by the temporal spacing of the spectral images and the chirp of the probe pulse. Therefore, the group velocity dispersion (see Section B.2.3) has to be calculated based on the optical parameters of the stretching material in the probe beam. Since multiple error sources are introduced, we chose a different approach. Two nine-frame images are created, differing in delay by 1000

[3] Collischon, 15 µm lattice constant.
[4] Omega Optical Inc.

steps of the motor of the delay stage. If a specific plasma size is observed in two different frames of both nine-frame images, one can check for the change in the frame number and unambiguously correlate frame-number and temporal delay. Knowing that 1000 steps equal a delay of 666 fs the frame-rate can be simply calculated. In the setup described above, a 3 cm glass rod resulted in a delay of 222 fs between each frame and a total observation time of 2 ps within a single-shot.

4.3 Interpretation of the Observation

An exemplary raw image of a single laser shot onto target is displayed in Fig. 4.1 (8) (bottom line). The image appears bright in areas, where the target remains transparent and dark in areas, where the target became opaque. The cause for this binary image information is the change in the optical transmission of the evolving plasma. When the free electron density becomes larger than the critical density $n_e > n_c$ (Eq. (2.33)), the plasma turns reflective for the incoming probe pulse. The horizontal dimension recorded in the image contains convoluted information since the laser and the orthogonal probe pulse both hit the target under an angle of 45 degree. At the same time, the orientation of the target with respect to the drive-beam implies that non-central parts of the target interact with the laser in out-of-focus planes causing a complex two-fold convolution of time and space. A spatial difference in horizontal dimension of 60 µm in the image corresponds to a time difference of 200 fs of both the laser and probe pulse hitting the target. For simplicity we therefore only consider the vertical dimension, where those effects do not play a role. The overdense plasma area (dark region) of the single-shot image sequence in Fig. 4.2 grows with about 30% of the speed of light. The first step was to examine the physical reason for this growth in more detail.

4.3.1 Relation of Laser Intensity and Plasma Contour

We therefore varied the laser energy and compared the spatial intensity distribution of the laser focus with the contour of the overdense plasma during the interaction and the hole in the target that is apparent after each shot. The laser energy was reduced by adding neutral density filters in the beam path of the laser before compression and thus, attenuating both the main pulse and the probe pulse. The corresponding intensities are shown in Table 4.1. The hole in the target after the shot with intensity I_5 is shown in Fig. 4.3c. Since the angle of the target was 45 degree with respect to

	Laser energy [J]	**Laser intensity** [$\mathrm{W\,cm^{-2}}$]	**Scaled edge contour intensity** I_{seci} [$\mathrm{W\,cm^{-2}}$]
I_0	0.37	$5.8 \cdot 10^{19}$	$5.7 \cdot 10^{13}$
I_1	$6.6 \cdot 10^{-2}$	$1.02 \cdot 10^{19}$	$3.2 \cdot 10^{14}$
I_2	$6.6 \cdot 10^{-3}$	$1.02 \cdot 10^{18}$	$3.2 \cdot 10^{15}$
I_3	$6.6 \cdot 10^{-4}$	$1.02 \cdot 10^{17}$	$3.2 \cdot 10^{16}$
I_4	$6.6 \cdot 10^{-5}$	$1.02 \cdot 10^{16}$	$3.2 \cdot 10^{17}$
I_5	$3.7 \cdot 10^{-5}$	$5.7 \cdot 10^{15}$	
I_6	$3.7 \cdot 10^{-6}$	$5.7 \cdot 10^{14}$	
I_7	$3.7 \cdot 10^{-7}$	$5.7 \cdot 10^{13}$	

Table 4.1 | Intensities used for TRIC. Different laser energies and corresponding intensities are introduced here. The scaled edge contour intensity will be explained later.

the laser axis and thus, also to the microscope (Fig. 4.3a), only the central vertical axis appears sharp. Comparison to a contour plot of the laser focus, taken with an attenuated beam (Fig. 4.3d), indicates great resemblance. The picture was taken with the same microscope. Comparison of the laser intensity profile (Fig. 4.3d) and the hole in the target after the shot (Fig. 4.3e) indicates the contour of the hole to be directly correlated to the shape of the laser focus at a certain intensity. The distinct spatial shape of the laser focus makes this effect more clear. In Fig. 4.3b we see the measured plasma shape with the probing technique at $t = 0$ (largest contour) with an intensity of I_4 of the main pulse. The hole in the target foil after the shot is shown in Fig. 4.3c and again the contours in Fig. 4.3b and Fig. 4.3c show close resemblance. This indicates that the threshold intensity I_{th}, where the Formvar target becomes opaque, and thus $n_{\mathrm{e}} \geq n_{\mathrm{c}}$ can be related to the contour of the hole in the target after the shot.

As a conclusion of this empirical observation we assume that the intensity at the measured contour of the plasma is also the contour of the intensity distribution of the laser focus reaching a certain threshold intensity. This threshold $I_{\mathrm{th}} = (6 \pm 5) \cdot 10^{13}$ $\mathrm{W\,cm^{-2}}$was determined by reducing the laser energy, and consequently the intensity, stepwise until no hole was observed at the target after the shot. In the previous part we have simplified a few physical aspects. The threshold intensity ($I_{\mathrm{th}} = (6 \pm 5) \cdot 10^{13}$ $\mathrm{W\,cm^{-2}}$) is significantly lower than relativistic intensities $\sim 10^{18}$ $\mathrm{W\,cm^{-2}}$, where other effects such as relativistic transparency [163], relativistic self-focusing [184] and self-phase-modulation [185] can play a role. We further assume, that the

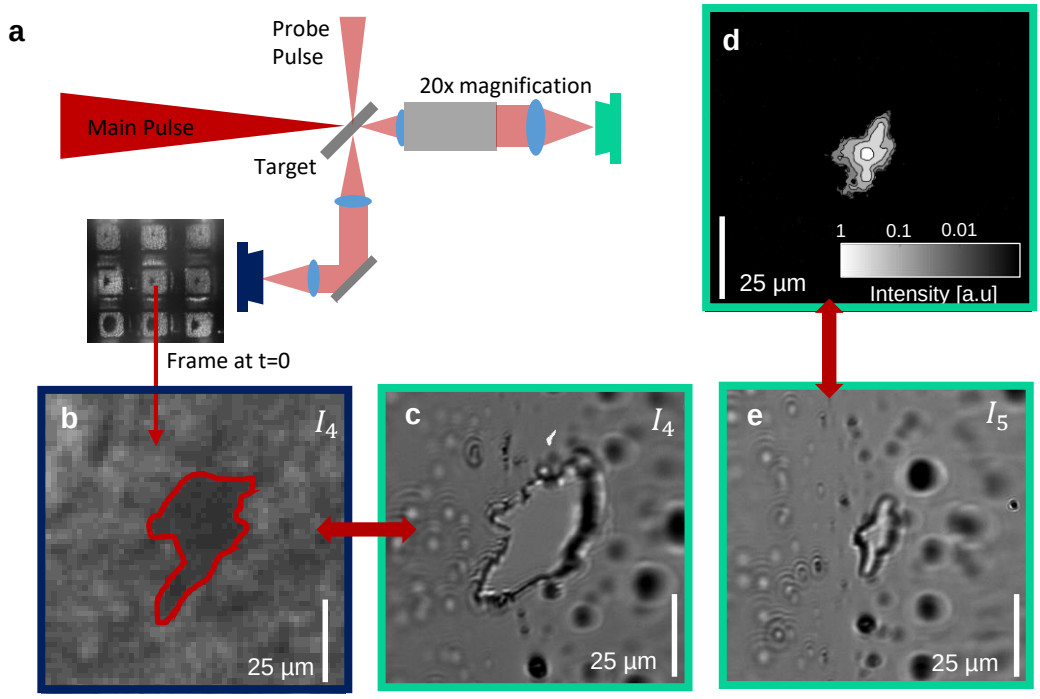

Figure 4.3 | Nexus of intensity distribution and plasma shape. This figure shows separately obtained images of the laser focus, the probe image and the hole in the target after the shot. The configuration can be seen in **a**, where a 20 times magnifying microscope views the target under an angle of 45° and also measures an attenuated laser pulse in the focal plane **d** (contour image). The hole in the target with intensity I_5 is shown in **e**. A shot with intensity I_4 compares the hole in the target **c** to the probe image **b**. The figure is adapted from [161].

enlargement of the plasma is caused, when the intensity distribution of the laser pulse reaches the threshold intensity and the target is ionized to reach free electron density beyond the critical density $n_e \geq n_c$. Another cause of an advancing plasma diameter could be the transverse expansion of the plasma itself by hot electrons [168, 186]. In the center of the laser focus at $t = 0$ the laser eventually reaches relativistic intensities for the shots with highest laser energy and thus in the inner part relativistic transparency, self-focusing and other effects can play a significant role. Also the electron temperature at the central part of the laser focus can be beyond the MeV level, resulting in expansion velocities approaching a large fraction of c. However, since the interesting region for TRIC is the outer contour of the plasma, where I(x,y,t) = I_{th}, those effects do not play a dominant role and the electron temperature is in the low keV region or smaller. In principle, fast electrons that are excited in the center, where the intensity is higher, could contribute to

the transversely expanding front. Because in our case the transverse expansion (in vertical dimensions) stagnates after $t = 0$ ps when the peak of the pulse has hit the target, we ignore this effect but note that it could become relevant for transversely steep intensity distributions. We observed a growth in horizontal dimension after $t = 0$ s for the highest intensities (see Fig. 4.1). One reason for this delayed growth is the orientation of the target, which we irradiate and view under an angle of 45°. Therefore, an intensity contour with transverse extension dx will cause an effect in the target that is delayed by dx/c, in our case ≈ 200 fs.

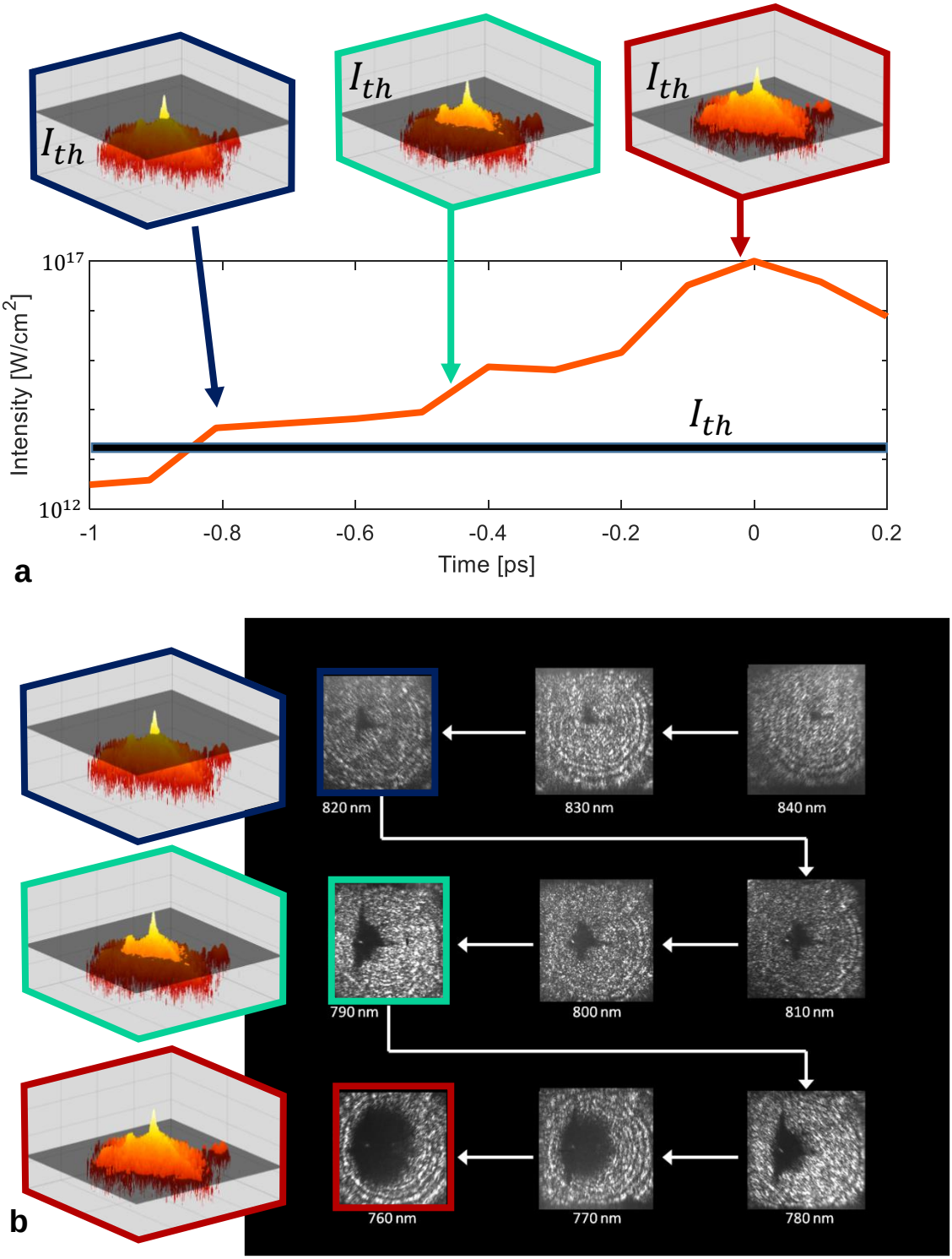

Figure 4.4 | Illustration of the principle of TRIC. In **a** the intensity increases with the time approaching zero. Consequently a larger fraction of the HDR laser focus perforates the intensity level of the threshold intensity I_{th}. An illustration how this effects results in a growing area with advancing time is given in **b**. Part of the figure is adapted from [151].

4.3.2 Determination of the Threshold Intensity

I_{th} was determined by focusing the main laser pulse onto a 200 nm thick plastic foil with a peak intensity that was calculated via equation 4.4. The target was examined after the shot with a 20 times magnifying microscope in the vacuum chamber. By reducing the intensity stepwise according to the values given in Table 4.1 we identified that the target had no visible hole after a single-shot with peak intensity $I_7 = 5.77 \cdot 10^{13}\ \mathrm{W\,cm^{-2}}$, whereas a clear hole was visible after a shot with $I_6 = 5.77 \cdot 10^{14}\ \mathrm{W\,cm^{-2}}$. We thus determined the threshold intensity of the 200 nm plastic target to be $I_{\mathrm{th}} = (6 \pm 5) \cdot 10^{13}\ \mathrm{W\,cm^{-2}}$. We also note, that we empirically found the intensity that was needed to create an overdense, and thus opaque plasma, also caused a hole in the target. Because we only use the transition from transparent to opaque for determining the contours, which happens for any free electron density $n_{\mathrm{e}} \geq n_{\mathrm{c}}$, our method is not sensitive to the exact damage mechanism. The threshold intensity $I_{th} = (6 \pm 5) \cdot 10^{13}\ \mathrm{W\,cm^{-2}}$ is therefore not necessarily associated with a damage threshold. Note, that the large error bar of I_{th} results from the course intensity filtering steps during the determination of the threshold intensity. It is thus an absolute error that can be regarded as an offset but does not change the shape of the STID.

4.4 Analysis and Evaluation of the Measurement

The measured contour lines originate from the STID reaching the threshold intensity $I_{\mathrm{th}} = (6 \pm 5) \cdot 10^{13}\ \mathrm{W\,cm^{-2}}$. The intensity at the edge contour is thus

$$I(x, y, t) = I_{\mathrm{th}}. \tag{4.1}$$

The intensity of the measured contour in the probe image is known but its inner intensity remains inaccessible due to the binary nature of the recorded data. Assuming that an attenuation of the beam by using neutral density filters with factors C_{i}, does not change the STID at focus, we can overcome this limitation. Repeating measurements with an additional attenuation by the factor C_{i} of the laser pulse yields a contour that encloses a smaller area because I_{th} is unaltered. Scaling this contour back to the full intensity of the pulse results in a scaled edge contour intensity I_{seci}:

$$I_{\mathrm{seci}}(x, y, t) = I_{\mathrm{th}} \cdot C_{\mathrm{i}}. \tag{4.2}$$

Repeating this for several C_i yields the absolute spatio-temporal intensity map as shown in Fig. 4.5. Each row corresponds to a single-shot with different attenuation coefficient, and thus the scaled contour corresponds to a different intensity I_seci. The summation over those measurements enables the retrieval of the absolute spatial intensity distribution of the laser focus at distinct time steps and is shown in Fig. 4.5b. Fig. 4.5b is thus the complete STID of a high-power laser pulse in the focal plane, at full pulse energy on target and represents the main result of TRIC. We note that the horizontal dimension is still temporally blurred due to the chosen probing geometry as described before. For further comparison a line-out at $x = 0$ µm (central vertical line) is used. The intensity map features measuring the spatial intensity profiles at select time steps and reveals the temporal shape at a given position. The most interesting cases are the spatial distribution of the peak intensity ($t = 0$) fs and the temporal contrast at the central point ($x = 0$ µm and $y = 0$ µm). We therefore evaluated the spatial intensity distribution $I(x, y, t = 189\ \mathrm{fs})$ as displayed in Fig. 4.6a, since it was the closest timestep past the interaction with the peak of the main pulse ($t = 0$) and the temporal intensity distribution $I(x = 0\ \mu\mathrm{m}$, $y = 15\ \mu\mathrm{m}$, t) as displayed in Fig. 4.6b. Due to in its current form limited spatial resolution we could not resolve the central area $\leq 25\,\mu\mathrm{m}$. Therefore the most intense measured contour represents the intensity not in the center of the focal spot, but in a transverse distance of $15\,\mu\mathrm{m}$ ($3.18 \cdot 10^{17}\ \mathrm{W\,cm^{-2}}$), well below the estimated peak intensity of $5.76 \cdot 10^{19}\ \mathrm{W\,cm^{-2}}$.

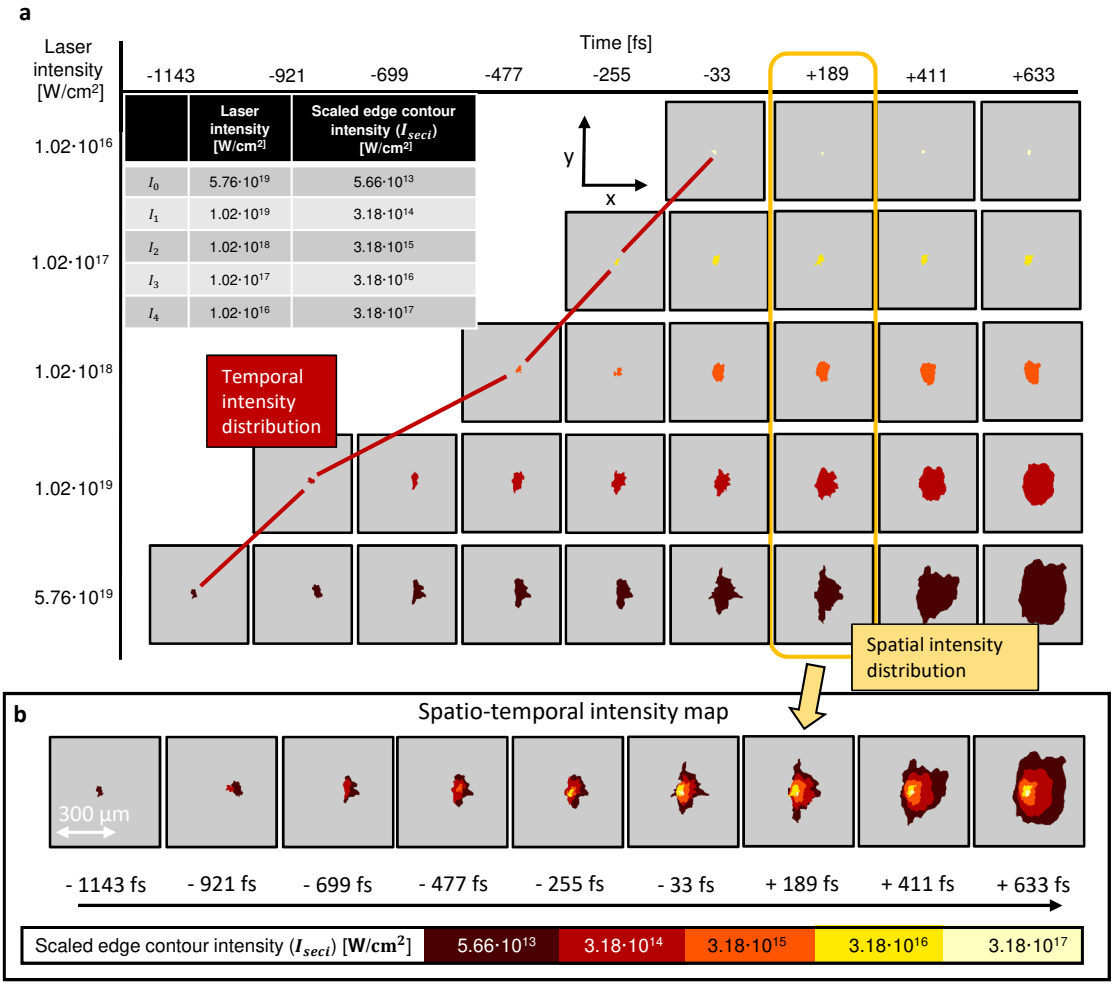

Figure 4.5 | Spatio-temporal intensity distribution. **a**, Shows I_{seci} exceeding a certain intensity I_{th}. Each row corresponds to a single-shot with a certain laser intensity (attenuation coefficient) of the laser pulse, and thus a different intensity of the scaled edge contour line. While the edges have the depicted intensity, the information about the inner part of the enclosed contour is limited to the fact that the intensity has risen above threshold before. The table shows the used peak laser intensities and the corresponding measured scaled edge contour intensity. The yellow frame shows the spatial distribution at the temporal peak of the laser pulse $t = 189$ fs (first frame after t=0) and the red line the temporal intensity distribution at $x = 0$ µm and $y = 15$ µm. **b**, Is the absolute spatio-temporal intensity map and is the main result. Due to spatial distortions of the imaging geometry under 45°, the horizontal dimension is not exact. Each timestep represents the overlapped contours in a column in **a**. The figure is adapted from [161].

4.4.1 Marginals of the Complete Distribution: Contrast Curve and Laser Focus

To assess our method we compared the extracted temporal and spatial intensity distribution to data obtained by conventional methods, a contrast profile of a third order auto-correlator (see Fig. 3.2) $g(t)$ and a high-dynamic-range (HDR) image of the laser in the focal plane (see Fig. 3.3) $f(x, y)$. Both of those standard measurements yield only relative information, which can be scaled to absolute values by using Eq. (2.21)

$$I(x, y, t) = E_{\text{Laser}} \cdot f(x, y) \cdot g(t), \tag{4.3}$$

where $E_{\text{Laser}} = 370$ mJ is the full laser pulse energy measured for each shot. The spatial shape function of the laser focus $f(x, y)$ and the temporal laser contrast-curve $g(t)$ are both normalized, $\int f(x, y)\, dx\, dy = 1$ and $\int g(t)\, dt = 1$. Note that this separation of the temporal and spatial profiles neglects effects of spatio-temporal-coupling [99] by definition.

4.4.2 Increased Dynamic Range of the Focus Picture

The HDR focus image is the integrated spatial distribution over the full duration of the laser pulse and can thus be normalized to $f(x, y)$. Assuming a Gaussian profile for the temporal distribution of the laser pulse, with a full-width at half-maximum $\tau_{\text{L}} = 30$ fs (laser pulse duration), the spatial intensity distribution of a measured HDR laser focus at time $t = 0$ using Eq. (2.22) is

$$I(x, y, t = 0) = \frac{0.94}{\tau_{\text{L}}} \cdot E_{\text{Laser}} \cdot f(x, y), \tag{4.4}$$

Figure 4.6a compares a line-out of this function along the vertical dimension (at x=0 µm) with the result obtained by TRIC at $t = 189$ fs. The focus, measured time-integrated with the camera, appears continuous since it has more data points due to a finer spatial resolution, while TRIC contributes a small number of points (dictated by the number of shots with different attenuation coefficients and its spatial resolution). In the overlap region, both methods yield similar results on the logarithmic scale. Importantly TRIC enables determining the distribution for intensity down to I_{th}, which exceeds the capability of HDR imaging as this is limited by damage of the camera. With an increased spatial resolution of TRIC the peak of the pulse could be resolved, such that seven orders of magnitude dynamic range

seem feasible. The horizontal error bar originates from the readout of the diameter of the contour. The rather large error bar for the evaluated intensities is due to the error of the determination in the threshold intensity, which is so far conservatively estimated.

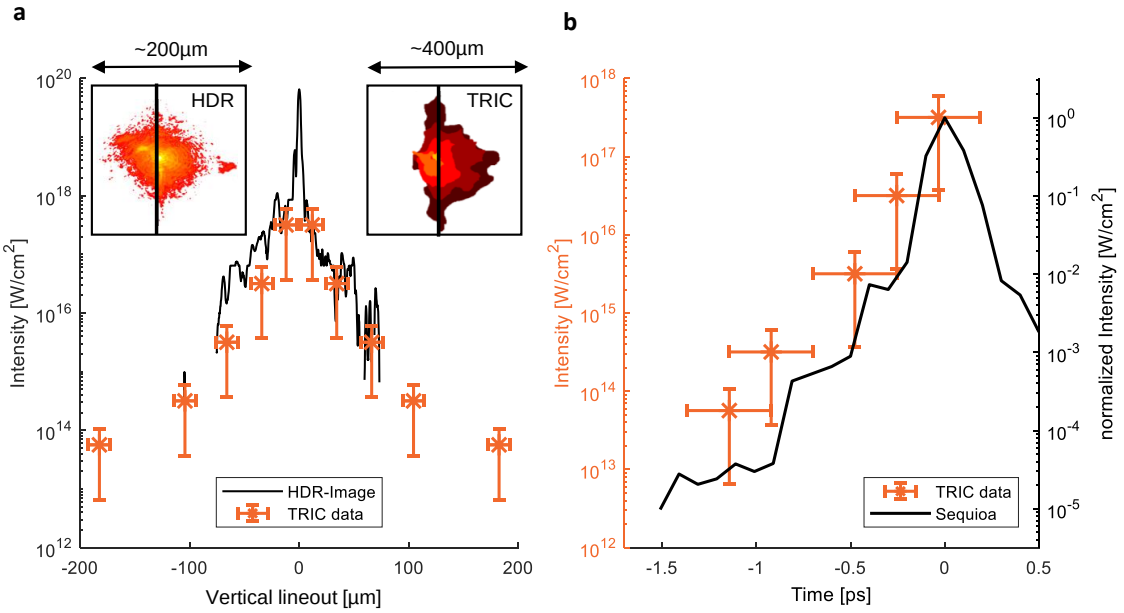

Figure 4.6 | Comparison of TRIC to contrast curve and HDR focus image. **a**, Compares the intensity distribution measured with TRIC and with a HDR camera. Lineouts of the HDR focus (left inset Fig. 3.3) and the TRIC focus (right inset) are shown. **b**, Shows the temporal contrast of TRIC at $x = 0$ µm and $y = 15$ µm. For comparison the right axis shows a normalization compared to the measurement taken with the Sequoia-autocorrelator. The large intensity error bars are absolute errors that indicate a potential offset but would not change the shape of both curves. The figure is taken from [161].

4.4.3 The Temporal Intensity Distribution

Comparison of the temporal intensity distribution measured with a Sequoia to the absolute temporal intensity evolution at a fixed spatial position, as accessible with TRIC, requires more assumptions. In principle, we must integrate the spatio-temporal distribution of which we only know the contours over x and y. The current resolution is insufficient, and we are thus restrained to compare the autocorrelator contrast curve to a normalized curve measured with TRIC as indicated in Fig. 4.6b (right axis). We normalized both intensities such that the temporal peak ($t = 0$) is

equal to one. The extent of temporal error bars of TRIC is attributed to the time interval correlated to the width of the bandpass filters for each timestep in addition to an increment from time delay uncertainty. The intensity error bars originate from the uncertainty of the determined threshold intensity $I_{\mathrm{th}} = (6 \pm 5) \cdot 10^{13}\ \mathrm{W\,cm^{-2}}$. It may be arguable, that this is a very conservative value which leaves room for further investigation. The TRIC values follow the shape of the autocorrelation trace but indicate reduced temporal contrast. The reason for this disagreement between the autocorrelation trace and the trace extracted from TRIC is not clear. It is one of the interesting questions that can be studied with TRIC. As mentioned earlier, spatio-temporal coupling [99], which can have diverse origins, manifests in focus (the simplest example is pulse lengthening by a pulse front tilt). Therefore, it seems likely that the spatio-temporal coupling will also manifest in differences between the temporal intensity profile when measured in focus or elsewhere. This is where TRIC can yield clarifying information. It provides a monitoring of the laser contrast on target at full energy, especially in the focal plane.

4.5 Summary and Discussion

By using a simple method of beam multiplexing we enable recording of nine images of the plasma evolution during the interaction of a high-power laser pulse with a thin solid density target in a single-shot. Our interpretation of the such obtained images in the framework of TRIC yields information about the absolute STID in the focus of a high-power laser pulse. We note though, that if the spatial intensity distribution on target was significantly steeper with respect to the radial coordinate, for example in the case of a perfect spatially Gaussian pulse, this interpretation can be misleading and the transversely streaming electrons could contribute or even dominate the observed expansion front. Determining the STID in focus at high peak intensity is specially interesting in combination with plasma mirrors [60] or other nonlinear techniques [187] that aim to manipulate the laser pulse close to target. TRIC gives access to the spatial intensity distribution at intensities above I_{th} ($\approx 10^{14}$ W cm^{-2}). We note that it requires still analytical effort to account for the horizontal dimension. Because the ignition of the plasma, and thus the change of opacity is irreversible on ultra-fast timescales, TRIC only yields information of the rising slope of the laser pulse and therefore requires the assumption of an intensity distribution that rises monotonically over time. Two short prepulses with intensities around 10^{-6} with respect to the peak at ~ 600 ps prior to the main pulse have been identified in the laser system using third-order autocorrelation (see Fig. A.14). If they were focused to a similar spot as the main pulse, they would have reached 10^{14} W cm^{-2} and thus just above the threshold intensity for the shots with highest energy of 370 mJ. Although exceeding the intensity threshold for TRIC, we have not observed a respective contour when probing at times as early as 100 ps before the main pulse. We note though, that the contour with a size of a few µm could have not been detected with TRIC with its currently limited spatial resolution. The absence of any sign of these prepulses on the other hand reconfirms that the measurement is not disturbed by transverse plasma-expansion initiated by very early prepulses at sufficiently low intensity, since no plasma shape is recorded in the probe beam until 1.3 ps prior to the peak of the pulse as evidenced in the last line of Fig. 4.5. It remains important to keep in mind such potential sources of misinterpretation though. For example when prepulses have a much higher intensity such pre-expansion can cause a plasma that indeed expands and mimics a contour that is not related to the intensity contour any longer. Such prepulses, however, would be easily identified in autocorrelation measurements and would not require

TRIC. Additional uncertainties can be caused by absorption or divergence of the probe pulse in the plasma. However the close resemblance between the contour of the hole and the plasma shape that we observed, does not indicate that this is relevant for extracting the contour lines from the images. Improving this resolution to a few µm will increase the sensitivity to prepulses just above I_{th}. A more detailed determination of the threshold intensity would further allow a reduction of this systematic error, and thus an even more accurate determination of the absolute intensity distribution on target. Nonetheless the relative shape of the STID is not affected by that error. The temporal contrast was evaluated at a certain position (x=0 µm and y=15 µm). A fair comparison to the contrast that is measured with the autocorrelation method would require an integration over the spatial distribution. This would further require an evaluation of the horizontal dimension and a two-dimensional interpolation.

The technique of acquiring multiple images by exploiting the natural features of a broadband highly intense laser pulse, can considerably simplify single-shot probe schemes that have been realized in the past [169, 170, 182, 188]. It further can be adapted to other, more complicated probing techniques, e.g. using holography [189, 190] instead of binary shadowgraphy. It can therefore add a temporal component to diverse probing experiments. Thus, we see TRIC as a very first step that is accessible with this technique. In the future we foresee a potential use of this probing scheme for different pump-probe modalities. Especially the intrinsic synchronization in laser-driven particle acceleration processes enables temporal resolved investigations of the interaction of ions, electrons and x-rays with matter.

Chapter 5

I-BEAT: Ion-Bunch Energy Acoustic Tracing

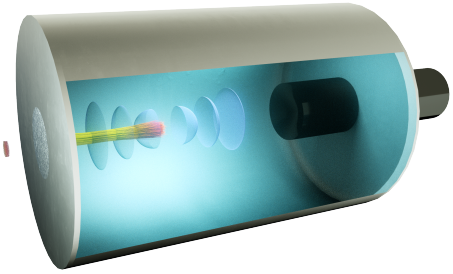

Schematic drawing of I-BEAT (see Fig. 5.1).

Contents

5.1 Ion Bunch Instrumentation - Detector Systems 82

5.2 Introduction to I-BEAT 83

5.3 Design and Development of I-BEAT 86

5.4 Experimental Campaigns and Results 95

5.5 Applications of I-BEAT at (Laser-Driven) Ion Sources . 104

5.6 Discussion and Outlook 108

This chapter describes the development and successful implementation of I-BEAT in several experiments. Tracing the acoustic signal that is generated when an ion bunch dissipates its energy in a medium allows the determination of the energy distribution of the ion bunch. This chapter closely follows the publication of I-BEAT[191].

Author contribution: *This work has been carried out in collaboration with all co-authors of[191], in particular Rong Yang[147] and Sebastian Lehrack[146]. The overall project, experiments and evaluation of the data was led and executed by the author. Rong Yang developed the retrieval algorithm and Sebastian Lehrack provided expertise in ionoacoustics.*

5.1 Ion Bunch Instrumentation - Detector Systems

While the scientific efforts in the field of laser-driven ion acceleration have been concentrated onto the understanding of acceleration mechanisms, the detection and analysis of the accelerated ion bunches has been a crucial part of experiments. The forth pillar of ILDIAS is dedicated to ion instrumentation and detection. The diagnostic of ions regarding their spectral, spatial and temporal distribution remains challenging; especially in circumstances where higher repetition rates are required.

5.1.1 Detector Schemes for Laser-Driven Ions

The early most devices that have been used for the characterization of laser-accelerated ions have been adapted from conventional accelerators. One of the prominent detectors in the early days of high energetic particles was the bubble chamber, which is based on the work of Glaser in 1952 [192–194]. The bubble chamber has been developed further and is still a useful tool. Another detection method that was adopted and implemented particularly in the early days of laser-plasma experiments has been based on TOF [195, 196]. Since the early high power laser-system were glass lasers with low repetition rates single-shot dosimetric films have been used widely [197, 198]. They are capable of measuring the absorbed dose accurately with high spatial resolution. Thus the particle number and angular distribution can be calculated. Using such films as a detector the ion energy can additionally be measured by using stacks of films. Another possibility is to deflect the ions within a magnetic field in a so called WASP [199]. By doing so the spatial information in one dimension is sacrificed for the good of the energy information. By an additional electric field the charge state can furthermore be measured, which has been demonstrated and widely used and is well known as Thomson-parabola spectrometer [200–202].

Current Developments

The advent of high power laser systems with higher repetition rates (1 shot every few minutes up to the 10 Hz regime) added additional requirements for detectors such as repetition rate and an online readout.

One approach is to combine a WASP or Thomson parabola and replace the dosimentric film with an online detector such as an **M**icro-**C**hannel **P**late (MCP)

[203] or the Radeye detector [108, 204, 205], a pixelated CMOS[1] sensor. Another approach is the revival of TOF [206, 207]. The measurement of the time-of-flight of the ions enables a determination of their energy. The advantage of TOF is its compactness and simplicity. It can further be scaled to give information about the spatial resolution, using pixelated detectors. One of the drawbacks is that the energy resolution decreases for higher energies, as the Δt between two distinct energies decreases. To compensate this, faster electronics or longer drift distances would be necessary. A third approach is the use of scintillators that directly give a spatial information in combination with a camera. Thus, they are compatible to high repetition rates and can further be stacked to enable a determination of the energy distribution [208–210].

Status

Several detection techniques to measure and characterize ion bunches have been developed over the years. The appropriate choice of the detector depends on the circumstances and has to be tailored to the experimental goals. The idea of I-BEAT was to develop a novel online detector, that is especially suitable for upcoming applications using short, high intense ion bunches at high repetition rates. Especially an online monitoring of ion energies is still challenging and was one major motivation for I-BEAT.

5.2 Introduction to I-BEAT

An acoustic wave is generated, whenever energy deposition within matter changes (see Section 2.5). Note that only a fast and localized energy deposition creates an energy-induced pressure wave, and thus an acoustic wave under thermal and stress confinement, that is when heating is fast. So just heating up a cup of water would not create an acoustic wave if the temperature gradient is small in time and space. It has also been shown that the underlying physical process can be thermal heating (absorption) or ionization. Heating can be induced by ions or by photons. Different notations have been created over the years and are explained and summarized in hereby.

[1] Complementary metal-oxide-semiconductor.

Notation	Heating process	Description
Photoacoustics	Absorption (photons)	This process describes the absorption of energy (often delivered by a laser) in matter and measurement of the hereby produced sound signal.
Protoacoustics	Ionization (protons)	This notation has been introduced by Jones [211].
Ionoacoustics	Ionization (ions)	Generalization of protoacoustic. Has been introduced by [212, 213].

Table 5.1 | Notation of different types of acoustics. Locally introduced heat causes pressure waves that can be measured acoustically. Dependent of the heat source different denotations are introduced.

5.2.1 Background

The first deliberate observation of such effects was observed by Bell in 1880 in the so called photophone [214]. Bell used a thin flexible mirror, that could be deformed by impinging sound waves. Sun light, reflected from this moving mirror was thereby modulated (e.g. varying the angle of reflectance). By using a photoelectric device this modulated light signal could be transformed back to a pressure signal. We can thus say that Bell demonstrated the creation of sound by light. Since then photoacoustics has been developed to a powerful tool especially in biomedical imaging[138]. The term photo hereby means that absorption of a laser pulse is the source of the acoustic wave. The first observation of the ionoacoustic effect has been described by Askaryan [215]. The effect of acoustic wave generation of ions dumped in a water tank were later extensively studied by Askariyan et al. [216] and Sulak et al. [217]. This work formed the basis of ionoacoustics and further studied thereafter [218, 219]. Even though the concept was known for several years it recently gained attention with increasing use of protons and ions in biomedical applications. In 1.6 the beneficial behavior of ions for irradiation have been shown. Due to the Bragg peak the energy can be distributed to a well defined area. This advantage though requires a precise knowledge of the range of the ions and thus, the stopping power of material. Ionoacoustic has been identified as a potential solution to measure and verify the range of protons and other ions in matter, especially water was extensively studied in the past years [143, 211, 212, 220, 221]. It has been shown that the range of ions can be determined with sub-millimeter resolution [213].

5.2.2 Concept of I-BEAT

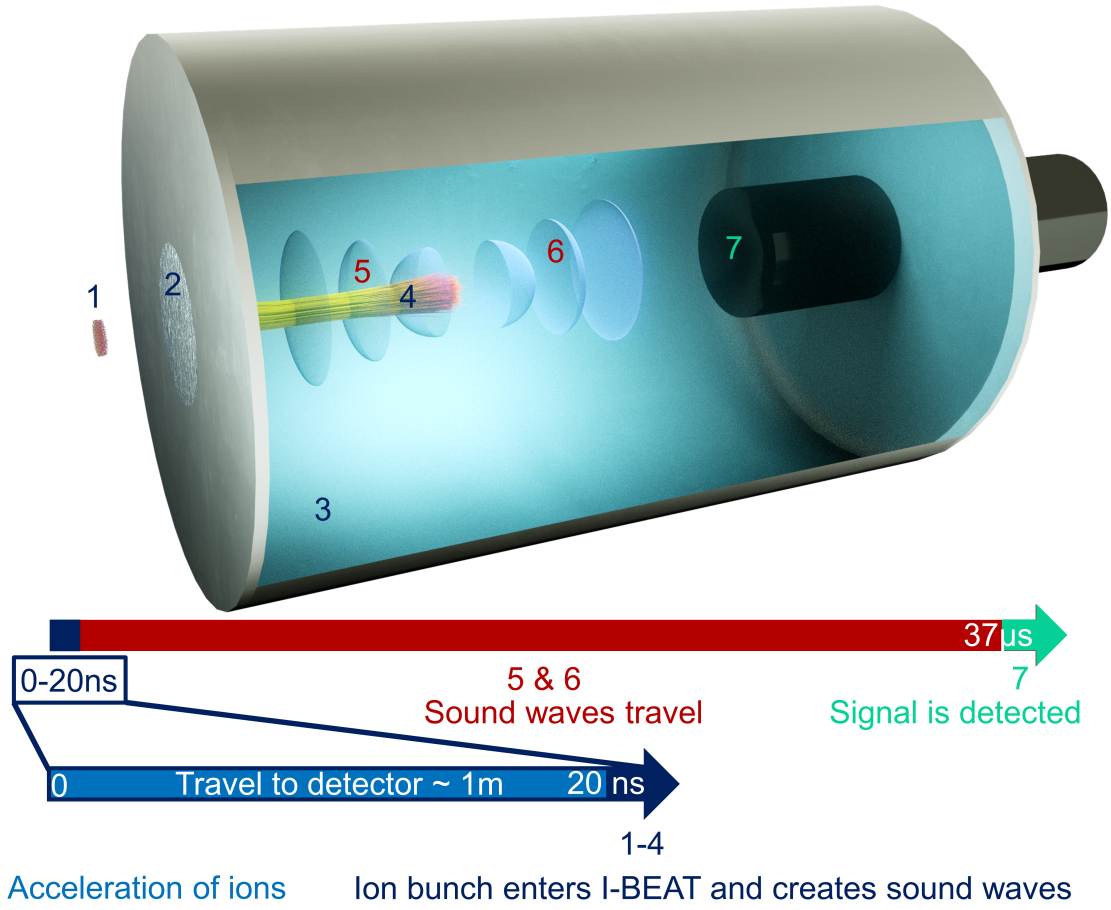

Figure 5.1 | I-BEAT. This illustrates the concept of I-BEAT. A short ion bunch (**1**) enters the detector through a thin foil (**2**). Within a water volume (**3**) the ions are stopped and dissipate their energy in the form of a Bragg-peak (**4**). The localized inserted energy causes pressure waves. The transducer (**7**) detects two signals. The direct pressure signal (**6**) and the reverse running wave (**5**) that eventually gets reflected at the entrance foil reaching the detector at later times. The temporal behavior of a measurement is sketched at the bottom elucidating the difference in time scales of the ion bunch and the sound wave.

The concept of I-BEAT is to record the pressure wave that has been created by a short ion bunch dissipating its energy within a water volume. In Fig. 5.1 the measurement process is sketched. A short ion bunch enters the water filled detector volume through a thin foil. The ions are stopped and dissipate their energy. This consequently time and space dependent heat source will create pressure waves, whereas the gradients will determine the strength of the signal (Eq. (2.51)). The transducer detects three signals. The direct pressure signal and the reverse running

wave that eventually gets reflected at the entrance foil reaching the detector at later times. A third signal is generated when the ion bunch traverses the entrance foil (different absorption coefficients increase the gradient). A typical signal for a mono-energetic proton bunch can be seen at Fig. 5.4. Further a time scale of the measurement is outlined elucidating relative fast energy deposition of the ions and the slow traveling speed of sound leaving ample time for negative electronic side effects such as EMP to decay.

5.3 Design and Development of I-BEAT

The work was carried out on the basis of broad knowledge of previous measurements for range verification of protons. This previous work was based on the evaluation of the travel time of the acoustic signal to the transducer, that could be correlated to the Bragg peak of a mono-energetic ion bunch, much like in the conventional use of ultrasound for sonar. Since the ion flux and thus, the signal strength of typical conventional ion sources such as a Tandem accelerator [222] is weak, a good signal to noise ratio required averaging over multiple shots (~ 100).

In contrast the proton bunch accelerated by a laser-plasma interaction is in particular suitable for such measurements. Its short bunch duration ($<$ ps directly at the interaction and $\sim$ ns in 1 m distance due to dispersion) and intense ion number causes steep energy gradients and consequently large acoustic signals. The broader and more complex energy distribution required the analysis of the complete acoustic signal and not only the center of the envelope (as in previous work) in a single-shot. The second challenge was to design a detector that can be operated also in vacuum.

5.3.1 Detector for I-BEAT

The most convenient solution for a prototype was to use a KF-40 vacuum pipe as the water tank. The transducer[2] (10 MHz, focusing Fig. 5.2c) was attached with a feed-through at the rear while a hole covered with an 11 µm titanium foil was used as an entrance window for the ion bunch. Figure 5.2 shows the employed detectors. Two geometries have been tested (Fig. 5.2a is used for the experiments at LEX Photonics and Fig. 5.2b for the experiments at the HZDR in Dresden).

[2] Olympus.

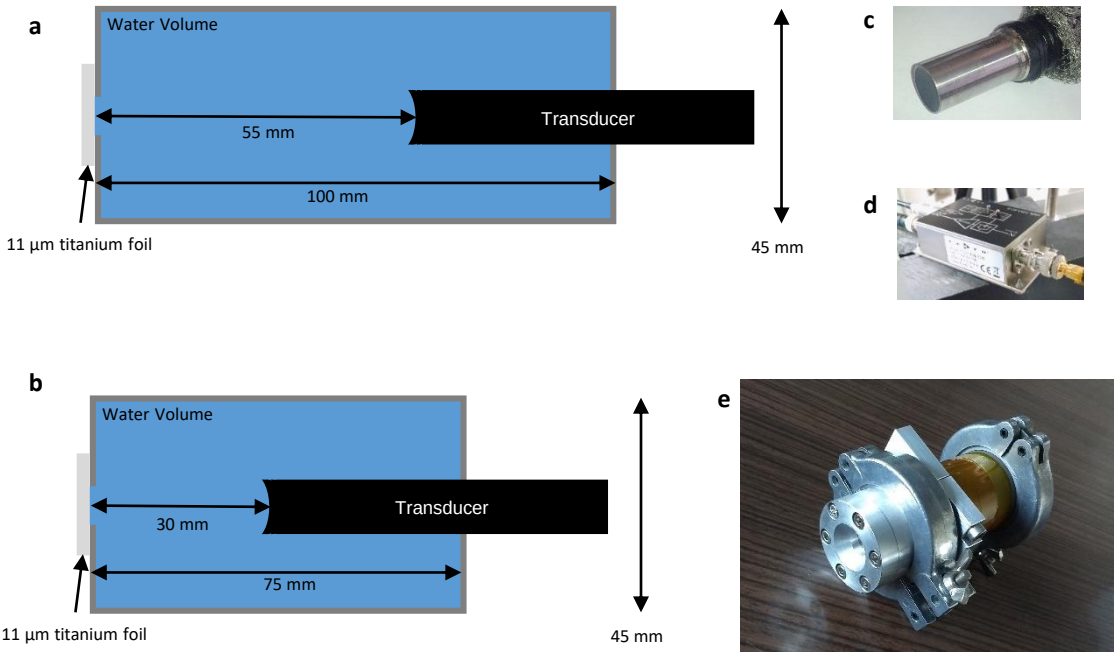

Figure 5.2 | The detector of I-BEAT. **a**, Sketch of the detector geometry used at LEX-Photonics. **b**, Geometry used at the Draco laser (HZDR). **c**, Picture of the transducer used during the experiments (focussing, 10 MHz). **d**, Picture of the voltage amplifier used in the experiments. **e** Picture of the tube accommodating the water sample (front view). The figure is adapted from [191].

5.3.2 Calibration

Before starting the measurements of laser-accelerated ion bunches, the detector was studied under well defined conditions. Therefore, I-BEAT was implemented at a proton beam generated by the MLL Tandem accelerator [222]. The setup that was used at the MLL can be seen in Fig. 5.3. A mono-energetic ($dE/E = 10^{-4}$) 10 MeV proton bunch (attenuated to 9.4 MeV at the detector entrance) with adjustable bunch duration (40 to few 100 ns) exits the acceleration beam line through an 11 µm titanium foil and traversing an air gap until entering the I-BEAT detector. Additional layers of aluminum could be added in the beam-path to attenuate the energy of the proton bunch (causing an increasing energy width due to straggling). A typical measurement of the acoustic trace that is generated by such a proton bunch is given in Fig. 5.4. The signal can be split into three segments. In addition to the pulse that propagates directly to the transducer and arrives 36.5 µs after proton impact (segment 1), a second pulse initially propagates in the opposite direction towards

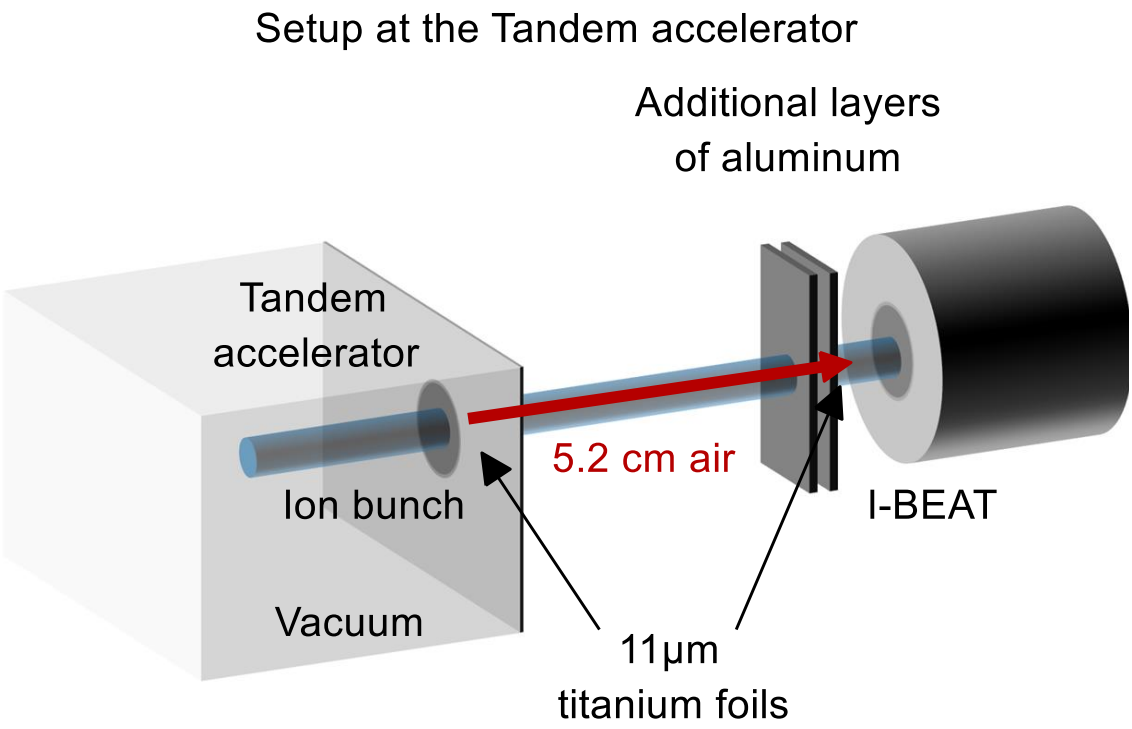

Figure 5.3 | Setup at the MLL Tandem. This sketch depicts the setup at the MLL Tandem accelerator. The ion bunch exits the accelerator vacuum via an 11 µm thick titanium window and enters the I-BEAT detector after 5.2 cm in air. Additional layers of aluminum can be added to attenuate the energy of the ion bunch prior entering the detector. The figure is adapted from [191].

the entrance window, and is subsequently reflected back towards the transducer (segment 3). The smaller intermediate signal (segment 2) originates from the energy deposition within the entrance window (large gradient due to density change).

Comparing the measurement with the simulated signal based on $p(t)$ (Eq. (2.64)) using the Bragg-curve of a mono-energetic 9.4 MeV proton bunch as the heating function shows deviations[3]. As in any measurement, the signal is influenced by the detector itself. This difference between an ideal acoustic trace and the real measurement is apparent and can be used to calculate the so called total detector response $T(f)$ from the real pressure signal $p(t)$ (Eq. (2.64)) and the measured one $S_m(t)$ by

$$T(f) = \frac{\mathcal{F}[S_m(t)]}{\mathcal{F}[p(t)]}, \tag{5.1}$$

where $\mathcal{F}$ is the Fourier transform of the acoustic traces (measured in time domain).

[3] A more detailed description of the simulations can be found in [223].

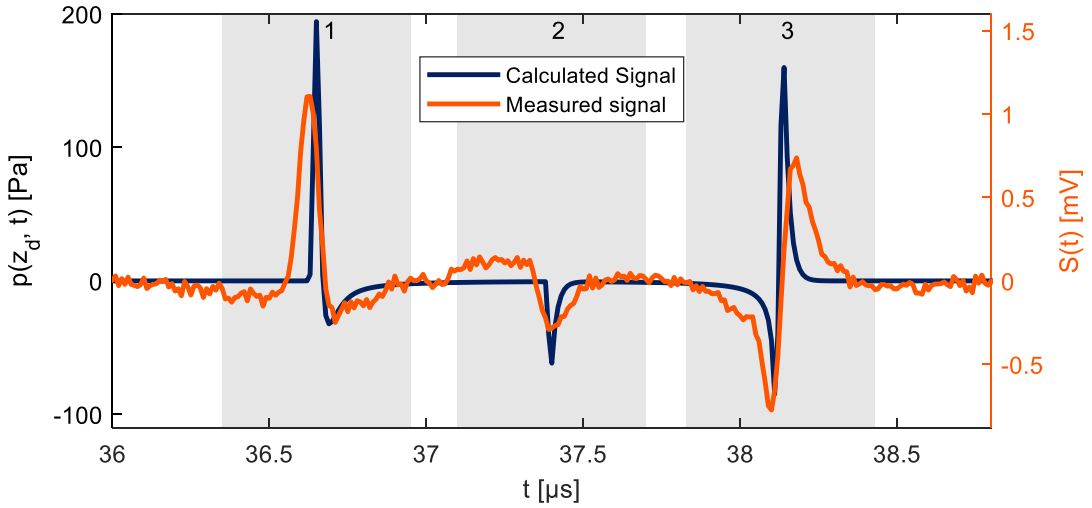

Figure 5.4 | Calibration required. The calculated signal of a 9.4 MeV proton bunch entering the I-BEAT detector (Fig. 5.2 a) is shown. The three segments show the direct (1), the reflected (3) signals. The middle signal (2) origins from the foil entrance. A comparison with the measured trace signal reveals the need for a calibration of the detector response. The figure is adapted from [191].

Since I-BEAT is taking the complete acoustic signal into account, the first step was the measurement of the detector response function in units V/Pa (see Fig. 5.5). The calibration is based on measurements at the MLL Tandem accelerator and outlined in Fig. 5.5. By inserting aluminum foils of 3 different thicknesses (90, 210 and 270 µm), the central energy entering the detector was gradually reduced from 9.4 MeV to 8.6, 7.2, 6.5 MeV. Since both the direct and the reflected signal contain the full information, 8 trace segments can be used for determination of the transfer function. By using multiple trace segments, effects of electronic noise and the varying spatial impulse response when the source has a different location are smoothed out. Figure 5.5b shows the averaged transfer function, whereas the error bar reflects the maximum deviation of the eight trace segments used for evaluation. The amplitude is quite stable with small error bars. Therefore, the same calibration can be used for energies in the range between 7 and 10 MeV. Increasing error bars beyond 10 MHz are due to the use of a 10 MHz transducer. The fact that $T(f)$ (frequency dependent transfer function) peaks around 2 MHz while a 10 MHz transducer is employed can be explained with the effect of geometry spatial response [224]. The used transducer Fig. 5.2c has a focal length of 25.4 mm. In our case we measured ultrasound signals with a source more than 50 mm away from the transducer. This out-of-focus opera-

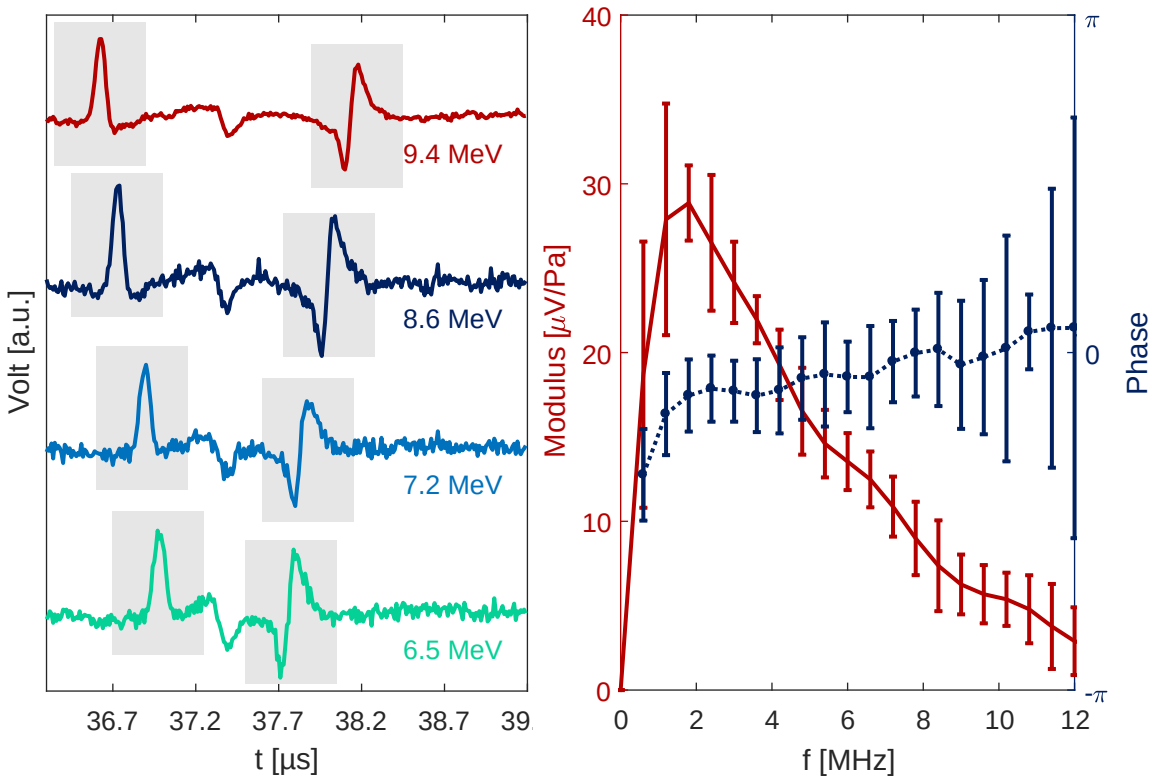

Figure 5.5 | Transferfunction of I-BEAT. **a**, Acoustic traces recorded with proton bunches at the MLL Tandem accelerator and outlined regions used for the calculation of the transfer function $T(f)$. **b**, Amplitude of the averaged complex transfer function $T(f)/N_i$ in units V/Pa and its phase , where error bars represent maximum deviation of the respective eight independently determined trace segments highlighted in **a**. The figure is adapted from [191].

tion causes that almost plane waves (see Section B.1) hit the curved detector surface and therefore excites it much longer (even if the acoustic signal was shorter). Those measurements were also used for a quantitative calibration. Therefore the number of protons per proton bunch was estimated via $N_\mathrm{i} = \int f\left(E_\mathrm{kin}\right) \cdot dE_\mathrm{kin} = I/\left(e \cdot f_\mathrm{rep}\right)$, where I is the average current that was delivered from the Tandem to the water volume, and $f_\mathrm{rep} = 5$ kHz is the bunch repetition rate. We estimated, considering the pinhole size of the detector entrance and the spot size of the beam, that 60 % of the bunch enters the detector such that current was estimated $= 0.6 \cdot 7$ nA$= 4.2$ nA. $S_\mathrm{m}\left(t\right)$ is thus quantitatively connected to the ideal pressure trace p(t) for an arbitrary ion energy distribution $f(E_\mathrm{kin})$ via

$$S_\mathrm{m}(t) = \mathcal{F}^{-1}[\mathcal{F}[p(t)] \cdot T(f)], \tag{5.2}$$

where $\mathcal{F}^{-1}$ is the inverse Fourier transformation. This calibration is one prerequisite in order to use the acoustic signal for the absolute determination of the heat source and consequently the energy spectrum of the ion bunch.

Reflection at the foil

We have seen that the later part of the signal is reflected from the entrance foil. So a modeling of the complete acoustic signal also requires an incorporation of the reflection at the foil. Analougously to the reflectivity of light under normal incidence (see Eq. (B.40) we can calculate the reflective index for the sound wave

$$R_{\mathrm{Sound}} = \frac{Z_{\mathrm{foil}} - Z_{\mathrm{water}}}{Z_{\mathrm{water}} + Z_{\mathrm{foil}}}, \tag{5.3}$$

with Z being the medium dependent impedance. With the impedance of water at room temperature $Z_{\mathrm{water}} \approx 1.5 \cdot 10^6\ \mathrm{N\,s\,m^{-3}}$and $Z_{\mathrm{foil}} \approx 18.6 \cdot 10^6\ \mathrm{N\,s\,m^{-3}}$, the reflectivity would be $R_{\mathrm{Sound}} \approx -0.85$. However since the Titanium foil was very thin (13 µm), Z_{foil} has to be calculated taking the thickness and the medium on the other side Z_{load} (in our case air or vacuum) into account (for details see [225]). It then yields

$$Z_{\mathrm{thinfoil}} = Z_{\mathrm{foil}} \frac{Z_{\mathrm{load}} - iZ_0 \cdot \tan\left(k_0 d_0\right)}{Z_{\mathrm{foil}} - iZ_{\mathrm{load}} \cdot \tan\left(k_0 d_0\right)}, \tag{5.4}$$

with $k_0 = 2\pi f_{\mathrm{s}}/c_{\mathrm{s}}$ and d_0 =11 µm the thickness of the foil. The equation simplifies with $Z_{\mathrm{load}} \approx 0$ (air or vacuum) to $Z_{\mathrm{thinfoil}} \approx iZ_0 \cdot \tan\left(k_0 d_0\right)$. With $R = -e^{i\Phi}$ we can calculate a phase shift of the reflection and get

$$\Phi = \mathrm{atan}\left(\frac{2 \cdot Z_{\mathrm{water}} Z_{\mathrm{foil}} \cdot \tan(k_0 d_0)}{Z_{\mathrm{water}}^2 - Z_{\mathrm{foil}}^2 \cdot \tan^2(k_0 d_0)}\right) \approx -1.1 \approx -\frac{1}{3}\pi, \tag{5.5}$$

for a frequency of 10 MHz. This phase shift between the direct and reflected signal, introduced when reflected, can be seen in Fig. 5.5.

5.3.3 Simulated Annealing

The reconstruction of the spectrum from the I-BEAT signal is based on the technique simulated annealing [226, 227]. The method of simulated annealing relies on varying an initial spectrum $f_{\mathrm{i}}(E_{\mathrm{kin}})$ (a little change applies to the estimated spectrum, and both its position and amplitude are decided by pseudo-random generators) to obtain a modified spectrum $f_{\mathrm{m}}(E_{\mathrm{kin}})$. As a starting point $f_{\mathrm{i}}(E_{\mathrm{kin}})$ was chosen to be zero for all energies. Typically, the maximum of the amplitude modification is set to be smaller than 1% of the maximum of f_{i}. With the input of the initial and the modified spectrum in Eq. (2.64) and Eq. (5.2) the predicted acoustic signals $S_{\mathrm{i}}(t)$, $S_{\mathrm{m}}(t)$ are calculated and compared to the acoustic signal $S_0(t)$. The residuals $\Sigma_{\mathrm{i}} = \Sigma_{\mathrm{j}} \left(S_{\mathrm{i}}^{\mathrm{j}} - S_{\mathrm{o}}^{\mathrm{j}}\right)^2$ and $\Sigma_{\mathrm{m}} = \Sigma_{\mathrm{j}} \left(S_{\mathrm{m}}^{\mathrm{j}} - S_{\mathrm{o}}^{\mathrm{j}}\right)^2$ are calculated employing the least squared method. If Σ_{m} is smaller than Σ_{i}, the algorithm continues with the modified spectrum as the updated input distribution for the next cycle. For Σ_{i} smaller than Σ_{m} , with probability $q = exp\left(-\left(\Sigma_{\mathrm{m}} - \Sigma_{\mathrm{i}}\right)/T\right)$, the algorithm continues with the modified spectrum, while, with the probability $1 - q$, it is rejected and the initial spectrum is taken into the next cycle. This additional random choice prevents from being caught in a local minimum. T is the annealing schedule temperature and was set to 1. After a sufficient amount of iterations $\approx 10^4$ the temperature during the iteration would become stable around the temperature global minimum (Σ_{i} converges) and the obtained proton energy spectrum is the retrieved spectrum. We can further include the lateral bunch size σ_{r} in the retrieval algorithm, treating it as a free parameter. In this case the complete process of simulated annealing depicted in Fig. 5.6 is repeated by varying σ_{r}. As a result the final residuals $\Sigma_{\mathrm{i}}(\sigma_{\mathrm{r}}^{\mathrm{j}})$ after a sufficient amount of steps (Σ_{i} converges) can be compared in dependency of the bunch diameter and smallest residual value determines the best fitting ion bunch diameter.

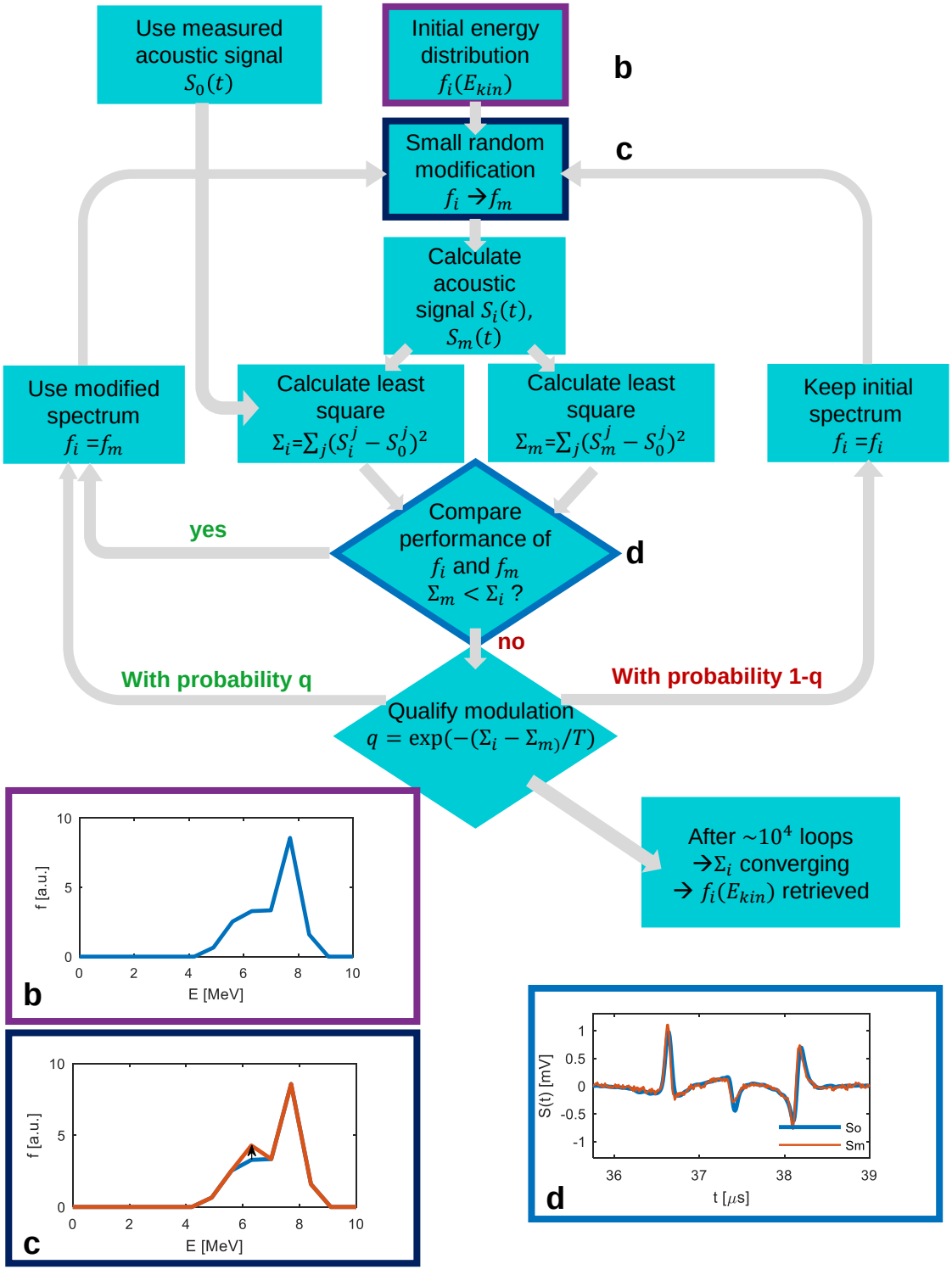

Figure 5.6 | Workflow of simulated annealing. **a**, The workflow of simulated annealing is shown. **b**, The initial spectrum (f_i) can be guessed or assumed to be zero for all energies. **c**, A small modulation to the initial spectrum is done (f_m). **d**, Acoustic signals corresponding to the initial f_i and initial f_m spectrum, are calculated and compared to the measured trace. The spectrum of the better fitting signal is with probability q taken as f_i for the next iteration step until it converges. The figure is adapted from [191].

5.3.4 Validation Measurements at the MLL Tandem Accelerator

The next important step was validation of the approach under known circumstances. So first tests were performed at the MLL Tandem accelerator at Garching with the same setup used for the calibration, using well defined proton bunches of 40 ns duration with 10 MeV $dE/E = 10^{-4}$, attenuated to 9.4 MeV at the detector (by the exit window and air gap). The initial energy of 9.4 MeV at the detector entrance was attenuated by inserting different thicknesses of aluminum in the beam path. The acoustic signals deriving from different energies were measured and are shown in Fig. 5.7a, where each trace represents an average of 100 proton bunches. Figure 5.7b

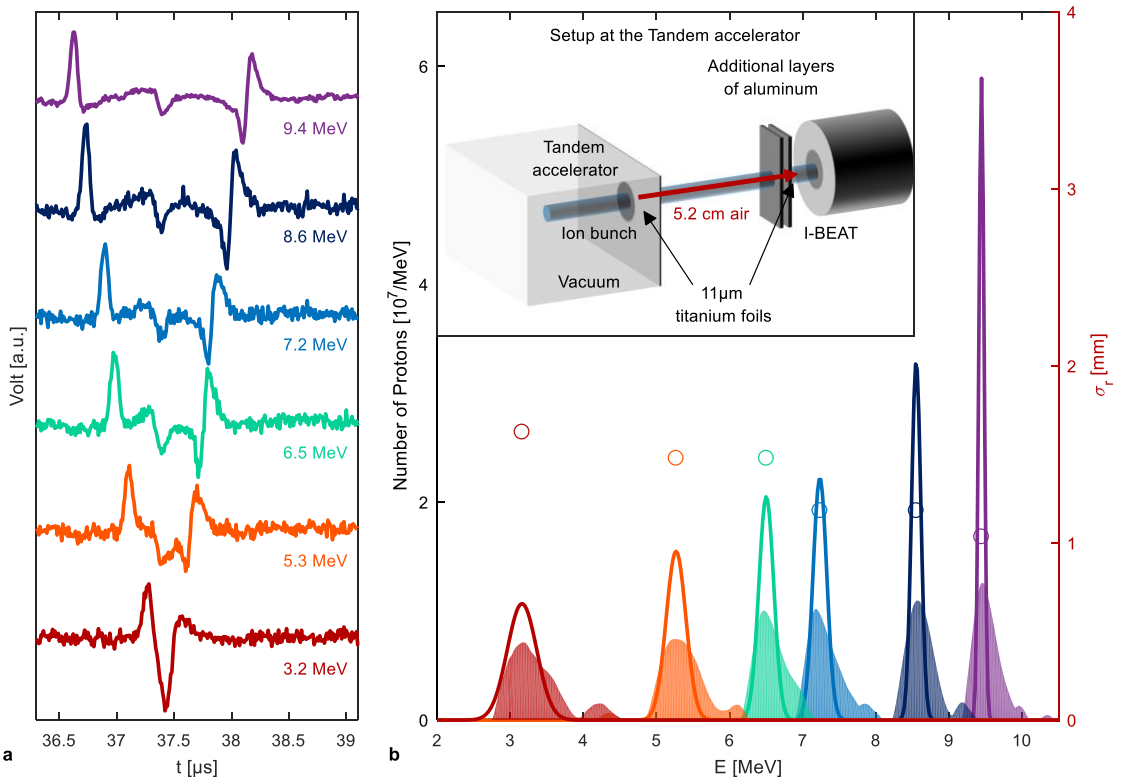

Figure 5.7 | I-BEAT at the MLL Tandem accelerator. **a**, Acoustic traces of 6 different proton bunch energies at the detector entrance recorded at the Tandem accelerator. Each trace represents an average of 100 proton bunches. **b**, Comparison of proton energy distributions simulated (curves) and retrieved data (filled), as well as reconstructed beam with standard deviation σ_r (circles), of the measured acoustic traces in **a**. The inset of **b** sketches the setup at the Tandem accelerator. The figure is adapted from [191].

compares the retrieved proton energy distributions to the energy distributions cal-

culated via SRIM (2013) [228] by taking into account the absorber material in the beam path. For the SRIM calculation, we employed a mono-energetic beam with 10 MeV, passing through 11 µm titanium (the exit window of the accelerator vacuum), 5.2 cm air, and 11 µm titanium (the entrance of the water tank). While the peak positions of the energy distributions (simulated and measured) agree within 1%, the larger energy spread and accordingly lower particle number of the I-BEAT data is due to a limited temporal and thus, spatial resolution. The narrow energy distribution cannot be resolved by the transducer and the retrieved spectra are broadened. The transducer and corresponding transfer function limits the temporal response, and thus also determines the limit for the longitudinal spatial resolution. Since the spatial resolution, to first order, is constant along propagation direction, the energy resolution intrinsically increases for higher ion energies and is only limited by energy loss straggling for high kinetic energies. We consider the effect of the transfer function on the FWHM of a mono-energetic ion peak to set the resolution limit. Our transfer function yields resolutions of 1.0 MeV at 5 MeV and 0.6 MeV at 10 MeV (increasing resolution towards higher energies). These resolution limits of I-BEAT, when applied to narrow energy spread proton bunches at low energies (< 20 MeV), are visible in Fig. 5.7b. The retrieved transverse beam size σ_r increases as expected with increasing aluminum thickness (i.e. decreasing bunch energy). This is due to the associated transverse straggling that becomes increasingly prominent.

5.4 Experimental Campaigns and Results

After a successful preparation of I-BEAT, two experimental campaigns were carried out. The first one at LEX Photonics was used for first tests and a demonstration of the method. Since the evaluated results comprised an absolute reconstruction of the proton spectrum and thus also directly the depth-dose profile of the protons, a second experiment was performed at the DRACO in Dresden to directly compare the measured dose to the well accepted measurement with RCF-stacks. This comparison was not possible at LEX Photonics because the proton energy was below 10 MeV, where RCF-stacks do not provide a good depth resolution.

5.4.1 Experimental Campaign at LEX Photonics

The first demonstration of I-BEAT with a laser-accelerated proton beam was at LEX Photonics. The detailed description of the Laser and the experimental setup

can be found in Chapter 3. For most of the I-BEAT campaign 250 nm gold targets were used since the proton energies were higher and more stable. The characteristic TNSA energy spectrum is shown in Fig. 3.7. The PMQ were adjusted to focus different design energies (7, 7.5, 8 and 8.5 MeV) to 1.53 m distance outside of the vacuum chamber. The design energy is the energy that is focused to the desired distance and is described in Section A.1.9. The DM was employed to clean the signal, i.e. directing potential contamination attributed to energetic electrons and low energy ions away from the I-BEAT detector entrance and further pre-selecting the proton energy. As a result, the spectrum in the focus is narrowed and modulated. After traversing the vacuum exit window (50 µm Kapton foil) it enters the I-BEAT detector (the setup can be seen in Fig. 3.6 and Fig. 5.9a). The results are depicted in Fig. 5.9.

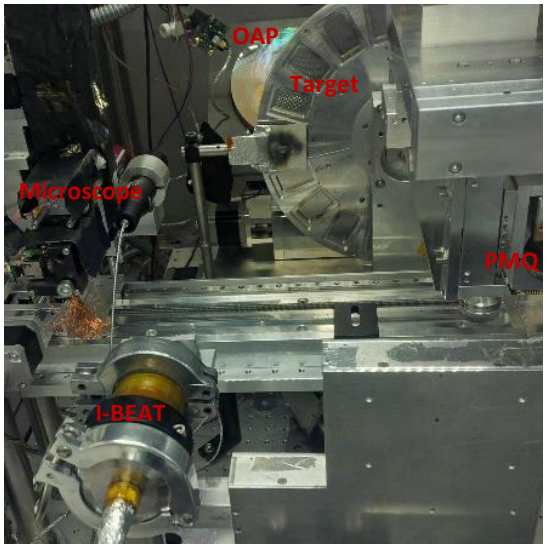

Figure 5.8 | I-BEAT in the vacuum chamber. This pictures has been taken at LEX Photonics where I-BEAT was positioned inside the vacuum chamber roughly 40 cm behind target. We demonstrated the capability of operating I-BEAT in vacuum and thus it can be positioned anywhere in the target chamber without much effort. The complete setup of LEX Photonics has been described in more detail in Chapter 3.

Acoustic traces corresponding to single proton bunches with design energies (7, 7.5, 8 and 8.5 MeV) attenuated to 6.2, 6.7, 7.3 and 7.8 MeV when entering the water tank are presented in Fig. 5.9b. A picture taken with an image plate can be seen in the inset of Fig. 5.9d. The spot size at the focus of the laser-accelerated proton bunch was distorted due to the broad input energy distribution and slight alignment errors of the relative rotation angles of the PMQ. The shape especially at lower dose values

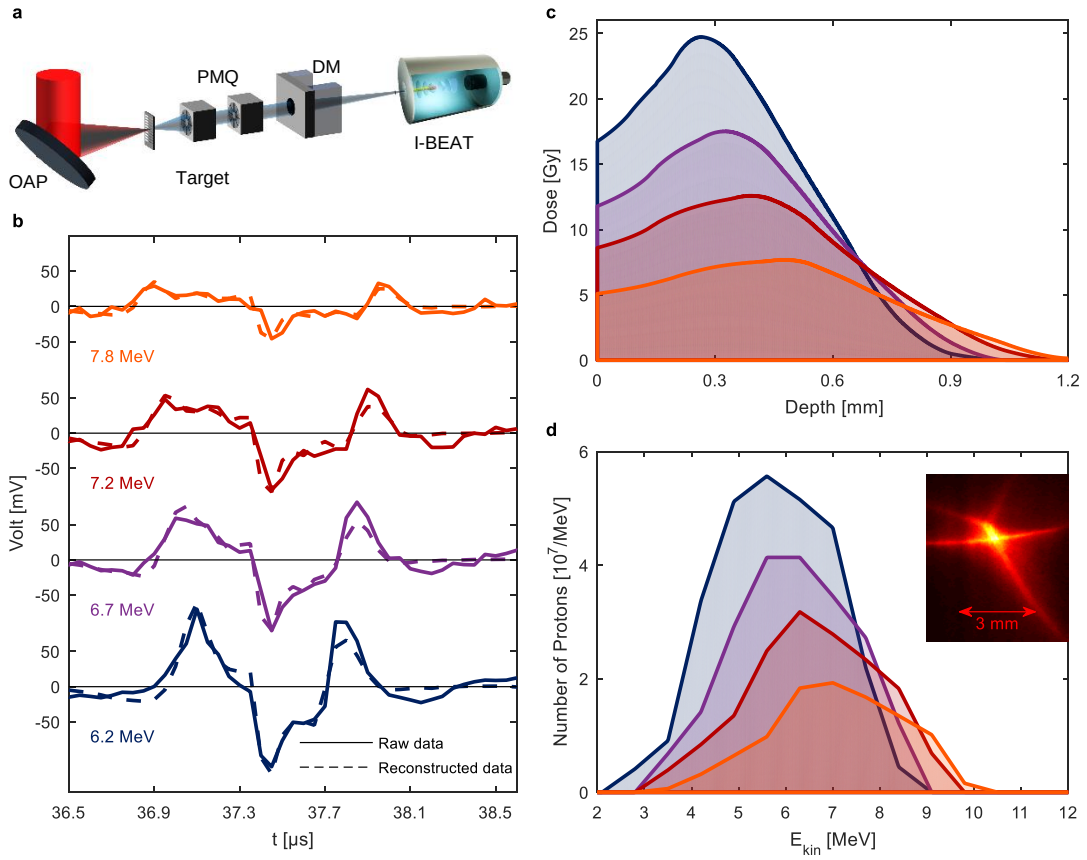

Figure 5.9 | I-BEAT at LEX Photonics. **a**, Shows the schematic of the experiment setup. A high power laser (ATLAS300) is focused with an OAP onto a foil target. Two PMQ are used to focus a short ion bunch. A DM is used to remove electrons and low energy ions from the swift ion bunch, which is focused within the Ionoacoustic detector. **b**, Acoustic signals of single proton bunches. The design energies attenuated to 6.2, 6.7, 7.2 and 7.8 MeV on entering the water volume, are set by positioning of the PMQ. The solid line is the measured acoustic signal and the dashed line corresponds to the calculated signal from the retrieved spectrum in d. **c**, Depth dose curves corresponding to the different energy settings. The dose on the central axis is $D(z) = 1/\rho \cdot 1/(2\pi\sigma_r^2) \cdot B_s(z)$. **d**, Absolute proton energy distributions of single proton bunches of the different design energy settings in the ion focus. The inset reveals a typical focal plane image of a single proton bunch at the position of the detector entrance, taken with an image plate. The σ_r is the resulting Gaussian width of I-BEAT. The figure is adapted from [191].

is typical for proton foci using PMQ [69]. While the most intense part is confined to an about 1-2 mm central spot, it extends up to about 3-4 mm. We have seen in Section 5.3.3 that the standard deviation of the lateral Gaussian distribution can be included in the retrieval. The generic results for the case of a design energy of 7 MeV (attenuated to 6.2 MeV at I-BEAT) is shown in Fig. 5.10a. In (Fig. 5.10) one

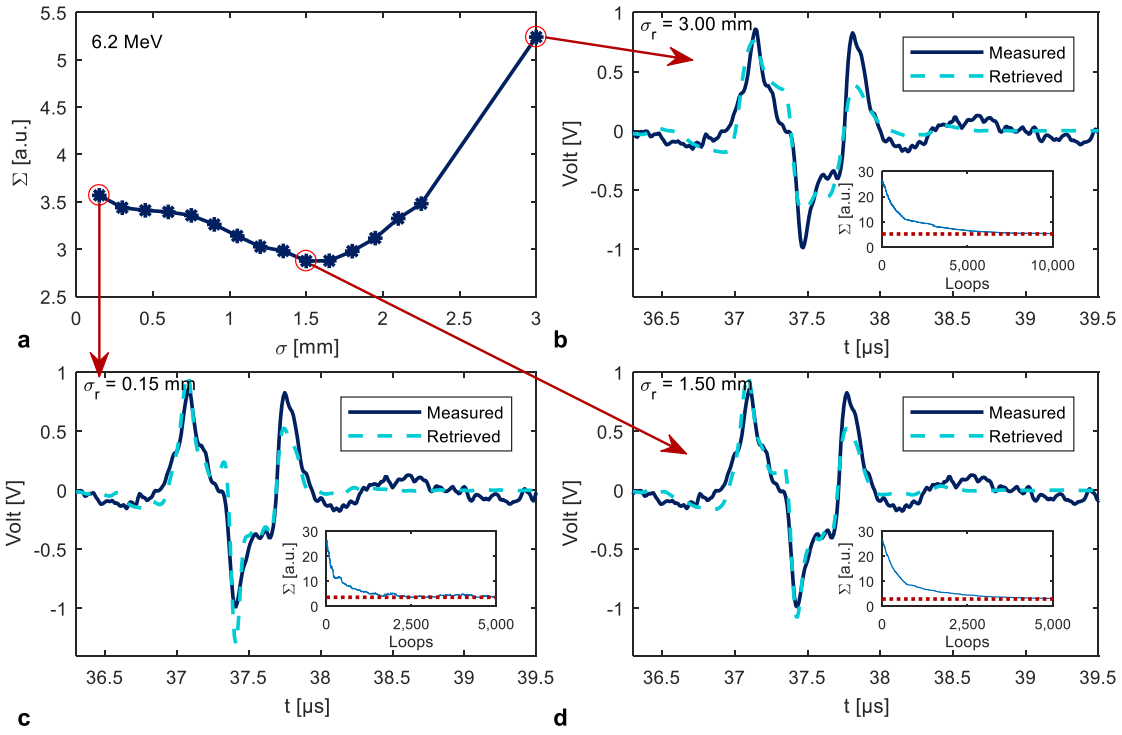

Figure 5.10 | Evaluation of different ion bunch diameters for I-BEAT. The evaluation is performed for the 6.2 MeV case at LEX Photonics. **a**, shows the residual Σ_i in dependency of the bunch diameter. **b**,**c**, and **d**, show the experimentally recorded signal (blue) and the calculated signal using the retrieved (simulated annealing) ion energy distribution. As an inset the development of Σ_i with the number of iterations is shown. The figure is adapted from [191].

can see that evaluation of the residuals Σ produced a comparable result as long as σ_r was less then 2.5 mm. The best fitting bunch size is $\sigma_r = 1.5 \pm 0.2$ mm (error is due to the step size of the fitting algorithm). To accelerate the reconstruction process σ_r was then fixed to 1.5 mm for the reconstruction of the different energy settings. This seems in reasonable agreement with the recorded image plate picture (Fig. 5.9d), where the corresponding diameter is indicated.

Retrieved absolute proton energy distributions in the PMQ doublet focal plane are presented in Fig. 5.9d. The integrated proton number of 10^8 may seem small but considering that the bunch length in 1.5m distance is about 15ns (for a proton bunch with spectrum covering 4 to 8 MeV) and a Gaussian width of 1.5mm, the proton flux is intense. For the case of 6.2 MeV in Fig. 5.9, the peak bunch current reaches about 1mA. The excellent conformity of the final retrieved and measured signals (see Fig. 5.9b)) demonstrates successful reconstruction of the ion energy

Energy QP	Energy I-BEAT	Distance QP	Solid angle	Result
[MeV]	[MeV]	[mm]	[msr]	[10^6 Protons / (MeV msr)]
7	6.2	33.5	12.0	4.3
7.5	6.7	35	11.0	3.5
8	7.2	36.5	10.1	2.7
8.5	8.8	37.8	9.7	1.7

Table 5.2 | Calculation of energy spectrum obtained with I-BEAT. This table gives the values of the design energy of the PMQ and the attenuated energy when it enters the I-BEAT detector. The distance of the PMQ to the target and the therefrom calculated solid angle are given. The laser column shows the calculated proton number per MeV and msr at the design energy of the PMQ

distribution. The corresponding on-axis depth dose distribution in Fig. 5.9c is of particular interest for biomedical application and is a natural byproduct of I-BEAT.

Comparison of Energy Spectra

We further compared the retrieved energy spectrum with the spectrum obtained with the WASP as shown in Fig. 3.7. We therefore assumed that, at the design energy of the PMQ, all particles inside the elliptic opening aperture of the first PMQ (radius $r_{\mathrm{PMQa}} = 3.3$ mm and $r_{\mathrm{PMQb}} = 1.3$ mm, see Fig. A.10c and [72]) will be focused into the I-BEAT detector. The covered solid angle can then be calculated with

$$\Omega = \frac{A}{d_{\mathrm{PMQ}}^2} \approx \frac{\pi \cdot r_{\mathrm{PMQa}} \cdot r_{\mathrm{PMQb}}}{d_{\mathrm{PMQ}}^2}. \tag{5.6}$$

A is the spherical surface area that is covered by the aperture of the PMQ. Since it is small, it can be approximated by the area of the aperture itself. The distance of the first QP to the source is d_{PMQ} and is dependent on the focus distance that in our case was set to 1.53 m and the design energy. We note, that this is an estimation since not all trajectories entering the PMQ will pass them, depending on the energy. A more accurate study of this can be found in [229]. In Section 5.4.1 the distances and therefrom resulting solid angles for all four settings of the PMQ are given. For comparison we used the particle number at the values of the attenuated energies at the detector of Fig. 5.9, given in $\mathrm{N_{protons}}$/MeV and divided it by the solid angle. As a result we got $\mathrm{N_{protons}}/(\mathrm{MeV} \cdot \mathrm{msr})$ which we compared to the spectrum evaluated with the WASP in Fig. 5.11.

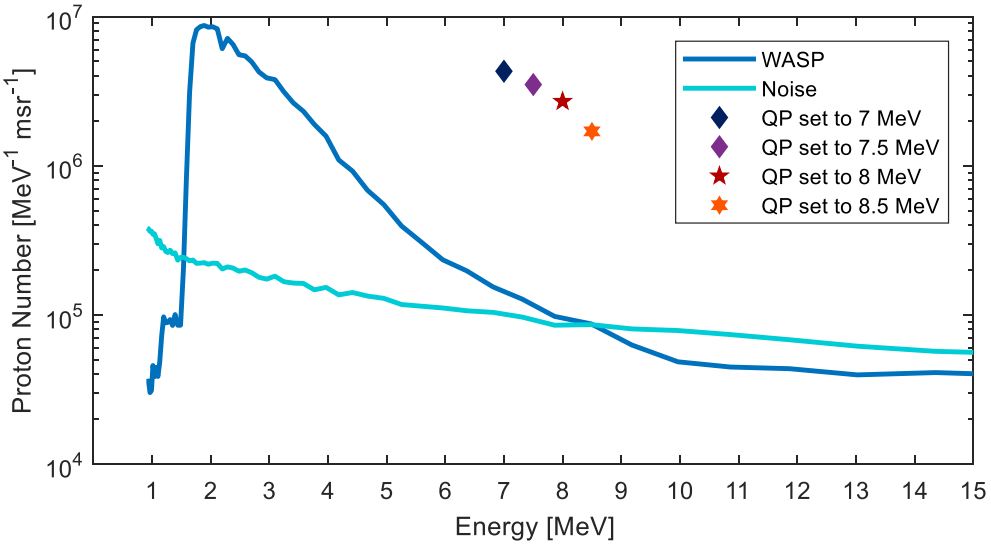

Figure 5.11 | Comparison of I-BEAT to the WASP The proton numbers obtained with I-BEAT are compared to the date of the WASP Fig. 3.7. The values of I-BEAT have been taken from Fig. 5.9 taking the solid angle of the PMQ into account.

We can see that the proton number obtained with I-BEAT is more than one order of magnitude larger than the one evaluated with the WASP. Even introducing an error bar for the values obtained with I-BEAT according to its noise level in the signal (Fig. 5.9) as it is shown in Fig. 5.14 would not explain this discrepancy. A potential source of errors for I-BEAT could have been introduced in the calibration with the Tandem accelerator, by assuming a wrong particle number. Another possible explanation at this point could also be the evaluation with the WASP. The conversion from signal to particle number has been evaluated in previous work [155]. In the used configuration with 1.16 m distance to the target and pixel (size of 50×50 µm) covers a solid angle of $\approx 2 \cdot 10^{-6}$ msr. A proton number of 10^6/ (MeV msr) would thus result in 1 proton per pixel. Even though the measurement is taken out integrating over several pixels per energy bin the detector is operated close to the threshold. Considering further that the used detector has experimented damage from previous measurements as a dark image that is used for referencing (Fig. 5.12) shows, the evaluated number has to be assessed cautiously. It is a valid option that the Radeye underestimates the particle numbers.

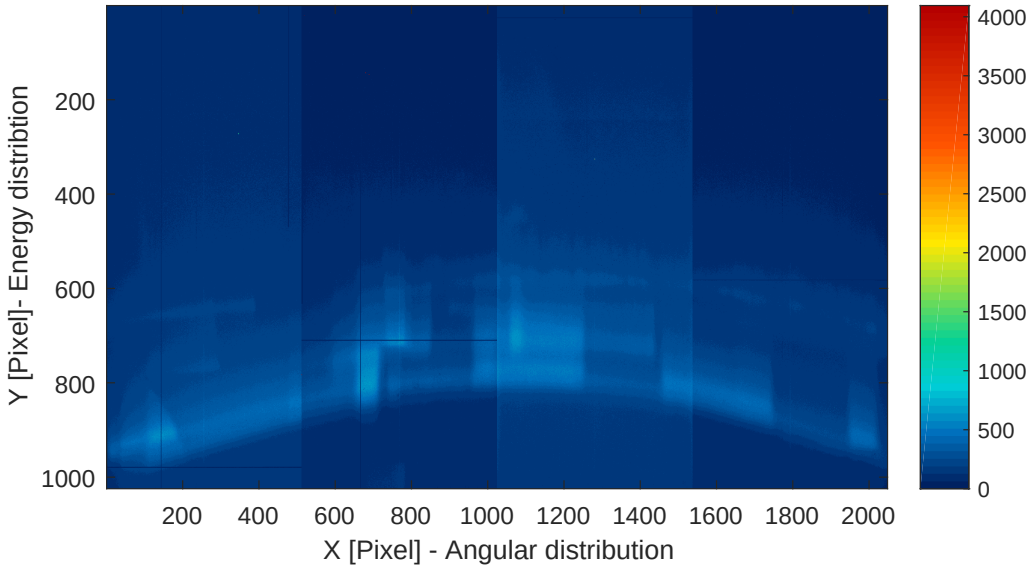

Figure 5.12 | Dark current of the Radeye. A dark current picture of the Radeye of Fig. 3.7 shows the radiation damage that could cause deviations in the measurement.

5.4.2 Experimental Campaign at the DRACO

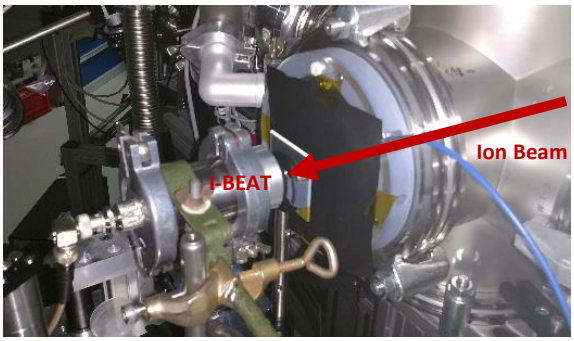

Figure 5.13 | I-BEAT at DRACO - setup. This picture shows the implementation of I-BEAT at DRACO. The detector was setup just outside the vacuum chamber about 2 m away from the ion source.

Due to the discrepancy between the I-BEAT and Radeye data, we conducted another experiment at the DRACO petawatt laser at HZDR [230], where the higher protons energies allowed to compare of I-BEAT to the well-established **R**acio**C**hromic **F**ilm (RCF) stack detector. It further allowed to demonstrate the feasibility of I-BEAT at a higher fluence level approaching 10^9 per bunch. The **DR**esden Laser **AC**celeration **S**ource (DRACO) at the **H**elmholtz-**Z**entrum **D**resden-**R**ossendorf (HZDR) is a Ti:sapphire system, capable of delivering up to 30 J within 30 fs at a

repetition rate of 1 Hz. In our experiment the energy was attenuated to about 12 J on target with enhanced temporal contrast using a re-collimating single plasma mirror [231]. Using plastic foil targets with a thickness of about 200 nm, the laser drives a TNSA proton source with cut-off energies in the range of 30 MeV. The pulsed, tunable solenoid magnet [18, 68] was positioned 80 mm behind the target and was therefore able to collect the high energetic part of the beam without particle loss. It acted as chromatic lens and was used to generate a focus of a desired central energy at the irradiation site in air about two meters downstream of the target. The energy bandwidth of the transported proton bunch amounted to about 20% (FWHM) at the focus position. For the presented experiment, a central proton energy of 15.4 MeV was focused into the I-BEAT detector, corresponding to a solenoid current of 12 kA leading to a magnetic field of about 10 T, accordingly. This proton energy has been chosen to optimize the signal-to-noise ratio recorded by the I-BEAT detector. The increased ion energy herein enabled a comparison with an RCF stack (EBT3 Gafchromic film, calibrated with an X-ray tube). Fig. 5.14 shows a shot for a design energy of about 16 MeV and its comparison to an RCF stack in two consecutive shots (small shot-to-shot fluctuations are ignored). This energy setting has been chosen to optimize the signal-to-noise ratio recorded by the I-BEAT detector. Fig. 5.14b shows the measured signal and the simulated signal using the reconstructed spectrum of Fig. 5.14c as an input. Fig. 5.14d validates that I-BEAT can reconstruct the depth dose distribution quantitatively. The depth resolution (horizontal spacing between data points) of I-BEAT is due to the sampling rate and transfer function and the error bar due to the limited band width of the transducer (10 MHz). The dose-error of I-BEAT results mainly from the calibration (e.g. fluctuations in the particle number) at the Tandem accelerator and electronic noise in the measured signal. For the RCF stack (EBT3-films) an overall accuracy in dose determination better than 5% can be obtained. However, due to higher **L**inear **E**nergy **T**ransfer (LET) in the Bragg peak region (with respect to the plateau region) of a mono-energetic proton beam, quenching effects might occur, which can lead to higher dose uncertainties. The gray bar in Fig. 5.14d t_{RCF} illustrates the water equivalent thickness and thus the theoretical lateral resolution of an RCF stack detector. Fitting a 2-D Gaussian to the Gafchromic film with the highest dose yields a horizontal σ_{h} of 3.6 mm and a vertical bunch diameter σ_{v} of 2.2 mm with an average of 2.9 mm. The fitting result of I-BEAT with $\sigma_{\mathrm{r}} = 3.0 \pm 0.2$ mm matches and shows that the transversal information can be estimated with a single transducer. Even though the error-bars

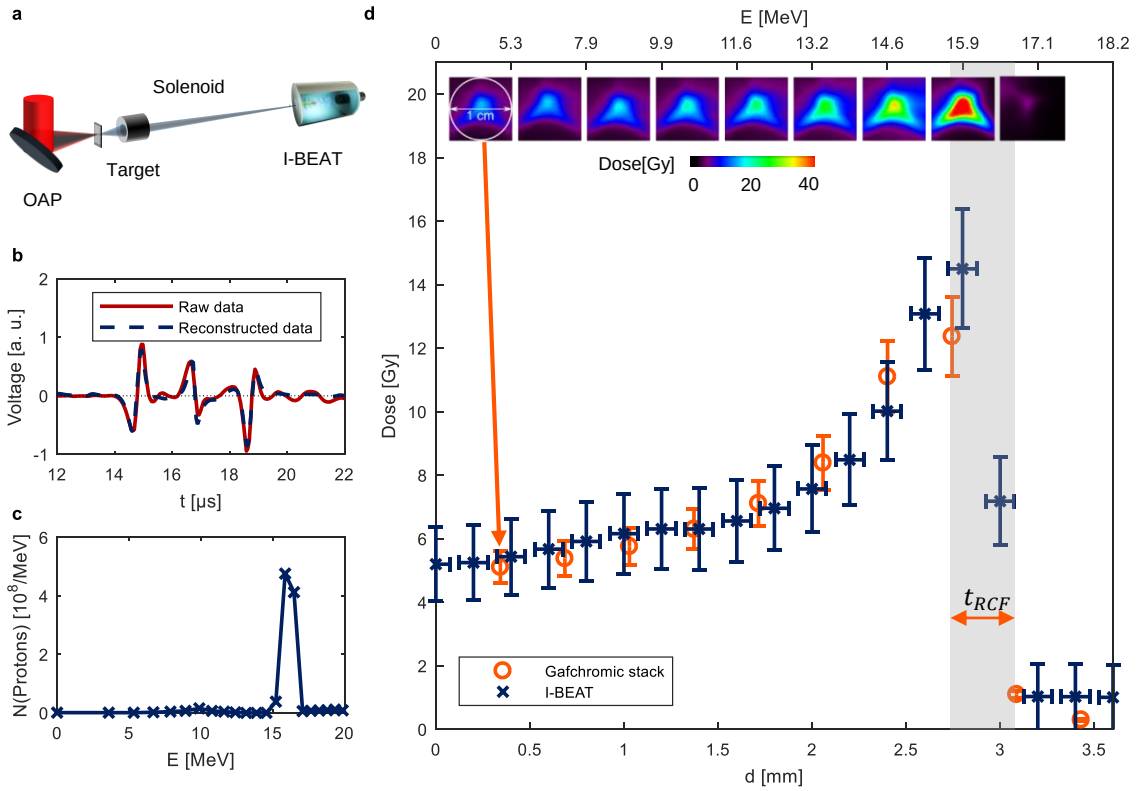

Figure 5.14 | I-BEAT at DRACO - results. **a**, is a sketch of the setup. A pulsed solenoid was used to focus a certain design energy. **b**, The measured signal and the reconstructed signal according to the energy distribution evaluated in **c** are shown. **c**, shows the final reconstructed proton spectrum. **d**, The depth dose distribution determined by I-BEAT is compared to the one obtained by an RCF stack in two consecutive shots. The corresponding layers of the stack are depicted and the dose (color coded in Gy) is evaluated over a circle of 1 cm diameter (entrance of the detector) for both the RCF stack and I-BEAT. The evaluated Gaussian profile determined by I-BEAT yields $\sigma_r = 3.0 \pm 0.2$ mm and fits very well to the dose of the RCF stack (shown in the second film picture of the stack). The upper axis shows the corresponding proton energy of different penetration depths. The error bar of I-BEAT on the y-axis is due to the calibration of the detector and the noise of measured signal. The error bar of the RCF stack is caused by calibration uncertainties [154]. The gray bar t_{RCF} illustrates the thickness of one RCF and thus the spatial resolution. The figure is adapted from [191].

of the measured dose obtained with I-BEAT are larger than the ones obtained with an RCF stack, the dose matches well. The error-bars of I-BEAT can be reduced with more advance calibration techniques. The energy resolution of I-BEAT at this stage is already better than that of the RCF stack (spatial resolution is nearly doubled, Fig. 5.14d).

5.4.3 Conclusion of the Measured Results

We have demonstrated the use of I-BEAT as a detector for laser-accelerated ions and in particular protons. Especially the comparison to the RCF stack in Fig. 5.14 shows the impressive performance of I-BEAT. The discrepancy to the data obtained with the WASP in Fig. 5.11 has to be studied in more detail but the results at DRACO hint that the error might be dominated by the evaluation of the WASP.

5.5 Applications of I-BEAT at (Laser-Driven) Ion Sources

In this section we investigate the functionality of I-BEAT at different condition typically occurring at laser-ion acceleration experiments. We show the performance of I-BEAT measuring a broad band exponential spectrum that is typically obtained close to target without any manipulation of the ion bunch. We also simulated the performance of I-BEAT in a multi species spectrum, using quadrupoles as charge state separator.

Simulation of I-BEAT Close to Target

In laser ion acceleration typically broad multi-species energy spectra emerge from the plasma target. We simulated the performance of I-BEAT positioned close to target without any manipulation of the energy distribution (e.g. magnetic quadrupoles or dipoles). The proton input spectrum was exemplarily taken from [56]. Note that other ion species are neglected in this consideration. The given input spectrum was used for a calculation of the expected signal (Fig. 5.15b). This signal was then evaluated with the I-BEAT algorithm and to retrieve the input spectrum. In Fig. 5.15a the original spectrum is compared to the ones retrieved with I-BEAT. The required signal to noise ratio, that is given by the particle number at the detector, sets a limit to the distance (to the source), where the I-BEAT detector can be placed. Assuming an opening aperture for the detector with an radius of 3 mm seems feasible and is supported by the measured data. It covers an area of about $A = 30\,\mathrm{mm}^2$. The measured spectrum provides more than 10^8 protons per msr (all energies summed up). In the case of 10^9 protons we have to cover a solid angle $\Sigma = 10$ msr. With $\Omega = A/d^2$ and d being the distance between target and the detector yields $d = 50$ mm. I-BEAT can thus function as the typical RCF stack,

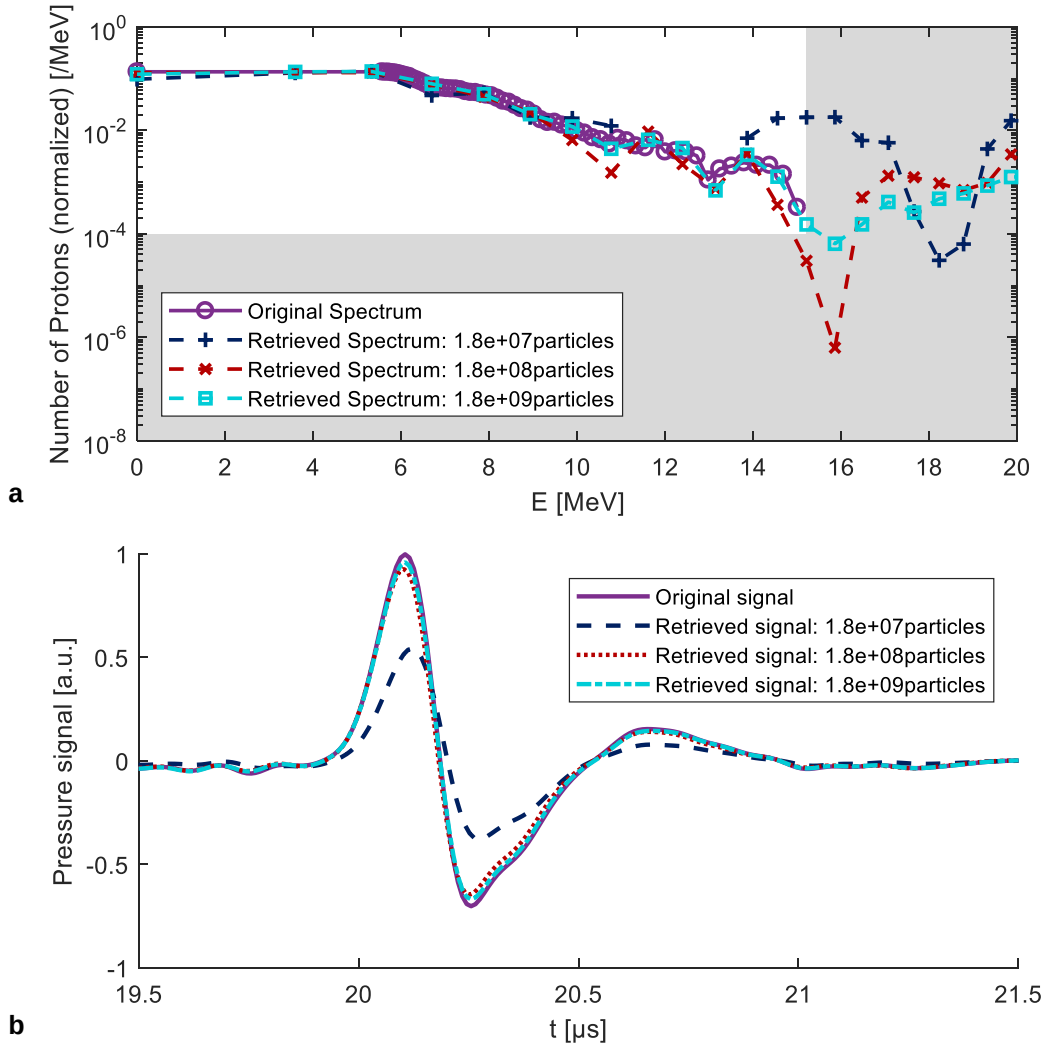

Figure 5.15 | I-BEAT in a TNSA regime. This figure shows the response of I-BEAT when it is utilized in a typical TNSA spectrum. An example spectrum has been measured at [56]. A typical TNSA spectrum is measured in Protons/ (MeV sr) . The different retrieved spectrum are simulated with a varying particle number at the detector and thus a changing SNR. This would experimentally mean a changing detector-target distance. The gray part of **a** marks the area where the SNR is poor and thus artifacts are generated in the signal. **b** shows the simulated pressure signal that would be detected with I-BEAT. The figure is adapted from [191].

without transverse resolution, that is positioned close to target offering an online evaluation of the proton spectrum.

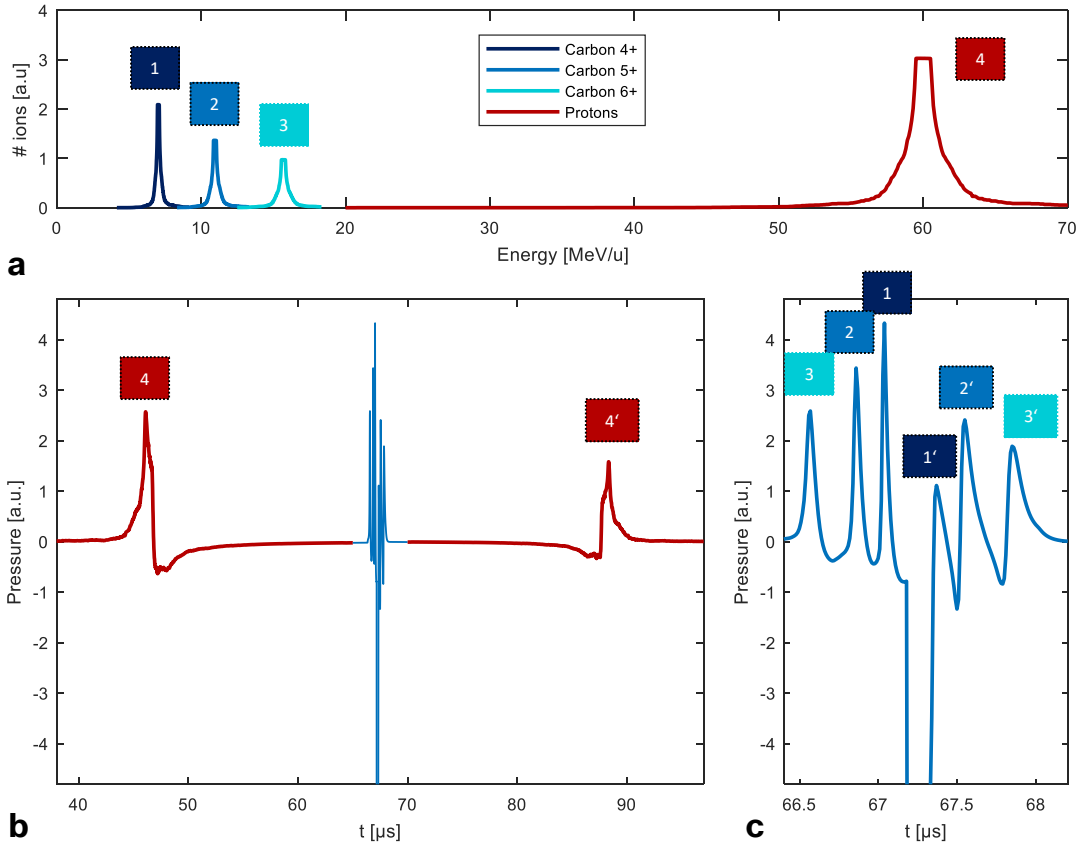

Figure 5.16 | A multi-species spectrum with I-BEAT. This figure points out how I-BEAT could be utilized to measure a multi species spectrum. Especially with the use of energy selective optics such as QPs that are set for 60 MeV protons a spectrum as depicted in **a** would be generated. The acoustic trace of such spectrum has been simulated in **b** and zoomed in the central part in **c**. The main contributions of each species to the spectrum can be seperated and thus evaluated independently. Therefore, a multi species spectrum can be evaluated when the energies and penetration depth can be separated. The figure is adapted from [191].

Measurement of Multi-Species Spectrum

Laser-driven plasmas accelerate not only protons but also other ion species depending on the target material. Especially carbons at different charge states are also emitted from the contamination layer of any target surface. Since the range in the water tank is dependent on the mass (not so much on the initial charge state) and the kinetic energy, I-BEAT is able to assign a certain energy to a certain charge and mass in combination with an energy selective focusing device (such as magnetic quadrupoles) and can thus, at least for certain configurations also reconstruct the

energy distribution of different ion masses and charges in a single-shot. An example calculation is presented in the Fig. 5.16. We assume flat spectra of carbon ions with charge states 4, 5 and 6, as well as protons. The PMQ focus all ions with the same synchrotron radius to the same point. The radius can be calculated (see [72] for detailed derivation) using the Lorentz force (see Eq. (2.24)) in a purely magnetic field equated with the centripetal force and is:

$$r_\mathrm{s} = \frac{m_\mathrm{i} v_\mathrm{i}}{q_\mathrm{i} B}. \tag{5.7}$$

Ion species with the same r_s that we used for the simulation are depicted in Fig. 5.16a. A simulation of the signal when such a multi-species ion bunch is measured with I-BEAT, is performed and the expected acoustic signal is shown in Fig. 5.16b and c. One can distinguish the contributions of the different ions to the acoustic wave form and hence measurement of this waveform will allow for reconstructing the numbers of ions in a given charge state and energy band. Of course, the information of the complete ion spectra emitted from the target remain inaccessible (as the PMQ selectively focus ions with the q/m dependence). I-BEAT can hence not replace the currently and valuable techniques of characterizing the composition of the ion-spray emitted from the target, such as provided by Thomson parabola spectrometers. But it will be an additional and complementary option to measure ion energies, that will give an experimentalist a new, very powerful, tool for future research at the application site of high flux ion bunches.

5.6 Discussion and Outlook

We demonstrated I-BEAT for determining the absolute kinetic energy distribution of single focused ultrashort proton bunches impinging into water using a single transducer. The retrieved particle number at the experiment in LEX Photonics could not be verified unambiguously. However, the depth-dose profile at the DRACO agreed with the comparative measurement of a RCF stack. This is the most important measure, since it is the direct accessible quantity. The therefrom reconstructed spectrum could potentially still have a systematic error induced by the calibration and therefore overestimate the proton number. A more detailed calibration, including the spatial impulse response, could further improve the detector's accuracy. The ultimate compelling measurement for the particle number would be a comparison with CR39. The high proton number though could likely saturate the CR39 detector and render such measurement complicated. In contrast to previous work [221], no averaging or scanning was required. The harsh conditions typically encountered near laser-plasmas (notably strong electromagnetic pulses [232, 233]) are key challenges in the design and evaluation of online electronic detectors. In I-BEAT, the relatively low speed of sound results in an inherent µs delay of the acoustic signal before readout. This allows ample time for the decay of prompt undesirable artifacts of the intense laser-plasma interaction, rendering I-BEAT measurements unaffected. While short, intense ion bunches typically saturate detectors (or even cause radiation damage), I-BEAT, using water as a medium, is nearly indestructible and offers a high dynamic range starting from 10^7 protons per mm^2 (Fig. 5.9). Particle numbers beyond 10^{10} per bunch are foreseen as realistic. Due to the temperature dependence of the Grüneisen coefficient (see Eq. (2.48)), a temperate control of the water could further increase the accuracy. Further key advantages of I-BEAT include compactness, robustness, simplicity of operation and low cost. With its demonstrated merits, especially in certain situations (e.g. focused beams), we see I-BEAT as a complement and promising addition to the pool of ion diagnostics for research and application at existing and upcoming high repetition rate laser-driven proton sources.

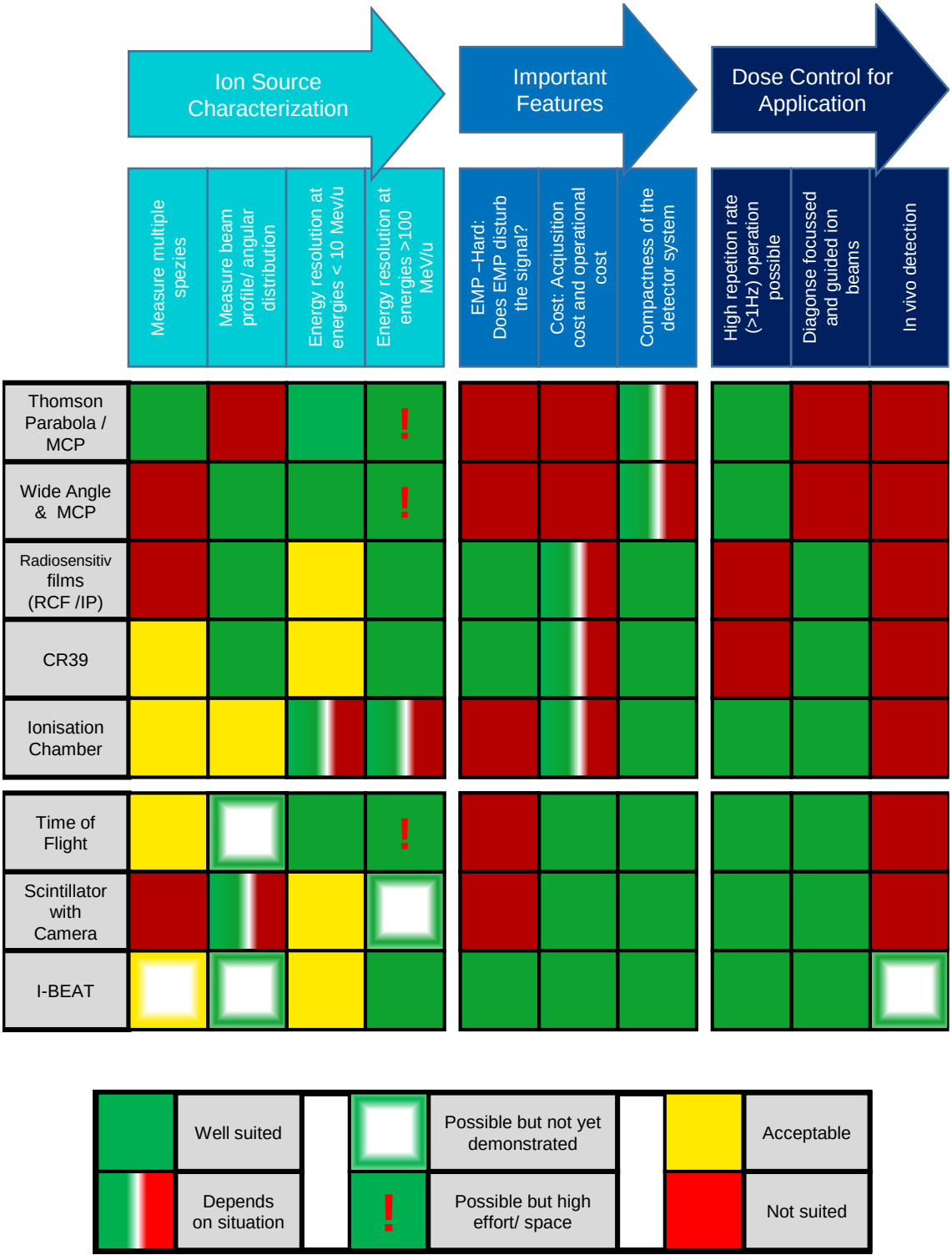

Figure 5.17 | The detector of I-BEAT. Comparison between different energy detectors. This table shows different techniques that have been used in laser ion acceleration in the past years. It compares the performance of Thompson Parabola [201, 202], a WASP [108, 199, 204], RCF [197], CR39 [234], Ionization Chamber [192–194], Time of Flight detectors [206, 207, 235] and Scintillators [208–210] to I-BEAT regarding different criteria.

In Fig. 5.17 the performance of different detectors that are used in laser-ion-acceleration is compared. They are judged at different aspects. Note, that this figure is not the ultimate truth since a clever design can often overcome some of the limitations. While the figure shows, that established and widely used diagnostics such as WASP, Thomson parabola or RCF are great to analyze the ion bunch, many diagnostics struggle to meet the requirements of currently advancing laser-ion-acceleration systems regarding the high repetition rate, focused and very intense beam with high flux and high energies where newly developed diagnostics such as I-BEAT reveal their strength.

Currently I-BEAT allows the reconstruction of the absolute depth-dose distribution at application sites, in particular downstream of energy selective transport and focusing optics. Furthermore the reconstruction of a broad proton spectrum, typically generated in TNSA-based acceleration schemes has been simulated (Fig. 5.15). In combination with magnetic energy selection optics (including quadrupoles or solenoids) the detailed diagnosis of more complicated particle bunches consisting of mixed species (for example protons and carbons), can be incorporated in the reconstruction algorithm (Fig. 5.16). The energy range in which I-BEAT operates can be adapted by proper choice of medium and size to accommodate the complete Bragg curve (starting from several MeV as presented in Fig. 5.9 up to several 100 of MeV protons [213]). The clear strength of I-BEAT is its potential for even higher repetition rate systems. The duration of the I-BEAT signal remains shorter than twice the range of ions divided by the speed of sound, for 100 MeV protons with a penetration depth of 77 mm in water, this is about 100 µs. The I-BEAT detector could thus be advanced to an operation with repetition rates up to 10 kHz. In I-BEAT the spatial resolution is directly connected with the temporal resolution, which in turn depends on the frequency window, in which the transducer is sensitive. An advancement of the detectors by for example using optical detectors [236] could further increase the spatial resolution. The ion induced pressure wave alters the refractive index of water and thus renders it sensitive to optical measurements. By employing more transducers in additional directions (see Fig. 5.18) tomographic reconstruction of the 3-D dose distribution seems feasible [221].

Detector calibration will become even more important with the development of more complex detector configuration. Since using the Tandem accelerator was elaborate, we aim to use laser-generated plasma for the determination of the transfer function. The plasma is hereby generated, when the laser intensities reaches the

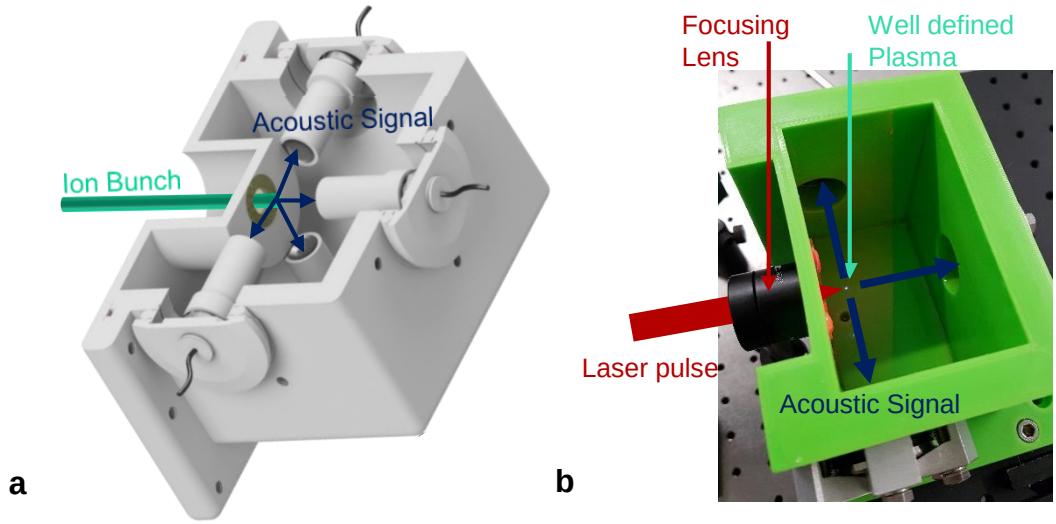

Figure 5.18 | I-BEAT 3-D. One of the next steps is the measurement of the heating function in three dimensions. Therefore different prototypes have been designed using more than one transducer. The design for a vacuum compatible cell using four transducers is depicted in **a**. The calibration of such systems are very important and could in future be implemented using a very small plasma as a heat source. In **b** a short laser pulse generated with the ZEUS laser system is focused in water, generating a short and small plasma that can be measured. Therefore, the detector could be calibrated for each point by positioning the plasma accordingly.

ionization threshold of water. The size and position of the plasma can thus be easily adjusted by the size, intensity and position of the laser focus and thus function as a point source. By scanning the laser focus in the water one can in principle generate a full 3-D response map of the spatial and spectral impulse response of the detector system. As a first test I-BEAT was implemented at the ZEUS[4] laser (see Figure 5.18b). In this work, we demonstrated the applicability of I-BEAT in air, but we recently demonstrated an operation of I-BEAT in vacuum at the PHELIX laser system in Darmstadt, where a 3-D version of I-BEAT, but also compact one dimensional detectors were used (see Figure 5.19). In another recent experiment in collaboration with Brendon Dromey (based an earlier studies such as [19]) the effect of ion interactions on the radiolytic yield of the solvated electron in water was studied. The proton bunch was sent into a water phantom very close to the ion source to preserve the high particle number. Since most detection methods rely on absorption of the proton energy in the detector itself, an evaluation of the proton energy, when used for application, is not directly possible. As the protons

[4]The ZEUS laser is a small version of the ATLAS-300 with up to 500 mJ in the pulse. It is located in one of the smaller laboratories in CALA (see Fig. A.12).

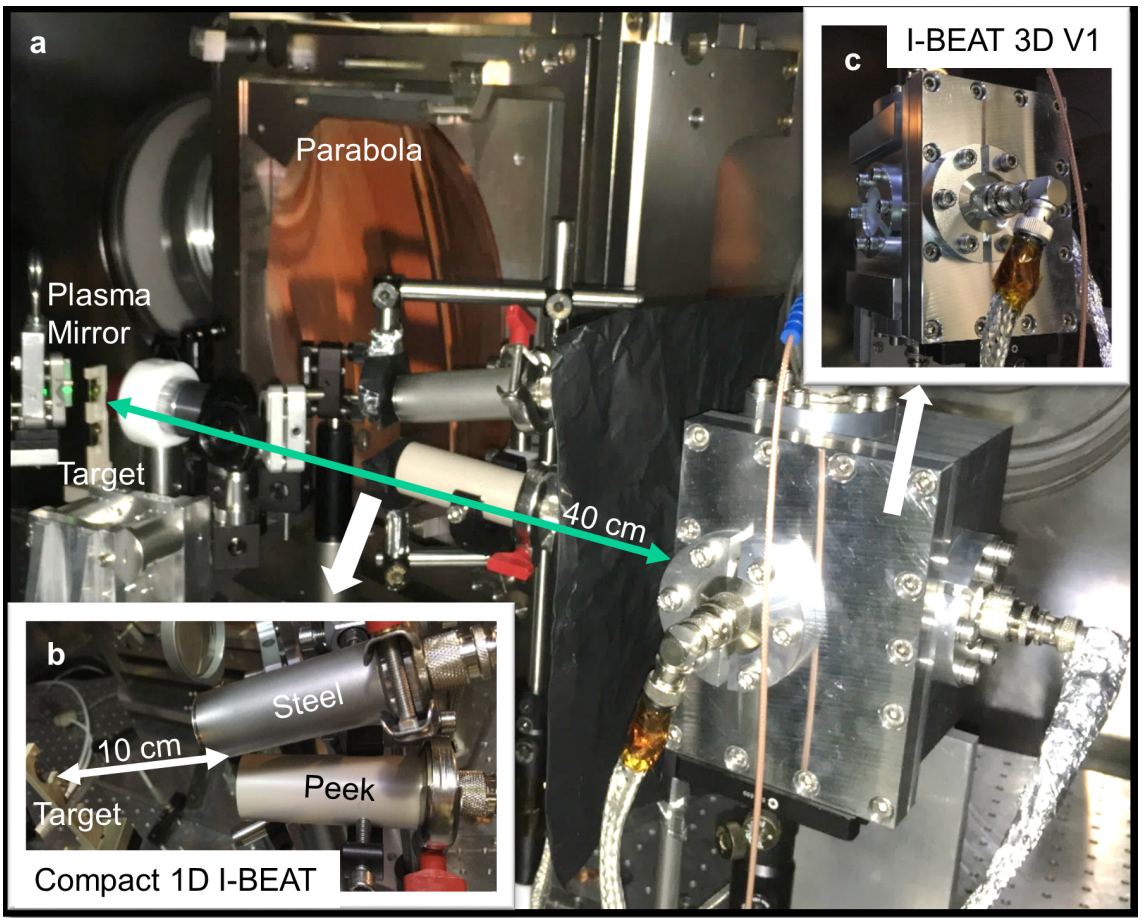

Figure 5.19 | I-BEAT at PHELIX. This picture shows recent implementation of I-BEAT at the PHELIX laser in Darmstadt. **b**, Shows two compact one dimensional detectors, positioned 10 cm behind the target with a 500 µm thick entrance window (steel and peek). The thickness of the entrance window was to prevent its breaking by any means. **c**, Shows the I-BEAT3D V1, about 40 cm away from the target and equipped with 4 transducers.

were anyway stopped within the water phantom, the uniqueness of I-BEAT allowed a monitoring of the proton spectrum without altering the application. This could in particular be attractive, when using protons for irradiation and dose control is required.

The time to begin writing an article is when you have finished it to your satisfaction. By that time you begin to clearly and logically perceive what it is that you really want to say.

Mark Twain, Notebook, 1902-1903

Chapter 6

Summary and Outlook

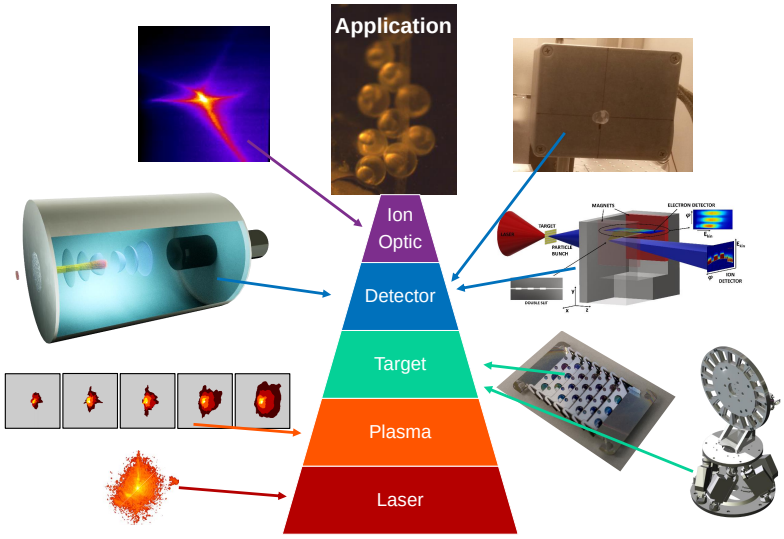

Scientific outcome of LEX Photonics (see Fig. 6.1).

Contents

6.1 Summary: LEX Photonics 116
6.2 Outlook: CALA 117
6.3 Epilogue: I-TRIC 120

6.1 Summary: LEX Photonics

The experimental campaigns at LEX Photonics with the two highlights TRIC and I-BEAT have been presented in this work. The motivation was to advance laser-based ion acceleration towards a viable laser-ion source. The development of tailored online diagnostics, with respect to the emerging need for online evaluation and high repetition rates, was a particular goal. In TRIC we used a multi frame single-shot probing technique to measure the plasma evolution with sub-ps temporal resolution. The combination of several shots allowed the retrieval of the spatio-temporal intensity distribution of the laser focus. The presented probing technique is not only limited to TRIC, but further allows to add a temporal dimension to other probing or imaging techniques. I-BEAT is a measurement technique to analyze the depth-dose distribution and ion energy spectrum of short and intense ion bunches. The herein presented results can be seen as the first demonstration of its potential.

The accomplishments in LEX Photonics are not limited to I-BEAT and TRIC but cover all pillars of ILDIAS. In Fig. 6.1 the achievements of the experimental campaigns in LEX Photonics are summarized. Figure 6.1 illustrates the importance of developments in all five pillars of ILDIAS for a successful application of laser-driven ions. The spatial laser intensity distribution has been analyzed [150]. TRIC can be used to measure the plasma evolution within a single-shot at full power and thus reveal more temporally resolved information about the plasma [161]. The target wheel has been successfully tested, and an operation with 0.5 Hz has been demonstrated [59]. The use of the integrated foil-based plasma mirror significantly increased the ion energies [43]. Using a WASP as simultaneous online diagnostic for ions and electrons has been demonstrated [204]. I-BEAT as a novel technique for measuring the ion-bunch has demonstrated its capabilities and is expected to become a core diagnostic for future experiments with intense ion bunches at high repetition rates, in particular for bio-medical applications [191]. The TOF diagnostic could also due to its simple usage become a more relevant scheme of future diagnostics [207]. The implementation of the quadrupoles further has enabled us to focus the ion bunch to an application site, providing a ns-short and intense ion bunch on an area of about 1 mm^2 . With the irradiation of the zebra-fish embryos and thus the first vertebrate organism, that has been investigated with laser-accelerated ions, we demonstrated its usability for a first bio-medical application[1]. A total number of 8000 shots, including one beam time with over 1000 shots within several hours,

[1]Publication is currently in preparation by Thomas Rösch.

is a milestone achievement. It is therefore fair to state LEX Photonics has served its purpose as a prototype facility for CALA. Weak spots (see *"lessons learned"* Section 3.3.1) have been identified and various key components (such as the target wheel, WASP, PMQ) have been tested and optimized and are now implemented in CALA.

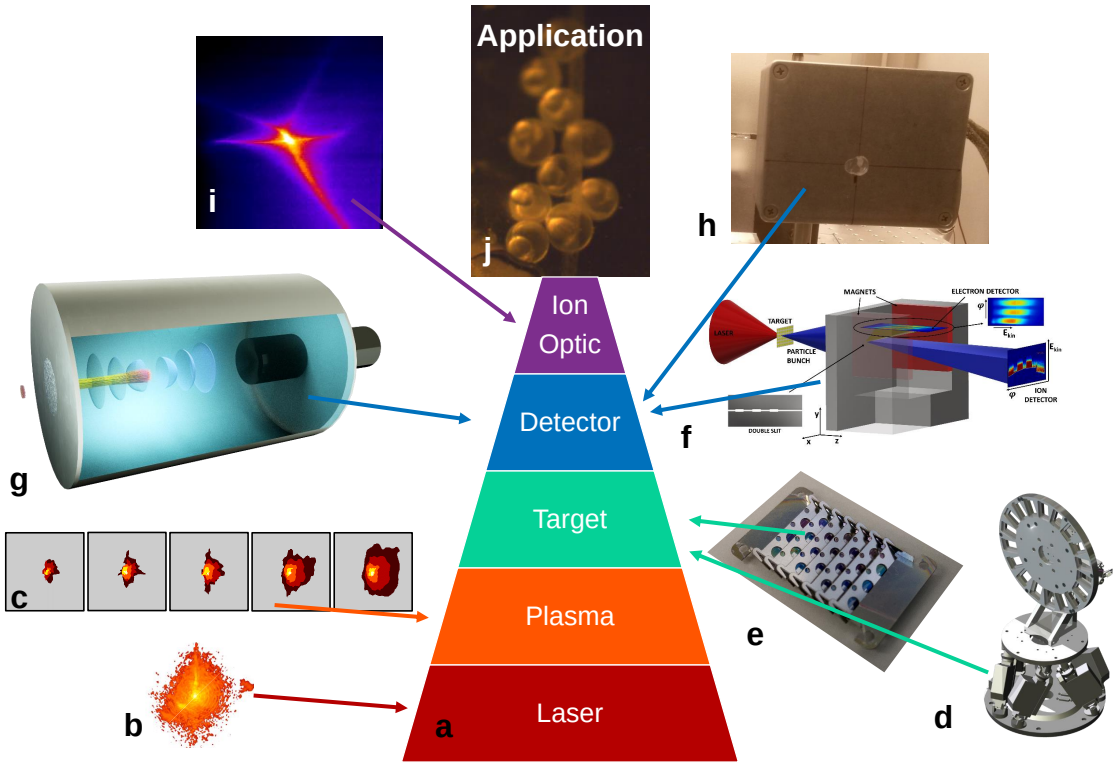

Figure 6.1 | Successful experimental campaigns at LEX Photonics. The experimental campaign at LEX Photonics is summarized showing the variety of results. Each pillar of ILDIAS (**a**) has been addressed and various topics have been published or submitted. The spatial laser contrast (**b**), TRIC (**c**), target wheel (**d**), integrated plasma mirror (**e**), WASP (**f**), I-BEAT (**g**), TOF (**h**), PMQ (**i**) and the irradiation of the Zebrafish embryos (**j**).

6.2 Outlook: CALA

Since the completion of the building for CALA in September 2016, the installations have begun. The experiences and *"lessons learned"* from the experimental campaigns in LEX Photonics were thoroughly examined and various modifications have been carried out to overcome previous limitations. In Fig. 6.2 the thirteen *"lessons learned"* and their respective solutions are summarized.

	Name	Modification at CALA
1	REGEN prepulse	A new REGEN in a ring configuration prevents the generation of direct prepulses and thus prepulses are significantly reduced
2	Back-reflection	The configuration in CALA enables an operation under non-zero degree such that the back-reflected light is suppressed significantly.
3	Pockels cell	A new large Pockels cell is prepared for the ATLAS-3000
4	Laser beam delivery	A 3 cm, 1 W cw diode is installed to align through the beamline and each mirror is equiped with reference switches
5	Incoming laser light	The leakage through Turning Mirror 1 (TM1) is taken to analyze it
6	Back-scattered light	The back reflected light is also analyzed via TM1, which has a leakage of about 1% for fundamental wavelength
7	Spatial Intensity	An adaptive optic including analyzis of near field and wavefront is installed
8	Debris	Since there is no solution yet, copper parabolas are used that are less expensive and can more easily be reworked
9	Plasma mirror	The foil based plasma mirror worked but was challenging to align. A novel foil based plasma mirror is currently developed by M. Speicher.
10	WASP calibration	The development of a Pablone would allow an intrinsic calibration of the WASP
11	Shielding QP	No solution yet
12	Orientation QP	The angle of the QP is now motorized and can be adjusted during operation
13	Data monitoring	New motorized and detection tools are built in order to be operable with a Tango system

Figure 6.2 | Lessons learned for CALA. This figure shows the lessens learned of Chapter 3 and the modifications that have been carried out to solve the problem for CALA. Solved issues are marked with green while red and orange indicate that no real solution has been found yet.

Even though the majority of the known issues had been solved, there are still open issues that need to be addressed. Increased challenges connected to EMP, debris or the destruction of neighboring targets due to higher laser energy and intensity, will be among the biggest issues. Another challenge is the intensity of the transmitted laser light (*lesson 11*) that is often discarded as negligible. But with thin foils, due to induced transparency, or simply because isolated micro-targets are used, dumping the non-converted laser energy becomes important (as in the case of laser-wakefield acceleration). The intensity will be about $10^{14}\mathrm{W\,cm^{-2}}$ at a distance of one sixth of the focal length of the OAP (behind TCC). This becomes in particular relevant for long focal length parabolas. The laser intensity (without attenuation) would be high enough to ionize matter up to 30 cm distance to TCC, when using the 1.50 m focal length OAP. This would lead to destruction and more debris in the chamber.

In June 2019 CALA has started its operation with reduced laser energy, which will now be steadily increased. A first successful acceleration of about 15 MeV protons emerging from 50 nm thick Formvar targets with roughly 4 J on target have been reported[2] on August 1st, 2019. A picture of the prepared experimental chamber of LION is shown in Fig. 6.3. More details about CALA and some relevant key components therein can be found in Section A.2.

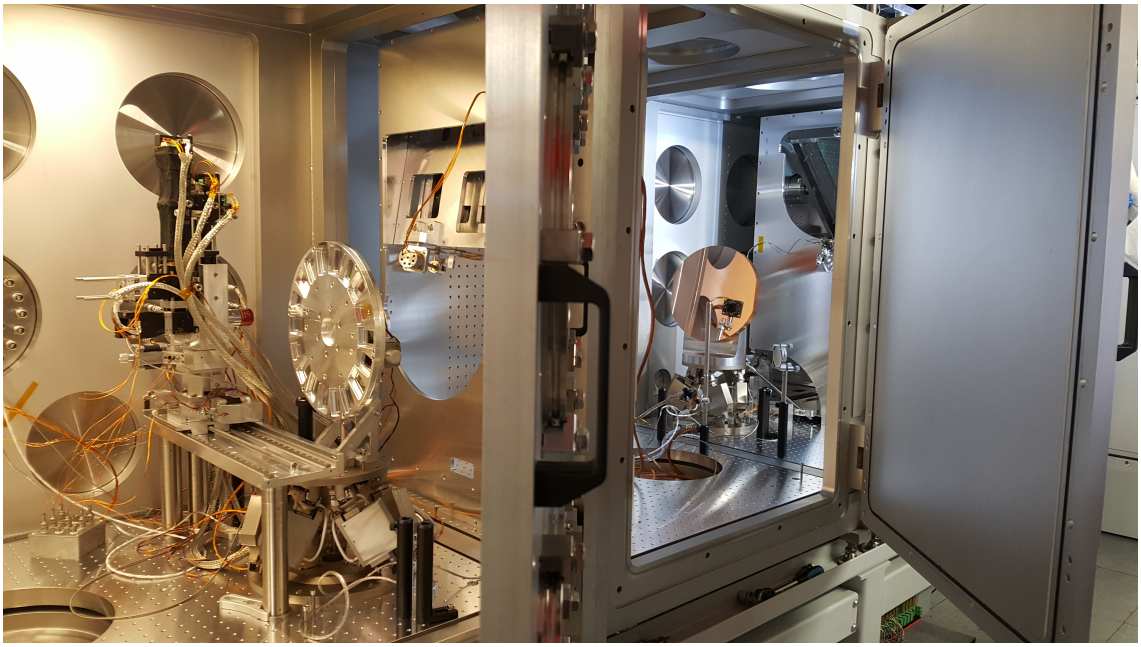

Figure 6.3 | Picture of the LION chamber. This picture shows the experimental chamber of LION. A more detailed description of the setup can be found in Section A.2.

Considering the improvements and the upgrade of the laser system, CALA is well poised for laser-driven ion acceleration in the next years. It is worth considering some immediate ideas and follow up tasks that can arise over the next years.

1. With the increased laser energy and meliorated contrast of the laser, proton energies of about 30-40 MeV should be achievable on a regular basis. Such ion energies will enable applications such as proton imaging and irradiation of more complex three dimensional biological models.

2. A second set of QPs allows for using the first set for collimation and the second set for refocusing (shorter focal length), thus generating higher peak dose rates in even smaller ion foci. Assuming that the focus of the PMQ would have a radius of 5 µm at 10 MeV with 1 % energy spread and a proton spectrum

[2]Private communication with Jens Hartmann.

of $10^8/(1\%\mathrm{E}\cdot\mathrm{msr})$, we could get about (assuming an acceptance of 10 msr) $1\cdot10^9$ protons within 78 µm^2 and thus about 10^{15} protons cm^2.

3. Besides the divergence, the energy spread of the ion bunch leads to increasing temporal dispersion with increasing distance from the source. A temporal re-compression of the ion bunch, typically referred to as re-bunching, could further increase the ion peak flux at application site.

4. The detector of I-BEAT is planned to be advanced to measure the 3D heating map and thus enable reconstructing the 3D spatio-energy distribution of the ion bunch.

5. With respect to advancing the target (ion source), it is planned to implement the Paul trap [237] into LION. Isolated micro-plasmas have shown great potential for laser-driven ion acceleration [54]. The temporal resolved probing technique could be used to study this interaction and acceleration process.

6. With improved contrast condition, the use of newly developed foil based plasma mirrors, higher laser intensities, and target optimizations, one long-term goals is to demonstrate an acceleration of ions beyond 100 MeV per nucleon.

6.3 Epilogue: I-TRIC

A good story sometimes connects different story-lines in the last chapter. Analogously would be a combination of I-BEAT and TRIC. We have already mentioned in Chapter 5 that an optical measurement of I-BEAT could potentially increase its spatial resolution. Implementing the multi frame probing technique, as used for TRIC, would add an ultra-fast temporal resolution to the measurement. This combination of both methods can be considered as a TOF method featuring the combination of a spatial resolution of few µm with temporal resolution below one ps. It could further become relevant for measuring the bunch duration of sub-ns ion bunches.

Appendix A

Experimental Setups in LEX Photonics and CALA

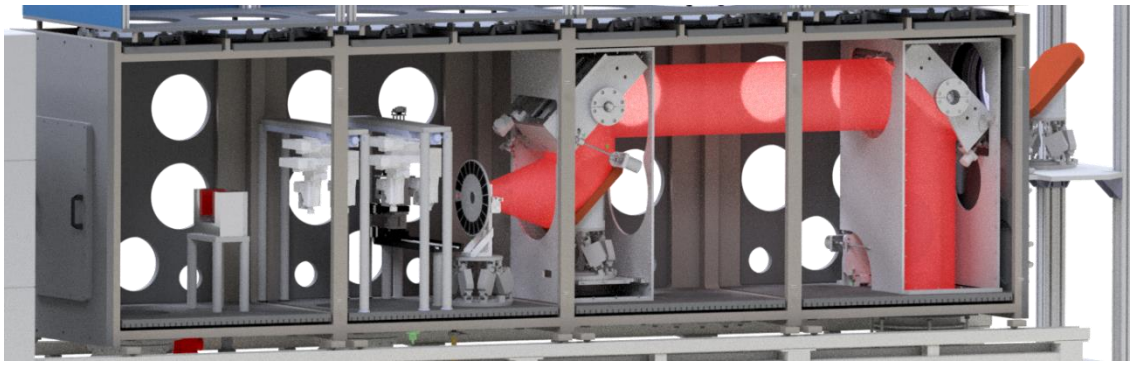

Setup of the LION chamber, explained in detail in Fig. A.17.

Contents

A.1 Laboratory for Extreme Photonics - Closer Look 122

A.2 Centre for Advanced Laser Applications 139

This chapter in particular describes the experimental setup in LEX Photonics and CALA in more detail.

Author contribution: *During the planning stage of CALA and the development of different concepts several parts were under the authors responsibility. The installation of the components has been carried out together with the technical staff of CALA and researchers associated with CALA under the supervision of Jens Hartmann.*

A.1 Laboratory for Extreme Photonics - Closer Look

A.1.1 Components of High Power Laser Systems

In Fig. 3.1 we have seen the setup of the ATLAS-300. Even though such high power lasers are very complex they are typically based on several components, whose purpose is quickly summarized:

1. **Oscillator:** Generation of short laser pulses with low energy and high repetition rate.
2. **Stretcher and compressor:** Basic ingredients for a CPA system to stretch and later compress the pulse in time.
3. **Multi-pass amplifiers:** A pumped crystal that is passed several times to amplify the laser pulse
4. **REGEN:** The **Regen**erative amplifier is a cavity based amplifier with multiple round trips. It has been identified to cause some prepulses and is thus treated in more detail
5. **Optical elements such as Pockels cells:** Pockel cells are a temporal switch that can select certain pulses and thus modify the repetition rate or just open shortly before the laser pulse and thus being able to block prepulses
6. **Dazzler:** The Dazzler can optimize the shape of the chirp of the laser pulse. Note that it typically absorbs a large amount of energy by doing so.
7. **Mazzler:** The Mazzler shapes the spectral profile of the laser pulse. A flat top like spectrum is important for short pulses. Transmission and amplification in the laser chain can degrade the spectral shape and therefore requires (pre-) compensation.
8. **Spatial filters:** Spatial filters are built by positioning a small pinhole in the focal plane of the laser pulse. In the Fourier plane, the higher spatial frequencies are further out and are blocked by a pinhole. After the recollimation, incident distinct sharp features in the beam profile are therefore smoothed out. Due tu to the increasing intensity when focusing the pulse, the spatial filter has to be operated in vacuum.

A.1.2 Optimization of the Laser Contrast

The laser contrast has been one of the greatest challenges for laser-driven ion acceleration. The laser contrast is typically measured with third order auto-correlators [148, 149] (see Section B.4.1). In LEX Photonics we observed that the temporal laser contrast has limited the acceleration of ions. In this section we outline different optimization stages of the laser contrast in LEX Photonics. A typical trace of the

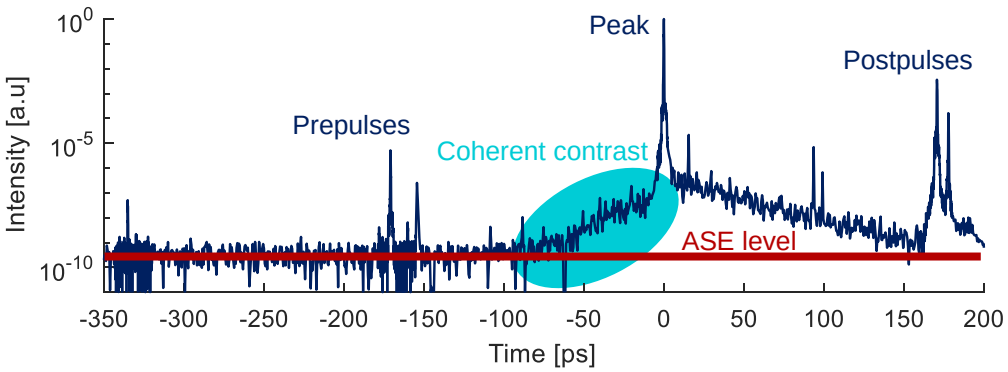

Figure A.1 | Laser contrast. This figure shows a typical laser contrast curve, recorded with an autocorrelator (see Section B.4.1). It shows the different segments of the temporal laser contrast. The level of ASE, the coherent contrast and the prepulses.

laser contrast is shaped by different processes and can be seen in Fig. A.1. Those are **A**mplified **S**pontaneous **E**mission, short prepulses and the so called coherent contrast.

1. **ASE**: Is created by spontaneous emission in any of the laser amplification media (e.g. Ti:sapphire crystals) that is further amplified in the laser chain. Its duration or influence can be minimized by pumping the crystals as short as possible prior to the laser pulse. It can be further suppressed by using an **O**ptical **P**arametric **A**mplification (OPA) [238] or **O**ptical **P**arametric **C**hirped **P**ulse **A**mplification (OPCPA) systems [239, 240], or implementing a cross (**X**) **P**olarized **W**ave generation (XPW) [241] or Pockels cells with fast raise times.

2. **Short prepulses:** Short prepulses are replicas of the main pulse. There are two possibilities how they can be created. The most common source is internal double reflection in transmissive optics. The resulting postpulse can further create a temporally mirrored prepulse in the CPA laser systems due to interference of main an prepulse in the stretched configuration and nonlinearities

in the material the laser passes. This effect is theoretically described by Didenko et al. [242] and is experimentally demonstrated in Fig. A.2. Secondly direct prepulses can be created in the cavity of the REGEN. In particular the surfaces of the Pockels cell, that are close to the cavity end-mirrors, can cause prepulses.

3. **Coherent contrast:** Coherent contrast is typically associated with the raising part of the laser pulse that starts a few tens of picoseconds prior to the peak of the laser pulse [243].

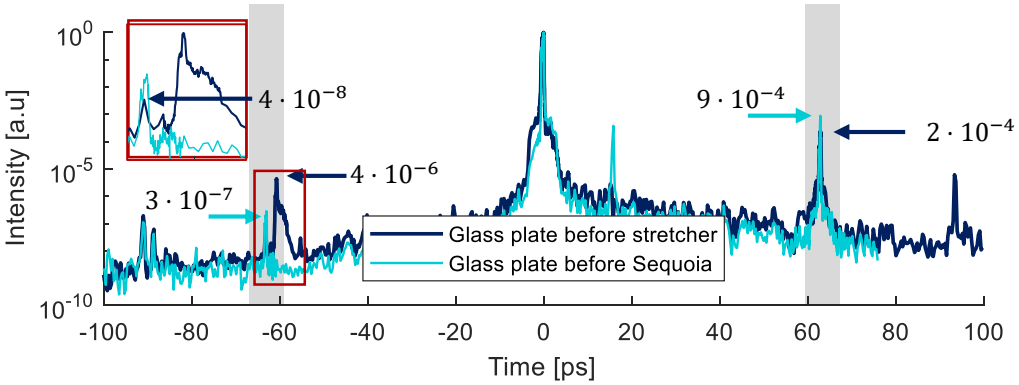

Figure A.2 | Generation of prepulses by postpulses. This graph shows that during CPA a postpulse can be transformed to a prepulse [242]. The contrast was measured once with a glass plate just before the measurement creating a postpulse. The measured prepulse is an artifact of the measurement (see Section B.4.1) and quadratically lower than the postpulse. In the second situation the glass plate was installed shortly after the oscillator and thus before the CPA stage and the amplification of the laser pulse. The measurement reveals the additional postpulse that has been broadened and slightly shifted in time. The postpulse is smaller since part of its energy is transformed to the prepulse and the artificial prepulse is still visible. However, the hereby created postpulse is smaller than the prepulse.

Identifying Contrast Limitations

The evaluation of the experimental data, especially the fraction of light transmitted through the target [244] and measured proton energies as a function of target thickness, are an indicator for the target density during interaction and thus also the laser contrast. Our experiments showed that we were not able to accelerate ions from foils thinner than about 100 nm and further the ion energies did not exceed 5 MeV at this stage. Since the measurement of the temporal contrast revealed some prepulses

while the ASE level seemed small, the effect of prepulses was studied in more detail. Zhou studied how short prepulses affect the target conditions, in particular the target density, during the arrival of the laser peak [245]. The target thickness and the arrival time of the prepulse were considered and simulations supported our experimental findings.

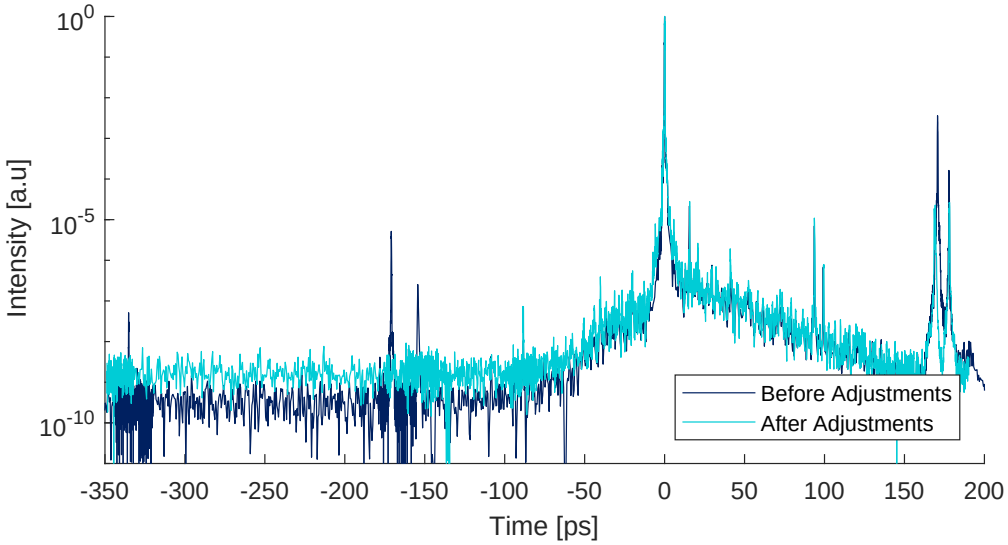

Figure A.3 | Optimization of the REGEN. This graph shows the optimization of the REGEN performed in January 2016. The exchange of the Pockels cells, in particular the extraction, suppressed the postpulses and consequently the prepulses at 150 and 170 ps.

After removing or at least suppressing prepulses around 170 ps prior to the main pulse (by exchanging Pockels cells in the REGEN) the contrast curve was improved (Fig. A.3). But to our disappointment the achieved proton energies and particle yield did not improve significantly. The implementation of a double plasma mirror, using an integrated plasma-mirror-target, resulted in proton energies of about 12 MeV corresponding to a doubling of the proton energy [43]. This observation proved that it was still the temporal contrast that limited the optimization of ion acceleration. One relevant cause for the limiting contrast was revealed when the contrast was measured with another third-order-auto-correlator (Tundra) capable of measuring up to two ns prior to the main pulse. Two significant prepulses (at $\approx$ 500 ps and $\approx$ 660 ps) were revealed in the trace. As illustrated in Fig. A.4, they originated from reflections of the surfaces of the Pockels cell within the cavity of the REGEN and were thus direct prepulses and not created from former postpulses. This is significant since the prepulse is typically less intense than its corresponding postpulse

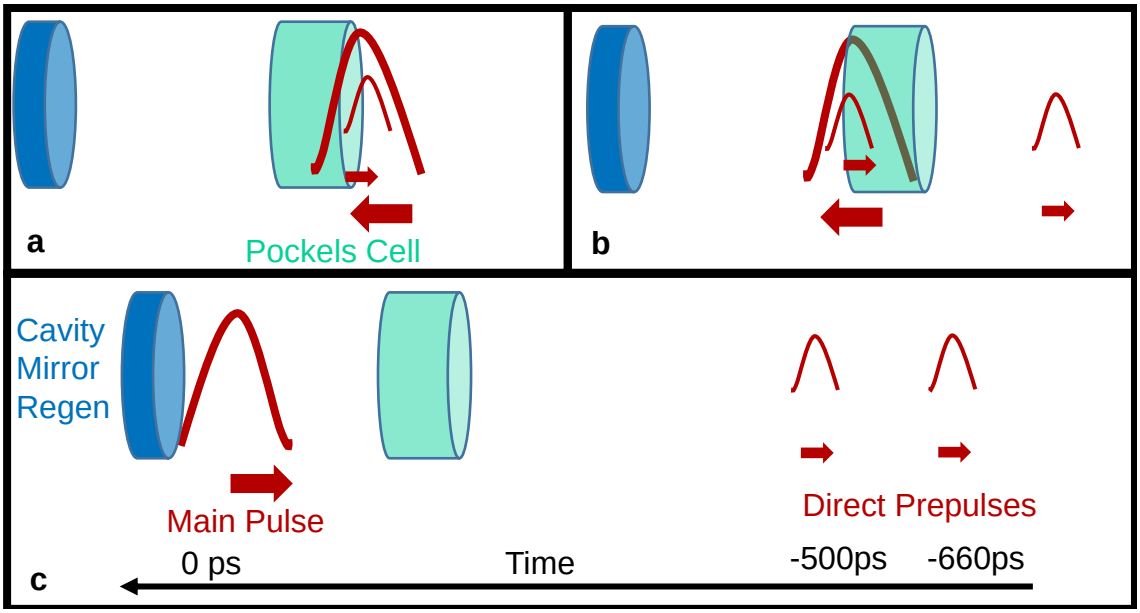

Figure A.4 | Generation of direct prepulses. The source of the 500 and 660 ps prepulses is illustrated. Reflections from the front surface (**a**) and the backside (**b**) of the cavity Pockels cells of the REGEN cause direct prepulses. The distance of those to the main pulse is dependent on the distance of the Pockels cell and the end cavity mirror.

(see Fig. A.2) and thus the direct prepulses have higher intensities. A small tilt of the Pockels cell lowered the intensity of the prepulses, but could also cause a reduced amplification and an increased ASE level of the REGEN. With this findings and modification the measured proton energies increased significantly (as can be seen in June and July 2016 Fig. 3.10). Nonetheless, it was no solution to the problem, since the prepulses were only attenuated and realignment and optimization of the REGEN impaired the contrast again.

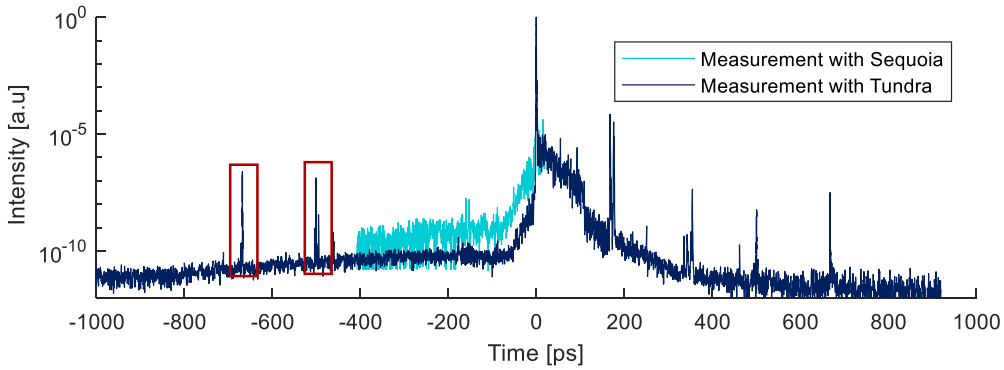

Figure A.5 | Discovery of more prepulses. Comparison of a short- (Sequoia) and long-range (Tundra) contrast measurement. Two significant prepulses at 500 and 660 ps prior to the main pulse have been identified. With the previously used short-range device they have not been detectable. In contrast to previous prepulses those are origin from direct reflections in the REGEN and not transformed from postpulses.

A.1.3 The Risk of Back-Reflection

During a laser plasma interaction the plasma can be highly reflective when the electron density is larger than the critical density Eq. (2.33). A reflection at the target under normal incidence will enter the same mode as the incoming laser light and thus travel all the way back to the oscillator. Considering the laser traversing the optical chain backwards, the energy will stay stable (only reduced by losses of each mirror) or even increase since the amplifying crystals can be still in an excited state. On top of this, the beam diameter decreases with every stage and so the increasing intensity is more likely to cause damage. There are typically two possible ways of dealing with this problem:

1. The first one requires optical elements in the laser chain that are capable of rotating the polarization and act as a switch for the back-reflected light. The most commonly used are Pockels cells (Section B.4.2) or Faraday rotators[1].

2. The second possibility is a rotation of the target surface with respect to the laser axis. This is commonly done because it is simple to implement and often even proves beneficial for optimizing TNSA.

During the commissioning phase of LEX Photonics we have implemented a simple monitor for the back-reflection. The leakage of a mirror just upstream of the Faraday

[1] A Faraday rotator turns the polarization of the laser dependent on the trajectory of the light pulse.

rotator (indicate in Fig. 3.1) that was placed under nearly zero degree was measured with a fast photo diode. The back-reflection was thus also visible on this diode. It was also positioned at a critical location because the Faraday rotator was already operated close to damage threshold. Already an increased intensity of a factor of 2 on the downstream way could thus have caused damage. Initial measurements revealed the necessity to shoot under an angle of incidence larger than 15 degree to avoid too strong back-reflection signals. The half-angle of the OAP in those measurements was about 14 degree[2].

Introduction of the Safety Pockels Cell

Since the planned experiments required an operation under normal incidence we introduced a large Pockels cell in the beam path between Propulse 1 and Propulse 2+3 where the laser-pulse has an energy of 500 mJ Fig. 3.1. The laser beam could take to a detour traversing the Pockels cell and its related polarizers. One periscope rotated the polarization by 90° prior to the Pockels cell, and the Pockels cell rotated the polarization back to its original orientation (when active). The decay time of the cell was sufficiently fast and the potential reflection from the target was securely blocked. We achieved a extinction ratio of about 1:100.

A.1.4 The Vacuum Microscope

The vacuum microscope was developed by Christian Kreuzer [107, 153] (Fig. 3.6b). The microscope as a very compact solution unites several advantages:

1. The simultaneous measurement of a low and a high magnification image, incorporated a good resolution for the focus diagnostic as well as a large field of view to locate the focus and overlap it with the target.

2. The compact setup with the cage system of Thorlabs was robust and prevented misalignments of the microscope itself.

3. An additional LED within the microscope enabled illumination of the target.

4. Only the x-axis of the microscope stage was used for positioning the microscope in the beam and park it in a secure position. TCC was defined by the microscope position and remained reproducible over several weeks.

[2]The focal length was 20 cm and the beam diameter 10 cm.

5. Its compactness and the fact that it is built in one piece renders it in particular suitable for experiments[3].

The microscope as it was used in LEX Photonics was the first and most simple version. Further upgrades will include an optional use of a white light interferometer [107, 246, 247] and the implementation of a wavefront sensor [248].

A.1.5 Transmitted Laser Light

A milky glass plate with a small 1 cm horizontal slit was installed in the laser-beam-path to analyze the transmitted laser-light through the plasma-target. A camera recorded the image of the glass plate at each shot as demonstrated in Fig. A.6a. Without a target the beam profile could be recorded and a misalignment of the beam, causing clips in the profile, could be discovered. The most important feature of measuring the transmitted light was the determination of the transmitted laser-energy, revealing information about the target density during interaction.

[3] Typically the laser is guided out of the vacuum chamber for focus analysis.

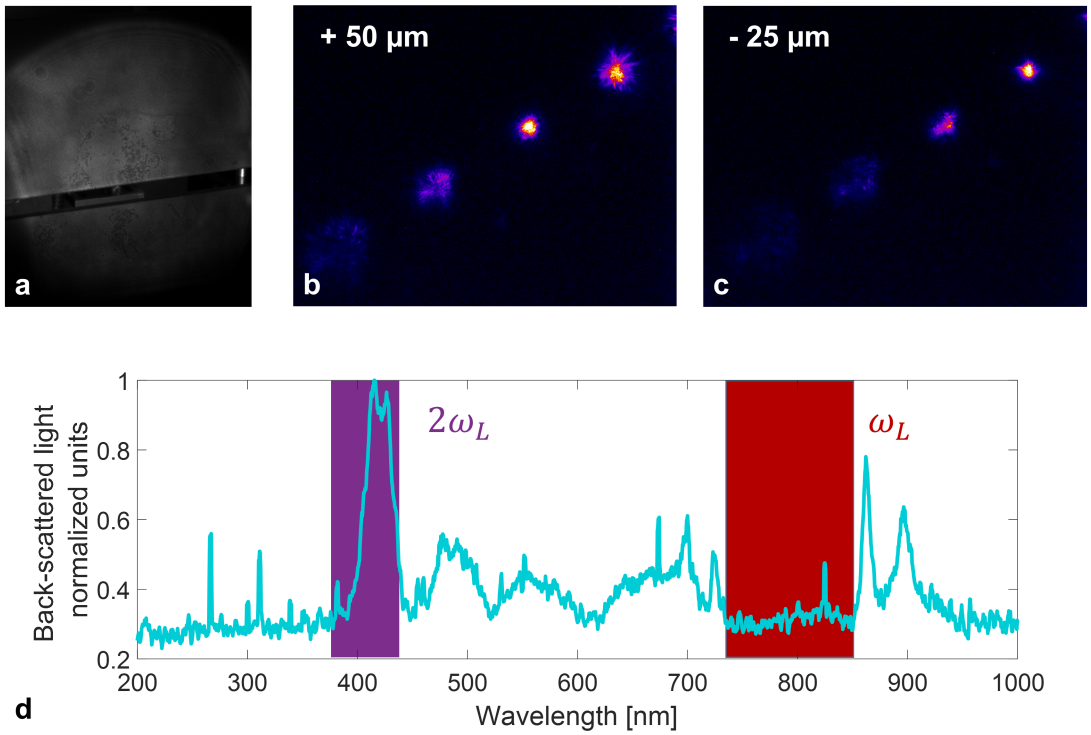

Figure A.6 | Plasma and light diagnostics. The transmitted light is measured on a milky glass plate in **a**. The back-scattered light is measured in a Fabry-Perot like setup. This enabled a clear distinction of the plasma position in TCC and 75 µm away (**b** and **c**). The back-scattered spectrum is shown in **d**. One can see that the majority of the light was in the second harmonic of the laser, while the fundamental wavelength is highly suppressed.

A.1.6 Back-Reflected / Back-Scattered Laser Light

We re-collimated the reflected (or back-scattered) laser-light with the focusing OAP and guided the beam out of the vacuum chamber, using the leakage through on dielectric mirror. Since the mirror was optimized to reflect 760-840 nm the fundamental laser wavelength is highly suppressed which was also visible in the spectrum, detected with an Ulbrichts-sphere. one very useful information is shown in Fig. A.6b and c. We imaged TCC onto a camera in a Fabry-Perot-like configuration. Two mirrors with the reflective surfaces facing each other and very close by with parallel orientation are put in the beam-path. The camera is in transmission of both mirrors detecting an attenuated signal. By tilting the mirror normal with respect to the propagation axis of the light, double reflections of both surfaces are transversally separated and further have an extended beam-path to the camera (see Hartmann [157]). Thereby several replicas were created, imaging different planes in the vicinity

of TCC. We were thus able to observe the longitudinal position with an accuracy of about 15 µm. This diagnostic served as a direct monitor, whether the target was hit at the right position and also revealed on first sight if things went completely wrong. Further we used the back-scatter arm for alignment and target control purposes. The target was imaged in order to control the position prior to an event. We also used this optical path for an alignment laser adjusting the position and direction of the laser-beam in an offline mode.

A.1.7 Targets for Laser-Driven Ion Acceleration

The target is one of the key parameters in laser-based ion acceleration. The material, the thickness, the density and also the geometry can alter the acceleration mechanism. It is further one of the most challenging issues to prepare targets at the same repetition rate as the laser is capable of, for example 1 Hz in the case of the ATLAS-300. In general there are two different approaches that take on the challenge of the repetition rate:

1. **Preparing the target in TCC.** The target is prepared directly at the position of the interaction. Different implementation of this approach have been tested. The use of mass-limited targets as in a Paul trap [237] or in cryogenic targets [60, 66, 249] has many advantages [20] but the repetition rate is still limited ($\ll$ 1 shot per minute). The use of liquid crystals seems very promising since the target thickness can be varied in the interesting range (several nm up to few 100 nm) [64]. Even though it has recently been improved the repetition rate is still about 1 shot per minute. Promising developments include hydrogen ribbon or jet targets. Thereby hydrogen jets are produced with high pressure forming a continuous target at TCC. The repetition rates of such systems are far beyond the Hz level. Drawbacks are the limited thickness (producing targets with thicknesses below one µm is challenging). Further the pressure in the vacuum environment of such experiments increases severely and has to be controlled.

2. **Offline production of the targets and fast positioning.** This approach describes a common production of targets that are mounted such that pre-produced targets can be positioned in focus without venting the chamber. The clear drawback is the limited amount of targets and the need for reloading. On the other hand this approach is flexible (any material and thickness, and

even more complicated target geometries or composites can be used). During the experimental campaign in LEX Photonics we used a target wheel accommodating up to 1683 targets. All target positions were scanned in advance so that during the experiment a repetition rate of 0.5 Hz was achieved [59].

Target Wheel

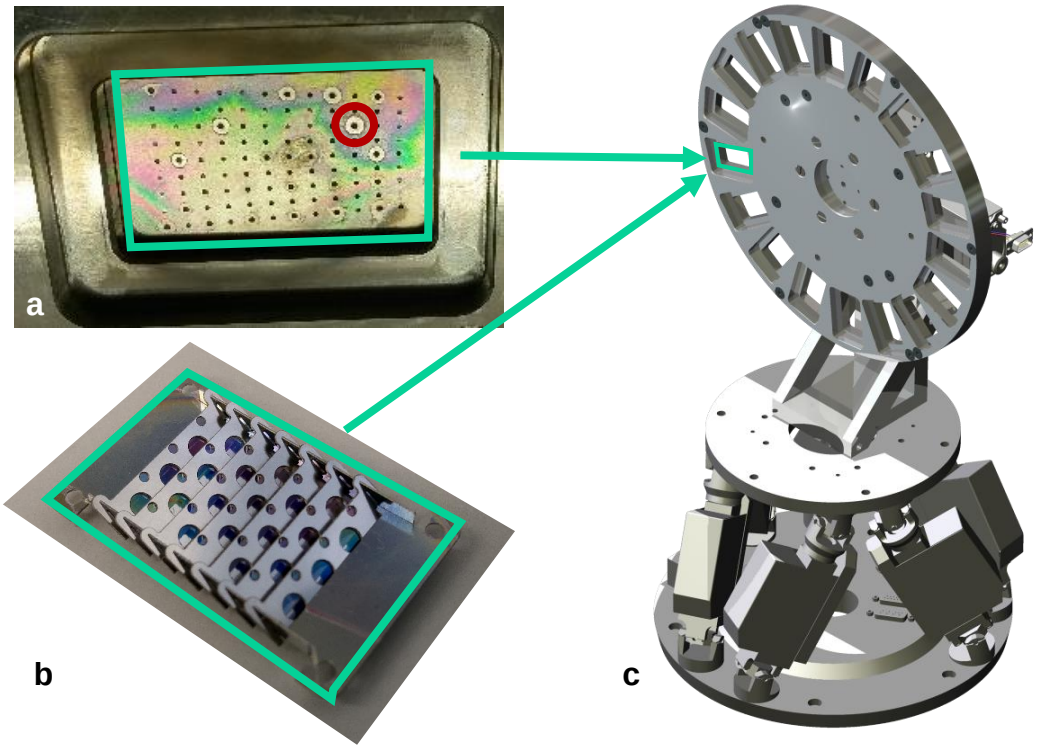

Figure A.7 | Target wheel. This figures shows the targetwheel system that was used in LEX Photonics. In **a**, a target holder is shown hosting 99 holes of 500 µm diameter for foil targets. One can clearly see which targets have been shot, since the interaction imprinted a signature larger than the target hole (red circle). In **b**, the integrated plasma mirror target is shown. It was developed to host 18 targets with a double plasma mirror and could also be mounted within the wheel [43]. The target wheel positioned onto an hexapod is shown in **c**. It enabled the operation with 0.5 Hz [59].

The **n**ano-**F**oil **T**arget **P**ositioning **S**ystem (n-FTPS) was developed in the framework of the master thesis of Ying Gao. We demonstrated 99 shots at a repetition rate of 0.5 Hz. The stability and performance are discussed in [59]. In a follow up campaign, we demonstrated beyond 1000 shots within several hours. During the experimental campaigns the target wheel enabled multiple experiments with different target thickness and material scans. The automatized positioning of the new

target allowed an allocation of man power and concentration to other task such as the development of diagnostics or the application itself. This way, we could accomplish several beam-times with few hundreds of shots each. Whereas the usage of the target-wheel greatly simplified procedures, several aspects are yet unsolved

1. Neighboring targets have been destroyed or modified during shots. This was particularly observed when the foil was placed on the laser side of the target holder.

2. Opaque foils could be only positioned on the front side of the target holder. Targets were positioned using the microscope from the back. An opaque foil on the back of the target holder would prevent the x-y-positioning of the holes in the holder since it is fully covert by the opaque foil.

3. The scanning process was semi-automatic.

4. The repetition rate was limited due to vibrations but more so the communication and timing between target-system and laser-trigger has to be improved .

Discussion

The target wheel has significantly improved and simplified the operation of the laser-ion acceleration system. The number of shots is large but limited and would, for an operation with one Hz, only last 30 min. Therefore, target systems that produce the target directly at TCC with unlimited supply are favorable for applications. But, and here the target wheel reveals its true strength, those target system are often limited in target thickness and more importantly cannot change their material composition. The target wheel can host host up to 17 different targets with varying thickness and material composition and thus perform extensive parameter scans within short times.

Plasma Mirror Based on Plastic Foil Targets

The temporal contrast plays a major role in the acceleration mechanism and thus, the highest kinetic ion energies. Therefore, we developed a target system containing an in-line double plasma mirror. The concept of plasma mirror for contrast enhancement is well explored [250–253]. The idea is that a transparent mirror is placed in a

converging part of the beam path. The laser pulse will be transmitted until eventually the intensity becomes high and a plasma is generated on the mirror substrate. Based on the idea of the liquid crystal targets [63] we used thin plastic foils serving as a plasma mirror. Due to our limited laser energy and the rather sharp focusing parabola our in-line plasma mirror had to be positioned very close to TCC. We also wanted to be able to use the plasma mirror together with the target wheel. We designed more advanced target holders consisting of 15 targets. Each target had its own double plasma mirror. The so called integrated plasma mirror target was developed by M.A.O. Haug [254] and is shown in Fig. A.7b. The implementation of the integrated plasma mirror target demonstrated its functionality and generated higher proton energies [43]. This further supported that the contrast was one of the major limitations while optimizing the ion energies.

A.1.8 Ion Wide Angle Spectrometer

The **W**ide **A**ngle **SP**ectrometer (WASP) measures the ion energy and hereby allows detection of a "wider" angle (typically a few degree) in one dimension. The energy determination is based on magnetic deflection in one dimension and was first demonstrated by Jung et al. [199]. The drawback is that ion species and in particular charge states are not resolved in contrast to for example a Thomson parabola. Previously the WASP has typically been equipped with an image plate [255] or with an MCP [203]. Since image plates require manual readout and exchange they are not suited for high repetition rates and the operation of MCPs is rather elaborate, we implemented Radeyes CMOS sensors in 2011 for the first time [154, 155]. This WASP was designed and operated under the supervision of Florian Lindner (see [108]) and can be seen in Fig. A.8. The specific configuration allowed for a simultaneous measurement of ions(protons) and electrons [204].

Additional Diagnostics - Time-of-Flight

In addition to the WASP a **T**ime-**O**f-**F**light spectrometer spectrometer was developed in LEX Photonics [207, 256]. The energy of the ions is thereby measured via their velocity. The velocity dependent time-of-flight from the source to the detector is measured and the corresponding energy calculated. The energy resolution of such detectors is coupled to the electronic read-out-time (the faster the better) and the distance of source and detector (the longer the better). A picture of the TOF, that was used during our experimental campaigns, is shown in Fig. A.9. The picture

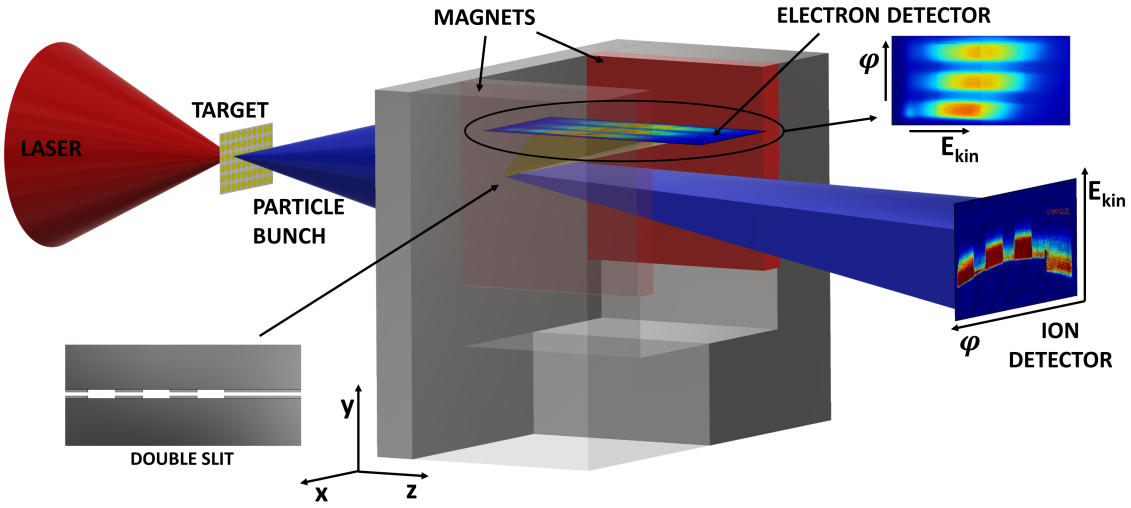

Figure A.8 | Wide angle Spectrometer at LEX Photonics. This figure shows the design of the WASP. The ion and electron bunch is traversing a slit with double slit width. The large width allows enough particles for a decent signal of the electrons deflected upwards to the top Radeye detector. The small slit provides a better energy resolution for the ions/protons. This picture is taken with courtesy from Lindner et al. [204].

further shows that multiple diagnostics were often positioned on a motorized stage. This enabled to switch between diagnostics during an experiment.

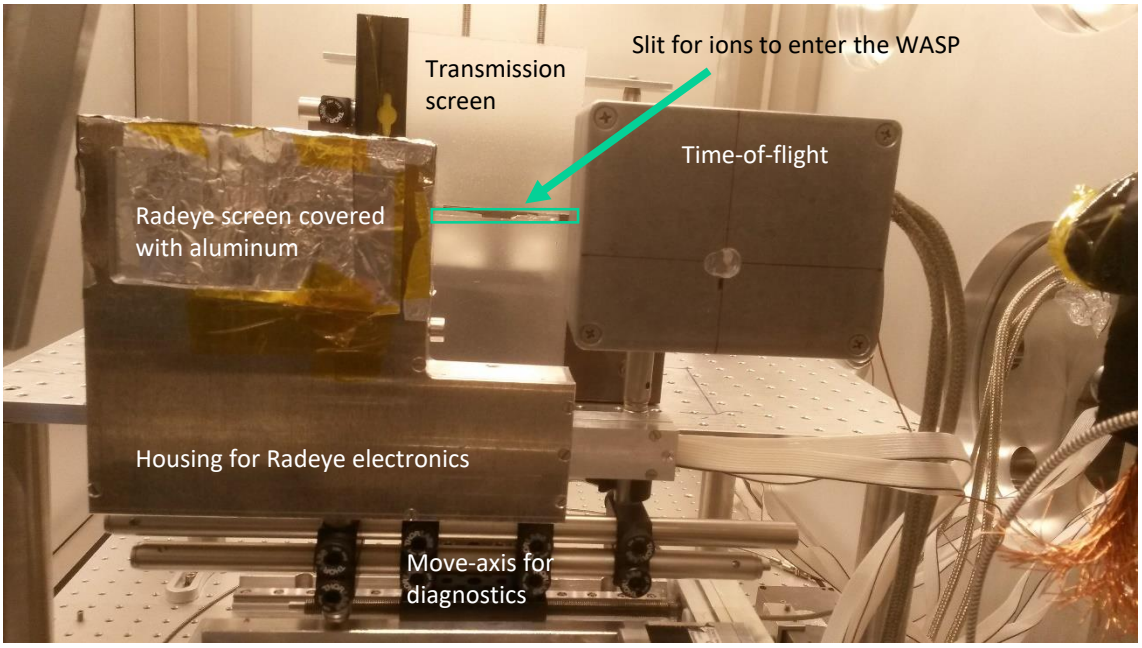

Figure A.9 | Ion diagnostic at LEX Photonics. A Radeye detector and a TOF detector were installed on a linear stage. A third position of the stage left the way to the transmission screen that has been used to analyze the transmitted light. In addition, the ions could pass the slit to propagate through the WASP. It was possible to change and test different diagnostics from shot to shot without breaking the vacuum.

A.1.9 Quadrupoles

Introduction to Ion Bunch Transport Optics

The 5th pillar of ILDIAS covers ion optics. The large angular divergence and broad energy spectrum of the ion bunch often does not suite the application and hence requires manipulation of the ion bunch post-acceleration. The easiest way of guiding an ion bunch is to exploit the Lorentz force within a magnetic field. The first important task is a modification of the ion spectrum. We have already seen that the WASP separates energies [4]. Another important task of ion optics is the focusing of an ion bunch to oppose the natural divergence and preserve the high ion flux at the location of interest. Using magnetic quadrupole fields will serve this functionality. In principle there are two different approaches (electromagnets and permanent magnets). Both approaches are valid and differ in certain aspects. The magnetic field of electromagnets or so called solenoids [18, 68] is adjustable and the selected energy can thus easily be adapted without changing the setup. Permanent magnets

[4] With more than one dipole magnet a chicane can be built in order to select certain energy bands [75, 76].

[69–72] have a static and fixed magnetic field. In order to change the selected (design) energy, the position of the magnets has to be modified. On the other side, electromagnets require high voltages which makes an operation in vacuum with high repetition rates a challenging task. Whereas the permanent magnet obviously can be used in any conditions at any repetition rates. A third approach with has not used in that context explicitly but in principle has similar effects is the implementation of a coil around the movement direction of the ion bunch [58]. A fourth option that is thus far mainly used for electrons is a plasma lens [73, 74].

Quadrupoles in LEX Photonics

Due to the aspired repetition rate of 1 Hz in LEX Photonics, we chose **P**ermanent **M**agnetic **Q**uadrupoles. Their design and the development was supervised by Thomas Rösch [71, 72] and Peter Hilz.

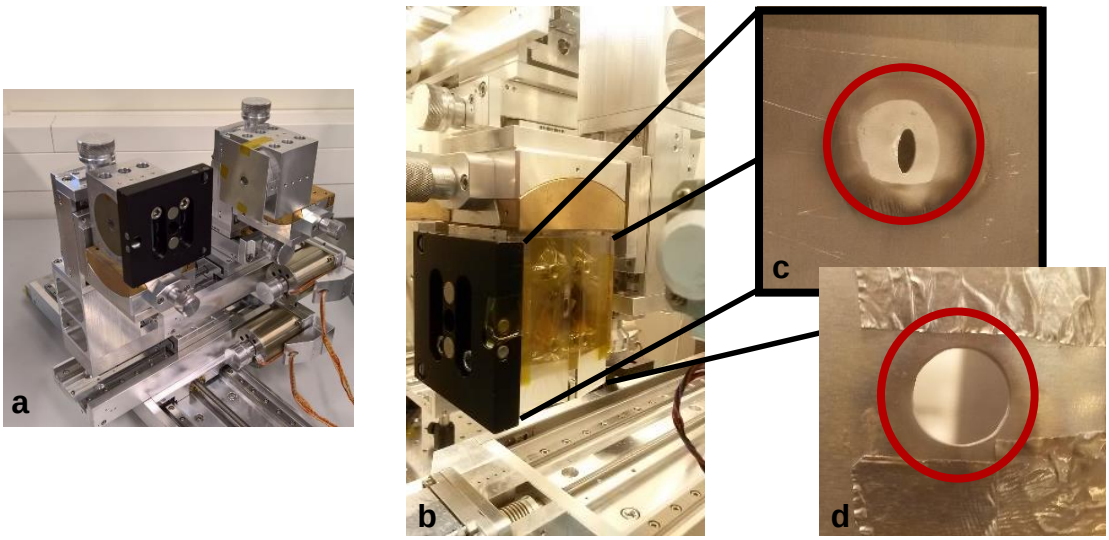

Figure A.10 | Quadrupoles at LEX Photonics. The QPs that were used in LEX Photonics are shown in **a**. **b**, Shows how the QPs were installed in LEX Photonics. The high laser intensity on the front plate of the QPs (shown in **c**) caused ablation of the aperture which coated the target from the backside with aluminum. To minimize such coating an aperture was inserted between the target and the QPs. In **d** one can see the debris that is blocked by the aperture. On the front plate of **b** glass plates with a certain angle are added as a first approach to minimize the effect.

A PMQ doublet was used to refocus the ion bunch to an application site and also narrow down the energy spectrum, i.e. selecting a certain, so called design energy (energy-band) to guide and focus the ion bunch. The design energy is the energy that is focused to the desired distance (application site) where the foci of both spatial

dimensions (x and y) overlap. The protons with energies not matching the design energy are not focused to a small spot but contribute to the signal in the focus. As a result, the spectrum in the focus is narrowed and modulated. The dipole magnet in our system further cleaned the ion bunch from contamination of low energetic particles or electrons in combination with the PMQ. The alignment of PMQ is very sensitive. Similar to an optical lens, small misalignments can distort the quality of the ion focus. Since this remains challenging especially in systems where repetition rates are a limitation, we developed an offline system to measure the magnetic fields and pre-align the complete quadrupole system. Even though, the star-like shape of the ion focus (see Fig. 3.8) indicates some misalignments of the PMQ doublet in combination with the wide energy spectrum and the WASP, the pre-alignment allowed for a focus on first shot. The complete system was motorized such that both the z distance of both PMQ could be adjusted. The complete system could be driven in and out of the ion beam in horizontal dimension as shown in Fig. A.10. Figure A.10 reveals another important aspect of the PMQ when implemented in the setup. In Fig. A.10c we can see burn of the laser on the aluminum prototype front-plate of the PMQ. The thereby spalling aluminum has coated the backside of the closed-by target. To prevent this effect an aperture has been introduced between target and PMQ (see Fig. A.10d) to block the aluminum. In the final version two glass plates were attached to the front with a small tilt such that the surface normal is redirected from the target.

A.2 Centre for Advanced Laser Applications

Figure A.11 | Evolution of the LION cave. The progress in the LION cave is shown. The cave construction site was finished in August 2016. The year after the framework for the experimental chamber and the chamber were installed. Within 2018 the experimental setup within the chamber has been installed. The cave in January 2019 is ready for experiments.

Figure A.12 | Centre for Advanced Laser Application. The graph shows CALA and the different experimental areas (LION, LUX, ETTF, SPECTRE and HF). It further shows the ATLAS-3000 and the ZEUS laser system.

The CALA building has been finished[5] in August 2016. Since then we have installed different components and are now[6] ready for operation. The progress in the LION cave is depicted in Fig. A.11. An overview of the relevant areas of CALA is given in Fig. A.12 (a more detailed version had already been shown Fig. 1.7). It contains 2 large clean rooms hosting the ATLAS-3000 laser and the PFS-pro. The ATLAS-3000 is connected to the LBD wherein the laser pulse can be guided towards 5 experimental areas. The PFS-pro will also been connected to the LBD in the future.

[5] Even though several technical issues had to be solved afterwards.
[6] March 2019.

A.2.1 ATLAS-3000

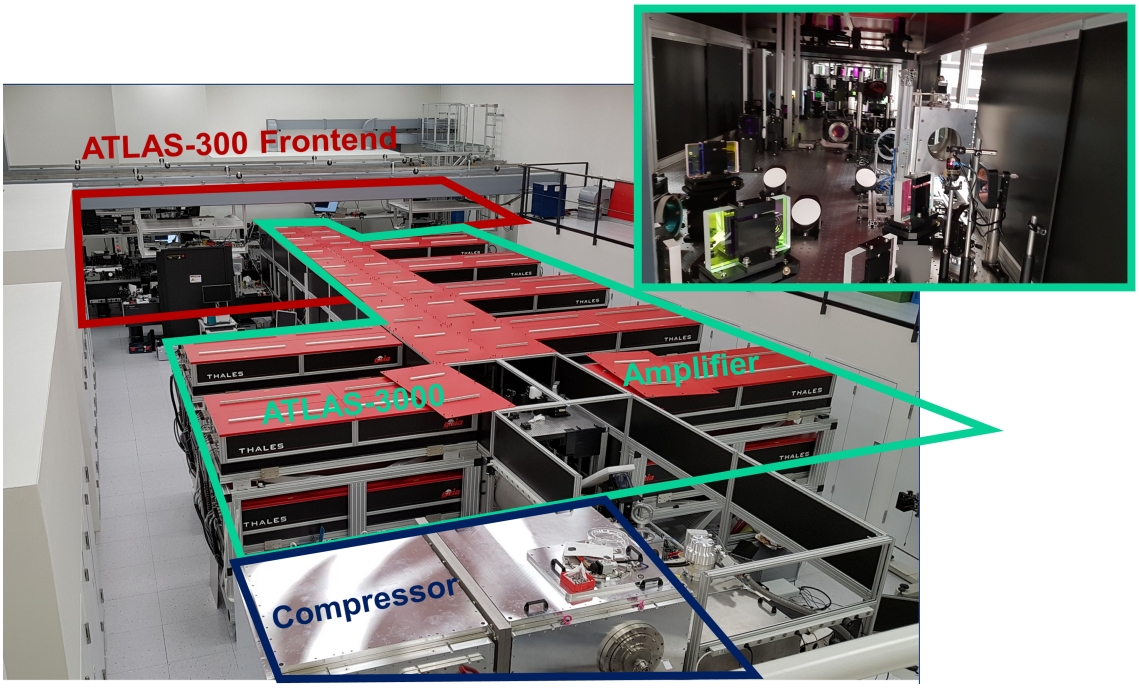

Figure A.13 | ATLAS-3000. The ATLAS-300 serves as a frontend for the new amplification stage of the ATLAS-3000. 14 Gaia pump lasers are used to pump two multi-path amplification stages. From the compressor on the laser pulse will be guided in vacuum.

The ATLAS-3000 laser is an upgrade to the ATLAS-300 (Section 3.1) with two additional amplification stages amplifying the laser energy from 6 J to 90 J. Te beam diameter (after compression) had to be increased from about 10 cm to 28 cm. The pulse energy reaches 90 J before compression and a 20 fs long laser pulse attenuated to 60 J on target is reaching a peak power of 3 PW on target seems reasonable.

Ring-REGEN

During the experimental campaign at LEX Photonics the regenerative amplifier was identified as the source of the most prominent prepulses at 500 and 660 ps. To avoid those prepulses two modifications were possible. An additional path length between the Pockels cell and the cavity mirror would further separate the prepulse and the main pulse in time such that upstream Pockels cells could be used to attenuate the prepulses. However the second approach to redesign the REGEN in a ring arrangement prevents the creation of those direct prepulses and was implemented

with the help of Amplitude Technologies. The laser pulse is therein performing round trips instead of being reflected. Therefore, no more direct prepulses can be generated in the REGEN and prepulses origin from postpulses are significantly smaller. The improved temporal contrast using the newly implemented REGEN is depicted in Fig. A.14 and compared to the situation before installing the Ring-REGEN. The improvement is obvious, nevertheless, new prepulses appear at 130 and 40 ps before the peak. Their origin seems related to trailing postpulses (see Fig. A.14b).

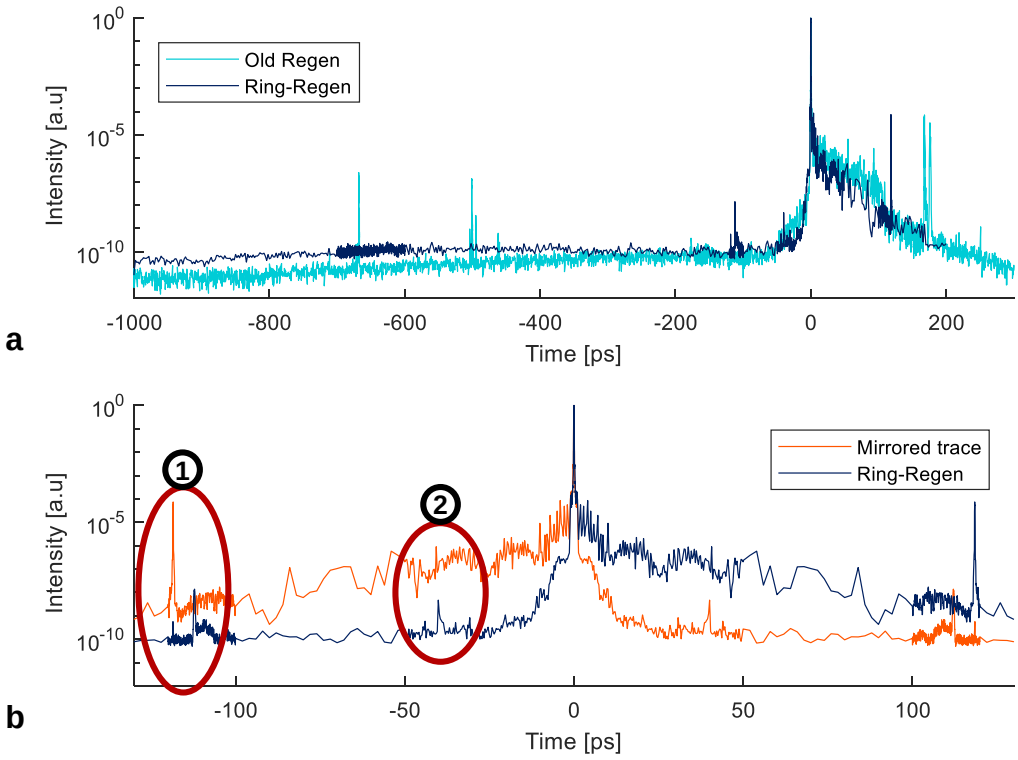

Figure A.14 | Contrast with the Ring-REGEN. This graph shows the temporal contrast measured with the newly implemented Ring-REGEN (**a**). The former prepulses are no longer existent due to the ring configuration that prevents the generation of direct prepulses. The prepulse at 130 ps (**1**) originates from its postpulse but seems to be transformed to a real one (**b**). The prepulse at 40 ps (**2**) also originates from its postpulse but also seems to be real.

Pockels Cell

In LEX Photonics we have explained the problems of back-reflection and the need for either avoiding normal incidence on targets or implement measures within the laser chain that are able to suppress the back-reflected light (see Section A.1.3). An additional large Pockels cell with an aperture of 73 mm is foreseen to be implemented

at the transition between the ATLAS-300 and ATLAS-3000. In LEX Photonics we had to change the beam path whenever we had to implement the Pockels cell in the beam-path complicating the alignment. Even though a permanent implementation of the Pockels cell is desired the flexibility to bypass was required. To avoid a modification of the beam path, the Pockels cell, including the polarizers, can be moved downwards inside the beam path with a motorized stage. To avoid an additional rotation of the polarization the Pockels cell is operated downstream and switched active, when the reflected laser pulse is passing it and thus attenuating the back-reflected light.

A.2.2 Laser Beam Delivery

The compressor of the ATLAS-3000 (Fig. A.13) is operated in vacuum. From thereon the laser pulse has to be guided in vacuum to avoid destruction of the pulse properties by nonlinear effects in air (Section B.3). The laser beam delivery (Fig. A.15) is prepared to connect the three laser systems (ATLAS-3000, ATLAS-300 and PFS-pro) with the five experimental areas. Every mirror is motorized which allows a precise guidance of the laser pulse. The beam line has been designed such that a simultaneous operation of two laser systems is possible for certain configurations[7]. Additionally, an adaptive mirror has been installed (Fig. A.15b). In combination with a wavefront sensor that is included in the vacuum microscope the wavefront can be corrected to optimize or even adjust the intensity distribution in focus. A detailed description of the setup and operation of the wavefront sensor and the interaction with the adaptive mirror can be found in the thesis of Leonard Doyle[248].

Mirror Control

The software interface of the LBD allows adjustment of the mirrors in the laser-beam line and enables to select one of up to three different laser systems and guide it to one of the five experimental areas. Therefore, the software gives an overview and control abilities for different components.

1. **Move axis:** The move axis positions a mirror and thus selects a specific route for a laser beam.

2. **Position sensor:** Hall sensors monitor the position of the move axis and continuously confirm to the ZS if the required route is active.

[7] For example using the ATLAS-3000 in LION and the PFS-pro in SPECTRE.

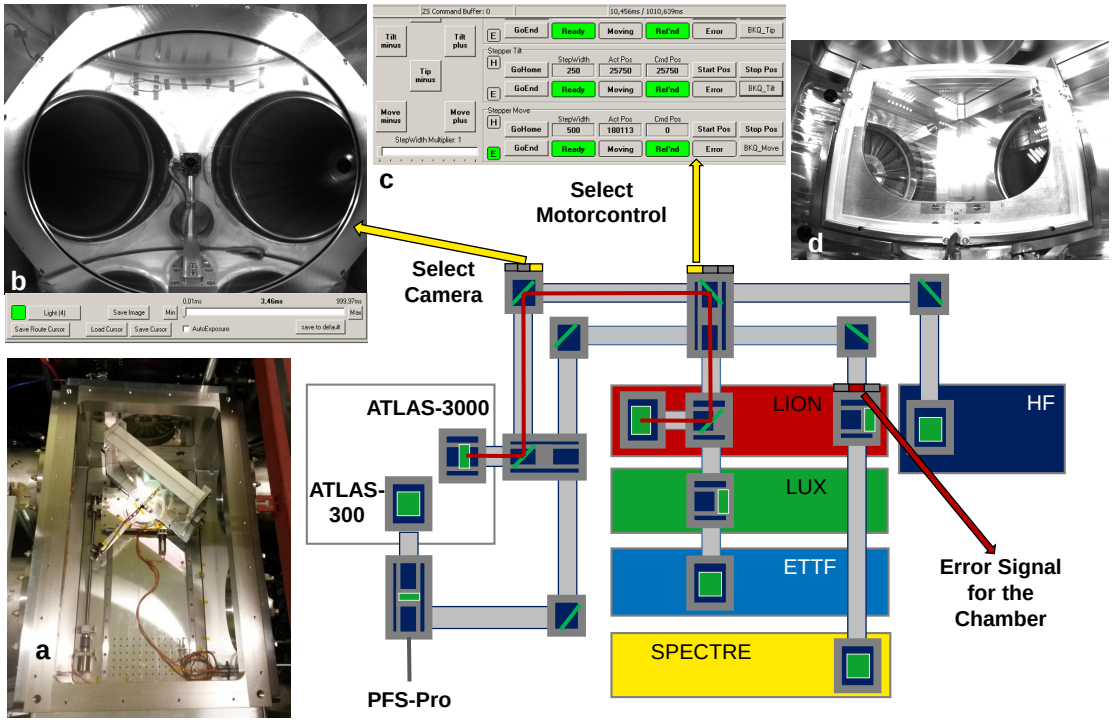

Figure A.15 | Laser beam delivery. Laser pulses from three different laser systems (ATLAS-3000, ATLAS-300 and PFS-pro) can be guided to the 5 experimental areas (LION, LUX, ETTF, SPECTRE and HF). The figure further shows the control software interface of the LBD. **a**, is a picture of a "switch box" where the mirror can be moved and rotated to various alignments. **b**, is a screenshot of the camera picture that images the adaptive mirror in the indicated box (UT3) as it opens in the software. The camera can be selected by the right button highlighted in yellow for each vacuum chamber. **c** is a screenshot of the motor control showing how the user can adjust the mirror position. The motor control of each mirror can be selected by the left button above the corresponding chamber. A picture of the typical multilayer mirror imaged by the camera in SB3 is shown in **d**.

3. **Alignment of the laser beam:** Each mirror is motorized in tip/tilt, enabling a guidance of the beam onto the respective next mirror.

4. **Monitoring:** Cameras image each mirror and the scattered light is observed and indicates the position of the laser beam on the mirror.

5. **Illumination**: LED's are installed in each chamber enable illumination.

Figure A.15 shows the graphical user interface that is employed in the software. Each vacuum box (that is used to redirect the beam) can be selected. The motor control opens by selecting the left button (Fig. A.15c); the camera, watching the mirror and the laser position on the mirror, with the right button (Fig. A.15b).

A.2.3 Experimental Cave(s)

Each of the five experimental areas (HF, LION, ETTF, LUX and SPECTRE (see Fig. A.12) is located within a radiation shielded bunker (cave). Figure A.16 views the LION cave. The LBD is located in the double floor and the laser is entering the experimental chamber from the bottom. A CW diode laser with 3 cm beam diameter can be coupled into the LBD (Fig. A.16 **(3)**) and serves for alignment, even when the laser is allocated to another cave. The additional beam dump ensures that radiation safety is ensured for carbon energies up to 400 MeV/u. The second chamber is not connected to the LBD yet. It can, for example be equipped with the optics that have been used in LEX Photonics and would be capable for experiments with the ATLAS-300. Its main purpose is the flexibility to perform prototype test and proof-of-principle measurements.

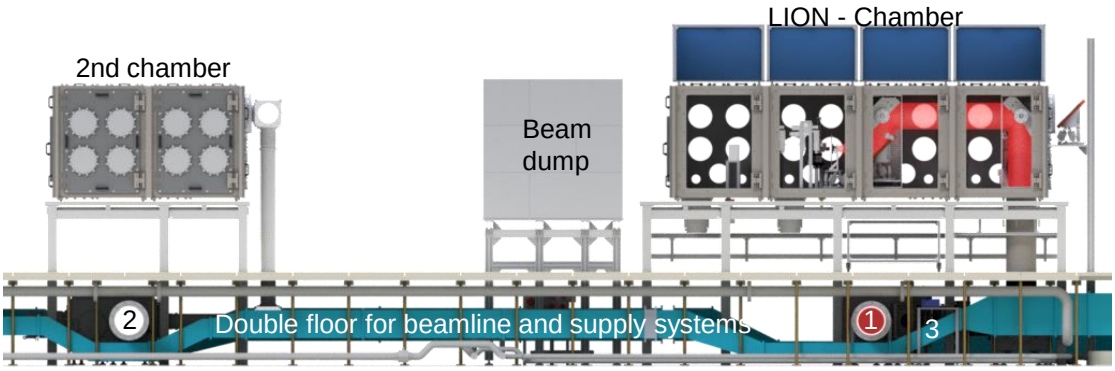

Figure A.16 | The LION cave. The double floor is hosting the LBD and supply cables for water, air conditioning, gases, electricity and signal cables. The laser **(1)** enters the cave in the double floor and is then guided to the vacuum chamber. A second arm of the beam line **(2)** can be used to guide, for example, the ATLAS-300 laser into the 2nd chamber that can be used for smaller experiments and test purposes. A CW diode laser of 1 W with 3 cm beam diameter can be coupled in for alignment purposes **(3)**. The beam dump strengthens radiation safety outside the cave during full operation of LION.

Chamber Design

The vacuum chamber of LION contains 4 chamber modules. The modules are the same as in LEX Photonics with minor modifications such as an optimized flange configuration of the doors. The four modules can be divided into two parts. The first two modules are used to guide and finally focus the beam onto TCC. They

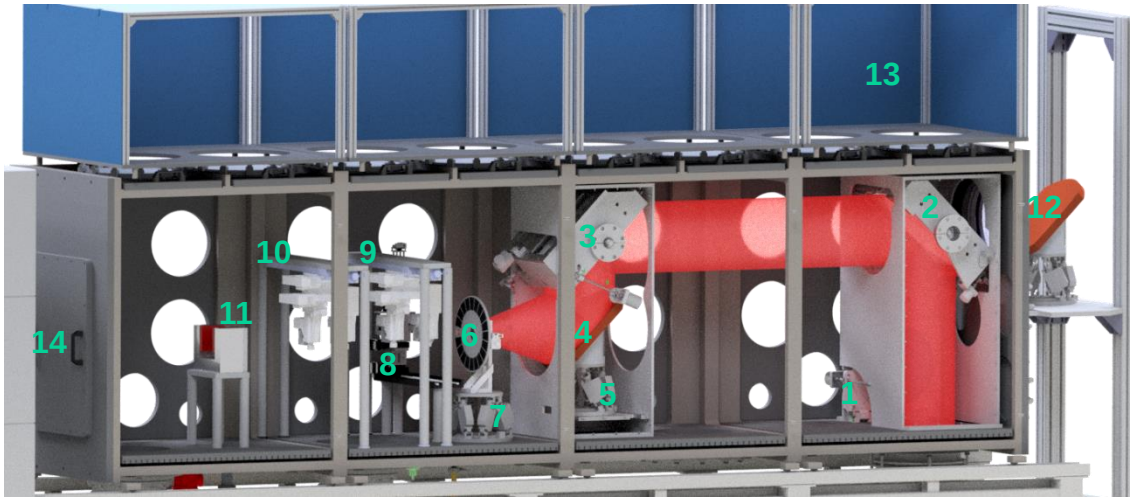

Figure A.17 | Experimental chamber and setup in LION. The laser with a beam diameter of 28 cm enters the chamber from the bottom. A BS can be used to block the laser **(1)**. The laser is guided over TM1 **(2)** and TM2 **(3)** to the OAP **(4)**, positioned onto a hexapod **(5)**, and eventually focused. The target wheel **(6)** is also mounted on a hexapod **(7)**. The laser and the target can be analyzed and positioned by means of the vacuum-microscope**(8)**. Two QPs-doublets can be inserted to guide the ion bunch **(9,10)**. The WASP contains the dipole magnet **(11)** and the Radeye detector at the back of the vacuum chamber(not visible here). The back reflected light is transmitted through TM1 and focused by another OAP **(12)** to reduce the beam diameter. The analysis of incoming and back reflected light is foreseen to be built on top of the chamber**(13)**. The ion bunch can eventually be guided out off the vacuum chamber through a foil window foreseen at the back end**(14)**. Drawing with courtesy of Martin Speicher.

contain 4 elements, **B**lock **S**hutter (BS), **T**urning **M**irror 1 (TM1),**T**urning **M**irror 2 (TM2) and the OAP. The third and the fourth chamber contain TCC and the further transport and diagnostic elements of the ions. As pointed out in Chapter 3 the setup of LEX Photonics was chosen such that the beam height and everything downstream from TCC can be tested and implemented in CALA. The complete setup design is depicted in Fig. A.17. One can clearly see that while the laser mirrors became larger, the components **(6-11)** are optimized versions of the setup in LEX Photonics (see Fig. 3.6). The first mirror in the chamber (TM1) is designed for 1% transmission. The incoming laser can thus be monitored as well as the reflected light that is re-collimated by the final focusing OAP. It will thus be possible to analyze the fundamental wavelength in the back reflected signal. TM2 has a silver coating and can thus be operated under different angles of incident, for example 10 and 45 degree. This flexibility allows to use different off-axis parabolic mirrors (see Table A.1) without exchanging mirrors. An overview of the available OAPs is

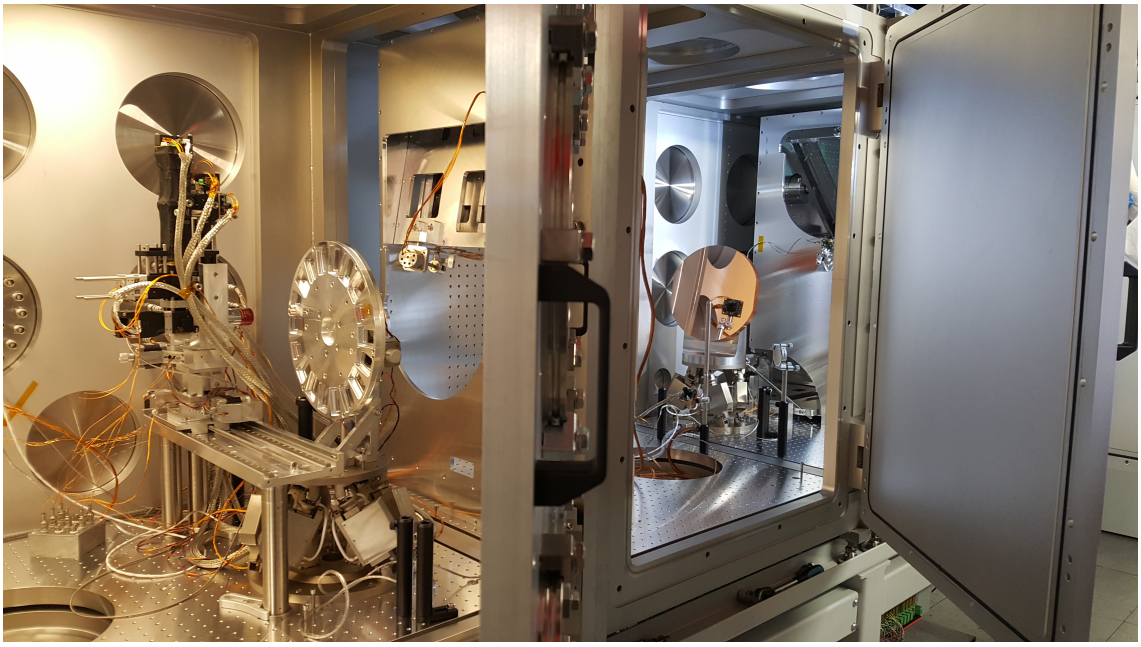

Figure A.18 | Picture of the LION chamber. A picture of the LION chamber with OAP Nr. 4.

Number	Off-axis angle	Effective focal length	Company and material
1	90°	30 cm	AOS - Glas
2	20°	150 cm	Layertec - Glas
3	90°	50 cm	Millpond - Copper
4	20°	150 cm	Millpond - Copper

Table A.1 | Parabolas for CALA. This table lists the parabolas that can be used in LION.

given in Table A.1. Apart from the choice of the focusing mirrors it can further be positioned rather freely within the first two chamber modules. This allows changing the direction of propagation and thus enables a further variation of the angle of incidence onto the target. This is important, because in our general elongated chamber geometry rotating the target is not a desirable option. Furthermore the polarization of the laser can be adjusted in the future. When impinging on the target, the laser polarization will be dominantly vertical. We have two large aperture $\lambda/4$ wave-plate to change the polarization to circular or horizontal.

Appendix B

Theoretical Parts - a Deeper Look

Contents

B.1 Solving the Wave Equation - Fourier Optics 147

B.2 Some Basics of (Laser) Light 161

B.3 Nonlinear Optics 164

B.4 Optical Devices for High-Power Laser Systems 166

B.1 Solving the Wave Equation - Fourier Optics

Many of todays measurements are based on interactions with light or waves in general. Since the location, where the measurement is executed, differs in most cases from the point of interest, where the interaction takes place, it is essential to reconstruct the evolution of the wave from the point of interaction to detection. Only with that understanding it is possible to retrieve the information that is sought. With the beginning of Huygens who stated that *"each point of a wavefront can be regarded as a point source of a spherical wave"* (see Eq. (B.26)), many great minds developed the theory of propagation of light as illustrated in Fig. B.1. The starting point of this theory is the time independent Helmholtz equation Eq. (2.3). Note that this theory describes the case of a time independent and thus purely monochromatic wave. A detailed derivation and collection of this theory has been written by Goodmann [257] and is summarized in Section B.1.

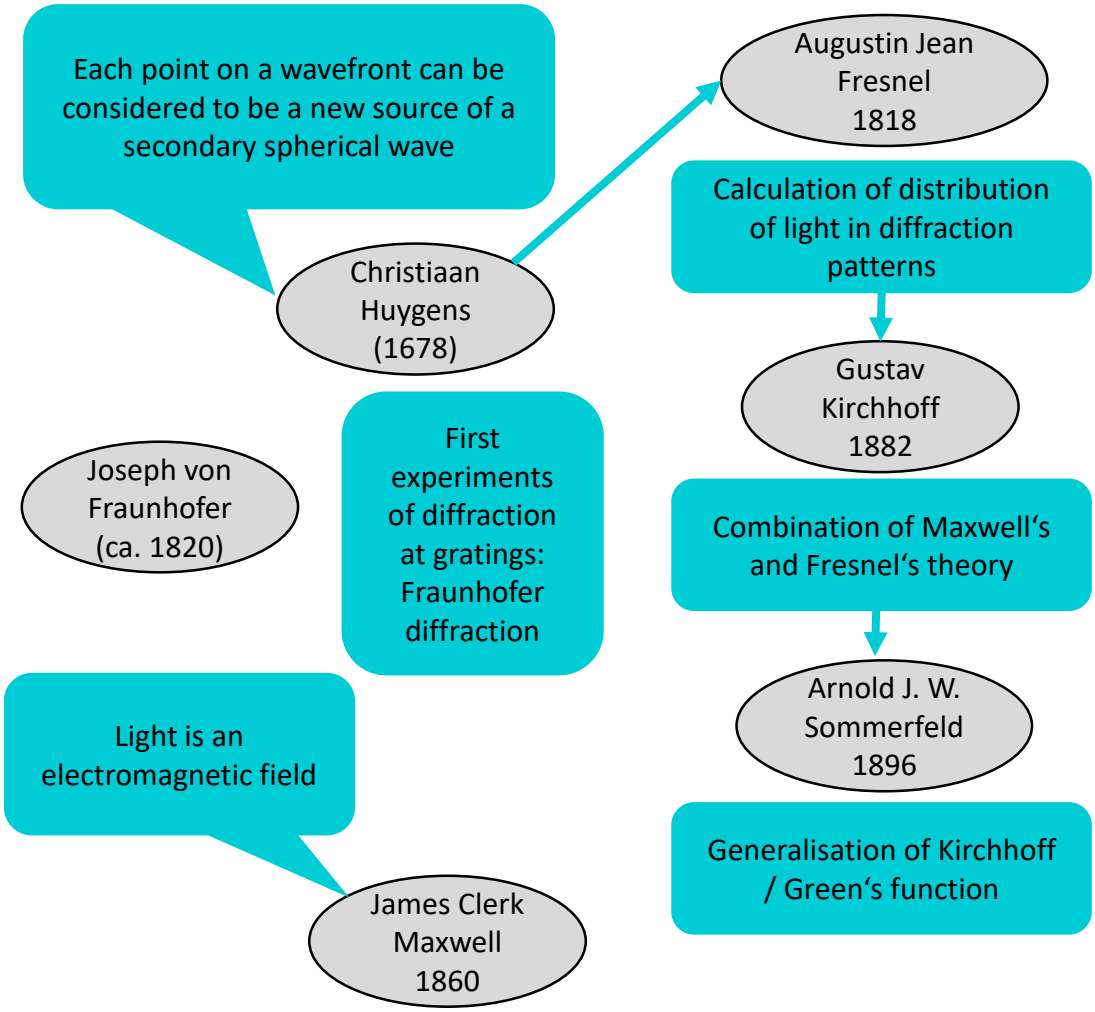

Figure B.1 | Historical development of wave theory. This figure gives an overview of the development of the wave theory, especially concerning the propagation of waves. It names some of the most famous physicists that have contributed significantly towards the development of the theory and whose principles and findings still form the basis of todays theory of light in many aspects.

B.1.1 Green's Theorem

One important tool in the derivation of Fourier optics is Green's theorem. Green's theorem is a special case of Kelvin-Stokes theorem and relates the integration over a volume to the integration over its enclosed surface.

$$\iiint_V \left(U\nabla^2 G - G\nabla^2 U\right) dV = \oiint_S \left(U\frac{\partial G}{\partial n} - G\frac{\partial U}{\partial n}\right) dS, \tag{B.1}$$

where $U(\vec{r})$ and $G(\vec{r'})$ are any two complex-valued functions of position. S is a closed surface surrounding a volume V.

B.1.2 Excursion Green's Function

Even though the Green's function[1] is used more as an auxiliary function the concept is rather important since it enables the basic formalism for solving the inhomogeneous wave equation. The principles of wave propagation are important at several points of this work and therefore it is worth to have a closer look at the wave formalisms. The Green's function G is an impulse response of a homogeneous linear differential operator L

$$LU(x) = f(x), \tag{B.2}$$

where $f(x)$ is a source term. The Green's function is the solution to the differential equation L with a point source as force term:

$$LG(x, x') = \delta(x' - x), \tag{B.3}$$

we can obtain a solution for $U(x)$ by multiplying Eq. (B.3) with the source function $f(x)$ and integrating over the full space yielding:

$$LU(x) = \int LG(x, x')f(x')dx'. \tag{B.4}$$

Since the operator L is linear and only acts on x it can be taken outside of the integration yielding

$$U(x) = \int G(x, s)f(s)ds. \tag{B.5}$$

We therefore can conclude that with the appropriate Green's function we can solve an inhomogeneous differential equation and thus also the wave equation. For a concrete example, we can look at an inhomogeneous wave equation with a source term

$$\underbrace{(\nabla^2 - \frac{1}{c^2}\frac{\partial^2}{\partial t^2})}_{L} U(\vec{r}, t) = -f(\vec{r}, t). \tag{B.6}$$

[1] The Green's function provides a solution for differential harmonic equations.

Using Eq. (B.3) we get:

$$\nabla^2 G(\vec{r},t;\vec{r'},t') - \frac{1}{c^2}\frac{\partial G(\vec{r},t;\vec{r'},t')}{\partial t^2} = -\delta(\vec{r}-\vec{r'})\delta(t-t'). \tag{B.7}$$

In the next step we multiply Eq. (B.6) with G and subtract Eq. (B.7) multiplied with U

$$G\nabla^2 U - U\nabla^2 G - G\frac{1}{c^2}\frac{\partial^2 U}{\partial t^2} + U\frac{1}{c^2}\frac{\partial^2 G}{\partial t^2} = -Gf + U(\vec{r},t)\cdot\delta(\vec{r}-\vec{r'})\delta(t-t'). \tag{B.8}$$

By integrating $\vec{r'}$ over the volume of interest V' and the time t', from $t=0$ to t, we can solve for $U(\vec{r},t)$:

$$U(\vec{r},t) = \int_0^t dt' \iiint_{V'} d\vec{r'} G(\vec{r},t;\vec{r'},t') f(\vec{r'},t') \tag{B.9a}$$

$$+ \int_0^t dt' \iiint_{V'} d\vec{r'} \left[G\nabla^2 U - U\nabla^2 G\right] \tag{B.9b}$$

$$+ \int_0^t dt' \frac{1}{c^2} \iiint_{V'} d\vec{r'} \left[U\frac{\partial^2}{\partial t^2}G - G\frac{\partial^2}{\partial t^2}U\right]. \tag{B.9c}$$

The equation Eq. (B.9) can be seen as the complete solution of the inhomogeneous wave equation accounting for a source term (Eq. (B.9a)), boundary conditions (Eq. (B.9b)) and initial conditions (Eq. (B.9c)). Using Green's theorem (Eq. (B.1)) for Eq. (B.9b) we get:

$$\int_0^t dt' \iiint_{V'} d\vec{r'} \left[G\nabla^2 U - U\nabla^2 G\right] = \int_0^t dt' \iint_{S'} \left(U\frac{\partial G}{\partial n'} - G\frac{\partial U}{\partial n'}\right) dS', \tag{B.10}$$

where S' is the surface enclosing V'. The part can thus often be neglected due to asymptotic fall-off condition. Note that in reality boundary conditions, such as reflections at the edges, could become important. An integration of Eq. (B.9c) over t' yields:

$$\frac{1}{c^2} \iiint_{V'} d\vec{r'} \left[U\frac{\partial}{\partial t}G - G\frac{\partial}{\partial t}U\right]_0^t. \tag{B.11}$$

In the case of a temporal induced source term we can assume equilibrium conditions at $t=0$ and choose t' large enough that equilibrium conditions has been established and thus Eq. (B.9c) can for such situations also be neglected.

In this work the concept of a Green's functions is applied twice. On the one hand it is used for the derivation of wave propagation with Sommerfeld, Fresnel and

Fourier in Section B.1. On the other hand it is employed to solve the inhomogeneous wave equation for the pressure wave that is generated by heat that is introduced by ions dissipating their energy in water. This is relevant for **I**on-**B**unch **E**nergy **A**coustic **T**racing in Chapter 5.

B.1.3 Integral Theorem of Helmholtz and Kirchhoff

The first step is the derivation of the integral theorem of Kirchhoff and Helmholtz. We consider the calculation of the field at P_0 (Fig. B.2) for a given source within the volume V' enclosed by S. The general approach, described in Section B.1.2, is to calculate the impulse response to a source at P_1 and later integrate over the complete volume and thus all possible point sources.

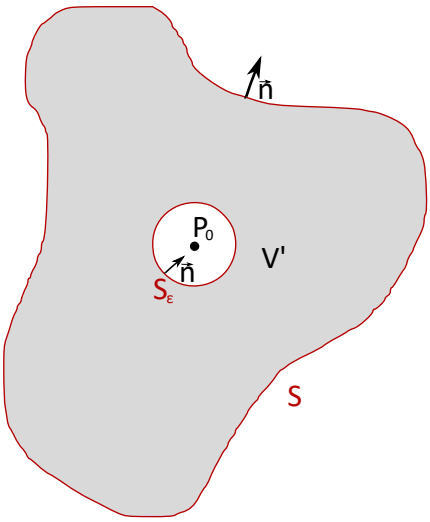

Figure B.2 | Integral theorem of Helmholtz and Kirchoff. This drawing introduces the quantities required for the derivation of the integral theorem of Helmholtz and Kirchhoff. The figure is adapted from Goodman [257].

We start with the Helmholtz equation Eq. (2.3) and the free-space Green's function, a unit-amplitude spherical wave expanding about P_1:

$$G(P_1) = \frac{e^{ikr_{01}}}{r_{01}}, \tag{B.12}$$

where r_{01} is the distance from P_0 to P_1. The inner circle of Fig. B.2 is introduced since G must be well defined within the enclosed volume V'. In the later calculation the radius ϵ of S_ϵ is approaching zero. It is therefore $S' = S_\epsilon + S$. Using the two

Helmholtz equations $(\nabla^2 + k^2)U = 0$ and $(\nabla^2 + k^2)G = 0$ and following the same steps as for Eq. (B.8) we obtain[2]

$$\iiint_{V'} \left(U\nabla^2 G - G\nabla^2 U\right) dV = \iiint_{V'} \left(UGk^2 - GUk^2\right) dV \equiv 0. \tag{B.13}$$

With the use of Green's theorem and keeping in mind that $S' = S + S_\epsilon$, we get:

$$\underbrace{-\iint_{S_\epsilon} \left(U\frac{\partial G}{\partial n} - G\frac{\partial U}{\partial n}\right) dS_\epsilon}_{\lim\limits_{\epsilon\to 0} = 4\pi U(P_0)} = \iint_S \left(U\frac{\partial G}{\partial n} - G\frac{\partial U}{\partial n}\right) dS. \tag{B.14}$$

This directly leads to the integral theorem of Kirchoff and Helmholtz

$$U(P_0) = \frac{1}{4\pi} \iint_S \left(U\frac{\partial G}{\partial n} - G\frac{\partial U}{\partial n}\right) dS. \tag{B.15}$$

It states that the field at any point P_0 can be calculated knowing the field and its derivative and its derivative at the boundary of any closed surface surrounding $\vec{r}$. In other words the field can be expressed by its boundary conditions.

B.1.4 Fresnel-Kirchhoff Diffraction Formula

In a next step we consider the diffraction of light by an aperture. We therefore assume an impinging wave from the left onto the aperture as illustrated in Fig. B.3. The field at P_0 behind the aperture is now calculated.

Using the integral theorem of Helmholtz and Kirchhoff (Eq. (B.15)) we get:

$$U(P_0) = \frac{1}{4\pi} \iint_{S_1+S_2} (U\frac{\partial G}{\partial n} - G\frac{\partial U}{\partial n})dS. \tag{B.16}$$

It can be shown that the integration over S_2 vanishes. Further the screen on S_1 is opaque in all areas but Σ. The integration will further vanish everywhere except inside the aperture when applying the Kirchhoff boundary conditions:

1. The field U and its derivative $\partial U/\partial n$ are not altered by the presence of the aperture.

2. On the surrounding of the aperture U and its derivative $\partial U/\partial n$ are zero

[2]Within V', G is simply an expanding spherical wave satisfying the Helmholtz equation.

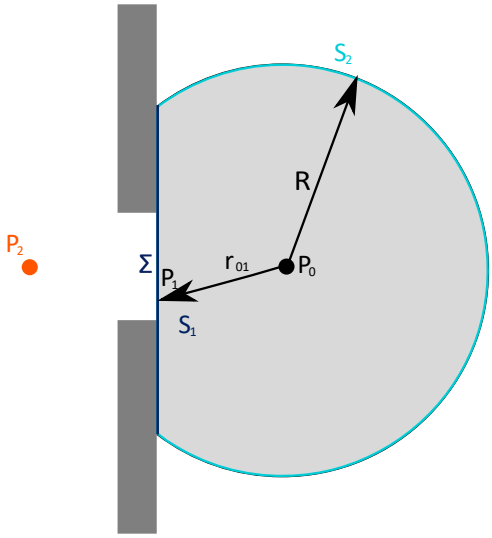

Figure B.3 | Fresnel, Kirchhoff, Sommerfeld. This drawing introduces the quantities that are required for the derivation of several regimes. The surface is S_1, including the aperture Σ, and S_2. The field at P_0 shall be calculated. The figure is adapted from Goodman [257].

$$U(P_0) = \frac{1}{4\pi} \iint_{\Sigma} (U \frac{\partial G}{\partial n} - G \frac{\partial U}{\partial n}) dS. \tag{B.17}$$

With the assumption that the observation point is many optical wavelengths away from the aperture ($k \gg r_{01}^{-1}$) we get:

$$\frac{\partial G(P_1)}{\partial n} = \cos(\vec{n}, \vec{n_{01}})(ik - \frac{1}{r_{01}}) \frac{e^{ikr_{01}}}{r_{01}} \tag{B.18a}$$

$$\approx ik \cos(\vec{n}, \vec{n_{01}}) \frac{e^{ikr_{01}}}{r_{01}}. \tag{B.18b}$$

The aperture is illuminated by a spherical wave arising from a point source at P_2, the field on the aperture is therefore:

$$U(P_1) = \frac{A e^{ikr_{21}}}{r_{21}}, \tag{B.19}$$

Using the same approximation ($k \gg r_{12}^{-1}$) and applying both to Eq. (B.17) we obtain

the Fresnel-Kirchhoff diffraction formula

$$U(P_0) = \iint_\Sigma \underbrace{\frac{1}{i\lambda}\left(\frac{Ae^{ikr_{21}}}{r_{21}}\right)\left(\frac{\cos(\vec{n},\vec{n_{01}}) - \cos(\vec{n},\vec{n_{21}})}{2}\right)}_{U'(P_1)} \frac{e^{ikr_{01}}}{r_{01}} ds. \tag{B.20}$$

This result can be interpreted that the field at P_0 arises from the integration of all spherical point sources with magnitude $U'(P1)$ located within the aperture and can thus directly be connected to Huygens principle. The Fresnel-Kirchhoff formulation is limited to one impinging spherical wave. It further does not give the correct result in the part of S_1 that lies in the shadow of the aperture Σ, since the diffraction there is not taken into account, and very close by, due to the approximation. Nonetheless the Kirchhoff boundary conditions apply to many situations and calculations for most cases are quite accurate. It fails though for certain situation for example when scattered light (e.g. back to the source from the edge of the aperture) interacts with the source again[258].

B.1.5 Rayleigh-Sommerfeld Formulation of Diffraction

The fact that boundary conditions had to be implied and internal inconsistencies[3] of the theory motivated for further studies. Sommerfeld hurdled the inconsistency of Kirchhoff by showing that there is one Green's function satisfying more mathematically correct boundary conditions (the field vanishes in Σ). With

$$G_- = G(r_{01}) - G(-r_{01}) = \frac{e^{ikr_{01}}}{r_{01}} - \frac{e^{ikr\tilde{_{01}}}}{r\tilde{_{01}}}, \tag{B.21}$$

which assumes a second mirrored point source of P_0 at $\tilde{P}_0$ oscillating with a 180 phase difference. Since G_- vanishes at all locations of Σ the previous equation Eq. (B.17) simplifies to

$$U(P_0) = \frac{1}{4\pi}\iint_\Sigma U\frac{\partial G_-}{\partial n} dS. \tag{B.22}$$

This is called the first Rayleigh-Sommerfeld solution. On the surface Σ we get:

$$\frac{\partial G_-}{\partial n}(P_1) = 2\cos(\vec{n},\vec{r_{01}})\left(ik - \frac{1}{r_{01}}\right)\frac{\exp(ikr_{01})}{r_{01}}. \tag{B.23}$$

[3] If a 2-D potential function and its normal derivative vanish simultaneously over any finite curve segment, the potential function must vanish over the entire plane.

Having the observation point again many optical wavelengths, away from the aperture ($k \gg r_{01}^{-1}$), the second term of Eq. (B.23) can be dropped. The first term is twice the normal derivative of the free space Green's G (see Eq. (B.12)) function used by Kirchhoff:

$$\frac{\partial G_-}{\partial n}(P_1) = 2\frac{\partial G}{\partial n}(P_1)\,. \tag{B.24}$$

With this relation Eq. (B.22) can be rewritten to:

$$U(P_0) = \frac{1}{4\pi}\iint_\Sigma U\frac{\partial G_-}{\partial n}dS = \frac{1}{2\pi}\iint_\Sigma U\frac{\partial G}{\partial n}dS. \tag{B.25}$$

Inserting Eq. (B.18b) we obtain:

$$U(P_0) = \frac{1}{i\lambda}\iint_\Sigma U(P_1)\frac{e^{ikr_{01}}}{r_{01}}\cos(\vec{n},\vec{n_{01}})ds. \tag{B.26}$$

This equation again incorporates the Huygens-Fresnel principle. It expresses the observed field $U(P_0)$ as a superposition of spherical waves originating from secondary sources located at each point P_1 located within the aperture Σ. The cosine is the so called obliquity factor accounts for the direction of r_{01} with respect to the surface normal. The only difference between the Kirchhoff and Sommerfeld solution is the obliquity factor (and the mathematically sane derivation).

B.1.6 Common Approximations for the Propagation of Waves

One of the most important outcomes of the derivation is the definition of three approximation that are widely used in many fields. Note that while up to now a general field U has been considered we now consider an electric field $\mathcal{E}$ assuming linear polarization for simplifications in this part.

The Rayleigh-Sommerfeld Formulation

The first approximation was already used in the derivation, namely that the observation point is many optical wavelengths away from the aperture plane ($k \gg r^{-1}$) yielding Eq. (B.26)

$$\mathcal{E}(P_0) = \frac{1}{i\lambda}\iint_\Sigma \mathcal{E}(P_1)\frac{e^{ikr_{01}}}{r_{01}}\cos(\vec{n},\vec{n_{01}})ds. \tag{B.27}$$

Since the calculation is still complicated two more approximations are commonly used in the calculation of propagating waves. Assuming a planar aperture Σ and a

parallel observation plane at a distance z, the distance r_{01} can be expressed as:

$$r_{01} = \sqrt{z^2 + (x-\xi)^2 + (y-\eta)^2}, \tag{B.28}$$

where x, y are the coordinates in the observation plane and $\xi\eta$ in the aperture plane. This propagation distance can now be approximated using the binomial expansion[4]

$$r_{01} \approx z\left(1 + \frac{1}{2}\left(\frac{x-\xi}{z}\right)^2 + \frac{1}{2}\left(\frac{y-\eta}{z}\right)^2\right). \tag{B.29}$$

This approximation is used for the exponent, while for the distance in the denominator of Eq. (B.27) only the first term is kept ($r_{01} \approx z$)

The Fresnel Approximation

In the Fresnel approximation the binomial expansion up to the second order in ξ, η is kept. It is valid when the lateral extent of the source and the detector are small compared to the distance between each other. It reads:

$$\mathcal{E}(x,y,z) = \frac{e^{ikz}}{i\lambda z}\iint_{-\infty}^{\infty}\mathcal{E}(\xi,\eta)e^{\frac{ik((x-\xi)^2+(y-\eta)^2)}{2z}}d\xi d\eta, \tag{B.30}$$

and denotes the so called **near-field**.

The Fraunhofer Approximation

The strongest approximation is the Fraunhofer stating that the source is much smaller than the distance between source and detector[5] $2z/k \gg (\xi,\eta)_{\max}$. Eq. (B.30) simplifies to

$$\mathcal{E}(x,y,z) = \frac{e^{ikz}}{i\lambda z}e^{\frac{ik}{2z}(x^2+y^2)}\underbrace{\iint_{-\infty}^{\infty}\mathcal{E}(\xi,\eta)e^{-\frac{ik}{z}(x\xi+y\eta)}}_{\text{Fourier transform}}d\xi d\eta. \tag{B.31}$$

The solution is called **far-field** and is directly the Fourier transform of the field distribution in the aperture (or more generally speaking of the source). Figure B.4 illustrates those three regimes.

[4] $\sqrt{1+b} = \frac{1}{2}b - \frac{1}{8}b^2 + ...$

[5] The word detector describes the location where the field is measured and in the frame work of this thesis is the region of interest.

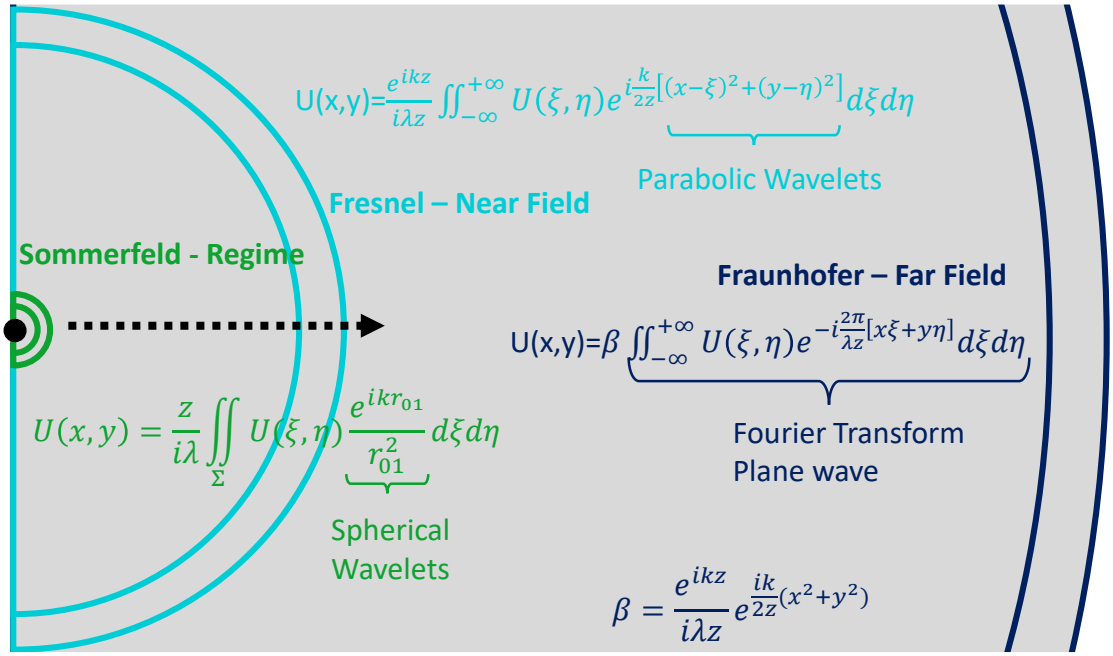

Figure B.4 | Approximations for near-field and far-field. This figure illustrates the propagation of waves. A spherical wave originating from a source is described in the Rayleigh-Sommerfeld approximation that is valid for all mono-energetic waves. In the so called near-field where the distance is larger than extensions of the source, the waveform can be approximated by parabolic wavelets. If the propagation distance is now much larger and the detection area small with respect to the source one can use the Fraunhofer approximation describing the so called far-field.

B.1.7 The Fourier Transform

We have thereby introduced one of the most powerful mathematical tools - the Fourier transformation[6] . In our case the Fourier transformation connects the electromagnetic field of a source to the field in its far-field. The Fourier transformation can be seen as a mathematical tool that is used to decompose a signal into its ingredients (frequency components). For example a complex sound signal can be dismantled into the different frequencies that it contains. This has the benefit that it is much easier to reproduce, modify or to filter existing transients out of the signal. The Fourier transform is essentially a base transformation, the convention used in

[6] *Fourier's theorem is not only one of the most beautiful results of modern analysis, but it may be said to furnish an indispensable instrument in the treatment of nearly every recondite question in modern physics,* Lord Kelvin in 1867.

this work is defined in this work as:

$$\mathcal{F}f\left(x\right) = \int_{-\infty}^{\infty} f\left(\xi\right) e^{i2\pi\xi x} d\xi \tag{B.32a}$$

$$\mathcal{F}^{-1}f\left(\xi\right) = \frac{1}{2\pi}\int_{-\infty}^{\infty} f\left(x\right) e^{-i2\pi\xi x} dx. \tag{B.32b}$$

The same holds true for a transformation from frequency f to time t. Equation (B.31) can thus be written as

$$\mathcal{E}(x,y,z) = \frac{e^{ikz}}{i\lambda z} e^{\frac{ik}{2z}(x^2+y^2)} \mathcal{F}\mathcal{E}\left(\frac{-x}{\lambda z}, \frac{-y}{\lambda z}\right). \tag{B.33}$$

With the spatial frequencies $-x/\lambda z$ and $-y/\lambda z$. This result shows that the field in the Fraunhofer approximation can be calculated by the Fourier transformation of its source term with some additional phase factors.

Focusing of a Laser Beam

Following Tyson [259] we can further show that starting with the Fresnel approximation in the focal plane of a thin lens yields the same result as the Fraunhofer approximation.. This remarkable results sets the basis of many imaging methods, since it allows the observation in the Fraunhofer regime for even larger source distributions without the need of long propagation distances.

Correlations of the Fourier Transform

One other direct consequence of the Fourier theorem that is of particular importance is the direct correlation between frequency-width (bandwidth) and pulse length. Two statements can be derived:

1. Short signal correlates with wide range of frequencies. This becomes relevant in the case of ultrashort laser pulses, requiring a large frequency bandwidth.

2. The Fourier transformation of a Gaussian is another Gaussian.

B.1.8 Time Dependence

In the derivation of the Kirchhoff/ Sommerfeld we considered a time-independent source and also a source that is located in a certain plane (perpendicular to the propagation direction z). The measured field was solely described as a function

of x,y and z. The source becomes time dependent for a non-monochromatic wave or simply time dependent source. This can mathematically realized by adding a temporal dependence to the Green's function. We can thus consider the field at the location of the detector $\vec{r}$ at a certain time t.

Another ansatz would be to describe a temporal dependent electrical field in its frequency domain using (Eq. (B.32))

$$\mathcal{E}\left(\vec{d},t\right) = \frac{1}{2\pi}\int_{-\infty}^{\infty}\tilde{\mathcal{E}}\left(\vec{d},\omega\right)e^{-i\omega t}d\omega. \tag{B.34}$$

Using the Rayleigh-Sommerfeld diffraction (Eq. (B.27)) for $\tilde{\mathcal{E}}\left(\vec{d}\right)$ yields

$$\begin{aligned}
\mathcal{E}\left(\vec{d},t\right) &= \frac{1}{2\pi}\int_{-\infty}^{\infty}\left[\frac{1}{i\lambda}\iint_{\Sigma}\tilde{\mathcal{E}}\left(\vec{s}\right)\frac{e^{ikr_{01}}}{r_{01}}\cos(\vec{n},\vec{n_{01}})ds\right]e^{-i\omega t}d\omega && \text{(B.35a)}\\
&= \frac{1}{2\pi}\iint_{\Sigma}\cos\left(\vec{n},\vec{n_{01}}\right)ds\int_{-\infty}^{\infty}\frac{i\omega}{2\pi c}\tilde{\mathcal{E}}\left(\vec{s}\right)\frac{e^{i\frac{\omega}{c}r_{01}-i\omega t}}{r_{01}}d\omega && \text{(B.35b)}\\
&= \frac{1}{2\pi}\iint_{\Sigma}\frac{\cos\left(\vec{n},\vec{n_{01}}\right)}{cr_{01}}ds\frac{1}{2\pi}\int_{-\infty}^{\infty}\left(-i\omega\right)\tilde{\mathcal{E}}\left(\vec{s}\right)e^{-i\omega\left(t-\frac{r_{01}}{c}\right)}d\omega && \text{(B.35c)}\\
&= \frac{1}{2\pi}\iint_{\Sigma}\frac{\cos\left(\vec{n},\vec{n_{01}}\right)}{cr_{01}}ds\frac{1}{2\pi}\int_{-\infty}^{\infty}\frac{\partial}{\partial t}\tilde{\mathcal{E}}\left(\vec{s}\right)e^{-i\omega\left(t-\frac{r_{01}}{c}\right)}d\omega && \text{(B.35d)}\\
&= \frac{1}{2\pi}\iint_{\Sigma}\frac{\cos\left(\vec{n},\vec{n_{01}}\right)}{cr_{01}}ds\frac{\partial}{\partial t}\mathcal{E}\left(\vec{s},t-\frac{r_{01}}{c}\right). && \text{(B.35e)}
\end{aligned}$$

This result again shows that the field measured at the detector at time t is dependent on the variation of the source at the retarded time (as introduced in Section 2.1).

B.1.9 Conclusion

We have derived the Rayleigh-Sommerfeld diffraction integral (Eq. (B.27)), stating that the electric field at any position behind a slit can be seen as the sum of individual spherical wave sources as stated by Huygens principle. The summed electric field can thus be seen as a sum of individual waves according to

$$\vec{\mathcal{E}}_{total} = \sum_{m}\vec{\mathcal{E}}_{m}\left(\vec{r},t\right)e^{i\phi_{\mathrm{m}}}. \tag{B.36}$$

This equation describes the superposition of fields. Superimposed fields will interfere with each other. Interference can amplify the field (constructive interference) or

attenuate it (destructive interference), depending on the phase-relation between the fields. We have further shown how the propagation of a wave can be calculated when the boundary conditions and source terms are given. The electrical field in the focus of a lens can for example be calculated with the Fourier transform when the field at the lens position is given and vice versa. In conclusion the amplitude and the phase of a wave carry all the information about its source (when the complete properties of the propagation are known).

Measurements

The ability to see is one of the most substantial human senses. It is thus reasonable that optical measurement and imaging techniques are among the most important ones. A common camera as well as our eyes detect only the intensity, allowing the reconstruction of the electric field amplitude, but lacking phase information. Many optical measurement techniques seek to not only acquire the amplitude but also the phase of a wave. This can be done by exploiting the interferometric nature of waves. Using interferometric methods further can increase the resolution and sensitivity significantly (smaller than a wavelength), exploiting that the phase changes by 2π over just a wavelength. One of the earliest realizations of such measurements has been done with a Michelson interferometer [260]. One example where such sensitivity has been pushed to its limits is the LIGO facility [261] leading to the discovery of gravitational waves [262]. Another prominent examples is holography [263]. In the framework of this thesis interferometric autocorrelation is used to measure the pulse length and temporal contrast of a laser pulse. A different approach of measuring the phase is typically applied to measure the wave front of light for laser systems but also very commonly in the field of astronomy using a Shack-Hartmann sensor [264].

B.2 Some Basics of (Laser) Light

This section describes some basic concepts of light and in particular laser light for a deeper understanding of several parts within this work. The section follows [265]. In Table B.1 we have summarized some important quantities of laser light. The Sellmeier formula can be used to calculate the refractive index for a certain

Name	Symbol	Calculation	Description
Wavelength	λ_L		The wavelength of a laser is determined by the material and geometrical setup of the cavity. It is the length of a complete wave period in space.
Frequency	f_L	$f = v \cdot \lambda_\mathrm{L}^{-1}$	With v being the velocity in a medium (speed of light (c) in vacuum).
Wavenumber	k	$k = 2\pi \cdot \lambda_\mathrm{L}^{-1}$	The wave number is commonly when describing the wave mathematically.
Angular Frequency	ω_L	$\omega_\mathrm{L} = 2\pi f_\mathrm{L}$	The angular frequency is more commonly used.
Refractive index	n	$n = v \cdot c^{-1}$	The refractive index is the ratio between the the velocity of light in the material (v) and vacuum (c). A wavelength dependent refractive index will thus disperse the beam. It can be calculated with the Sellmeier formula (see Eq. (B.37)).

Table B.1 | Laser quantities. This table summarizes a few of the most important quantities of light and in particular laser pulses.

wavelength of a material, whereas A_i and λ_i are material dependent properties:

$$n(\lambda) = \sqrt{1 + \sum_{i=1}^{3} \frac{A_\mathrm{i} \cdot \lambda^2}{\lambda^2 - \lambda_\mathrm{i}^2}}. \tag{B.37}$$

B.2.1 Polarization of Light

The polarization describes the orientation of the electric field oscillations of a wave. A linear polarized wave oscillates along one axis. Conversely, in circularly polarized

light the polarization rotates constantly while the field magnitude stays constant. Elements cleaning the temporal laser contrast change the orientation of polarization and uses polarizers to filter the beam. The polarization of light plays an important role when impinging onto material. If part of the polarization is directed along the normal of of the material's surface it is called p-polarized. If all parts are parallel it is called s-polarized.

B.2.2 Reflectance and Brewster Angle

The reflectance R of a reflecting surface is defined by the Fresnel equation and yields for non-magnetic media

$$R_\mathrm{s} = \left[\frac{n_1 \cos\Theta_\mathrm{i} - n_2 \cos\Theta_\mathrm{t}}{n_1 \cos\Theta_i + n_2 \cos\Theta_\mathrm{t}}\right]^2 \qquad R_\mathrm{p} = \left[\frac{n_1 \cos\Theta_t - n_2 \cos\Theta_\mathrm{i}}{n_1 \cos\Theta_\mathrm{t} + n_2 \cos\Theta_\mathrm{i}}\right]^2, \tag{B.38a}$$

where Θ_i and Θ_t are the angles of the incoming and transmitted light. With the use of Snell's law $n_1 \sin\Theta_\mathrm{i} = n_2 \sin\Theta_\mathrm{t}$ one can find an angle Θ_B where R_p becomes zero. This so called Brewster angle is defined as

$$\Theta_B = \arctan\frac{n_2}{n_1}, \tag{B.39}$$

and is favorable when introducing a transmissive optics in a laser chain in order to minimize losses. In the case of normal incidence the reflectance coefficient reduces to

$$R_0 = \left[\frac{n_1 - n_2}{n_1 + n_2}\right]^2. \tag{B.40}$$

Note that the reflectance R is associated with the intensity of light. The reflectivity r in contrast is used for the electromagnetic wave with $R = |r|^2$.

B.2.3 Group Velocity Dispersion

Another important quantity is the GVD. Let us consider a short laser pulse. The pulse consists of the envelope and the underlying oscillating signal. The phase velocity describes the propagation of the phase in space and is defined as $v_\mathrm{p} = \omega/k$. The group velocity instead is the the movement speed of the envelope and thus also the only transportation of information. It is defined as $v_\mathrm{g} = \partial\omega/\partial k \leq c$ and is limited to the speed of light. Another important quantity is the dispersion relation that describes the wavelength dependent behavior of a wave traveling through a

medium. The most important quantity in the framework of this thesis is the phase velocity $v = v(\lambda)$. This frequency dependent velocity causes GVD, describing the dispersion of a short pulse within a medium. In particular when a short laser pulse travels through a medium the pulse will disperse and thus typically be stretched in time. Another important aspect is the wavelength dependent diffraction or reflection angle that is key element of high power lasers as it is the key to the CPA mechanism.

B.2.4 Spatial Intensity Distribution

When the spatial intensity distribution is mentioned it is often referred to as *"focal size"*. This expression is not clearly defined but most commonly describes either the FWHM or beam waist of a Gaussian distribution. The focal plane of a laser with Gaussian beam profile is depicted in Fig. B.5. We have seen in Section B.1 that the electric field of a wave in the focus of length can be obtained by the Fourier transformation of the collimated beam. Therefore, the shape in focal plane of a Gaussian laser pulse is another Gaussian. One important quantity is the Rayleigh

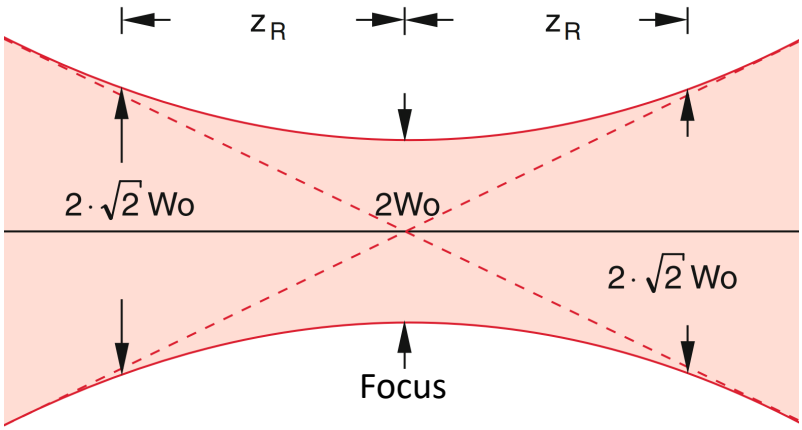

Figure B.5 | Sketch of a laser focus. This sketch shows the geometry of a Gaussian laser focus. It thus introduces the Rayleigh length z_R and the Gaussian width W_0. Adapted from [266].

length z_R. The Rayleigh length defines the distance to the focal plane where the area has doubled and thus the intensity is halved.

$$z_R = \frac{\pi 2 W_0}{\lambda_\mathrm{L}}, \tag{B.41}$$

where $2W_0$ is again the focal spot size. In many laser systems due to the damage threshold of the optics the collimated beam profile is designed to be flat top (homogeneous intensity distribution). Its Fourier transformation is a sinc-function and thus the focal size could also be attributed as the area to the first minimum of the sinc.

B.2.5 Resolution of an Optical System

The resolution of an optical system is limited by the Abbe criterion. The minimum distance d_A of two lines or points that can be resolved is:

$$d_{\mathrm{A}} = \frac{\lambda}{2NA}. \tag{B.42}$$

The second commonly accepted criteria for resolution is the Rayleigh limit. In the image plane (focus of the lens) a point source creates a diffraction pattern (Fraunhofer limit). This diffraction pattern is defined by the Bessel function. Rayleigh states that two point sources can be resolved when maximum of the second is at the minimum of the first. The Abbe limit thus is evolved to

$$d_{\mathrm{R}} = 1.22\frac{\lambda}{2NA}. \tag{B.43}$$

B.3 Nonlinear Optics

The field of nonlinear optics describes a nonlinear reaction to the electric field $\vec{\mathcal{E}}$ of light. It has first been experimentally demonstrated with the generation of second harmonics [267]. Including the nonlinear refractive index, the total refractive index can be calculated

$$n = n_0 + n_2 I + \mathcal{O} = n_0 + n_2'|E|^2 + \mathcal{O}, \tag{B.44}$$

with the nonlinear refractive index $n_2$in SI units and n_2' in esu units, and $\mathcal{O}$ representing higher orders of nonlinearity. The nonlinearity is highly material dependent defined by the nonlinear refractive index n_2' [268, 269]

$$n_2'(10^{-13}esu) = \frac{68(n_d-1)(n_d^2+2)^2}{v_{\mathrm{d}} \cdot \sqrt{1.52 + v_{\mathrm{d}}\frac{(n_{\mathrm{d}}^2+2)(n_{\mathrm{d}}+1)}{6n_{\mathrm{d}}}}}, \tag{B.45}$$

where v_d is the Abbe number and n_d the refractive index at 587 nm[7]. With

$$n_2 = n_2' \frac{40\pi}{c n_0}, \tag{B.46}$$

its value in SI units can be calculated. Since the value for n_2 is typically really small it can be neglected for most applications. Only if the electromagnetic field is intense such as for high power lasers, its influence starts to become significant. In such cases the nonlinearity can severely alter the laser pulse, caused by different mechanisms:

1. **Self-focusing**: In the case of a **Gaussian spatial** distribution the inner and more intense parts will be retarded and can lead to self-focusing at a certain intensity.

2. **Self-phase-modulation**: In the case of a **Gaussian temporal** distribution the central part of the temporal envelope experiences higher intensities and thus intensified nonlinear effects leading to a broadening of the pulse and a modulation of its phase.

One relevant quantity is the so called B-integral.

$$B_\mathrm{int} = \frac{2\pi}{\lambda_0} \int \frac{\Delta n(I)}{n_0} dl \leq 1, \tag{B.47}$$

where $\Delta n(I) = n_2 I + \mathcal{O}$ describes all higher order effects that are accumulated over a certain length l. The condition of $B \leq 1$ is equal to the accumulated phase shift $< \lambda$. This limit is a rule of thumb and describes until when effects can be handled. The B-Integral can be minimizing by reducing the path length through material or lowering the intensity therein. Since the first option is often not possible the intensity has to be reduced, which is one motivation for CPA.

Despite several drawbacks, nonlinear effects play a significant role in many optical fields and also in the generation of high power laser systems. Two examples are:

1. **Pump laser**: In the framework of this work the laser was based on Ti:sapphire systems. The laser crystals are typically pumped by Nd:YAG-lasers, whose frequency of 1064nm is doubled to 532nm using nonlinear effects.

2. **XPW**: An XPW uses nonlinear effects to rotate the polarization of light. In a setup with crossed polarizers it can be adjusted such that only the highest

[7] $v_\mathrm{d} = (n_d - 1)/(n_\mathrm{F} - n_\mathrm{c})$ and the n are the refractive indices at certain wavelength n_F ($\lambda_F = 486nm$), n_d ($\lambda_\mathrm{d} = 587nm$) and n_c ($\lambda_c = 656nm$).

intensity is rotated by 90 degree within the crystal and therefore the temporal pulse profile can be steepened.

B.4 Optical Devices for High-Power Laser Systems

B.4.1 Sequoia and Tundra: Third-Order Autocorrelators

Autocorrelation describes the correlation of a signal with itself. Thereby the signal is duplicated and both are overlapped with a varying delay. The frequency of the duplicated signal can hereby be modified to its second harmonic (second-order autocorrelation) or third harmonic (third-order autocorrelation). High power laser systems use third-order auto-correlation to scan the temporal contrast of the system [148, 149]. One of the arms is frequency doubled with a nonlinear crystal. Overlapping both arms in second nonlinear crystal leads to an intensity dependent generation of the third harmonic that further is measured. By changing the delay between both arms the temporal distribution is scanned. The drawback of a second-order autocorrelator is that a prepulse will create a measurement artifact as a postpulse and vice versa. A third-order autocorrelator has the advantage that the intensity of the artifact, even though still detected, will only the square-root of its origin and can thus be recognized. The commonly used devices are the Sequoia[8] or the Tundra[9].

B.4.2 Pockels Cell

The core part of a Pockels cell is an electro-optical crystal with electric field dependent birefringence. By applying or changing an adjacent electric field the birefringence can be changed. This can in the right configuration cause a rotation of the polarization. This effect has been studied by Pockels [270]. By adjusting the high voltage that creates the electric field and the length of the Pockels cell the polarization can be set to rotate by 90 degree (half-wave operation). With the use of polarizers a very fast (sub ns) switch can be created. The typical configuration is to position the Pockels cell between two polarizers that are rotated by 90 degree

[8] Amplitude Technologies.
[9] Ultrafast Innovation.

with (cross polarized). In this configuration the light will be blocked (e.g. redirected by the second polarizer) and the ratio between the reflected and transmitted light is the called extinction ratio $r_e = P_t/P_r$, where P is the power of the light. When the Pockels cell now is switched active, the polarization rotates by 90 degree and the complete light is transmitted. In high power laser systems this is used as an ultra-fast (sub ns) optical switch. In the configuration for CALA the polarizers are oriented parallel and only when the Pockels cell is switched on the polarization will be turned and the laser light blocked. The Pockels cell will thus be operated when the reflected light is on its way downstream. Although this approach involves the risk of causing damage whenever the Pockels cell is malfunctioning[10], it can be positioned in the beam-path optionally without the need of further optics to rotate the polarization by another 90 degree. The polarizers are typically operated at the Brewster angle (see Section B.2.2). A set of polarizers is used to account for the beam offset that is introduced when traversing one polarizer. Further note that the Pockels cell will modify the stretch of the pulse due to the nonlinear refractive index and further introduce a pulse front tilt, since the optics are wedged in order to prevent the generation of postpulse in the same mode.

[10]The risk is obsolete when turned on active upstream, since a malfunctioning cell would prevent the beam from propagating further at first hand.

List of Symbols and Abbreviations

Symbols

Abbreviation		SI unit/value
c	speed of light in vacuum	299792458 ms^{-1}
ϵ_0	vacuum permittivity	$8.854...\times10^{-12}$ $\mathrm{A}^2\mathrm{s}^4\mathrm{kg}^{-1}\mathrm{m}^{-3}$
μ_0	vacuum permeability	$4\pi \times 10^{-7}$ TmA^{-1}
k_B	Boltzmann constant	$1.38064852(79) \times 10^{-23}$ JK^{-1}
e	elementary charge	$1.6021766208(98) \times 10^{-19}$ C
r_e	classical electron radius	2.8179403227(19) fm
m_e	electron rest mass	$9.10938356(11) \times 10^{-31}$ kg
m_p	proton rest mass	$1.672621898(21) \times 10^{-27}$ kg
N_A	Avogardo's number	$6.022140857(74) \times 10^{23}$ mol^{-1}
λ	wavelength	m
ω, ω_0	angular frequency	s^{-1}
I	intensity	Wm^{-2}
E	energy	J
eV	electronvolt	1.60218×10^{-19} J
$\mathcal{E}$	electric fields	Vm^{-1}
$\mathcal{B}$	magnetic fields	T
T_e, $(T = k_\mathrm{B}T_\mathrm{e})$	temperature	K, (J)

Abbreviations

ASE **A**mplified **S**pontaneous **E**mission

ATLAS-3000 **A**dvanced **T**i:Sapphire **LAS**er **3000** Terawatt

ATLAS-300 **A**dvanced **T**i:Sapphire **LAS**er **300** Terawatt

BIRD **B**road **I**nfra**r**ed **D**iagnostics

BS **B**lock **S**hutter

BSI **B**arrier **S**uppression **I**onization

CALA **C**entre for **A**dvanced **L**aser **A**pplications

CCD **C**harge **C**oupled **D**evice

CPA **C**hirped **P**ulsed **A**mplification

CW **C**ontinuos **W**ave

DRACO **DR**esden Laser **AC**celeration **S**ource

DM **D**iploe **M**agnet

EMP **E**lectro **M**agnetic **P**ulse

ETTF **E**lectron and **T**homson **T**est **F**acility

FEL **F**ree **E**lectron **L**asers

FWHM **F**ull **W**idth at **H**alf **M**axiumum

GVD **G**roup **V**elocity **D**ispersion

HDR **H**igh **D**ynamic **R**ange

HF **H**igh **F**ield Physics

HZDR **H**elmholtz-**Z**entrum **D**resden-**R**ossendorf

I-BEAT **I**on-**B**unch **E**nergy **A**coustic **T**racing

ILDIAS **I**ntegrated **L**aser-**D**riven **I**on **A**ccelerator **S**ystem

IP **I**mage **P**late

Laser **L**ight **A**mplification by **S**timulated **E**mission of **R**adiation

LIGO **L**aser **I**nterferometer **G**ravitational-Wave **O**bservatory

LBD **L**aser-**B**eam-**D**elivery

LET **L**inear **E**nergy **T**ransfer

LEX Photonics **L**aboratory for **EX**treme Photonics

LION **L**aser-driven **ION** acceleration

LUX **L**aser-driven **U**ndulater **X**-ray source

MCP **M**icro-**C**hannel **P**late

MLL **M**aier-**L**eibnitz **L**aboratory

MPI **M**ulti-**P**hoton **I**onization

MuCLs **Mu**nich **C**ompact **L**ight **s**ource

n-FTPS **n**ano-**F**oil **T**arget **P**ositioning **S**ystem

OAP **O**ff-**A**xis **P**arabolic mirror

OPA **O**ptical **P**arametric **A**mplification

OPCPA **O**ptical **P**arametric **C**hirped **P**ulse **A**mplification

PHELIX **P**etawatt **H**och-**E**nergie **L**aser für Schwer**I**onene**X**perimente

PFS **P**etawatt **F**ield **S**ynthesizer

PMQ **P**ermanent **M**agnetic **Q**uadrupole

QPs **Q**uadru**P**oles

REGEN **Regen**erative amplifier

RCF **R**acio**C**hromic **F**ilm

RPA **R**adiation **P**ressure **A**cceleration

SB3 **S**witch **B**ox **3**

SNR **S**ignal to **N**oise **R**atio

SPECTRE **S**ource for **P**owerful **E**nergetic **C**ompact **T**homson **R**adiation **E**xperiments

STC **S**patio-**T**emporal **C**oupling

STID **S**patio-**T**emporal **I**ntensity **D**istribution

TCC **T**arget **C**hamber **C**enter

Ti:sapphire **T**itanium **S**apphire

TNSA **T**arget **N**ormal **S**heath **A**cceleration

TM1 **T**urning **M**irror 1

TM2 **T**urning **M**irror 2

TOF **T**ime-**O**f-**F**light spectrometer

TRIC **T**emporally **R**esolved **I**ntensity **C**ontouring

WASP **W**ide **A**ngle **SP**ectrometer

XPW cross (**X**) **P**olarized **W**ave generation

ZEUS **Z**inths **E**xtremely **U**seful **S**uperlaser

ZS **Z**entrale **S**teuerung

Publications and Conference Contributions

Peer-Reviewed Publications

Diagnostics for Laser Plasma Experiments

1. **D. Haffa**, J. H. Bin, M. Speicher, K. Allinger, J. Hartmann, C. Kreuzer, E. Ridente, T. M. Ostermayr and J. Schreiber. Temporally Resolved Intensity Contouring (TRIC) for characterization of the absolute spatio-temporal intensity distribution of a relativistic, femtosecond laser pulse. *Scientific Reports volume 9*, Article number: 7697, 2019.

2. **D. Haffa**, R. Yang, J. H. Bin, S. Lehrack, F. Brack, H. Ding, F. S. Englbrecht, Y. Gao, J. Gebhard, M. Gilljohann, J. Gtzfried, J. Hartmann, S. Herr, P. Hilz, S. D. Kraft, C. Kreuzer, F. Kroll 5,6, F. H. Lindner 1, J. Metzkes-Ng, T. M. Ostermayr, E. Ridente1, T. F. Rsch1, G. Schilling, H. Schlenvoigt, M. Speicher, D. Taray, M. Wrl1, K. Zeil, U. Schramm, S. Karsch, K. Parodi, P. R. Bolton, W. Assmann and J. Schreiber. I-BEAT: Ultrasonic method for online measurement of the energy distribution of a single ion bunch. *Scientific Reports volume 9*, Article number: 6714 , 2019.

3. M. Würl, F. S. Englbrecht, S. Lehrack , C. Gianoli, F. H. Lindner , T. F. Rsch, **D. Haffa**, F. Olivari, M. Petasecca, M. L. F. Lerch, A. Pogossov, L. T. Tran, W. Assmann, J. Schreiber , A. B. Rosenfeld and K. Parodi. Time-of-flight spectrometry of ultra-short, polyenergetic proton bunches. *Rev. Sci. Instrum. 89*, 123302, 2018.

4. F. Lindner, J. Bin, F. Englbrecht, **D. Haffa**, P.R. Bolton, Y. Gao, J. Hartmann, P. Hilz, C. Kreuzer, T. Ostermayr, T. Rösch, M. Speicher, K. Parodi, P. Thirolf and J. Schreiber. A novel approach to electron data background treatment in a new online wide- angle spectrometer for laser-accelerated ion and electron bunches. *Rev. Sci. Instrum. 89, 013301*, 2018.

5. J. Hartmann, **D. Haffa**, M. Speicher, J. H. Bin, P. Hilz, C. Kreuzer, T.

Ostermayr, S. Lehrack, J. Schreiber. The spatial contrast challenge for intense laser-plasma experiments, *IOP Conf. Series: Journal of Physics: Conf. Series 1079 012003*, 2018.

Target Development for Laser-Driven Ion Acceleration

6. T. Ostermayr, **D. Haffa**, P. Hilz, V. Pauw, K. Allinger, K.-U. Bamberg, P. Böhl, C. Bömer, P. R. Bolton, F. Deutschmann, T. Ditmire, M. E. Donovan, G. Dyer, E. Gaul, J. Gordon, B. M. Hegelich, D. Kiefer, C. Klier, C. Kreuzer, M. Martinez, E. McCary, A. R. Meadows, N. Moschüring, T. Rösch, H. Ruhl, M. Spinks, C. Wagner, and J. Schreiber. Proton acceleration by irradiation of isolated spheres with an intense laser pulse. *Physical Review E*, 94(3):033208, 2016.

7. P. Hilz, T. Ostermayr, A.Huebl, V.Bagnoud, M.Bussmann, M.Gallei, **D. Haffa**, T.Kluge, C.Schaefer, B.Zielbauer and J. Schreiber, Isolated proton bunch acceleration by a petawatt laser pulse, *Nature Communications* Volume 9, Article number: 423, 2018.

8. M. Speicher, **D. Haffa**, M. A. O. Haug, J. H. Bin, Y. Gao, J. Hartmann, P. Hilz, C. Kreuzer, F.H. Lindner, T. Ostermayr, T.F. Rösch, R. Yang, J. Schreiber. Integrated double-plasma-mirror targets for contrast enhancement in laser ion acceleration, *IOP Conf. Series: Journal of Physics:* Conf. Series 1079 012002, 2018.

9. Y. Gao, J. H. Bin, **D. Haffa**, C. Kreuzer, J. Hartmann, M. Speicher, F. H. Lindner, T. Ostermayr, P. Hilz, T. F. Rösch, S. Lehrack, F. S. Englbrecht, S. Seuferling, M. Gilljohann, H. Ding, W. Ma, K Parodi, J. Schreiber, An automated, 0.5 hz nano-foil target positioning system for intense laser plasma experiments. *High Power Laser Science and Engineering*, 5, 2017.

10. T. Ostermayr, J. Gebhard, **D. Haffa**, D. Kiefer, C. Kreuzer, K. Allinger, C. Bömer, J. Braenzel, M. Schnürer, I. Cermak, J. Schreiber, and P. Hilz. A transportable Paul-trap for levitation and accurate positioning of micron-scale particles in vacuum for laser-plasma experiments. *Review of Scientific Instruments* 89, 013302, 2018.

11. M. Zhou, J. H. Bin, **D. Haffa**, X. Q. Yan and J. Schreiber. The impact of femtosecond pre-pulses on nanometer thin foils for laser-ion acceleration. *Plasma Phys. Control. Fusion 59*, 055020 (5pp), 2017.

12. S. Seuferling, M. A. O. Haug, P. Hilz, **D. Haffa**, C. Kreuzer and J. Schreiber. Efficient offline production of freestanding thin plasticfoils for laser-driven ion sources. *High Power Laser Science and Engineering*, Vol. 5, e8, 2017.

Applications for Laser-Driven Ion Sources

13. F. Lindner, **D. Haffa**, J. H. Bin, F. Englbrecht, Y. Gao, J. Gebhard, J. Hartmann, P. Hilz, C. Kreuzer, S. Lehrack, T. Ostermayr, T. Rösch, M. Speicher, M. Würl, K. Parodi, J. Schreiber, and P. Thirolf. Towards swift ion bunch acceleration by high-power laser pulses at the center for advanced laser applications (CALA). *Nuclear Instruments and Methods in Physics Research Section B*, 2017.

Submitted Manuscripts

14. T. M. Ostermayr, C. Kreuzer, F. S. Englbrecht, J. Gebhard, J. Hartmann, **D. Haffa**, P. Hilz, K. Parodi, J. Wenz,1 M. E. Donovan, G. Dyer, E. Gaul, J. Gordon, M. Martinez, E. Mccary, M. Spinks, G. Tiwari, B. M. Hegelich and J. Schreiber. Simultaneous single-shot radiographic imaging with a laser-driven x-ray and 2 proton micro-source. *Submitted*, 2019.

15. T. F. Rösch, Z. Szabó, **D. Haffa**, J. H. Bin, S. Brunner, F. S. Englbrecht, A. A. Friedl, Y. Gao, J. Hartmann, P. Hilz, C. Kreuzer, F. H. Lindner, T. M. Ostermayr, R. Polanek, M. Speicher, E. R. Szabó, D. Taray, T. Tőkés, M. Würl, K. Parodi, K. Hideghéty and J. Schreiber. A feasibility study of zebrafish embryo irradiation with laser accelerated protons. *Submitted*, 2019

Conference Contributions

- **Invited:** *Towards viable Laser-driven ION (LION) sources for applications LION at the Center for Advanced Laser Applications (CALA)*, 3rd ELIMED Workshop, Catania, 2016
- **Invited:** *Towards viable Laser-driven ION (LION) sources for applications LION at the Center for Advanced Laser Applications (CALA)*, 4th ELI-Alps User Workshop, Hungary, 2016
- **Poster:** *Viable Laser-driven Ion Source for Application at CALA*, 3rd European Advanced Accelerator Concepts Workshop, La Biodola (Isola d'Elba), Italy, 2017
- **Oral:** *CALA and I-BEAT - Laser-based Ion acceleration and detection in Munich*, LIGHT Meeting, Darmstadt, Germany, 2018

Bibliography

[1] D. Goodstein and J. R. Goodstein. *Feynman's Lost Lecture*. Pap/Com. W. W. Norton & Company, Nov. 2009.

[2] W. Röntgen. "Ueber Eine Neue Art von Strahlen. Vorläufige Mitteilung." In: Sitzungsberichte Der Physikalisch-Medicinsichen Gesellschaft Zu Würzburg 9. Würzburg: Verlag und Druck der Stahel'schen K. Hof- und Universitäts-Buch- und Kunsthandlung, 1895, pp. 132–141.

[3] W. Röntgen. "Ueber Eine Neue Art von Strahlen. 2. Mitteilung." In: Sitzungsberichte Der Physikalisch-Medicinsichen Gesellschaft Zu Würzburg. Würzburg: Verlag und Druck der Stahel'schen K. Hof- und Universitäts-Buch- und Kunsthandlung, 1896, pp. 1–9.

[4] W. Röntgen. "Weitere Beobachtungen Über Die Eigenschaften Der X-Strahlen." In: vol. Band Erster Halbband. Sitzungsberichte Der Königlich Preußischen Akademie Der Wissenschaften Zu Berlin. Berlin: Verl. d. Kgl. Akad. d. Wiss., 1897, pp. 576–592.

[5] J. Thariat et al. "Past, Present, and Future of Radiotherapy for the Benefit of Patients." In: *Nature Reviews Clinical Oncology* 10.1 (Jan. 2013), pp. 52–60.

[6] F. M. Khan and J. P. Gibbons. *Khan's the Physics of Radiation Therapy*. OCLC: 863383298. 2014.

[7] H. Paganetti. *Proton Beam Therapy*. 2399-2891. IOP Publishing, 2017.

[8] W. D. Newhauser and R. Zhang. "The Physics of Proton Therapy." In: *Physics in Medicine and Biology* 60.8 (Apr. 2015), R155–R209.

[9] S. Matsumoto et al. "High Gradient Test at Nextef and High-Power Long-Term Operation of Devices." In: *Nuclear Instruments and Methods in Physics Research Section A: Accelerators, Spectrometers, Detectors and Associated Equipment* 657.1 (2011), pp. 160–167.

[10] A. Degiovanni, W. Wuensch, and J. Giner Navarro. "Comparison of the Conditioning of High Gradient Accelerating Structures." In: *Phys. Rev. Accel. Beams* 19.3 (Mar. 2016), p. 032001.

[11] E. Esarey, C. B. Schroeder, and W. P. Leemans. "Physics of Laser-Driven Plasma-Based Electron Accelerators." In: *Reviews of Modern Physics* 81.3 (Aug. 2009), pp. 1229–1285.

[12] M. Roth et al. "Bright Laser-Driven Neutron Source Based on the Relativistic Transparency of Solids." In: *Physical Review Letters* 110.4 (Jan. 2013).

[13] K. Khrennikov et al. "Tunable All-Optical Quasimonochromatic Thomson X-Ray Source in the Nonlinear Regime." In: *Physical Review Letters* 114.19 (May 2015).

[14] A. Macchi, M. Borghesi, and M. Passoni. "Ion Acceleration by Superintense Laser-Plasma Interaction." In: *Reviews of Modern Physics* 85.2 (May 2013), pp. 751–793.

[15] H. Daido, M. Nishiuchi, and A. S. Pirozhkov. "Review of Laser-Driven Ion Sources and Their Applications." In: *Reports on Progress in Physics* 75.5 (2012), p. 56401.

[16] J. Schreiber, P. R. Bolton, and K. Parodi. "Invited Review Article: "Hands-on" Laser-Driven Ion Acceleration: A Primer for Laser-Driven Source Development and Potential Applications." In: *Review of Scientific Instruments* 87.7 (July 2016), p. 071101.

[17] T Cowan et al. "Ultralow Emittance, Multi-MeV Proton Beams from a Laser Virtual-Cathode Plasma Accelerator." In: *Phys. Rev. Lett.* 92.20 (May 2004), p. 204801.

[18] S. Busold et al. "Towards Highest Peak Intensities for Ultra-Short MeV-Range Ion Bunches." In: *Scientific Reports* 5.1 (Dec. 2015).

[19] B. Dromey et al. "Picosecond Metrology of Laser-Driven Proton Bursts." In: *Nature Communications* 7 (Feb. 2016), p. 10642.

[20] T. Ostermayr. "Relativistically Intense Laser-Microplasma Interactions." PhD Thesis. Munich: LMU Munich, 2017.

[21] T. Maiman. "Stimulated Optical Radiation in Ruby." In: *Nature* 187 (Aug. 1960), pp. 493–494.

[22] J. Schreiber. "Ion Acceleration Driven by High-Intensity Laser Pulses." PhD thesis. Ludwig-Maximilians-Universität, München, 2006.

[23] G. A. Mourou, T. Tajima, and S. V. Bulanov. "Optics in the Relativistic Regime." In: *Rev. Mod. Phys.* 78.2 (Apr. 2006), pp. 309–371.

[24] V. Yanovsky et al. “Ultra-High Intensity- 300-TW Laser at 0.1 Hz Repetition Rate.” In: *Optics Express* 16.3 (2008), p. 2109.

[25] S.-W. Bahk et al. “Generation and Characterization of the Highest Laser Intensities (10 22 W/Cm 2).” In: *Optics letters* 29.24 (2004), pp. 2837–2839.

[26] F. J. McClung and R. W. Hellwarth. “Giant Optical Pulsations from Ruby.” In: *Journal of Applied Physics* 33.3 (1962), pp. 828–829.

[27] T. Brabec et al. “Kerr Lens Mode Locking.” In: *Opt. Lett.* 17.18 (Sept. 1992), pp. 1292–1294.

[28] J. Kerr LL.D. “XL. A New Relation between Electricity and Light: Dielectrified Media Birefringent.” In: *Philosophical Magazine Series 4* 50.332 (1875), pp. 337–348.

[29] J. Kerr LL.D. “LIV. A New Relation between Electricity and Light: Dielectrified Media Birefringent (Second Paper).” In: *Philosophical Magazine Series 4* 50.333 (1875), pp. 446–458.

[30] D. E. Spence, P. N. Kean, and W. Sibbett. “60-Fsec Pulse Generation from a Self-Mode-Locked Ti:Sapphire Laser.” In: *Opt. Lett.* 16.1 (Jan. 1991), pp. 42–44.

[31] D. Strickland and G. Mourou. “Compression of Amplified Chirped Optical Pulses.” In: *Optics Communications* 56.3 (1985), pp. 219 –221.

[32] P. Maine et al. “Generation of Ultrahigh Peak Power Pulses by Chirped Pulse Amplification.” In: *IEEE Journal of Quantum Electronics* 24.2 (Feb. 1988), pp. 398–403.

[33] P. F. Moulton. “Spectroscopic and Laser Characteristics of Ti:Al2O3.” In: *J. Opt. Soc. Am. B* 3.1 (Jan. 1986), pp. 125–133.

[34] Committee on Opportunities in the Science, Applications, and Technology of Intense Ultrafast Lasers et al. *Opportunities in Intense Ultrafast Lasers: Reaching for the Brightest Light*. Washington, D.C.: National Academies Press, Jan. 2018.

[35] V. Veksler. “Coherent Principle of Acceleration of Charged Particles.” In: *CERN Symposium on High Energy Accelerators and Pion Physics* 1 (1956), p. 80.

[36] T. Tajima and J. M. Dawson. “Laser Electron Accelerator.” In: *Phys. Rev. Lett.* 43 (1979), pp. 267–270.

[37] E Esarey, C Schroeder, and W Leemans. "Physics of Laser-Driven Plasma-Based Electron Accelerators." In: *Reviews of Modern Physics* 81.3 (Aug. 2009), pp. 1229–1285.

[38] R. A. Snavely et al. "Intense High Energy Proton Beams from Petawatt-Laser Irradiation of Solids." In: *Phys. Rev. Lett.* 85.14 (2000).

[39] E. L. Clark et al. "Measurements of Energetic Proton Transport through Magnetized Plasma from Intense Laser Interactions with Solids." In: *Phys. Rev. Lett.* 84.4 (Jan. 2000), pp. 670–673.

[40] A. Maksimchuk et al. "Forward Ion Acceleration in Thin Films Driven by a High-Intensity Laser." In: *Physical Review Letters* 84.18 (May 2000), pp. 4108–4111.

[41] G. D. Tsakiris et al. "Experimental Studies of the Bilateral Ion Blowoff from Laser-Irradiated Thin Plastic Foils." In: *Physical Review Letters* 46.18 (May 1981), pp. 1202–1206.

[42] S. J. Gitomer et al. "Fast Ions and Hot Electrons in the Laser–Plasma Interaction." In: *Physics of Fluids* 29.8 (1986), p. 2679.

[43] M. Speicher et al. "Integrated Double-Plasma-Mirror Targets for Contrast Enhancement in Laser Ion Acceleration." In: *Journal of Physics: Conference Series* 1079 (Aug. 2018), p. 012002.

[44] F. Wagner et al. "Maximum Proton Energy above 85 MeV from the Relativistic Interaction of Laser Pulses with Micrometer Thick CH 2 Targets." In: *Physical Review Letters* 116.20 (May 2016).

[45] I. J. Kim et al. "Radiation Pressure Acceleration of Protons to 93 MeV with Circularly Polarized Petawatt Laser Pulses." In: *Physics of Plasmas* 23.7 (2016), p. 070701.

[46] A. Higginson et al. "Near-100 MeV Protons via a Laser-Driven Transparency-Enhanced Hybrid Acceleration Scheme." In: *Nature Communications* 9.1 (Dec. 2018).

[47] P. R. Bolton, K. Parodi, and J. Schreiber. *Applications of Laser-Driven Particle Acceleration*. 1st ed. Boca Raton: Taylor & Francis Inc, June 2018.

[48] T. Sokollik et al. "Directional Laser-Driven Ion Acceleration from Microspheres." In: *Phys. Rev. Lett.* 103 (2009), p. 135003.

[49] S Ter-Avetisyan et al. "Quasimonoenergetic Deuteron Bursts Produced by Ultraintense Laser Pulses." In: *Phys. Rev. Lett.* 96.14 (Apr. 2006), p. 145006.

[50] S Ter-Avetisyan et al. "Generation of a Quasi-Monoergetic Proton Beam from Laser-Irradiated Sub-Micron Droplets." In: *Physics of Plasmas* 19.7 (2012), p. 073112.

[51] T. Ditmire et al. "Nuclear Fusion from Explosions of Femtosecond Laser-Heated Nuclear Fusion from Explosions of Femtosecond Laser-Heated Deuterium Clusters." In: *Nature* 398 (1999), p. 489.

[52] Y. Fukuda et al. "Energy Increase in Multi-MeV Ion Acceleration in the Interaction of a Short Pulse Laser with a Cluster-Gas Target." In: *Phys. Rev. Lett.* 103.16 (Oct. 2009), p. 165002.

[53] T. M. Ostermayr et al. "Proton Acceleration by Irradiation of Isolated Spheres with an Intense Laser Pulse." In: *Physical Review E* 94.3 (Sept. 2016), p. 033208.

[54] P. Hilz et al. "Isolated Proton Bunch Acceleration by a Petawatt Laser Pulse." In: *Nature Communications* 9.1 (Dec. 2018).

[55] T. Z. Esirkepov et al. "Proposed Double-Layer Target for the Generation of High-Quality Laser-Accelerated Ion Beams." In: *Phys. Rev. Lett.* 89.17 (Oct. 2002), p. 175003.

[56] J. H. Bin et al. "Ion Acceleration Using Relativistic Pulse Shaping in Near-Critical-Density Plasmas." In: *Phys. Rev. Lett.* 115.6 (2015), p. 064801.

[57] H Schwoerer et al. "Laser-Plasma Acceleration of Quasi-Monoenergetic Protons from Microstructured Targets." In: *Nature* 439.7075 (Jan. 2006), pp. 445–448.

[58] S. Kar et al. "Guided Post-Acceleration of Laser-Driven Ions by a Miniature Modular Structure." In: *Nature Communications* 7 (Apr. 2016), p. 10792.

[59] Y. Gao et al. "An Automated, 0.5 Hz Nano-Foil Target Positioning System for Intense Laser Plasma Experiments." In: *High Power Laser Science and Engineering* 5 (2017).

[60] L. Obst et al. "Efficient Laser-Driven Proton Acceleration from Cylindrical and Planar Cryogenic Hydrogen Jets." In: *Scientific Reports* 7.1 (Dec. 2017).

[61] C Spindloe et al. "High Volume Fabrication of Laser Targets Using MEMS Techniques." In: *Journal of Physics: Conference Series* 713 (Apr. 2016), p. 012002.

[62] M. Noaman-ul-Haq et al. "Statistical Analysis of Laser Driven Protons Using a High-Repetition-Rate Tape Drive Target System." In: *Physical Review Accelerators and Beams* 20.4 (Apr. 2017).

[63] P. L. Poole et al. "Experiment and Simulation of Novel Liquid Crystal Plasma Mirrors for High Contrast, Intense Laser Pulses." In: *Scientific Reports* 6.1 (Oct. 2016).

[64] P. L. Poole et al. "Liquid Crystal Films as On-Demand, Variable Thickness (50–5000 Nm) Targets for Intense Lasers." In: *Physics of Plasmas* 21.6 (2014), p. 063109.

[65] S. Seuferling et al. "Efficient Offline Production of Freestanding Thin Plastic Foils for Laser-Driven Ion Sources." In: *High Power Laser Science and Engineering* 5 (2017).

[66] D. Margarone et al. "Proton Acceleration Driven by a Nanosecond Laser from a Cryogenic Thin Solid-Hydrogen Ribbon." In: *Physical Review X* 6.4 (Nov. 2016).

[67] P. Bolton et al. "Instrumentation for Diagnostics and Control of Laser-Accelerated Proton (Ion) Beams." In: *Physica Medica* 30.3 (May 2014), pp. 255–270.

[68] S. Busold et al. "Focusing and Transport of High-Intensity Multi-MeV Proton Bunches from a Compact Laser-Driven Source." In: *Physical Review Special Topics - Accelerators and Beams* 16.10 (Oct. 2013), p. 101302.

[69] F. Schillaci et al. "Characterization of the ELIMED Permanent Magnets Quadrupole System Prototype with Laser-Driven Proton Beams." In: *Journal of Instrumentation* 11.07 (July 2016), T07005–T07005.

[70] M. Schollmeier et al. "Controlled Transport and Focusing of Laser-Accelerated Protons with Miniature Magnetic Devices." In: *Physical Review Letters* 101.5 (Aug. 2008).

[71] T. F. Rösch et al. "Considerations on Employing a PMQ-Doublet for Narrow and Broad Proton Energy Distributions." In: *Current Directions in Biomedical Engineering* 3.2 (Jan. 2017).

[72] T. F. Rösch. "A Permanent Magnet Focusing Structure for Laser-Accelerated Ions." Master Thesis. Munich: LMU Munich, 2015.

[73] J. J. Su et al. "Plasma Lenses for Focusing Particle Beams." In: *Physical Review A* 41.6 (1990), p. 3321.

[74] J. P. Palastro et al. "Plasma Lenses for Ultrashort Multi-Petawatt Laser Pulses." In: *Physics of Plasmas* 22.12 (2015), p. 123101.

[75] V. Scuderi et al. "Development of an Energy Selector System for Laser-Driven Proton Beam Applications." In: *Nuclear Instruments and Methods in Physics Research Section A: Accelerators, Spectrometers, Detectors and Associated Equipment* 740 (Mar. 2014), pp. 87–93.

[76] D. Margarone et al. "ELIMAIA: A Laser-Driven Ion Accelerator for Multidisciplinary Applications." In: *Quantum Beam Science* 2.2 (Apr. 2018), p. 8.

[77] S. V. Bulanov and V. S. Khoroshkov. "Feasibility of Using Laser Ion Accelerators in Proton Therapy." In: *Plasma Physics Reports* 28.5 (May 2002), pp. 453–456.

[78] E Fourkal et al. "Particle Selection for Laser-Accelerated Proton Therapy Feasibility Study." In: *Medical physics* 30.7 (July 2003), pp. 1660–1670.

[79] V. Malka et al. "Practicability of Protontherapy Using Compact Laser Systems." In: *Medical Physics* 31.6 (May 2004), p. 1587.

[80] M. Roth et al. "Energetic Ions Generated by Laser Pulses: A Detailed Study on Target Properties." In: *Physical Review Special Topics - Accelerators and Beams* 5.6 (June 2002).

[81] M Borghesi et al. "Multi-MeV Proton Source Investigations in Ultraintense Laser-Foil Interactions." In: *Phys. Rev. Lett.* 92.5 (Feb. 2004), p. 055003.

[82] J. A. Cobble et al. "High Resolution Laser-Driven Proton Radiography." In: *Journal of Applied Physics* 92.4 (Aug. 2002), pp. 1775–1779.

[83] B. Hidding et al. "Laser–Plasma-Accelerators—A Novel, Versatile Tool for Space Radiation Studies." In: *Nuclear Instruments and Methods in Physics Research Section A: Accelerators, Spectrometers, Detectors and Associated Equipment* 636.1 (Apr. 2011), pp. 31–40.

[84] B. Hidding et al. "Laser-Plasma-Based Space Radiation Reproduction in the Laboratory." In: *Scientific Reports* 7.1 (Dec. 2017).

[85] B. A. Remington. "Modeling Astrophysical Phenomena in the Laboratory with Intense Lasers." In: *Science* 284.5419 (May 1999), pp. 1488–1493.

[86] M. Roth et al. "Fast Ignition by Intense Laser-Accelerated Proton Beams." In: *Phys. Rev. Lett.* 86.3 (Jan. 2001), pp. 436–439.

[87] F. Lindner et al. "Towards Swift Ion Bunch Acceleration by High-Power Laser Pulses at the Centre for Advanced Laser Applications (CALA)." In: *Nuclear Instruments and Methods in Physics Research Section B: Beam Interactions with Materials and Atoms* (2017).

[88] D. Habs et al. "Introducing the Fission-Fusion Reaction Process: Using a Laser-Accelerated Th Beam to Produce Neutron-Rich Nuclei towards the N=126 Waiting Point of the r Process." In: *Applied Physics B* 103.2 (May 2011), pp. 471–484.

[89] F. H. Lindner et al. "En-Route to the Fission-Fusion Reaction Mechanism: A Status Update on Laser-Driven Heavy Ion Acceleration." In: *Plasma Physics and Controlled Fusion* (2019).

[90] M. Fuchs et al. "Laser-Driven Soft-X-Ray Undulator Source." In: *Nature Physics* 5.11 (Nov. 2009), pp. 826–829.

[91] D. A. G. Deacon et al. "First Operation of a Free-Electron Laser." In: *Physical Review Letters* 38.16 (Apr. 1977), pp. 892–894.

[92] P. Emma et al. "First Lasing and Operation of an Ångstrom-Wavelength Free-Electron Laser." In: *Nature Photonics* 4.9 (Sept. 2010), pp. 641–647.

[93] *CALA - Centre for Advanced Laser Applications: Mainpage*. https://www.cala-laser.de/. 2019.

[94] E. Eggl et al. "The Munich Compact Light Source: Initial Performance Measures." In: *Journal of Synchrotron Radiation* 23.5 (Sept. 2016), pp. 1137–1142.

[95] J. D. Jackson. *Classical Electrodynamics*. 3rd ed. Wiley, New York, 1999.

[96] L. Lorenz. "XXXVIII. On the Identity of the Vibrations of Light with Electrical Currents." In: *The London, Edinburgh, and Dublin Philosophical Magazine and Journal of Science* 34.230 (1867), pp. 287–301.

[97] A Einstein. "Zur Quantentheorie Der Strahlung." In: *Phys. Zeitschrift* 18 (1917), pp. 121–128.

[98] T. H. Maiman. "Stimulated Optical Radiation in Ruby." In: *Nature* 187 (1960), pp. 493–494.

[99] S. Akturk et al. "Spatio-Temporal Couplings in Ultrashort Laser Pulses." In: *Journal of Optics* 12.9 (Sept. 2010), p. 093001.

[100] A. Macchi, M. Borghesi, and M. Passoni. "Ion Acceleration by Superintense Laser-Plasma Interaction." In: *Reviews of Modern Physics* 85.2 (May 2013), pp. 751–793.

[101] P. Gibbon. *Short Pulse Laser Interaction with Matter: An INtroduction*. Imperial College Press, 2005.

[102] S. Karsch. "Applications of High-Intensity Laser-Pulses." Lecture Notes. Munich, 2015.

[103] F. F. Chen and F. F. Chen. *Introduction to Plasma Physics and Controlled Fusion*. 2nd ed. New York: Plenum Press, 1984.

[104] W. L. Kruer. *The Physics of Laser Plasma Interactions*. Addison-Wesley, 1988.

[105] J. Bin. "Laser-Driven Ion Acceleration From Carbon Nano-Targets With TI:Sa Laser Systems." PhD Thesis. Munich: LMU Munich, 2015.

[106] D. Kiefer. "Relativistic Electron Mirrors from High Intensity Laser Nanofoil Interactions." PhD thesis. Munich: LMU Munich, Dec. 2012.

[107] C. Kreuzer. "Technological Developments for Laser Ion Acceleration." PhD Thesis. Munich: LMU Munich, 2018.

[108] F. H. Lindner. "Online Diagnostics for Laser Accelerated Ions and Electrons." Master Thesis. Munich: LMU Munich, 2015.

[109] A. Vogel et al. "Mechanisms of Femtosecond Laser Nanosurgery of Cells and Tissues." In: *Applied Physics B* 81.8 (Dec. 2005), pp. 1015–1047.

[110] W. Lotz. "An Empirical Formula for the Electron-Impact Ionization Cross-Section." In: (1968), p. 7.

[111] B. C. Stuart et al. "Nanosecond-to-Femtosecond Laser-Induced Breakdown in Dielectrics." In: *Physical Review B* 53.4 (Jan. 1996), pp. 1749–1761.

[112] K Soong, E. R. Colby, and C McGuinness. "Experimental Determination of Damage Threshold Characteristics of IR Compatible Optical Materials." In: *New York* (2011), p. 3.

[113] P. A. Zhokhov and A. M. Zheltikov. "Optical Breakdown of Solids by Few-Cycle Laser Pulses." In: *Scientific Reports* 8.1 (Dec. 2018).

[114] D. R. Austin et al. “Femtosecond Laser Damage of Germanium from Near- to Mid-Infrared Wavelengths.” In: *Optics Letters* 43.15 (Aug. 2018), p. 3702.

[115] J. P. Freidberg et al. “Resonant Absorption of Laser Light by Plasma Targets.” In: *Phys. Rev. Lett.* 28.13 (Mar. 1972), pp. 795–799.

[116] D. W. Forslund, J. M. Kindel, and K. Lee. “Theory of Hot-Electron Spectra at High Laser Intensity.” In: *Physical Review Letters* 39.5 (Aug. 1977), pp. 284–288.

[117] F. Brunel. “Not-so-Resonant, Resonant Absorption.” In: *Phys. Rev. Lett.* 59.1 (July 1987), pp. 52–55.

[118] W. L. Kruer and K. Estabrook. “J×B Heating by Very Intense Laser Light.” In: *The Physics of Fluids* 28.1 (1985), pp. 430–432.

[119] J. Fuchs et al. “Laser-Driven Proton Scaling Laws and New Paths towards Energy Increase.” In: *Nature Physics* 2.1 (Jan. 2006), pp. 48–54.

[120] S. C. Wilks et al. “Absorption of Ultra-Intense Laser Pulses.” In: *Phys. Rev. Lett.* 69.9 (Aug. 1992), pp. 1383–1386.

[121] R. A. Snavely et al. “Intense High-Energy Proton Beams from Petawatt-Laser Irradiation of Solids.” In: *Physical Review Letters* 85.14 (2000), p. 2945.

[122] S. C. Wilks et al. “Energetic Proton Generation in Ultra-Intense Laser–Solid Interactions.” In: *Physics of Plasmas* 8.2 (2001), pp. 542–549.

[123] S. P. Hatchett et al. “Electron, Photon, and Ion Beams from the Relativistic Interaction of Petawatt Laser Pulses with Solid Targets.” In: *Physics of Plasmas* 7.5 (2000), pp. 2076–2082.

[124] A. J. Mackinnon et al. “Enhancement of Proton Acceleration by Hot-Electron Recirculation in Thin Foils Irradiated by Ultraintense Laser Pulses.” In: *Phys. Rev. Lett.* 88.21 (May 2002), p. 215006.

[125] T Esirkepov et al. “Highly Efficient Relativistic-Ion Generation in the Laser-Piston Regime.” In: *Phys. Rev. Lett.* 92.17 (Apr. 2004), p. 175003.

[126] A. Macchi et al. “Laser Acceleration of Ion Bunches at the Front Surface of Overdense Plasmas.” In: *Phys. Rev. Lett.* 94.16 (Apr. 2005), p. 165003.

[127] A. Henig et al. “Radiation-Pressure Acceleration of Ion Beams Driven by Circularly Polarized Laser Pulses.” In: *Phys. Rev. Lett.* 103.24 (Dec. 2009), p. 245003.

[128] M. S. Wei et al. "Ion Acceleration by Collisionless Shocks in High-Intensity-LaserUnderdense-Plasma Interaction." In: *Phys. Rev. Lett.* 93.15 (Oct. 2004), p. 155003.

[129] L. O. Silva et al. "Proton Shock Acceleration in Laser-Plasma Interactions." In: *Phys. Rev. Lett.* 92.1 (Jan. 2004), p. 015002.

[130] A. Henig et al. "Laser-Driven Shock Acceleration of Ion Beams from Spherical Mass-Limited Targets." In: *Phys. Rev. Lett.* 102.9 (Mar. 2009), p. 095002.

[131] T. Ditmire et al. "High-Energy Ions Produced in Explosions of Superheated Atomic Clusters." In: *Nature* 386.6620 (Mar. 1997), pp. 54–56.

[132] T. Z. Esirkepov et al. "Coulomb Explosion of a Cluster Irradiated by a High Intensity Laser Pulse." In: *Laser and Particle Beams* 18.03 (2000), pp. 503–506.

[133] S. Sakabe et al. "Generation of High-Energy Protons from the Coulomb Explosion of Hydrogen Clusters by Intense Femtosecond Laser Pulses." In: *Phys. Rev. A* 69.2 (2004).

[134] A. A. Andreev, P. V. Nickles, and K. Y. Platonov. "Quasi-Coulomb Explosion of Multicomponent Laser Cluster Plasma." In: *Physics of Plasmas* 17.2 (2010), p. 023110.

[135] S. S. Bulanov et al. "Directed Coulomb Explosion Regime of Ion Acceleration from Mass Limited Targets by Linearly and Circularly Polarized Laser Pulses." In: *arXiv* (2010), p. 1007.3963.

[136] S. V. Bulanov. "Ion Acceleration in a Dipole Vortex in a Laser Plasma Corona." In: *Plasma Physics Reports* 31.5 (2005), p. 369.

[137] T. Nakamura et al. "High-Energy Ions from Near-Critical Density Plasmas via Magnetic Vortex Acceleration." In: *Physical Review Letters* 105.13 (Sept. 2010).

[138] M. Xu and L. V. Wang. "Photoacoustic Imaging in Biomedicine." In: *Rev. Sci. Instrum.* (2006), p. 23.

[139] "Appendix. Stopping Power and Range Tables for Charged Particles." In: *Journal of the ICRU* 14.1 (Apr. 2014), pp. 79–98.

[140] H. Bethe. "Zur Theorie des Durchgangs schneller Korpuskularstrahlen durch Materie." In: *Annalen der Physik* 397.3 (1930), pp. 325–400.

[141] F. Bloch. "Zur Bremsung rasch bewegter Teilchen beim Durchgang durch Materie." In: *Annalen der Physik* 408.3 (1933), pp. 285–320.

[142] D. E. Groom and S. R. Klein. "Passage of Particles through Matter." In: *The European Physical Journal C* 15.1-4 (Mar. 2000), pp. 163–173.

[143] K. C. Jones et al. "Acoustic Time-of-Flight for Proton Range Verification in Water: Acoustic Time-of-Flight Proton Range Verification Water." In: *Medical Physics* 43.9 (Aug. 2016), pp. 5213–5224.

[144] L. V. Wang, H.-i. Wu, and H.-I. Wu. *Biomedical Optics : Principles and Imaging*. Somerset, UNITED STATES: John Wiley & Sons, Incorporated, 2012.

[145] L. Doyle. "Studies on Coherent Ionoacoustics." Bachelor Thesis. Munich: LMU Munich, 2016.

[146] S. Lehrack. "Investigating Accuracy and Precision of Ionoacoustics for Range Determination of Ion Beams in Water." PhD Thesis. Munich: LMU Munich, 2018.

[147] R. Yang. "Ion Bunch Energy Acoustic Tracing (I-BEAT)." Master Thesis. Munich: LMU Munich, 2017.

[148] E. I. Blount and J. R. Klauder. "Recovery of Laser Intensity from Correlation Data." In: *Journal of Applied Physics* 40.7 (June 1969), pp. 2874–2875.

[149] S Luan et al. "High Dynamic Range Third-Order Correlation Measurement of Picosecond Laser Pulse Shapes." In: *Measurement Science and Technology* 4.12 (Dec. 1993), pp. 1426–1429.

[150] J. Hartmann et al. "The Spatial Contrast Challenge for Intense Laser-Plasma Experiments." In: *Journal of Physics: Conference Series* 1079 (Aug. 2018), p. 012003.

[151] M. Speicher. "Optical Probing for On-Target Laser Contrast Measurement." Master Thesis. Munich: LMU Munich, 2016.

[152] D. Adams 1952-2001. *The Hitchhiker's Guide to the Galaxy*. First American edition. New York : Harmony Books, 1980. ©1979, 1980.

[153] M. Kögler. "Construction of a Vacuum Microscope." Bachelor Thesis. Munich: LMU Munich, 2014.

[154] S. Reinhardt et al. "Comparison of Gafchromic EBT2 and EBT3 Films for Clinical Photon and Proton Beams." In: *Medical Physics* 39.8 (), pp. 5257–5262.

[155] S. Reinhardt. "Detection of Laser-Accelerated Protons." PhD Thesis. Munich: LMU Munich, 2012.

[156] D. Taray. "Analysis of Laser Accelerated Ion Foci Created with Permanent Magnet Quadrupoles." Bachelor Thesis. Munich: Ludwig-Maximilians-Universität, 2017.

[157] J. Hartmann. "From a Laser Focus to an Ion Focus." Master Thesis. Munich: LMU Munich, 2017.

[158] V. Bagnoud et al. "Commissioning and Early Experiments of the PHELIX Facility." In: *Applied Physics B* 100.1 (July 2010), pp. 137–150.

[159] J. Bin et al. "A Laser-Driven Nanosecond Proton Source for Radiobiological Studies." In: *Applied Physics Letters* 101.24 (Dec. 2012), p. 243701.

[160] K. Zeil et al. "Dose-Controlled Irradiation of Cancer Cells with Laser-Accelerated Proton Pulses." In: *Applied Physics B* 110.4 (Mar. 2013), pp. 437–444.

[161] D. Haffa et al. "Temporally Resolved Intensity Contouring (TRIC) for Characterization of the Absolute Spatio-Temporal Intensity Distribution of a Relativistic, Femtosecond Laser Pulse." In: *Scientific Reports* 9.1 (May 2019).

[162] P. McKenna et al. "High-Intensity Laser-Driven Proton Acceleration: Influence of Pulse Contrast." In: *Philosophical Transactions of the Royal Society A: Mathematical, Physical and Engineering Sciences* 364.1840 (Mar. 2006), pp. 711–723.

[163] S. Palaniyappan et al. "Dynamics of Relativistic Transparency and Optical Shuttering in Expanding Overdense Plasmas." In: *Nature Physics* 8.10 (Oct. 2012), pp. 763–769.

[164] D. Kiefer et al. "Relativistic Electron Mirrors from Nanoscale Foils for Coherent Frequency Upshift to the Extreme Ultraviolet." In: *Nature Communications* 4 (Apr. 2013), p. 1763.

[165] J. Schreiber et al. "Complete Temporal Characterization of Asymmetric Pulse Compression in a Laser Wakefield." In: *Phys. Rev. Lett.* 105.23 (Dec. 2010), p. 235003.

[166] K. Khrennikov et al. "Tunable All-Optical Quasimonochromatic Thomson X-Ray Source in the Nonlinear Regime." In: *Phys. Rev. Lett.* 114.19 (May 2015), p. 195003.

[167] A. Buck et al. "Real-Time Observation of Laser-Driven Electron Acceleration." In: *Nature Physics* 7.7 (Mar. 2011), pp. 543–548.

[168] J Metzkes et al. "Reflective Optical Probing of Laser-Driven Plasmas at the Rear Surface of Solid Targets." In: *Plasma Physics and Controlled Fusion* 58.3 (Mar. 2016), p. 034012.

[169] J. S. Green et al. "Single Shot, Temporally and Spatially Resolved Measurements of Fast Electron Dynamics Using a Chirped Optical Probe." In: *Journal of Instrumentation* 9.03 (Mar. 2014), P03003–P03003.

[170] M. C. Kaluza et al. "Time-Sequence Imaging of Relativistic Laser–Plasma Interactions Using a Novel Two-Color Probe Pulse." In: *Applied Physics B* 92.4 (Sept. 2008), pp. 475–479.

[171] Y. Wang et al. "Single-Shot Measurement of >1010 Pulse Contrast for Ultra-High Peak-Power Lasers." In: *Scientific Reports* 4.1 (May 2015).

[172] T. Oksenhendler et al. "High Dynamic, High Resolution and Wide Range Single Shot Temporal Pulse Contrast Measurement." In: *Optics Express* 25.11 (May 2017), p. 12588.

[173] K. Poder et al. "Experimental Signatures of the Quantum Nature of Radiation Reaction in the Field of an Ultraintense Laser." In: *Physical Review X* 8.3 (July 2018).

[174] A. Link et al. "Development of an *in Situ* Peak Intensity Measurement Method for Ultraintense Single Shot Laser-Plasma Experiments at the Sandia Z Petawatt Facility." In: *Review of Scientific Instruments* 77.10 (Oct. 2006), 10E723.

[175] O. Har-Shemesh and A. Di Piazza. "Peak Intensity Measurement of Relativistic Lasers via Nonlinear Thomson Scattering." In: *Optics Letters* 37.8 (Apr. 2012), p. 1352.

[176] G. Pariente et al. "Space–Time Characterization of Ultra-Intense Femtosecond Laser Beams." In: *Nature Photonics* 10.8 (Aug. 2016), pp. 547–553.

[177] J. Hartmann et al. "The Spatial Contrast Challenge for Intense Laser-Plasma Experiments." In: *Journal of Physics: Conference Series* 1079 (Aug. 2018), p. 012003.

[178] R. Trebino et al. "Measuring Ultrashort Laser Pulses in the Time-Frequency Domain Using Frequency-Resolved Optical Gating." In: *Review of Scientific Instruments* 68.9 (Sept. 1997), pp. 3277–3295.

[179] J. Collier et al. "A Single-Shot Third-Order Autocorrelator for Pulse Contrast and Pulse Shape Measurements." In: *Laser and Particle Beams* 19.2 (Apr. 2001), pp. 231–235.

[180] S. Kahaly et al. "Investigation of Amplitude Spatio-Temporal Couplings at the Focus of a 100 TW-25 Fs Laser." In: *Applied Physics Letters* 104.5 (Feb. 2014), p. 054103.

[181] P. Gabolde and R. Trebino. "Single-Frame Measurement of the Complete Spatiotemporal Intensity and Phase of Ultrashort Laser Pulses Using Wavelength-Multiplexed Digital Holography." In: *Journal of the Optical Society of America B* 25.6 (June 2008), A25.

[182] K. Nakagawa et al. "Sequentially Timed All-Optical Mapping Photography (STAMP)." In: *Nature Photonics* 8.9 (Sept. 2014), pp. 695–700.

[183] C. G. Morgan. "Laser-Induced Breakdown of Gases." In: *Reports on Progress in Physics* 38.5 (May 1975), pp. 621–665.

[184] H. Hora. "Theory of Relativistic Self-Focusing of Laser Radiation in Plasmas." In: *Journal of the Optical Society of America* 65.8 (Aug. 1975), p. 882.

[185] I. Watts et al. "Measurements of Relativistic Self-Phase-Modulation in Plasma." In: *Physical Review E* 66.3 (Sept. 2002).

[186] E. Martinolli et al. "Fast Electron Heating of a Solid Target in Ultrahigh-Intensity Laser Pulse Interaction." In: *Physical Review E* 70.5 (Nov. 2004).

[187] M. Hornung et al. "Generation of 25-TW Femtosecond Laser Pulses at 515 Nm with Extremely High Temporal Contrast." In: *Applied Sciences* 5.4 (Dec. 2015), pp. 1970–1979.

[188] C. W. Siders et al. "Efficient High-Energy Pulse-Train Generation Using a 2n̂-Pulse Michelson Interferometer." In: *Applied Optics* 37.22 (Aug. 1998), p. 5302.

[189] C. Y. Chien et al. "Single-Shot Chirped-Pulse Spectral Interferometry Used to Measure the Femtosecond Ionization Dynamics of Air." In: *Optics Letters* 25.8 (Apr. 2000), p. 578.

[190] S. P. Le Blanc et al. "Single-Shot Measurement of Temporal Phase Shifts by Frequency-Domain Holography." In: *Optics Letters* 25.10 (May 2000), p. 764.

[191] D. Haffa et al. "I-BEAT: Ultrasonic Method for Online Measurement of the Energy Distribution of a Single Ion Bunch." In: *Scientific Reports* 9.1 (May 2019).

[192] D. Taylor and J. Sharpe. "Nuclear Particle and Radiation Detectors. Part 1: Ion Chambers and Ion-Chamber Instruments." In: *Proceedings of the IEE - Part II: Power Engineering* 98.62 (Apr. 1951), pp. 174–190.

[193] L. Karsch. "Derivation of Formulas to Calculate the Saturation Correction of Ionization Chambers in Pulsed Beams of Short, Nonvanishing Pulse Durations." In: *Medical physics* 43.11 (2016), pp. 6154–6164.

[194] D. A. Glaser. "Some Effects of Ionizing Radiation on the Formation of Bubbles in Liquids." In: *Physical Review* 87.4 (1952), p. 665.

[195] F. E. Irons, R. W. P. McWhirter, and N. J. Peacock. "The Ion and Velocity Structure in a Laser Produced Plasma." In: *Journal of Physics B: Atomic and Molecular Physics* 5.10 (Oct. 1972), pp. 1975–1987.

[196] A. W. Ehler. "High-energy Ions from a CO2 Laser-produced Plasma." In: *Journal of Applied Physics* 46.6 (1975), pp. 2464–2467.

[197] M. J. Butson et al. "Radiochromic Film for Medical Radiation Dosimetry." In: *Materials Science and Engineering: R: Reports* 41.3-5 (Sept. 2003), pp. 61–120.

[198] T. W. Jeong et al. "CR-39 Track Detector for Multi-MeV Ion Spectroscopy." In: *Scientific Reports* 7.1 (Dec. 2017).

[199] D. Jung et al. "A Novel High Resolution Ion Wide Angle Spectrometer." In: *Review of Scientific Instruments* 82.4 (Apr. 2011), p. 043301.

[200] J. Thomson. "XXIV. On the Structure of the Atom: An Investigation of the Stability and Periods of Oscillation of a Number of Corpuscles Arranged at Equal Intervals around the Circumference of a Circle; with Application of the Results to the Theory of Atomic Structure." In: *The London, Edinburgh, and Dublin Philosophical Magazine and Journal of Science* 7.39 (Mar. 1904), pp. 237–265.

[201] K. Harres et al. "Development and Calibration of a Thomson Parabola with Microchannel Plate for the Detection of Laser-Accelerated MeV Ions." In: *Review of Scientific Instruments* 79.9 (2008), p. 093306.

[202] J. A. Cobble et al. "High-Resolution Thomson Parabola for Ion Analysis." In: *Review of Scientific Instruments* 82.11 (Nov. 2011), p. 113504.

[203] D. Ruggieri. "MICROCHANNEL PLATE IMAGING DETECTORS." In: *IEEE (Inst. Elec. Electron. Eng.), Trans. Nucl. Sci. NS-19: No. 3, 74-84(Jun 1972).* (Jan. 1972).

[204] F. H. Lindner et al. "A Novel Approach to Electron Data Background Treatment in an Online Wide-Angle Spectrometer for Laser-Accelerated Ion and Electron Bunches." In: *Review of Scientific Instruments* 89.1 (2018), p. 013301.

[205] S. Reinhardt et al. "A Pixel Detector System for Laser-Accelerated Ion Detection." In: *Journal of Instrumentation* 8.03 (2013), P03008.

[206] V. Scuderi et al. "Time of Flight Based Diagnostics for High Energy Laser Driven Ion Beams." In: *Journal of Instrumentation* 12.03 (Mar. 2017), pp. C03086–C03086.

[207] M. Würl et al. "Time-of-Flight Spectrometry of Ultra-Short, Polyenergetic Proton Bunches." In: *Review of Scientific Instruments* 89.12 (Dec. 2018), p. 123302.

[208] F. Kroll, J. Pawelke, and L. Karsch. "Preliminary Investigations on the Determination of Three-Dimensional Dose Distributions Using Scintillator Blocks and Optical Tomography." In: *Medical physics* 40.8 (2013).

[209] M. Goulet et al. "Novel, Full 3D Scintillation Dosimetry Using a Static Plenoptic Camera." In: *Medical physics* 41.8Part1 (2014).

[210] J. Metzkes et al. "An Online, Energy-Resolving Beam Profile Detector for Laser-Driven Proton Beams." In: *Review of Scientific Instruments* 87.8 (Aug. 2016), p. 083310.

[211] K. C. Jones et al. “Proton Beam Characterization by Proton-Induced Acoustic Emission: Simulation Studies.” In: *Physics in Medicine and Biology* 59.21 (Nov. 2014), pp. 6549–6563.

[212] K. Parodi and W. Assmann. “Ionoacoustics: A New Direct Method for Range Verification.” In: *Modern Physics Letters A* 30.17 (June 2015), p. 1540025.

[213] S. Lehrack et al. “Submillimeter Ionoacoustic Range Determination for Protons in Water at a Clinical Synchrocyclotron.” In: *Physics in Medicine & Biology* 62.17 (Aug. 2017), pp. L20–L30.

[214] A. G. Bell. “On the Production and Reproduction of Sound by Light.” In: *American Journal of Science* s3-20.118 (Oct. 1880), pp. 305–324.

[215] G. A. Askaryan. “Hydrodynamic Radiation from the Tracks of Ionizing Particles in Stable Liquids.” In: *The Soviet Journal of Atomic Energy* 3.8 (Aug. 1957), pp. 921–923.

[216] G. Askariyan et al. “Acoustic Detection of High Energy Particle Showers in Water.” In: *Nuclear Instruments and Methods* 164.2 (Aug. 1979), pp. 267–278.

[217] L. Sulak et al. “Experimental Studies of the Acoustic Signature of Proton Beams Traversing Fluid Media.” In: *Nuclear Instruments and Methods* 161.2 (May 1979), pp. 203–217.

[218] N. A. Baily. “A Review of the Processes by Which Ultrasound Is Generated through the Interaction of Ionizing Radiation and Irradiated Materials: Some Possible Applications.” In: *Medical Physics* 19.3 (), pp. 525–532.

[219] R. Lahmann et al. “Thermo-Acoustic Sound Generation in the Interaction of Pulsed Proton and Laser Beams with a Water Target.” In: *Astroparticle Physics* 65 (May 2015), pp. 69–79.

[220] S. K. Patch et al. “Thermoacoustic Range Verification Using a Clinical Ultrasound Array Provides Perfectly Co-Registered Overlay of the Bragg Peak onto an Ultrasound Image.” In: *Physics in medicine and biology* 61.15 (2016), p. 5621.

[221] S. Kellnberger et al. “Ionoacoustic Tomography of the Proton Bragg Peak in Combination with Ultrasound and Optoacoustic Imaging.” In: *Scientific Reports* 6.1 (Sept. 2016).

[222] W. Assmann et al. "The Munich MP Tandem." In: *Nuclear Instruments and Methods* 122 (Nov. 1974), pp. 191–203.

[223] A. Edlich. "Ionoacoustic K-Wave Simulations." Bachelor Thesis. Munich: LMU Munich, 2014.

[224] M. A. A. Caballero et al. "Optoacoustic Determination of Spatio- Temporal Responses of Ultrasound Sensors." In: *IEEE Transactions on Ultrasonics, Ferroelectrics, and Frequency Control* 60.6 (June 2013), pp. 1234–1244.

[225] L. M. Brekhovskikh. *Waves in Layered Media / L.M. Brekhovskikh ; Translated by Robert T. Beyer*. 2d ed. Academic Press New York, 1980.

[226] S. Kirkpatrick, C. D. Gelatt, and M. P. Vecchi. "Optimization by Simulated Annealing." In: *Science* 220.4598 (May 1983), pp. 671–680.

[227] S. Kirkpatrick. "Optimization by Simulated Annealing: Quantitative Studies." In: *Journal of Statistical Physics* 34.5-6 (Mar. 1984), pp. 975–986.

[228] J. F. Ziegler. "SRIM." In: (2013).

[229] M. Youssef. "An Analytical Approach for the Transmission of Polychromatic Divergent Proton Beams through a Magnetic Quadrupole Doublet." Bachelor Thesis. Munich: LMU Munich, 2018.

[230] U Schramm et al. "First Results with the Novel Petawatt Laser Acceleration Facility in Dresden." In: *Journal of Physics: Conference Series* 874 (July 2017), p. 012028.

[231] L. Obst et al. "On-Shot Characterization of Single Plasma Mirror Temporal Contrast Improvement." In: *Plasma Physics and Controlled Fusion* (Mar. 2018).

[232] M. J. Mead et al. "Electromagnetic Pulse Generation within a Petawatt Laser Target Chamber." In: *Review of Scientific Instruments* 75.10 (Oct. 2004), pp. 4225–4227.

[233] M. De Marco et al. "Basic Features of Electromagnetic Pulse Generated in a Laser-Target Chamber at 3-TW Laser Facility PALS." In: *Journal of Physics: Conference Series* 508 (Apr. 2014), p. 012007.

[234] T. W. Jeong et al. "CR-39 Track Detector for Multi-MeV Ion Spectroscopy." In: *Scientific Reports* 7.1 (May 2017).

[235] M Würl et al. "Experimental Studies with Two Novel Silicon Detectors for the Development of Time-of-Flight Spectrometry of Laser-Accelerated Proton Beams." In: *Journal of Physics: Conference Series* 777.1 (2017), p. 012018.

[236] B. Fischer. "Optical Microphone Hears Ultrasound." In: *Nature Photonics* 10.6 (June 2016), pp. 356–358.

[237] T. M. Ostermayr et al. "A Transportable Paul-Trap for Levitation and Accurate Positioning of Micron-Scale Particles in Vacuum for Laser-Plasma Experiments." In: *Review of Scientific Instruments* 89.1 (Jan. 2018), p. 013302.

[238] R. Baumgartner and R. Byer. "Optical Parametric Amplification." In: *IEEE Journal of Quantum Electronics* 15.6 (June 1979), pp. 432–444.

[239] I. Jovanovic et al. "Optical Parametric Chirped-Pulse Amplifier as an Alternative to Ti:Sapphire Regenerative Amplifiers." In: *Appl. Opt.* 41.15 (May 2002), pp. 2923–2929.

[240] H. Kiriyama et al. "High-Contrast, High-Intensity Laser Pulse Generation Using a Nonlinear Preamplifier in a Ti:Sapphire Laser System." In: *Opt. Lett.* 33.7 (Apr. 2008), pp. 645–647.

[241] A. Jullien et al. "10^10 Temporal Contrast for Femtosecond Ultraintense Lasers by Cross-Polarized Wave Generation." In: *Optics Letters* 30.8 (Apr. 2005), p. 920.

[242] N. V. Didenko et al. "Contrast Degradation in a Chirped-Pulse Amplifier Due to Generation of Prepulses by Postpulses." In: *Optics Express* 16.5 (2008), p. 3178.

[243] C. Hooker et al. "Improving Coherent Contrast of Petawatt Laser Pulses." In: *Optics Express* 19.3 (Jan. 2011), p. 2193.

[244] J. H. Bin et al. "Dynamics of Laser-Driven Proton Acceleration Exhibited by Measured Laser Absorptivity and Reflectivity." In: *Scientific Reports* 7 (Mar. 2017), 43548 EP–.

[245] M. L. Zhou et al. "The Impact of Femtosecond Pre-Pulses on Nanometer Thin Foils for Laser-Ion Acceleration." In: *Plasma Physics and Controlled Fusion* 59.5 (May 2017), p. 055020.

[246] V. G. Gisbert. "Applied Optical Metrology Methods for Target Positioning and Profiling in Vacuum for Laser Plasma Interaction." Master Thesis. Munich: LMU Munich, 2016.

[247] S. Herr. "Design and Implementation of an Integrated Device for Laser Beam and Target Analysis for Laser Ion Acceleration." Master Thesis. Munich: LMU Munich, 2017.

[248] L. Doyle. "Implementation of an Adaptive Optics System for Focus Optimization at the Centre for Advanced Laser Applications." Master Thesis. Munich: LMU Munich, 2019.

[249] A Boukharov et al. "Dynamics of Cryogenic Jets: Non-Rayleigh Breakup and Onset of Nonaxisymmetric Motions." In: *Phys. Rev. Lett.* 100.17 (May 2008), p. 174505.

[250] B. Dromey et al. "The Plasma Mirror—A Subpicosecond Optical Switch for Ultrahigh Power Lasers." In: *Review of Scientific Instruments* 75.3 (Mar. 2004), pp. 645–649.

[251] G. Doumy et al. "Complete Characterization of a Plasma Mirror for the Production of High-Contrast Ultraintense Laser Pulses." In: *Physical Review E* 69.2 (Feb. 2004).

[252] C. Thaury et al. "Plasma Mirrors for Ultrahigh-Intensity Optics." In: *Nature Physics* 3.6 (June 2007), pp. 424–429.

[253] C. Ziener et al. "Specular Reflectivity of Plasma Mirrors as a Function of Intensity, Pulse Duration, and Angle of Incidence." In: *Journal of Applied Physics* 93.1 (Jan. 2003), pp. 768–770.

[254] M. A. O. Haug. "Plastic Nano Foil Based Plasma Mirror Solutions." Master Thesis. Munich: LMU Munich, 2016.

[255] J. Miyahara et al. "A New Type of X-Ray Area Detector Utilizing Laser Stimulated Luminescence." In: *Nuclear Instruments and Methods in Physics Research Section A: Accelerators, Spectrometers, Detectors and Associated Equipment* 246.1-3 (May 1986), pp. 572–578.

[256] M. Würl. "On the Spectrometry of Laser-Accelerated Particle Bunches and Laser-Driven Proton Radiography." PhD Thesis. Munich: LMU Munich, 2018.

[257] J. W. Goodman. *Introduction to Fourier Optics*. Fourth edition. New York: W. H. Freeman, May 2017.

[258] T. J. Cox and P. D'Antonio. *Acoustic Absorbers and Diffusers: Theory, Design and Application*. CRC Press, Jan. 2002.

[259] R. K. Tyson. *Principles and Applications of Fourier Optics*. IOP Expanding Physics. Bristol, UK: IOP Publishing, 2014.

[260] T. Preston. "The Interferometer." In: *Nature* 59.1539 (Apr. 1899), p. 605.

[261] A. Abramovici et al. "LIGO: The Laser Interferometer Gravitational-Wave Observatory." In: *Science* 256.5055 (Apr. 1992), pp. 325–333.

[262] B. P. Abbott et al. "Observation of Gravitational Waves from a Binary Black Hole Merger." In: *Phys. Rev. Lett.* 116.6 (Feb. 2016), p. 061102.

[263] C. M. Vest. *Holographic Interferometry*. 1 edition. New York: Wiley-Interscience, Feb. 1979.

[264] B. C. Platt and R. Shack. "History and Principles of Shack-Hartmann Wavefront Sensing." In: *Journal of Refractive Surgery* 17.5 (Sept. 2001), S573–S577.

[265] S. Karsch. "Generation of Ultraintense Laserpulses." Lecture Notes. Munich, 2013.

[266] W. Demtröder. *Experimentalphysik 2*. Springer Berlin Heidelberg, Nov. 2008.

[267] P. A. Franken et al. "Generation of Optical Harmonics." In: *Physical Review Letters* 7.4 (Aug. 1961), pp. 118–119.

[268] R. Adair, L. L. Chase, and S. A. Payne. "Nonlinear Refractive-Index Measurements of Glasses Using Three-Wave Frequency Mixing." In: *Journal of the Optical Society of America B* 4.6 (June 1987), p. 875.

[269] X. Lu et al. "Measurement of Nonlinear Refractive Index Coefficient Using Emission Spectrum of Filament Induced by Gigawatt-Femtosecond Pulse in BK7 Glass." In: *Applied Optics* 51.12 (Apr. 2012), p. 2045.

[270] F. C. A. Pockels. *Lehrbuch der Kristalloptik*. Leipzig und Berlin: B.G. Teubner, 1906.

Acknowledgements

Nun am Ende meiner Arbeit und somit auch am Ende eines besonderen Abschnitts möchte ich mir die Zeit nehmen und allen danken die mich unterstützt und begleitet haben und letztendlich dazu beigetragen haben, dass ich diese Worte jetzt schreiben kann.

Mein ganz besonderer Dank geht an Jörg Schreiber für die wunderbare Betreuung in all den Jahren. Ganz besonders für das große in mich gesetzte Vertrauen bezgüglich LEX und CALA. Aber auch für viele Stunden an Gesprächen mit physikalischen Anregungen, kritischen Diskussionen und vielem anderen. Ich danke Dir für alles!

Natürlich auch danke, dass du es geschafft hast, die beste Arbeitsgruppe aufzubauen, die man sich wünschen kann. Ich danke Tobias Ostermayr für jahrelange Büronachbarschaft, Betreuung und wahre Unterstützung. Peter Hilz für die vielen Gespräche, und Diskussionen und dafür, dass du mich von Anfang an immer so mit eingebunden hast, obwohl du schon fast fertig mit deinem Doktor warst. Christian Kreuzer für eine tolle Zusammenarbeit und dafür dass du immer eine kreative Lösung parat hattest. Danke an Daniel Kiefer, der mich am Anfang in das Projekt LEX/CALA eingewiesen hat. A warm thanks goes to Jianhui Bin for all the short questions and especially for supporting me in LEX taking a lot of the pressure aside. Ich möchte mich bei Florian Lindner und Thomas Rösch für wunderbare Jahre, produktive Strahlzeiten und alles bedanken, was ihr in die Gruppe gebracht habt. I want to thank Ying Gao for his unstoppable effort with the target wheel. Danke an Johannes Gebhard für Innovation und Struktur und Spaß, welchen du mitgebracht hast. Die Schafkopfrunden und Debatten über Fußball oder jeden anderen Sport mit Flo, Jo und Martin werden immer ein kleines Highlight bleiben. Ich danke den besten Masterstudenten die man haben konnte: Jens Hartmann, Martin Speicher, Enrico Ridente, Rong Yang und Leonard Doyle. Danke Jens und Martin, dass ich mich immer auf euch verlassen konnte und ihr auch in LEX immer bis zum bitteren Ende da gewesen seid. Thank you Rong for all your effort, brilliance and endurance with I-BEAT. Ganz besonders bedanken möchte ich mich bei Lenny dafür, dass du das Projekt des adaptiven Spiegels zum Erfolg geführt hast und natürlich auch für die vielen Diskussionen unserer gemeinsamen Bibzeit. I want to thank Paul Bolton for discussions and guidance with my publications and many inspiring discussions. Ich möchte aber auch allen anderen danken, die im Laufe der Jahre meinen Weg begleitet haben, u.A. Felix Balling, EG, Andreas Welzmüller, Max Kögler, Derya Taray, Wenju Ma, Meilin Zhou, Matthew Sng, Klaus Allinger.

Mein besonderer Dank geht an Ulrich Schramm, für die Zweitkorrektur dieser Arbeit und die Zusammenarbeit bei I-BEAT. Mein Dank geht an das ganze Team vom DRACO, vor allem an Karl Zeil, Hans-Peter Schlenvoigt, Florian-Emanuel Brack und Florian Kroll.

I want to thank Valentina Scuderi, Katalin Hideghéty and Wolfgang Rohringer for very interesting and productive collaborations.

Ich möchte dem ganzen Team der Ionoakkustik für die Hilfe und Unterstützung bei der Entwicklung von I-BEAT danken. Ganz besonders Walter Assmann, Sebastian Lehrack für seine Hilfsbereitschaft und Anna Schmidt.

Ich möchte allen Mitarbeitern des Targetlabors danken: Jerzy Szerypo, Ulli Friebel, Simon Storck, Daniel Hahner, Sebastian Seuferling und Matthias-Alexander-Otto Haug.

Ein ganz großer Dank an unsere mechanische Werkstatt unter der Leitung von Rolf Oehm für die Geduld mit vielen Extrawünschen und schlechten Zeichnungen; ebenso der Konstruktion mit Johannes Wulz, Christoph Rahm, Klaus Wirgler und der elektronischen Werkstatt unter der Leitung von Johann Krapfl.

Danken möchte ich dem ganzen Techniker-Team von CALA: Oliver Gosau, Nik Gjotev, Dennis Gültekin, Markus Poitner, Florian Saran für die Unterstützung in jeder Lebenslage und eine wunderbare und produktive Zusammenarbeit. Ich danke Rainhardt Satzkowski für die vielen Fahrten.

Mein Dank geht an das ganze PHELIX Team in Darmstadt für den technischen, aber auch menschlichen Support bei den Strahlzeiten. Ganz besonders danke ich Bernhard Zielbauer für so vieles und dass du immer ein offenes Ohr für mich hattest!

Ich möchte mich beim ganzen Planungsteam von CALA bedanken, vor allem bei Michael Bäuerle, Martin Groß, Hans Wirth, Harald Türck und Gerhard Hagemann. Die Erfahrungen, aber auch die Wertschätzung die ich erfahren durfte haben mich persönlich sehr viel weiter gebracht. Mein Dank auch an Katharina Adler und dem ganzen Team der Buchhaltung.

Ich danke dem gesamten Lehrstuhl für Medizinphysik, im besonderen Katia Parodi, Peter Thirolf, Andrea Leinthaler, Jona Borthfeld, Felix Rauscher, Romy Knab, vor allem aber auch Franz Englbrecht und Matthias Würl für die fachlich und persönlich tolle Zusammenarbeit.

Ein ganz besonderer Dank geht an das gesamte ATLAS Team. Ich danke Stefan Karsch für seinen Einsatz, der es erst ermöglicht solch einen Laser zu betreiben. Den größten Dank an Gregor Schilling, Max Gilljohann, Hao Ding, Johannes Götzfried, Moritz Foerster, Andreas Döpp, Sabine Schindler, Johannes Wenz, Matthias Heigoldt, Konstantin Khrennikov fürs stundenlange Öckeln; für eure großartige Hilfsbereitschaft und einfach eine tolle und spaßige Zusammenarbeit, auch wenn Galgenhumor manchmal unumgänglich war.

Zu guter Letzt möchte ich mir noch Zeit, nehmen den wichtigsten Menschen die mich in meinem Leben begleiten bedanken. Meinen Freunden, die immer und in jeder Lebenslage zu mir stehen. Meinen Eltern und meiner Schwester, die mich während des Studiums und meines ganzen Lebens auf so viele Arten unterstützt haben, aber auch dem Rest meiner Familie, meiner Oma, meiner Tante und allen anderen. Aber vor allem möchte ich meinen beiden Mädels danken: Nina und Mia danke, dass ihr mein Leben jeden Tag wertvoller macht!